ISSN 2542-2049

Saint-Petersburg State University

19 International School-Conference

Magnetic resonance and its applications

Proceedings

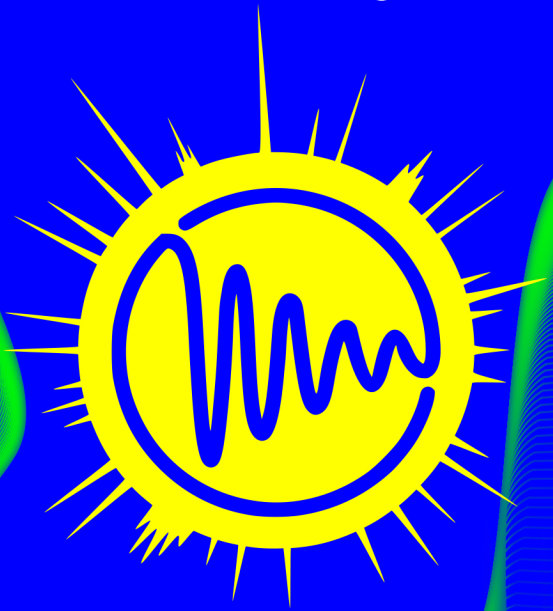

Spinus

28 March — 1 April 2022

Saint-Petersburg, Russia

SAINT PETERSBURG STATE UNIVERSITY
Department of Nuclear Physics Research Methods

19th International School-Conference

MAGNETIC RESONANCE AND ITS APPLICATIONS

Proceedings

March 28 — April 1, 2022
Saint Petersburg, Russia

Magnetic Resonance and its Applications. Spinus-2022.
Proceedings. Saint Petersburg State University, 2022. 271 pp.
ISSN 2542-2049

Schola Spinus

19th International School-Conference
MAGNETIC RESONANCE AND ITS APPLICATIONS
SPINUS-2022

ORGANIZING COMMITTEE

Chairman	Prof. Denis Markelov, SPSU
Vice-chairman	M. Sc. Alexandr Ievlev, researcher, SPSU
Committee members	Prof. Marina Shelyapina, SPSU Dr. Andrey Egorov, associate professor, SPSU Dr. Andrey Komolkin, associate professor, SPSU Dr. Pavel Kupriyanov, assistant, SPSU Dr. Konstantin Tyutyukin, senior teacher, SPSU M. Sc. Timofey Popov, SPSU
Layout of proceedings	Aleksandr Selivanov

CONTACTS

1, Ulyanovskay st., Peterhof, 198504, St. Petersburg, Russia
Department of Nuclear Physics Research Methods
St. Petersburg State University

Tel.	+7-953-350-0640
Fax	+7-812-428-7240
E-mail	spinus@spinus.spb.ru
Website	spinus.spb.ru

PROGRAM COMMITTEE

SCIENTIFIC ADVISER OF THE SCHOOL-CONFERENCE

Vladimir Chizhik	Honored Scientist of Russian Federation Honorary Professor of Saint Petersburg State University

ADVISORY BOARD

C. Cabal	Professor, Havana University, Cuba
V. I. Chizhik	Professor, St. Petersburg State University, Russia
S. V. Dvinskikh	Professor, Royal Institute of Technology, Stockholm, Sweden
J. Fraissard	Professor, University Pierre and Marie Curie, Paris, France
L. Yu. Grunin	Associate Professor, CEO, Resonance Systems, Russia
E. Lahderanta	Professor, Lappeenranta Technical University, Finland
W. S. Price	Professor, Western Sydney University Australia
B. Rameev	Professor, Gebze Technical University, Turkey
N. R. Skrynnikov	Professor, St. Petersburg University, Russia, Purdue University, USA
M. S. Tagirov	Professor, Kazan Federal University, Russia
L. M. Varela	Professor, University Santiago de Compostela, Spain
S. Vasiliev	Professor, University of Turku, Finland

Spinus

Saint Petersburg State University
spbu.ru

plscientific.se

Magicplot Systems, LLC
magicplot.com

MRRC "Spinus" SPbU, LLC
magres.ru

Contents

Preliminary Schedule

19-th International School-Conference

«Magnetic Resonance and its Applications.

Spinus-2022»

March 28 - April 01, 2022

St. Petersburg

	MONDAY – 28 March 2022
10:00 – 10:20	**Opening**
10:20 – 11:00	**Vladimir Chizhik (Saint-Petersburg, Russia)** **Lecture:** NMR in magnetic field of the Earth (NMREF)
11:00– 11:20	**Oleg Shushakov (Novosibirsk, Russia)** **Oral report:** Heat exchange impact on NMR logging while drilling
11:20 – 11:45	**Kev Salikhov (Kazan, Russia)** **Lecture:** On the theory of nutation of electron spins

11:50 – 12:10	**COFFEE BREAK**
12:10 – 12:50	**Marina Shelyapina (Saint-Petersburg, Russia)** **Lecture:** Characterization of zeolites with hierarchical porosity: Combined adsorption, spectroscopic, microscopic and diffraction techniques
12:50 – 13:10	**Ilya Sevastyanov (Kazan, Russia)** **Oral report:** Study of structural features Cu1-XPdXFeS2 compounds
13:10 – 13:20	**Natalia Gervits (Moscow, Russia)** **Oral report:** Magnetic and crystal structure of Tb-doped BiFeO3
13:20– 13:35	**Natalia Cherepanova (Novosibirsk, Russia)** **Oral report:** The investigation of SAPO-11 structure by the combination of solid-state 27Al, 29Si, 31P NMR spectroscopy and DFT calculations
13:35– 13:50	**Alina Pichugina (Surgut, Russia)** **Oral report:** The method of electron spin resonance in the evaluation of spin properties of scale and precipitation of natural waters
13:50– 14:05	**Anastasia Chepeleva (Saint-Petersburg, Russia)** **Oral report:** Development and study of novel pervaporation mixed matrix membranes based on polyphenylene oxide modified with graphene oxide for dehydration of ethylene glycol
14:05– 14:20	**Vladislav Liamin (Saint-Petersburg, Russia)** **Oral report:** Development and investigation of pervaporation membranes based on polydimethylsiloxane-block-polyphenylene oxide copolymer
14:20– 14:35	**Valerii Karpov (Saint-Petersburg, Russia)** **Oral report:** Computational aspects of carbon-lithium spin-spin coupling constants
14:50 – 15:50	**LUNCH**
15:50– 16:10	**Andrey Gavrilenko (Kazan, Russia)** **Oral report:** NMR 133Cs IN CsPbBr3+Bi Perovskites Crystals
16:10– 16:30	**Andrey Anisimov (Saint-Petersburg, Russia)** **Oral report:** Stress-controlled zero-field spin splitting of defects in SiC
16:30– 16:50	**Arseniy Slobodyuk (Vladivostok, Russia)** **Oral report:** Structure and 19F MAS NMR spectra of pentafluoridozirconic acid hydrates according to NMR spectroscopy
16:50– 17:05	**Alina Pichugina (Surgut, Russia)** **Oral report:** Characterization of spin properties of organomineral aggregates
17:05– 17:20	**Dmitry Zasukhin (Moscow, Russia)** **Oral report:** Evaluation of zeolites acidity by 31P MAS NMR spectroscopy of adsorbed phosphine oxides
17:20– 17:35	**Juan Carlos García Naranjo (Santiago de Cuba, Cuba)** **Oral report:** Proton Magnetic Relaxation in human urine
	TUESDAY – 29 March 2022
10:00 – 10:40	**Elena Tupikina (Saint-Petersburg, Russia)** **Lecture:** Investigating the mechanism of catalytic action of antioxidant enzyme glutathione peroxidase in the redox reactions of peroxides by means of quantum chemistry

10:40– 10:55	**Oleg Shavykin (Saint-Petersburg, Russia)** **Oral report:** The local orientational mobility of collapsed and swollen lysine-based dendrimer with double histidine insertions
10:55– 11:10	**Edem Chakalov (Saint-Petersburg, Russia)** **Oral report:** Formation of AHAHA– anionic clusters via out-protonation of DMAN proton sponge by phosphoric acid
11:10– 11:25	**Nadezhda Antonova (Saint-Petersburg, Russia)** **Oral report:** The stability of beta amyloid fibrils studied by molecular dynamics simulation
11:25– 11:40	**Anna Titova (Saint-Petersburg, Russia)** **Oral report:** DFT investigation of systems with three coupled NHN hydrogen bonds
11:40– 11:55	**Polina Nikiforova (Mocsow, Russia)** **Oral report:** NMR resonance assignments of NAD-dependent formate dehydrogenase
11:55 – 12:10	**COFFEE BREAK**
12:10 – 13:00	**Uwe Eichhoff (Gaggenau, Germany)** **Lecture:** In memoriam Richard Ernst Fourier Transform NMR in one and more dimensions and its significance for analytical instrumentation
13:00– 13:15	**Vladislav Koloskov (Saint-Petersburg, Russia)** **Oral report:** Improving fMRI at 1.5T with high permittivity materials
13:15– 13:30	**Viktor Puchnin (Saint-Petersburg, Russia)** **Oral report:** Demonstration of the targeted breast MRI concept at 1.5 T.
13:30– 13:45	**Anna Kalugina (Saint-Petersburg, Russia)** **Oral report:** Improving fetal MRI at 3T with compact metasurface-based pad
13:45– 14:00	**Aleksei Nasonov (Saint-Petersburg, Russia)** **Oral report:** Radiofrequency safety assessment of a volumetric wireless coil for MRI of wrist joint at 3 T
14:00– 14:15	**Olga Pavlova (Moscow, Russia)** **Oral report:** 1H and 19F MRI of the lungs in clinical and preclinical studies
14:15– 14: 30	**Julia Marcolan (São Carlos, Brazil)** **Oral report:** Coarse Resonance search for the CIERMag Digital Magnetic Resonance Spectrometer (DMRS)
14:30– 14:45	**Carlos Cabal Mirabal (Havana, Cuba)** **Oral report:** Some comments concerning the MRI impact and development
14:50 – 15:50	**LUNCH**
15:50 – 16:30	**Yuri Pirogov (Moscow, Russia)** **Lecture:** Magnetic resonance imaging on the sodium-23 and fluorine-19 nuclei
16:30– 16:50	**Nikolay Anisimov (Moscow, Russia)** **Oral report:** Multinuclear measurements on a 0.5T clinical scanner
16:50– 17:05	**Gustavo Solcia (São Carlos, Brazil)** **Oral report:** Computational fluid dynamics and magnetic resonance imaging: a study of the circle of Willis blood flow

17:05– 17:20	**Israel Reyes-Molina (Havana, Cuba)** **Oral report:** Methodology for determination of contrast agent relaxivity using MRI
17:20– 17:35	**Ariel Viña-González (Havana, Cuba)** **Oral report:** Structural Magnetic Resonance Imaging in Alzheimer's Disease. NeuroEPO Clinical Trial
	WEDNESDAY – 30 March 2022
10:00 – 10:40	**Eugeny Pestryaev (Ufa, Russia)** **Lecture:** When is the Anderson-Weiss approach to be modified by the time-domain Pake doublet?
10:40 – 11:00	**Marina Gorbunova (Chernogolovka, Russia)** **Oral report:** Influence of the structure of hard segments on crystallinity and phase separation of thermoplastic polyurethanes on the basis of poly(butylene adipate) as it's seen by solid echo Time-Domain NMR
11:00 – 11:15	**Maria Ivanova (Yoshkar-Ola, Russia)** **Oral report:** TD-NMR techniques for characterization of wood and cellulose
11:15 – 11:30	**Aleksandr Bogaychuk (Kazan, Russia)** **Oral report:** The new pulse sequence for Time Domain NMR for diamagnetic solids
11:30 – 11:45	**Anna Kosogornova (Saint-Petersburg, Russia)** **Oral report:** Synthesis and NMR relaxometry studies of self-assembling nanoclusters of SPIONs conjugated with bioactive ligands
11:50 – 12:10	**COFFEE BREAK**
12:10 – 12:50	**Yury Bunkov (Moscow, Russia)** **Lecture:** Prototypes of magnon qubit
12:50 – 13:10	**Victor Soltamov (Saint-Petersburg, Russia)** **Oral report:** Supramolecular interaction between macrocyclic Gd (III) complexes and polyaromatic systems as innovative way to enhance relaxivity
13:10 – 13:25	**Alexander Makarchenko (Kazan, Russia)** **Oral report:** Preliminary studies of the helium-3 hyperpolarization method in magnetized plasma
13:25 – 13:40	**Allisher Vasilev (Kazan, Russia)** **Oral report:** Investigation of liquid-liquid phase transition in gallium alloys under nanoconfinement
13:40 – 13:55	**Ilya Yakovlev (Novosibirsk, Russia)** **Oral report:** Application of 59Co Internal Field NMR for determination of size and structure of Co nanoparticles
13:55 – 14:10	**Denis Kan (Kazan, Russia)** **Oral report:** The 3He gas self-diffusion in oriented Al2O3 aerogels at 77 K
14:10 – 14:25	**Aleksei Semakin (Turku, Finland)** **Oral report:** Experiments with ultra-cold atomic hydrogen

14:25 – 14:40	**Georgii Andreev (Kazan, Russia)** **Oral report:** Low-temperature study of magnetization and magnetostriction of LiYbF4 in strong magnetic fields
14:40 – 14:55	**Guzel Musabirova (Kazan, Russia)** **Oral report:** Do 5-HT Receptor Ligands Modulate the Phase Behavior of Complex Lipid Bilayers?
14:55 – 15:50	**LUNCH**
15:50 – 18:40	**POSTER SESSION** Oral blitz reports of young scientists (5min × 15);

	THURSDAY – 31 March 2022
10:00 – 10:40	**Vladimir Matveev (Saint-Petersburg, Russia)** **Lecture:** Relatively novel liquid electrolytes: comparison of macroscopic and microscopic properties
10:40 – 11:00	**Sergey Dvinskikh (Stokholm, Sweden)** **Oral report:** NMR study of hydrogen bonding in mesogenic ionic liquids
11:00 – 11:15	**Milosh Ubovich (Saint-Petersburg, Russia)** **Oral report:** Effect of addition of Al(NO3)3 on molecular mobility in ethylammonium nitrate. A molecular dynamics simulation study
11:15 – 11:30	**Julia Pronina (Saint-Petersburg, Russia)** **Oral report:** Regio-isomers of 2,5,6,7,8-pentaaryl-1H-azepino[3,2,1-ij]quinazoline-1,3(2H)-dione containing various aryl substituents in the azepine ring: structures determination using NMR methods
11:30– 11:45	**Alexander Khudozhitkov (Novosibirsk, Russia)** **Oral report:** 2H NMR study of structure, hydrogen bond dynamics and phase transition in a model ionic liquid electrolyte
11:50 – 12:10	**COFFEE BREAK**
12:10– 12:30	**Sergey Vasil'ev (Chernogolovka, Russia)** **Oral report:** The self-diffusion of 128-arm star-shaped polydimethylsiloxanes with a dendritic branching center
12:30– 12:45	**Nadezhda Pokhvishcheva (Saint-Petersburg, Russia)** **Oral report:** Application of NMR-diffusometry for diffusion studies in plasticized polymeric membranes of ion-selective sensors
12:45– 13: 00	**Valeriya Shpotya (Dolgoprudniy, Russia)** **Oral report:** Diffusion ordered spectroscopy (DOSY NMR) for solutions of biocompatible compounds with similar structure but different mass
13: 00– 13: 15	**Nikita Slesarenko (Chernogolovka, Russia)** **Oral report:** Investigation of Mechanism of Ionic and Molecular Transport in the Nafion Membrane by NMR
13: 15– 13: 30	**Mark Kaplanskiy (Saint-Petersburg, Russia)** **Oral report:** Quantum-chemical investigation of factors driving the extremal value of 1H NMR chemical shift for central symmetric hydrogen bonds

13: 30– 13: 45	**Sergei Sheludiakov (Pittsburgh, US)** **Oral report:** Purely spatial diffusion of H atoms in solid normal and para-hydrogen films
13: 45– 14: 00	**Olga Lezova (Saint-Petersburg, Russia)** **Oral report:** Investigation by 1H NMR spectroscopy of the composition of the reaction mixture at the production of hybrid ion-conducting membranes based on polyvinyl alcohol
14: 00– 14: 15	**Korostelev Vladislav (Saint-Petersburg, Russia)** **Oral report:** The NMR Chemical Shift of a Helium-3 Atom as a Probe for Aromatic and Antiaromatic compounds
14: 15– 14: 35	**Tatiana Gavrilova (Kazan, Russia)** **Oral report:** Magnetic properties of Li3V2(PO4)3/C and Li3V2(PO4)3/Li3PO4 composites: ESR measurements
14:35– 16:00	**MEETING OF AWARDING COMMISSION**
16:00 – 16:30	**AWARDING and CLOSING**

POSTER SESSION (Wednesday, 15:50 – 18:40)			
1	Stanislav	Garkavyi	Magnetic fields in natural semiconductor materials from NMR data.
2	Nina	Djapic	The COSY spectrum in the sugar unit of a tetrapyrrole
3	Viktor	Demidov	Inhibitors of tumor cells proliferation, fungicides and DNA complexones — electron-rich 1,10-phenanthrocyanines of d-elements, structural analogues and potential antagonists of NADH: ESR spectroscopy of temperature accessible excited electronic triplet biradical states
4	Alexey	Salin	Identification of diastereomeric forms of vicinal bisphosphonates and bisphosphine oxides using NMR spectroscopy
5	Vasilii	Pelipko	Homo- and heteronuclear experiments of NMR spectroscopy in the structural study of polysubstituted furans
6	Igor	Veyshtort	Hole burning in ODMR spectra in isotope-modified SiC
7	Milosh	Ubovich	Orientational and translational mobility in ionic liquid propylammonium nitrate
8	Alexander	Selivanov	Transport properties of Ionic Liquid [BMIM][SCN] obtained by Molecular Dynamic Method
9	Lyubov	Kozinskaya	Comparison of calculated and experimental data of 1H and 13C-NMR spectra of 4′,4′′-di-(1-methyl-1-hydroxyethynyl)-dibenzo-18-crown-6
10	Dmitriy	Blokhin	Structure of the amyloidogenic peptide SEM1(68-107) by NMR spectroscopy and molecular dynamics
11	Mariia	Dmitrenko	Development and study of polyacrylonitrile membranes modified with titanium dioxide for enhanced pervaporation dehydration
12	Aleksandra	Kusova	FIBRINOGEN TRANSLATIONAL DIFFUSION AND INTERMOLECULAR INTERACTIONS DEPENDING ON ELECTROLYTE SOLUTION
13	Sharipova	Leila	Internal mobility of hydroquinone pillar[5]arene fragment in a inclusion complex according to NMR spectroscopy data
14	Aleksandra	Korniak	Development and investigation of ultrafiltration polyacrylonitrile membranes modified with titanium dioxide
15	Anna	Kuzminova	Development and characterization of novel pervaporation and ultrafiltration membranes based on polyphenylenesulphone
16	Nataliia	Garaeva	NMR assignments of the Ribosome maturation factor P of Staphylococcus aureus (SaRimP)
17	Vladislav	Stanishevskiy	Mapping of experimental vs quantum-calculated 15N-C spin interactions sharply increases the reliability of elucidating the structure of nitrogen-containing compounds
18	Danila	Myznikov	Novel pervaporation membranes based on hydroxyethyl cellulose/sodium alginate for separation of isopropanol/water mixture

19	Sharipova	Leila	Interaction of surfactant with albumin protein according to NMR data
20	Daria	Bychkova	Relaxation of protons and heteronuclei in cyclosporins
21	Polina	Skvortsova	Structure and membranotropic properties of peptides and synthetic macrocycles
22	Mark	Smirnov	1H High-resolution NMR relaxometry for olive oil research
23	Anna	Kuzminova	Development and characterization of novel Zr-MOFs-modified membranes based on polyvinyl alcohol
24	Irina	Yefimova	Molecular Dynamics simulation of Zinc(II) and Copper(II) binding to amyloid-β(1–16) peptide in aqueous solution, saline solution and double saline solution with Na+ ion
25	Anastasia	Nikitina	MRI methods in the diagnosis of accumulation of iron complexes in the brain
26	Anna	Faleva	Determination of differences in the chemical structure of softwood dioxane lignin using chemometric analysis of two-dimensional HSQC spectra
27	Vladislav	Panov	NMR studies of two polymorphic MoTe2 modifications at room temperature
28	Ivan	Mershiev	Composite pulses with discrete phase modulation, optimized using genetic algorithm
29	Albina	Gafarova	Multifrequency EPR Study and DFT-Assisted Identification of Radicals in γ Irradiated Sodium Gluconate
30	Vladimir	Bazaykin	Diffusion of Toluene and Methanol in composopzite systeme: Poly-m-Phenyleneisophthalomide and MOF By Molecular Dynamics Simulations
31	Arseniy	Slobodyuk	Ionic properties of pentafluoridozirconic acid hydrates according to NMR spectroscopy
32	Artyom	Skomorokhov	Study of the influence of mechanical stress on the splitting of spin sublevels in hexagonal SiC
33	Anastasiya	Kovalenko	Study of TiO2@SiO2 composite nanoparticles by solid state NMR 29Si
34	Valerii	Bezrodnyi	Histidine-rich lysine-based dendrimer and its interaction with molecules of therapeutic tetrapeptide at two different pH
35	Adeliya	Garaeva	Anomalous magnetic properties of micro- and nanoscale DyF3 powders.
36	Kenan	Mamedgasanov	Ionic liquid in the process of extraction cleaning of various fractions of Azerbaijani oil

Spinus

The School-Conference "Spinus" of Saint Petersburg State University

The St. Petersburg State University (SPbSU) holds International School-Conference "Magnetic resonance and its application" (Spinus) since 2004. "Spinus" is organized in according to the subjects of researches and Master Programs, which have been developed and implemented in the SPbSU. In modern physics, the term "magnetic resonance" refers to a set of phenomena accompanied with the emission or absorption of electromagnetic waves of the radiofrequency diapason by quantum systems (nuclei, electrons, atoms, molecules, etc.). These phenomena, the physical nature of which is of independent interest, provided the basis of radiospectroscopic methods for studying the structure of matter and physical-chemical processes in it. They are also used for the creation of quantum generators, amplifiers, and magnetometers. For the development of ideas and applications of magnetic resonance six Nobel Prizes were awarded in the areas of physics, chemistry, biology, physiology and medicine (the latter was in 2003).

Primarily, magnetic resonance methods are:

- Nuclear Magnetic Resonance (NMR)
- Electron Paramagnetic Resonance (EPR)
- Nuclear Quadrupole Resonance (NQR)

These methods, being contactless, do not destroy an object under a study, that makes them unique and in demand not only in physics and chemistry, but also in medicine, geology, biology, archeology. Now, any medical center with high reputation has a magnetic resonance imaging (MRI). In Russia, NMR is used in oil well logging, laboratory analysis of the productivity of oil-bearing reservoirs, analysis of oil content and moisture of seeds; EPR technique is used for geological research, non-destructive control of precious stones, as well as for the dating of paleontological artifacts; there are NQR applications for remote detection of solid explosives and narcotics. Magnetometry methods based on magnetic resonance are indispensable for carrying out archaeological researches.

Earlier the school organizers worked at the Department of quantum magnetic phenomena (QMPh) of the St. Petersburg State University, which was founded in 1993 on the initiative of Professor V. I. Chizhik on the basis of the laboratory, created in the 50s of the last century by F. I. Skripov at the Department of Radio Physics (the branch "Quantum Radiophysics"). On January 1, 2014, the Department of QMPh joined the united Department of nuclear-physics research methods (Head of the Department is Corresponding Member of the Russian Academy of Sciences, Professor Mikhail Kovalchuk). The QMPh collective has a number of priority works in the field of nuclear magnetic resonance. One of the most significant achievements was the first in the world implementation (in 1958) of the Fourier transform of a free induction signal in order to obtain a NMR spectrum (see the details in [1]). Concurrently with the research activity, the staff of the department are actively involved in the development of practical applications of magnetic resonance. The department graduates work not only in Russia and the CIS, but also in Sweden, USA, New Zealand, England, Cuba, Germany, France, Italy, occupying positions from a highly advanced operator of radiospectrometers to a professor.

The main research areas developing in the team of quantum magnetic phenomena:

- Nuclear magnetic relaxation in liquids;
- Nuclear magnetic resonance in solids, including magnetically ordered materials;
- NMR in liquid crystals;
- NMR in heterogeneous systems;
- MRI in weak magnetic fields;

- Electron paramagnetic resonance;
- Nuclear magnetic resonance in the magnetic field of the Earth;
- The quantum magnetometry in archeology.

It is evident from the above that the scope of our research interests is quite wide. We are always open for the collaboration with researchers from various fields of science.

Our team has published a series of monographs, textbooks and training manuals on Magnetic Resonance. For example:

1. Vladimir I. Chizhik, Yuri S. Chernyshev, Alexey V. Donets, Viatcheslav Frolov, Andrei Komolkin, Marina G. Shelyapina. Magnetic Resonance and Its Applications. 2014, Springer-Verlag. 782 pp. *(Now more than 35000 chapter downloads).*
2. Квантовая радиофизика: магнитный резонанс и его приложения. Учеб. пособие. 2-е изд., перераб. Под ред. В. И. Чижика. – СПб.: Изд-во С.-Петерб. ун-та, 2009. 700 с.
3. В. И. Чижик. Ядерная магнитная релаксация. Учеб. пособие. 3-е изд. – СПб.: Изд-во С.-Петерб. ун-та, 2004. 388 с.
4. Практикум по магнитному резонансу. Учебное пособие. Под ред. В. И. Чижика. – СПб.: Изд-во С.-Петерб. ун-та, 2003. 184 с.

Due to the COVID-19 coronavirus pandemic and the continued ban on holding any public events, the Organizing Committee of “Spinus-2022” have decided to implement the School-Conference in the on-line format using ZOOM (not in a face-to-face format). We hope that next “Spinus 2023” will be held the usual format! We will be very glad to see you at next conference! Welcome!

Dr. Sci., Professor, SPbSU, Denis A. Markelov
Chairman of Organizing committee of the 19th School-conference
“Magnetic resonance and its applications” Spinus-2022

References

1. V.I. Chizhik. On the history of the Fourier transform in NMR spectroscopy. 2018, BULLETIN DU GROUPEMENT AMPERE, 67, № 4 (273), p 5-6.

Lectures

Prototypes of the magnon qubit.

Yu. M. Bunkov

Russian Quantum Center, Skolkovo, 143025 Moscow, Russia.
Email: y.bunkov@rqc.ru

Magnon Bose-Einstein condensation (MBEC) was discovered in the famous experiments on pulsed NMR in superfluid ^{3}He, in which it led to a narrowing of the magnetic resonance line by a thousand times [1]! Then magnonic BEC was discovered in antiferromagnets [2] and finally in a film of yttrium iron garnet (YIG) at room temperature [3,4]. The unique properties of MBEC open new possibilities for its application to quantum computing. Unlike the traditional quantum system based on several oscillators, the magnon BEC is a collective macroscopic system of magnons in the same coherent quantum state. It has several fundamental advantages over previously developed systems for quantum computing.

1. **Critical temperature**. The critical temperature that destroys the quantum memory of quantum qubit is determines by its working frequency w. For the qubit to function, its temperature must be significantly lower than hw/k. In the case of MBEC, we are dealing with a macroscopic ensemble of oscillators in a single coherent state. Their number can reach values of the order of 10^{20}! Therefore, the absorption of a finite number of thermal excitations cannot change the state of the MBEC. To destroy quantum memory, the number of excitations must be increased by a factor of N or SQRT(N), where N is a density of particles in MBEC. In any case, we are reaching temperatures above room temperature. This means that a quantum qubit based on MBEC can operate at room temperature.
2. **Temperature.** Currently, the most developed are qubits based on superconductivity, which exists at temperatures of several kelvins. Even lower temperatures require qubits based on atomic BEC. Magnons are quasiparticles, and the formation of MBEC requires not a decrease in temperature, but the excitation of a sufficient number of nonequilibrium magnons. Theoretically, it is shown that for the formation of MBEC at room temperature, it is sufficient to deviate the equilibrium magnetization in yttrium iron garnet (YIG) by an angle of more than 3° [5].
3. **Quantum information.** Usually, reading the state of a qubit leads to its destruction. In the case of MBEC, the use of a certain number of magnons for reading information does not change the state of the qubit. Therefore, the process of quantum computing and reading information can be continuous.
4. **Permanent state of MBEC.** Magnons are quasiparticles whose density decreases with time. Therefore, a magnon qubit can operate at times much shorter than the decay time, or under conditions of continuous pumping of magnons. In the latter case, it should be taken into account that the newly born magnons fall into the MBEC state according to the laws of quantum mechanics and therefore do not destroy the quantum state of the qubit.
5. **Permanent read out.** Usually, reading the state of a qubit leads to its destruction. In the case of MBEC, the use of a certain number of magnons for reading information does not change the state of the qubit. Therefore, the process of quantum computing and reading information can be continuous.

At the Russian Quantum Center, we are working on the creation of quantum qubits based on magnon Bose condensate. In particular, a 5 mm MBEC platform was obtained, on

which the MBEC exists continuously in the region far from RF pumping. In addition, we managed to create an optical readout of the magnon density [6]. The report will present projects of possible qubits based on MBEC [7, 8].

The work is made in a frame of Russian Roadmap on Quantum Technologies by Rosatom. Financial support by the Russian Science Foundation within the Grant 19-12-00397 “Spin Superfluids” is gratefully acknowledged.

References

1. A.S. Borovik-Romanov, et al. JETP Letters, 40, 1033 (1984).
2. Yu. M. Bunkov, et al., Phys. Rev. Lett. 108, 177002 (2012).
3. Yu. M. Bunkov, et al., Scientific Reports, 11, 7673 (2021).
4. M. Schneider, et al., Nat. Nanotechnol. 15, 457–461 (2020)
5. Yu. M. Bunkov and V. L. Safonov, J. Magnetism Magnetic Materials, 452, 30–34 (2018).
6. P. E. Petrov, et al., Optics Express 30, 1737 (2022)
7. P. M. Vetoshko, et al., JETP Lett., 112, 299 (2020).
8. Yu. M. Bunkov, JETP, 131, 18 (2020).

NMR in magnetic field of the Earth (NMREF)

Vladimir I. Chizhik, Pavel A. Kupriyanov

Faculty of Physics, Saint-Petersburg State University, Ulianovskaya 1, 198504, Saint-Petersburg, Russia
E-mail: v.chizhik@spbu.ru

In the Saint-Petersburg State University, the fundamental researches in the area of nuclear magnetic resonance have been carrying out since the beginning of the 50-ies of the last century. Basing on them, a number of practical applications have been developed, and the results, obtaining in the area of NMR in the magnetic field of the Earth, are presented in the report.

The NMR sensitivity strongly depends on the magnitude of a static magnetic field B0, but the experience shows that the registration of NMR signals is possible even in the Earth magnetic field (~0,5·10–4 Tl). To compensate the decrease in NMR signals in the Earth magnetic field some techniques are used, in particular: (i) an additional magnetic field for the pre-polarization of nuclei and (ii) receiving coils of complex geometry, which allows the neutralization of external electromagnetic hindrances. New aspects and possibilities of the NMR spectroscopy in the Earth magnetic field were elucidated in the last decades (see, for example, [1, 2]). Even in the best modern NMR spectrometers an instrumental broadening is about 100 mHz and this value is worse than a natural NMR line width in many liquids (at least for protons). The Earth magnetic field is very homogeneous and therefore the natural line width can be detected. It is worth to be reminded that the first in the world practice real Fourier-transform of a nuclear free induction signal for the obtaining of a NMR spectrum was performed in experiments in the Earth magnetic field [3].

The new original developments of NMR in the magnetic field of the Earth are presented: (i) The pre-polarization of nuclei using the alternating magnetic field of low frequency can provide the increase in sensitivity of the method and/or decrease in power consumption of a spectrometer. The description of the process can be carried out on the basis of the Bloch equation using the “swinging” coordinate system. The application of the alternating magnetic field can help to decrease transient processes in an NMR sensor if the polarization current is switched off at the certain phase. At the moment, we have managed to implement 50 Hz. (i) The neutralization of the effect of fluctuations of the Earth magnetic field gives the possibility to realize necessary accumulation of NMR signals for the detection of weak satellites in spectra (Fig. 1).

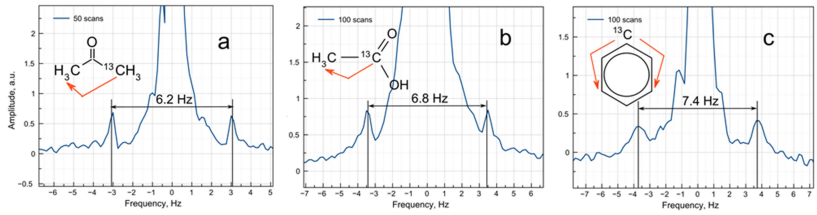

Fig. 1. NMR spectra in Earth field of acetone (a), acetic acid (b) and benzene (c). The figures show the J-coupling constants. The amplitude of the main line is 100 a.u.

The method considered allows the analysis of liquids enclosed in sealed containers (including bottles) of various volumes and shapes. Besides, it is possible to analyze liquids in containers (cans), the shells of which are made from thin non-magnetic metals (see Fig. 2) but

in this case the thickness of shell walls must be much less than a skin-layer for electromagnetic waves in a metal. The NMR frequency for ^{1}H nuclei in the Earth magnetic field is about 2 kHz and the skin-layer for copper and aluminum is approximately of 2 mm.

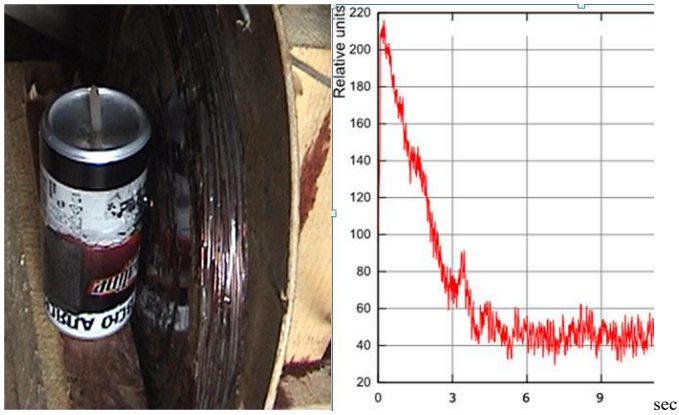

Fig. 2. A signal from water inside an aluminum can (right) using a disc-shaped sensor (left).

Besides, the NMREF allows the investigation of macroscopic flows in big pipes and open reservoirs [4]. It is also possible to use NMR for exploration of underground water deposits.

The first publications on MRI in the Earth magnetic field (EFMRI) appeared in 80-ies. The following development of EFMRI is reflected, for example, in the works [5, 6].

References

1. S. Appelt, H. Kühn, F. W. Häsing and B. Blümich, Nature Physics, v. 2, 105 (2006)
2. S. Appelt, F. Häsing, H. Kühn, U. Sieling, B. Blümich. Chem. Phys. Letters. № 440, 144 (2007)
3. A.A. Morozov, A.V. Melnikov, F.I. Skripov. Bulletin of the Academy of Sciences of the USSR, Physical Series (in English), Vol. 22, 1127 (1958).
4. N.M. Vecherukhin, A.V. Melnikov, and P.M. Borodin. Applied Magnetic Resonance, v. 22, 483 (2002).
5. A. Mohorič, G. Planinšič, M. Kos, A. Duh, J. Stepišnik, Instrum. Sci. Technol., v. 32, 655–667 (2004)
6. J. Stepišnik, V. Eržen, M. Kos, Magn. Reson. Med., v. 15, 386 (1990)

In memoriam Richard Ernst Fourier Transform NMR in one and more dimensions and its significance for analytical instrumentation

Uwe Eichhoff

Bruker BioSpin GmbH retired; D 76571 Gaggenau, Germany, Max Hildebrandt-Str.40
e-mail: barbara.uwe@t-online.de

Introduction

I was inspired to this lecture after reading the autobiography of Richard Ernst, awarded with the Nobel Price in Chemistry 1991. He who died at the fourth of june this year. Unfortunately his autobiography appeared only at a small swiss editor specialized in swiss celebrities and in german language. I believe it should be of interest to everybody interested in NMR. I knew Richard Ernst over a long time, I had often listened to his lectures, held seminars with him and visited him in his laboratory. I was not only fascinated by his extraordinary work but as well by his personality. With this lecture I hope to transfer a bit of my feelings for him to you. Along with citations from his autobiography I will shortly go through his scientific achievements which extend far beyond NMR.

Richard Ernst: first steps into NMR and Fourier Transform NMR

Richard Ernst studied physical chemisty1952-1956 at the ETH Zürich and obtained a degree as chemical engineer ETH. For his PHD-thesis „NMR spectroscopy with stochastic HF-fields“ under the supervision of Hans Primas and Hans Heinrich Günthard he received the silver medal of the ETH Zürich in 1961. In 1963 he joined the instrument division of Varian Associates in California to work with Wesley Andersons on optimization of NMR spectrometers. In 1964 they discovered the Pulse-Fourier-Transformation-NMR [1]. We can follow this discovery in the laboratoty diary of Richard Ernst. He had been very successfull at Varian, but in 1968 the situation at Varian had changed. The Varian brothers had died and the new managers at Varian had no understanding of the potential of Fourier-methods, although this could have been a real gold-mine. Therefore Ernst decided to go back to the ETH Zürich, where Hans Heinrich Günthard had offered him a job an job as assistant in the laboratory of physical chemistry. Finally it was not Varian but the swiss-german company Bruker, who in 1969 consequently developed a new spectrometer concept based of Fourier-transformation. At Bruker the first ^{13}C-spectra have been measured, a revolution for organic chemistry. The multiplex advantage of FT-NMR finally increases sensitivity by a factor up to 1000 and extended NMR from the most sensitive nuclei ^{1}H, ^{19}F and ^{31}P to all magnetic nuclei of the Mendeleev periodic table. But still many scientists still did not believe in the advantages of Fourier-spectroscopy. In 1972 Bruker developed the first pure Fourier spectrometer, omitting all the complicated electronics for cw-spectroscopy. This was the ancestor for all future spectrometer generations until today. But looking back, the return to the ETH Zürich in spring 1968 after the productive and inspiring years in California appeared to Ernst like falling back into the middle age. His work was simply ignored or there was no interest in innovations. He was 36 years old and afraid, that he would miss his scientific goals. The frustrating work at the ETH on Eastern 1970 resulted in a complete nervous breakdown, which could have easily stopped his further scientific career.

A new chance: Two-dimensional NMR Spectroscopy [2]

In 1971 fortune gave Ernst a new chance. One of his PHD-students brought him an inestimable finding from a summer school for young scientists in Baške Polje. In a lecture,

which he never published, Jean Jeneer proposed to excite the spin system with two pulses and to record the signal after the second pulse after interaction of the spins with each other. This should give more information on the state and position of the atoms in the molecule. Ernst had understood the idea of 2D-spectroscopy immediately. He writes: *It appeared to me as if I listened to music. The sounds from the various instruments follow each other, they overlap in a crescendo and diminuendo, forte, piano, pianissimo. The spins react, they speed up or slow down with a second pulse, some of them have a gloomy, some a bright sound, some of them can hardly be heard. My feeling of harmony and disharmony for wavelike appearings and decreasing sounds and frequencies helped me enormously to transfer myself into the world of NMR and to develop further the idea of Jean Jeneer.* He discussed with his students, if it was`nt unethic to publish his results, before Jeneer published his idea. But he never published it. He kept had permanent contact with Jeneer and informed him regularly about his our results. Later he told Ernst, that he was always happy to receive news from Zürich. In 1976 Ernst got together with his collegue Kurt Wüthrich [3] funds for a common project *development and application of 2D-NMR in biomolecules*. This was the starting point of a ten years lasting successfull cooperation, which became famous as the *Zürich group*. The basic idea of Jeener finally led Ernst into the field of medical imaging. He had the idea to apply the Fourier transform technique to imaging instead of the projection-recovery method used by Paul Lauterbur [4]. This Fourier-imaging method [5] is now the basis for almost all NMR imaging techniques.

Nobel Price in Chemistry 1991

In 25 years of hard work Richard Ernst had revolutionized NMR. The introduction of Fourier Transform had increased its sensitivity by a factor of 1000, had opened NMR for all magnetic nuclei of the periodic table, multidimensional NMR had increased the information content of the technique by orders of magnitude, furthermore Fourier imaging had become the basis for all modern MRI methods. The Nobel price was the final recognition for all his achievements. He writes: *For me receiving the Nobel price was an unbelievable satisfaction. Many years every day I had taken the train from Winterthur to Zürich to be at 7h in my office, then at 20h back to supper at home and three more hours to work at home. I almost never had holidays. I was delighted to receive the Nobel price but at the same time painfully touched, because I was the only laureate. Normally the price is divided between three or at least two scientists. Today success in science is the result of a team work. The main reason for this feeling was my colleague Kurt Wüthrich, who also was believed to be a candidate. He believed to have lost any chances, because it seemed unlikely, that in the near future another price would awarded in this field. He went really furious and asked me in a letter never more to mention his results in my lectures. This ended in 2002 when nevertheless he himself got the Nobel price. I immediately sent him a letter and wrote into my diary: Now I feel free. I understood, that we had gone on different ways and now accepted each other. A month later he visited me in my laboratory and we had a very open discussion and he apologized for his annoyance in 1991.*

Fourier spectroscopy in analytical instrumentation

The Fourier technique introduced by Ernst was not limited to NMR [6]. The first method, which comes to our mind, is its elder brother, EPR. Nevertheless it took more than 20 years until its full implementation and Arthur Schweiger [7] in the group of Richard Ernst played a major role. Many problems which had to be overcome. The electron relaxation times are about a thousand times shorter than in NMR. No such fast analog/digital converters were aavailable. To excite the broad EPR spectra short microwave pulses were necessary and this meant high microwave power. The available resonators had long dead times and the signals

disappeared before recording. Lowering the Q of the resonator means loss of sensitivity. Therefore for most samples EPR-Fourier-spectroscopy does not lead to an increase in sensitivity like in NMR.

In 1979 combining a modified NMR console with a horizontal superconducting magnet Bruker entered the field of Mass spectroscopy with the first commercial Fourier Mass Spectrometer based on the principle of Ion Cyclotron Resonance [8]. The heart of the FTMS spectrometer is the ion cyclotron resonance cell. The ions are guided to an electrostatic cell located in the center of the superconducting magnet. The potential on the plates of this cell traps the ions which perform a rotation with the cyclotron frequency $\omega_c = qB_0/m$, which is inversely proportional to their mass. These rotating ions induce a mirror current in the plates of the cell. The signal is similar to a free induction decay in NMR and Fourier transformation yields the mass spectrum. Since frequency is the physical parameter, which can be measured with the highest accuracy, the resolution is much higher than for any other mass-spectroscopic method and can reach several millions. In FTMS ionization and detection are locally well separated and therefore any ionization method can be used.

The next and probably best known Fourier method is IR-spectroscopy[9]. In the classical Michelson interferometer half of the intensity of the IR beam passes the beamsplitter, is reflected back from the fixed mirror and passes the beamsplitter to the detector. The second half is passed through the beamsplitter, reflected from the moving mirror and reflected to the detector, where both halves interfere with each other. Fourier transformation of the interferogram yields the IR spectrum. The application extend from atmopheric research to investigation of art objects under a microscope. Tankas, tibetian roll paintings were a passion of Richard Ernst. Using a FT-Raman-microscope in his home-laboratory he became a well known expert in investigation of pigments and dating of these art objects.

Richard Ernst the legacy

Nobel price winners become persons of public interest and often are asked to speak about general problems. Richard Ernst concentrated on the questions of ecology and education. He told the public: *I understand education in an all-comprising sense. It should build a complete personality and character. It should give not only knowledge from books but lasting values. It should include all religions and philosophies. Only such an education will create critical personalities, which are able to estimate our situation. Multidisciplinary education is a must for all people working at the frontiers of science. I am convinced that a scientist with experience in many fields will bring more intuition into his work. Therefore for me it was important to put my life on more than one leg. For me this were art, especially the tibetian paintings, and classical music. The arts create worlds, which include the complete bandwidth of all human values, from the cold science over fancy dreams to overwhelming emotions, which cannot be expressed in words. For me music played this role.. My life was a hard journey full of emotional heights and depths. This might be true for any sensitive person, but I believe to be rather excessive in this respect. I often felt thrown from one extreme to the other and when ever I had arrived at a summit I was frightened to a fall down into a deep bottomless gorge. I do not remember how I appeared and I probably will not recognize when I will be ready to go. Sometimes I awake and do not remember, how and where I fell asleep. It is like a slow departure, not painful, not frightening, only in the wish to find my eternal rest.* This finally happened on the fourth of june 2021.

References

1. .R.Ernst, W.A.Anderson, Rev.Sci.Instrum. 37, 93 (1966)
2. R.R.Ernst, G.Bodenhausen, A.Wokaun, Clarendon Press Oxford 1987, Principles of Nuclear Magnetic Resonance in One and Two Dimensions
3. K.Wüthrich, NMR of Proteins and Nucleic Acids, Wiley New York 1986

4. P. C.Lauterbur, Nature 242, 190 (1973)
5. A.Kumar, D.Welti, R.R.Ernst, J.Magn.Reson. 18, 69 (195)
6. A.G.Marshall,F.R.Verdun, Fourier Transforms in NMR, Optical, and Mass Spectrometry, Elsevier Amsterdam-Oxford-New York-Tokio 1990
6. A.Schweiger, G.Jeschke, Oxford University Press, Oxford 2001, Principles of Pulse Electron Paramagnetic Resonance
7. M.V.Buchanan, CS Symposium Series 359, Fourier Transform Mass Spectrometry:Evolution,Innovation and Applications
8. J.Bell, Introductory Fourier Transform Spectrometry Academic Press New York 1972

Relatively novel liquid electrolytes: comparison of macroscopic and microscopic properties

Vladimir V. Matveev

Department of Nuclear Physics Research Methods, Saint Petersburg State University, 199034, 7/9 Universitetskaya nab., Saint Petersburg, Russia
E-mail: v.matveev@spbu.ru

Two relatively new types of electrolytes have attracted particular attention in the last two to three decades. The first group is the so-called "3rd generation ionic liquids" (ILs), i.e. low-temperature molten salts with organic cations. Usually, this group is divided into several subgroups. The main ones are:

1. Protic ILs. These include, in particular, the original, historical IL, EAN, i.e. ethylammonium nitrate, $[CH_3CH_2NH_3]NO_3$.

2. Aprotic ILs. These are the most common and numerous systems in which the cation does not contain hydrogen atoms associated with oxygen, nitrogen, etc. (examples will be given in the lecture).

3. Inorganic ILs. There is still some uncertainty of terminology, but this term is mainly applied to solutions of inorganic salts in the ILs of the first two groups. Obviously, this group can include a fairly extensive list of objects.

It was also found that some of the traditional highly concentrated solutions of inorganic salts in water and/or organic (non-aqueous) solvents exhibit properties characteristic of ionic liquids, therefore can be attributed (formally or substantially) to group 3.

It turned out that this new class of liquid systems namely, ionic liquids, have significant potential for practical application in various branches of chemistry and technology. Without dwelling on all possible applied aspects, we have noted only their use as electrolytes for supercapacitors and metal-ion batteries. As a result, a significant number of studies of pure ionic liquids and ILs-based electrolytes have been carried out to date. This applies both to the study of traditional chemical (bulk) properties, such as density, viscosity, electrical conductivity etc. and properties at the molecular level (diffusion, NMR spectra and NMR relaxation, etc.). Such a volume of data allows for a more or less systematic comparison of the bulk and molecular characteristics of the same systems in order to establish connections between these characteristics. In the presented lecture, some comparisons of this type will be summarized, based both on literature data and the results of our own experiments.

The second group is the so-called "deep eutectic solvents, DES", which are mixtures of two (or more) substances with a melting point significantly lower than that of each of the constituent substances. A significant part of such objects is based on the use of the “choline" cation salts, i.e. on systems close to ionic liquids. These systems, DES, have proved to be promising solvents for a number of processes in chemistry and chemical technology and, as a result, are actively being investigated. There are not yet large amounts of data that allow for a systematic comparison of macroscopic and microscopic parameters, however some examples of this kind are given in the lecture as well.

The main part of NMR measurements has been carried out in the Center for Magnetic Resonance of Research Park of Saint Petersburg State University.

When is the Anderson-Weiss approach to be modified by the time-domain Pake doublet?

Eugeny M. Pestryaev

Department of Physics, Ufa State Petroleum Technological University, Ufa, Kosmonavtov St., 1, 450062, Russian Federation
E-mail: physics_usptu@mail.ru

Introduction

A shape of the NMR free induction decay (**FID**) in polymer melts undergoes qualitative changes at transition from oligomers to entangled polymers. Along with the Lorentzian exponential – typical for liquids – the Gaussian-like-exponential component – typical for solids – arises and grows in population, what had been disclosed by J.P. Cohen-Addad [1] as early as in 1974 and V.D. Fedotov & V.M. Chernov [2] in 1975. To date, it has been established in multiple experiments that the slow relaxing liquid-like component is caused by the relatively free moving polymer chain ends. The initial fast relaxing solid-like component of the largest population is due to anisotropy of the segmental high-frequency fluctuations that, in turn, is induced by entanglements, which are mostly quasi-static in the NMR time scale.

Several researchers, including both pioneers [3, 4], have later found variety of the approximate theoretical descriptions of the initial dominant component during the past more than 40 years. The variety of such solutions has just demonstrated the incompleteness of these searches and required the physical understanding this inconsistency, what has been realized by the molecular dynamics simulation.

Simulating the FID shape in entangled polymer melt

The first attempt to simulate the entangled melt FID, $g(t)$, by the conventional Anderson-Weiss approach (**AWA**) [5] has been failed [6]: It has not reproduced the liquid-like component [4], although all chain Kuhn segments were used in the FID calculation. It implied that the most theoretical studies actually based on this approach have implicitly used untenable assumption that the spin system of the entangled chain represents an ergodic ensemble. The second attempt has been more successful [7, 8] because it was based on the FID definition [9] accounting for not only the possible non-ergodicity but also dynamic heterogeneity of the entangled chain:

$$g(t) = \frac{2}{N}\sum_{i=1}^{N/2}\langle\cos\varphi_K\rangle, \quad \varphi_K = S(i)\cdot b_K\int_0^t[3\cos^2\theta_i(t') - 1]\,dt'. \qquad (1)$$

Here, N is the number of Kuhn segments in the freely jointed chain with entanglement length N_E; φ_K is the precession cumulative phase due to the segmental motion; $\theta_i(t)$ is the fluctuating in time t angle of the i-th segment relative to the external magnetic field. Two multipliers before integral defines a dipolar coupling (**DC**) carried by separate segment and being a function of its position in chain, *S(i)*: several chain-end segments move freely therefore $S(i \leq 2\cdot N_E) < 1$ and asymptotically tends to 1; middle-chain segments are constrained therefore $S(i > 2\cdot N_E) = 1$ and the DC amplitude is b_K, which is carried by the Kuhn segments and is the simulation variable. The angle brackets denote the average over pairs of identical segments for all chains in the simulated monodisperse melt.

This approach has permitted to observe in the simulation all features of the experimental FIDs, including appearance of the solid-like component followed by the liquid-like one as the obvious consequence of the entanglements due to chain-length increase. Furthermore, it has revealed that when the entangled melt is near the glass-transition temperature its FID becomes oscillating, what has been observed in several experiments but

remained unexplainable [10-13]. In this simulation, the oscillating FID has been evident consequence of quasi-static motion of the chain parts between two adjacent entanglements – primitive segments in the reptation-model terminology – which are carriers of the residual DC (**RDC**). This circumstance has motivated the author to revise the previous theories of the FID initial component in attempt to find an expression for its oscillating shape [14, 15].

Theoretical analyzing the FID initial component shape

Repeating the AWA-derivation [5, 9] shows that, starting from the fundamental relaxation theory, at some stage it becomes applicable only to an ergodic system, for example, a low-molecular liquid. This narrowing is due to considering the Gauss φ_K-distribution centered at zero, i.e., after neglecting the average value of this distribution, $\langle\varphi_K\rangle$. But, for a separate primitive segment $\langle\varphi_K\rangle \equiv \langle\varphi_P\rangle = const{\times}t$ instead of the integral in (1) – it defines the non-ergodic part of the DC further governed by primitive segment [14] – because each primitive segment inherits RDC, which is non-averaged by all its Kuhn segments. Hence, the resultant expression for the FID governed also by the primitive segments gets the form:

$$g(t) = \langle\cos\varphi_K\rangle = Re\langle\exp[\varphi_K]\rangle \equiv Re\left\{\exp\left[\langle i\varphi_K\rangle + \tfrac{1}{2}\left(\langle i^2\varphi_K^2\rangle - \langle i\varphi_K\rangle^2\right)\right]\right\} =$$
$$= \cos\langle\varphi_P\rangle \cdot \exp\left[-\tfrac{1}{2}\left(\langle\varphi_K^2\rangle - \langle\varphi_P\rangle^2\right)\right] = \cos\varphi_P \cdot g_K(t)$$

This expression explicitly shows that the RDC precession phase, φ_P, influences the initial solid-like component of the FID; consequently it must be subtracted in the exponent, because, firstly, the exponential now describes the ergodic part of DC; secondly, it is agreed with defining the generalized autocorrelation function, which characterizes a system quantity with a non-zero equilibrium value [16]. Further, to get the FID initial component for a chain, which differs from the total melt NMR-signal merely by statistics, only the first multiplier should be averaged over the entangled chain primitive segments, because $g_K(t)$ is already averaged inside each primitive segment. Owing to the quasi-static state and isotropic orientations of the primitive segments inside chain there is applicable the conventional "powder averaging" transformed into the time domain [17-19]. In other words, we get the well-known exponential $g_K(t)$, multiplied by the Pake-doublet [20] Fourier-image:

$$g(t) = \langle\cos\varphi_P\rangle \cdot g_K(t) = g_K(t) \cdot \{C_x\cos(b_P t) + S_x\sin(b_P t)\}/x. \qquad (2a)$$

$$C_x = \int_0^x \cos\left(\tfrac{1}{2}\pi z^2\right) dz, \quad S_x = \int_0^x \sin\left(\tfrac{1}{2}\pi z^2\right) dz, \quad x = \sqrt{6b_P t/\pi}\,. \qquad (2b)$$

It involves two oscillating non-analytical Fresnel integrals, C_x and S_x, depending on aggregative argument x, which does not require a fit, since it is the simple function of chain structural parameter $b_P \sim b_K / N_E$ [14]. $g(t)$-structure permits to explain the oscillating FID appearance in high-molecular polymer melt as well as the difficulty of its registration. It could only be observed if the special pulse sequence filters the quasi-static FID initial component [10-12]; or the primitive segments themselves are in the quasi-static state due to being in the narrow temperature interval near the glass-transition temperature [13]. The difficulty in observation is caused by small ratio b_P / b_K, at which the FID initial component occurs as the smoothed Gauss-like exponential [14].

Conclusion

Considering the primitive segment of entangled chain as a carrier of RDC – a conceptual idea specified by simple expression $\langle\varphi_K\rangle \equiv \langle\varphi_P\rangle = const{\times}t$ – permits to join two fundamental NMR theories – the time-domain Pake-doublet and Anderson-Weiss approach – into a generalized theory describing the transverse relaxation in very viscous high-molecular polymer melt without a fitting parameter but using only structural ones. In other words, these classical theories represent two asymptotic cases for the solid-phase relaxation, Pake theory,

and for the liquid-phase one, the Anderson-Weiss theory. Transfer from the first asymptotic case to the second case is specified by dominant multiplier in $g(t)$-expression (2a): when φ_P prevails over φ_K then $g_K(t)$ describes a typical broadening interaction for the NMR-absorption line in time-domain [17-20]; when φ_P tends to zero, $g_K(t)$ describes a "pure" liquid-phase relaxation.

The last case is traditionally used to describe NMR-relaxation of the chain middle Kuhn segments in the entangled polymer melt by representing $g_K(t)$ as product of three multipliers owing to the large difference in correlation times of the chain various kinetic units [21], i.e., the next approximation of the Anderson-Weiss approach is used. In contrary, accounting for the dominant b_P-contribution to the FID (1) with concurrent neglecting b_K transforms the complicated integrand – rarely integrable – into the linear time-function, what allows to find an approximate FID-expression in the high-temperature entangled melt [22]. The long-time asymptote of this expression reveals an unknown FID feature caused by the chain one-dimensional diffusion in the tube, what is also corroborated by the simulation [23].

References

1. J.P. Cohen-Addad – *J. Chem. Phys.*, **60**, 2440-2453 (1974).
2. V.D. Fedotov, V.M. Chernov – *Dokl. Akad. Nauk SSSR,* **224**, 891-894 (1975).
3. J.P. Cohen-Addad – *Progr. Nucl. Magn. Reson. Spectr*., **25**, 1-316 (1993).
4. V.D. Fedotov, V.M. Chernov, T.N. Khazanovich – *Polym. Sci. USSR*, **20**, 1037-1047 (1978).
5. P.W. Anderson and P.R. Weiss – *Rev. Modern Phys*., **25**, 269-276 (1953).
6. E.M. Pestryaev – *J. Phys.: Conf. Ser.*, **324**, 012031 (2011). https://iopscience.iop.org/article/10.1088/1742-6596/324/1/012031
7. E.M. Pestryaev – *Proc. Ufa Sci. Centre Rus. Acad. Sci.: Phys*., **4**, 32-36 (2014) (in Russian). https://www.elibrary.ru/item.asp?id=22111055
8. E.M. Pestryaev, *Structure and dynamics of molecular systems*, IPCE Rus. Acad. Sci., **23**, 378-380 (2016). www.elibrary.ru/item.asp?id=26804550
9. A. Abragam. The principles of Nuclear Magnetism – Clarendon Pr., Oxford, 1961.
10. R. Kimmich, E. Fischer, P. Callaghan et al – *J. Magn. Res. A*, **117**, 53-61 (1995).
11. K. Saalwachter, M. Kluppel et al – *App. Magn. Reson*., **27**, 401-417 (2004).
12. F.V. Chavez and K. Saalwachter – *Macromolecules*, **44**, 1549-1559 (2011).
13. V.M. Chernov and G.S. Krasnopol'skii – *Russ. J. Exp. Theor. Phys*, **107**, 302-312 (2008). https://link.springer.com/content/pdf/10.1134/S1063776108080141.pdf
14. E.M. Pestryaev – *Polym. Sci.: Ser. A*, **60**, 530-551 (2018). https://link.springer.com/article/10.1134%2FS0965545X18040090
15. E.M. Pestryaev – "*Polymer Science and Composite Materials*", Virtual int. conf. – Bucharest, 2021; https://polymersconference.yuktan.com/
16. Yu.Ya. Gotlib, A.A. Darinskii, Yu.E. Svetlov. Physical Kinetics of Macromolecules (in Russian) – Khimiya, L., 1986.
17. S.E. Svanson – *Acta Chemica Scandinavica*, **16**, 2212-2220 (1962). http://actachemscand.org/pdf/acta_vol_16_p2212-2220.pdf
18. D.C. Look and I.J. Lowe and J.A. Northby – *J. Chem. Phys.*, **44**, 3441-3452 (1966).
19. B.A. Van Baren, S. Emid, C. Steenbergen – *J. Magn. Reson*. **4**, 466-474 (1972).
20. G.E. Pake – *J. Chem. Phys.*, **6**, 327-336 (1948).
21. P. Kulagina, V.A. Varakina et al – Rus. J. Phys. Chem. B, **8**, 391-395 (2014).
22. N.F. Fatkullin, T. Korber, E.A. Rossler – *Polymer*, **142**, 310-315 (2018): In memoriam of Yu.Ya. Gotlib. https://doi.org/10.1016/j.polymer.2018.03.050
23. E.M. Pestryaev – *Polym. Sci.: Ser A*, **61**, 392-396.

Magnetic resonance imaging on the sodium-23 and fluorine-19 nuclei

Yury Pirogov[1],, Nikolay Anisimov[2],, Mikhail Gulyaev[2],, Olga Pavlova[1,2],

[1]*Faculty of Physics, Lomonosov Moscow State University, Moscow, Russia*
[2]*Faculty of Fundamental Medicine, Lomonosov Moscow State University, Moscow, Russia*
E-mail: yupi937@gmail.com

Unlike traditional MRI studies based on the registration of NMR signals from hydrogen nuclei (1H, protons), multinuclear MRI approaches deal with nuclei heavier than protons. It is necessary to develop multinuclear MRI due to the need to visualize in vivo living tissues or drugs that do not contain hydrogen atoms introduced into the body. For example, there is a diagnostic need to determine the pathways of circulation and localization in the body of the Perftoran blood substitute introduced into the bloodstream, the molecules of which contain only carbon and fluorine atoms. To visualize it, it is necessary to tune the transmit-receive path of the MRI scanner to the Larmor frequency of fluorine-19. When setting up the scanner for fluorine-19 nuclei, it is possible to solve many important fundamental and applied problems - to visualize the functional tissues of the lungs filled with fluorine-containing gas, to monitor the progress of capsules containing the fluorine preparation along the gastrointestinal tract, to determine (with help recording signals from the corresponding fluorine markers) location of targeted drugs, etc. Fluorine MRI has a number of undoubted advantages - the NMR signal from fluorine-19 nuclei has almost the same intensity as the proton signal; the Larmor frequency of fluorine differs by only 5% from the proton frequency, allowing the use of branded proton coils slightly retuned in frequency. Another significant advantage of MRI on fluorine nuclei is that due to the almost complete absence of fluorine in the body of humans and animals, the fluorine MRI signal from the injected drug is clearly visualized against the zero background of living tissues that do not contain fluorine atoms.

Another important task of multinuclear MRI is associated with determining the place of accumulation in the body and measuring the concentration of substances containing sodium-23 nuclei. Deficiency or excess of sodium in the body, primarily NaCl salt, is the cause of widespread socially significant diseases - blood pressure disorders (hyper- or hypotension), diabetes, kidney failure, gallstone pathologies, etc. MRI scanner configured on the resonant frequency of sodium-23 nuclei, allows to non-invasively determine the location of organs with violations of the norm of the sodium concentration in the human body. Using the 23Na-MRI method, one can also solve some important technological problems of measuring, for example, the salinity of canned food products - fish, sausage, salted vegetables. This report presents the results of multinuclear diagnostic studies on fluorine-19 and sodium-23 nuclei, performed using Bruker MRI devices - a medical 0.5-T scanner and a 7-T biospectrotomograph.

Research has been supported by RFBR grant No.19-29-10015 and Interdisciplinary Scientific and Educational School of Moscow University "Photonic and Quantum Technologies. Digital Medicine".

Characterization of zeolites with hierarchical porosity: Combined adsorption, spectroscopic, microscopic and diffraction techniques

M.G. Shelyapina[*,1], D. Nefedov[1], R. Yocupicio-Gaxiola[2], V. Petranovskii[2], S. Fuentes[2]

[1]Saint Petersburg State University, 7/9 Universitetskaya nab., Saint Petersburg 199034, Russia
[2]Centro de Nanociencias y Nanotecnología, Universidad Nacional Autónoma de México, Ensenada, B.C., 22860 México
E-mail: marina.shelyapina@spbu.ru
http://www.yoursite.ru

Zeolites are porous crystalline solid aluminosilicates with ordered micropores (< 2 nm), and a large specific porosity. Due to their ability to adsorb various molecules and large adsorption capacity, these materials are used in industries as molecular sieves. Depending on the mechanism of charge compensation related to Al substitution for Si, zeolites can exhibit either basic or acidic properties that is widely applied in catalysis. However, the small pore size of three-dimensional zeolites imposes diffusion restrictions, which reduces their efficiency in industrial use. An increase in transport properties of zeolites can be achieved by creating a secondary porosity consisting of mesopores (2-50 nm) or macropores (> 50 nm), i.e. by creating zeolites with hierarchical porosity. Such zeolites can be used as a reactor for a number of important catalytic processes where mass transfer is very significant.

The usual strategy for creating mesoporous zeolites is based on post-modification of three-dimensional zeolites. Subsequent processing, including the processes of selective desilication or dealumination, is basically a destructive procedure, as a result of which part of the zeolite crystals is sacrificed to create larger meso- or macropores [1]. This usually leads to a loss of crystallinity, and the resulting secondary porosity is often beyond control. However, a number of studies confirm a relationship between the quality of mesopores and catalytic efficiency.

Zeolites with hierarchical porous structure can also be synthesized directly using the following strategies [2]: (i) the development of intercrystalline mesoporosity due to aggregation of nanocrystals; (ii) the emergence of intracrystalline mesoporosity, which is formed by amorphous gels that control crystallization; (iii) mesoporosity created between self-pillared two-dimensional zeolite nanosheets. The latter can be obtained by synthesizing lamellar zeolites in the presence of organic structure directing agents followed by introduction of metal alkoxides molecules into the interlayer space, their subsequent hydrolysis and formation of oxide columns separating the layers of two-dimensional zeolite, and finally evacuation of organic molecules by calcination [3].

Despite the fact that hierarchical zeolites provide almost infinite possibilities for their modification, the relationship between the synthesis method and the effectiveness of the catalyst in a particular reaction is not obvious. The development of the synthesis methodology should include a comprehensive characterization of such materials, preferably at all stages of synthesis.

Among mesoporous zeolites obtained by self-organization, zeolites with ZSM-5 structure are the most tested [4]. They exhibit greater efficiency in several catalytic processes as compared to post-treated mesoporous zeolite systems. The study of mesoporous zeolites with the structure of mordenite in such reactions has not yet been carried out. Mordenite, due to the specificity of the structure, namely the presence of side pockets, is distinguished by the flexibility of regulating both Lewis and Bronsted acidity [5], which is important for the development of catalysts for specific chemical reactions.

In this contribution we report on the results of our complimentary study of pillared zeolites (with ZSM-5 and mordenite structures). It involves structural characterization (X-ray diffraction, small angle X-ray scattering, nuclear magnetic resonance,), elemental (energy dispersive X-rays spectroscopy, X-ray photoelectron spectroscopy) and morphological analysis (scanning electron microscopy), thermal gravimetric analysis, studies of textural (nitrogen adsorption) and electronic (diffusive reflectance spectroscopy) properties, and probe of dynamics of guest molecules by nuclear magnetic resonance.

Acknowledgements

The samples were synthetized at CNyN-UNAM and studied at the Research Park of Saint Petersburg State University (Centre for X-ray Diffraction Studies, Interdisciplinary Resource Centre for Nanotechnology, Centre for Diagnostics of Functional Materials for Medicine, Pharmacology and Nanoelectronics, Centre for Optical and Laser Materials Research, Centre for Surface Investigation, Centre of Thermal Analysis and Calorimetry, Centre for Magnetic Resonance).

References

1. H. Zhang, Z. Hu, L. Huang, H. Zhang, K. Song, L. Wang, Z. Shi, J. Ma, Y. Zhuang, W. Shen, Y. Zhang, H. Xu, Y. Tang, – *ACS Catal.* **5**, 2548–2558 (2015).
2. M. Ravi, V.L. Sushkevich, J.A. van Bokhoven – *Chem. Sci.* **12**, 4094 (2021)
3. M.G. Shelyapina R.I. Yocupicio-Gaxiola I.V. Zhelezniak, M.V. Chislov, J. Antúnez-García, F.N. Murrieta-Rico, D. Homero Galván, V. Petranovskii. S. Fuentes-Moyado, – *Molecules* **25** 4678 (2020).
4. Z, Qin, K.A. Cychosz, G. Melinte, H. El Siblani, J.-P. Gilson, M. Thommes, C. Fernandez, S. Mintova, O. Ersen, V. Valtchev, – *J. Am. Chem. Soc.* **139**, 17273–17276 (2017).
5. X. Jia, W. Khan, Z. Wu, J. Choi, A.C. Yip, – *Adv. Powder Technol*. **30**, 467–484 (2019).

Investigating the mechanism of catalytic action of antioxidant enzyme glutathione peroxidase in the redox reactions of peroxides by means of quantum chemistry

Elena Tupikina, Valerii Karpov, Peter Tolstoy

Institute of chemistry, St. Petersburg State University
E-mail: elenatupikina@gmail.com

Introduction

Selenium is one of the microelements a man needs. Deficiency of selenium in the body leads to diseases such as Keshan's disease (disorders of heart rhythm, enlargement of heart size), the development of which leads to heart failure, as well as a number of other diseases, including cardiovascular and neurodegenerative diseases [1]. Recent clinical studies show, however, that the additional intake of selenium benefits only certain groups of population (e.g. genetically predisposed to selenium deficiency), while for others it may be either useless or even harmful [2]. Selenium is present in the active sites of proteins (selenoproteins) in the form of one or more residues of selenocysteine (an amino acid that differs from cysteine by replacing the sulfur atom with selenium). There are 25 different types of selenoproteins in human cells, the functions of which are largely related to the protection of the body from oxidative damage, for example, the mechanism of hemoglobin protection from oxidation in the cytoplasm of red blood cells. At the same time, the mechanism of their work and properties, in general, remain poorly investigated.

This work is devoted to a quantum-chemical investigation of the mechanism of catalytic reduction of peroxides with the participation of selenoprotein glutathione peroxidase (GPx-1). This enzyme protects biomolecules from oxidative damage and prevents the development of cardiovascular and neurodegenerative diseases. The relevance of this study is due to the problems of modern biochemistry, in particular in the field of design of new targeted antioxidant drugs.

Problem statement

The main problem of this work is a detailed understanding of the catalytic reactions involving glutathione peroxidases enzyme, which is involved in the mechanism of defense of a human body against oxidative stress. The main goal of this work is to model the selenocysteine moieties at the active site of glutathione peroxidase and track the changes in the electronic shell features of the selenium atom. Namely, to show how the reactivity of the selenocysteine fragment in the active site of the enzyme changes at each step of catalytic cycle (Figure 1) and how these changes are associated with a change in its electronic shell.

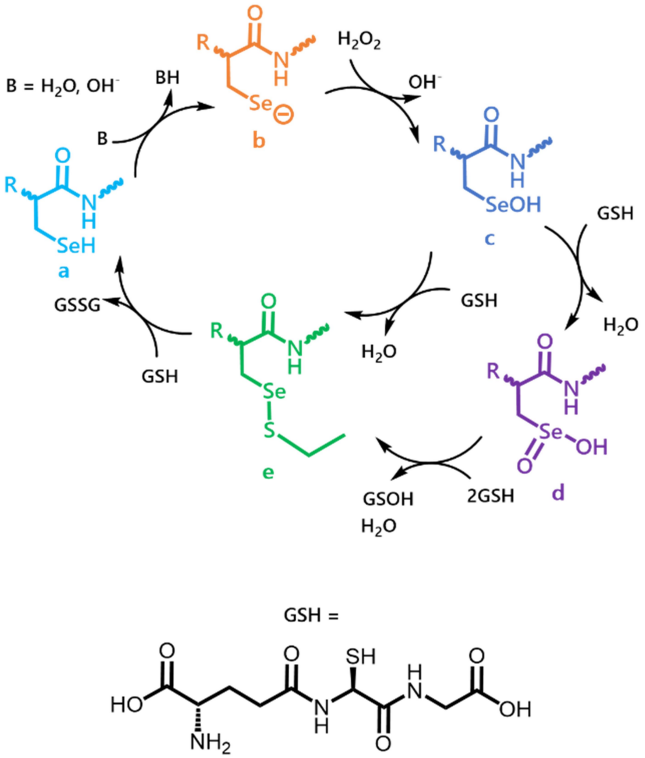

Figure 1. Mechanism of peroxide reduction by the selenocysteine fragment (part of the active site of the GPx-1 enzyme).

Methods

Calculations were carried out using the Gaussian16 software. Computational resources were provided by Computer Center of Saint-Petersburg University Research Park (http://www.cc.spbu.ru/). Electronic shell features were calculated using MultiWFN.

Visualization was performed in GaussView 6.0 and Matlab 2021b software packages.

Acknowledgements

This work is supported by the RSCF grant 20-73-00099.

References

1. Rayman, M. P. (2000). The Importance of Selenium to Human Health. The Lancet, 356(9225), 233-241
2. Flohé, L. (2011). Selenium and Human Health: Snapshots from the Frontiers of Selenium Biomedicine. In Selenium and Tellurium Chemistry (pp. 285-302). Springer, Berlin, Heidelberg. S. Fisher, B. I. Yachtman. – *Vacuum State Comm.*, **7**, 1234-1237 (2003).

Electrophoretic NMR assembly

Extending the capability of conventional NMR instruments

P&L Scientific

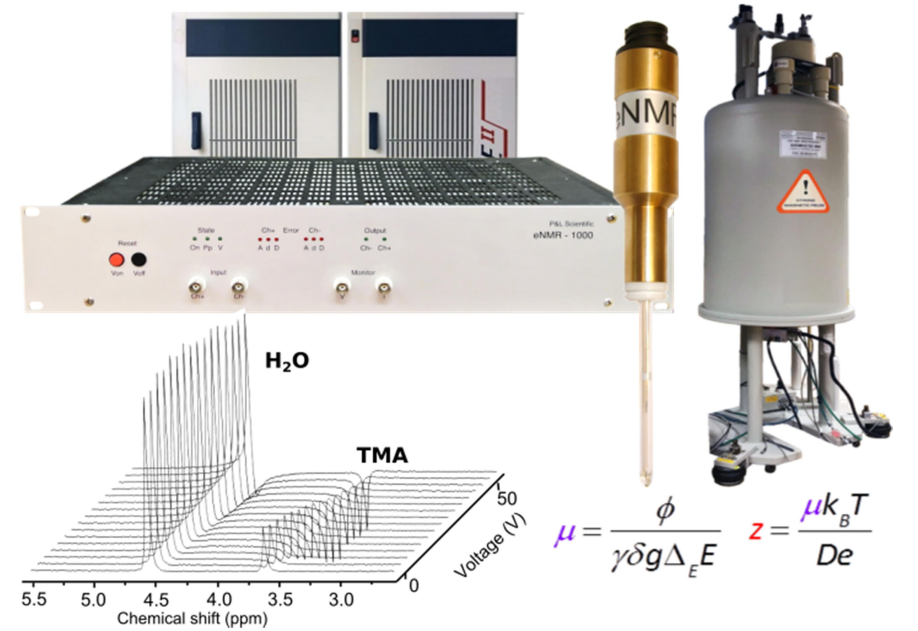

The electrophoretic mobility and the effective charge can be obtained by recording the variation of spectral phase by increasing electric field

Key features

- Well-established scientific background and proven technology
- Operates as add-on for any conventional NMR spectrometer and probe with gradient; requires no additional hardware or software
- Advanced sample cell and RF filter system
- Straightforward embedding of high voltage pulse generation in conventional NMR pulse programs
- Probe and user protection system

info@plscientific.se

Specifications

Output voltage:	0 to ±1000 V
Digital To Analogue converter size:	2×12 bit
Output current	
at ±1000 V:	0 to ±100 mA
at ±500 V:	0 to ±200 mA
Output power:	
Peak power	300 W
Mean power	30 W
Minimum/maximum pulse length:	500 µs / 1 s
Duty cycle:	30 %
Output pulse shapes:	Rectangular
Slew rate:	Greater then 25 V / µs
Settling time (to 2%):	Less than 200 µs for 2 kV step
Stability	
Drift with time	Less than 200 ppm/hr, non-cumulative
Drift with temperature	Less than 300 ppm/°C
RF Filters	10 MHz low pass
Power consumption:	80 W for 220 V AC
Dimensions of the main unit:	430×340×90 (fits in standard 19″ rack); weight - 8 kg

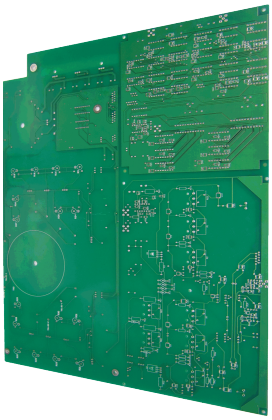

Selected applications

Physical chemistry – ion pairing and association in simple and complex (polyelectrolytes) ionic mixtures.

Batteries and fuel cells - chemically selective measurement of ionic migration.

Biochemistry – biomolecular charge and association.

Analytical chemistry – electrophoretic analysis of complex ionic mixtures

Pharmaceutical chemistry – release and association of charged drugs

Metallorganic chemistry – the structure of supramolecular complexes from the observed charge

info@plscientific.se

2D electrophoretic mobility spectroscopy (2D MOSY) based on eNMR

Extending the power of 2D NMR spectroscopy

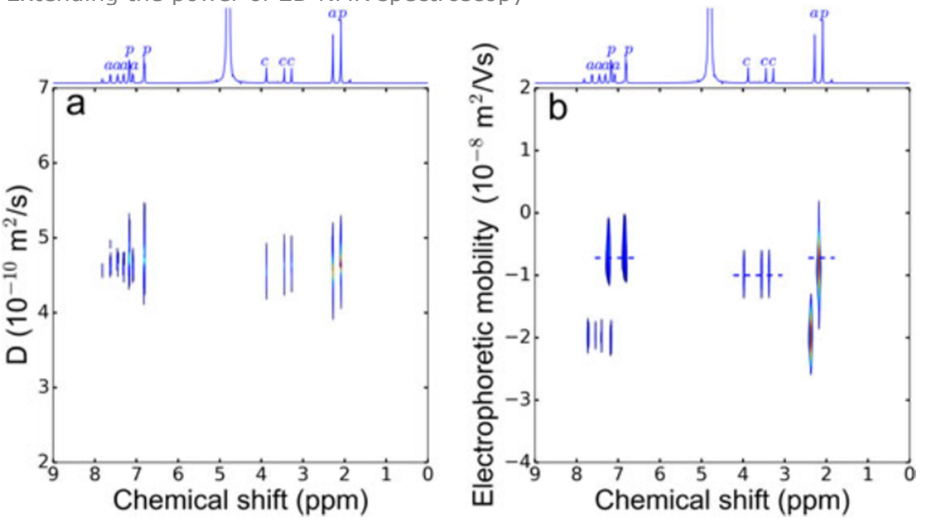

Direct comparison of 2D DOSY (a) and 2D MOSY (b) experiments for a dissolved Thomapyrin® tablet clearly illustrates the superior performance of the 2D MOSY in selection of the different species

Selected articles for eNMR applications

Y. Fang, P. V. Yushmanov, and I. Furó, Assessing 2D electrophoretic mobility spectroscopy (2D MOSY) for analytical applications, Magn. Reson. Chem. 55 DOI: 10.1002/mrc.4558 (2017).

E. Bialik, B. Stenqvist, Y. Fang, Å. Östlund, I. Furó, B. Lindman, M. Lund, and D. Bernin, Ionization of cellobiose in aqueous alkali and the mechanism of cellulose dissolution, J. Phys. Chem. Lett. 7 5044-5048 (2016).

M. Giesecke, F. Hallberg, Y. Fang, P. Stilbs, and I. Furó, Binding of monovalent and multivalent metal cations to polyethylene oxide in methanol probed by electrophoretic and diffusion NMR, J. Phys. Chem. B 120 10358−10366 (2016).

M. Bielejewski, M. Giesecke and I. Furó, On electrophoretic NMR. Exploring high conductivity samples, J. Magn. Reson. 243 17-24 (2014).

L. Patel, O. Mansour, M. Crossman, P. Griffiths, Electrophoretic NMR characterization of charged side chain cationic polyelectrolytes and their interaction with the anionic surfactant, sodium dodecyl sulfate, Langmuir 2019, 35, 28, 9233-9238

info@plscientific.se

Our NMR services

Repair and modification of the NMR spectrometers and hardware components

- RF amplifiers
- Gradient units
- Synthesizer and SGU 400 - 1000 boards
- Power supplies and shim system
- Temperature and MAS controllers

Repair of the NMR probes:

- Solving arcing problems; bad sensitivity and RF tuning/matching
- Replacing broken glass and ceramics in the probe body
- Repairing certain gradient coils in diffusion and high-resolution probes
- Repair of MAS probes; arcing and spinning problem
- Repair of probe accessories for temperature control

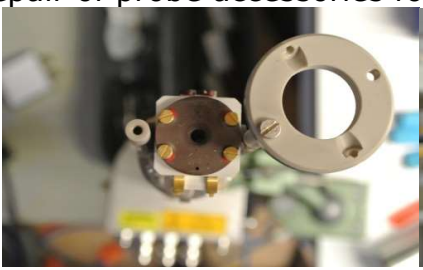

Modification of the NMR probes

- Adaptation of an existing NMR probe to a different spectrometer or NMR frequency.
- Change of RF coil position and configuration
- Adaptation of temperature control components and connectors
- Change of body geometry, dimensions and mounting
- Modification NMR inserts used in several diffusion NMR probes (like Bruker Diff30) to different frequency or double-tuned configuration

info@plscientific.se

Oral Reports

Low-temperature study of magnetization and magnetostriction of $LiYbF_4$ in strong magnetic fields

G.Iu. Andreev[1], I.V. Romanova[1], S. Abe[2], M.A. Cherosov[1], I.F. Gilmutdinov[1], A.G. Kiiamov[1], S.L. Korableva[1], K. Matsumoto[2], O.A. Morozov[1,3], D.S. Nuzhina[1], A.S. Semakin[1], K. Ubukata[2], M.S. Tagirov[1,4]

[1]Kazan Federal University, Kremlevskaia str, 18, Kazan, 420008, Russia
[2]Kanazawa University, Kakuma-machi, Kanazawa, 920-11, Japan
[3]Zavoisky Physical-Technical Institute, FRC Kazan Scientific Center of RAS, Sibirskii trakt, 10/7, Kazan, 420029, Russia
[4]Institute of Applied Research of Tatarstan Academy of Sciences, Levobulachnaia 36a, Kazan, 420111, Russia
E-mail: ujif28@mail.ru

Lithium–rare-earth double fluorides attract interest as model objects in physics of dipolar magnetism. These fluorides share scheelite type, $I4_1/a$ crystal symmetry, unit cell contains two magnetically equivalent rare-earth Re^{3+} ions at sites with the S_4 point symmetry that compose two sublattices. Concentrated tetrafluoride $LiYbF_4$ is XY-dipolar antiferromagnet, $T_N = 0.130$ K, magnetic moments are ordered in (001) plane [1, 2, 3, 4].

Single crystals of $LiYbF_4$ were grown by Bridgeman-Stockbarger method. Powder of $LiYbF_4$ was synthesized by sintering powders of fluorides taken in proportions according to the phase diagrams [3, 5, 6]. Magnetostriction measurements were performed on a home-made capacitive dilatometer [7] in static magnetic fields in the field range 0-8 T. Magnetization of the samples of $LiYbF_4$ was measured by vibration sample magnetometer *VSM* at *PPMS* system at the temperature range 2-300 K and applied magnetic field range 0-9 T. Theoretical analysis was performed using Hamiltonian of rare earth ion, diagonalized in the full space of the energy states of $4f^{13}$ electronic configuration [8].

The qualitative and quantitative agreement between experimental data and simulations has been got both for the powder sample (magnetization measurements) and the single crystal samples (magnetization, longitudinal and transverse magnetostriction measurements) at low temperatures. Also, our theoretical approach explains $LiYbF_4$ single crystal inverse susceptibility experimental data from [2] in an external magnetic field $B = 0.05$ T, $\mathbf{B} \parallel [100]$ and [001], better than the original calculations.

Acknowledgements

The financial support of the Russian Science Foundation (project 22-22-00257) is gratefully acknowledged.

The authors are grateful to Prof. B.Z. Malkin for helpful discussions.

References

1. L.K. Aminov et al. – *Handbook on the Physics and Chemistry of Rare Earths,* **22**, 295-506 (1996).
2. P. Babkevich, et al. – *Physical Review Letters,* **116**, 197202 (2016).
3. R.E. Thoma et al. – *Inorganic Chemistry,* **9**, 1096-1101 (1970).
4. C. Keller, H. Schmutz. – *Journal of Inorganic and Nuclear Chemistry*, **27**, 900-901 (1965).
5. P.P. Fedorov. – *Russian Journal of Inorganic Chemistry*, **44**, 11, 1703–1727 (1999).
6. P.P. Fedorov et al. – *Growth of Crystals*, **21**, 141-154 (2002).
7. S. Abe et al. – *Cryogenics,* **52**, 452-456 (2012).
8. I.V. Romanova, M.S. Tagirov. – *Magn. Reson. Solids,* **21**, 19412 (2019).

Stress-controlled zero-field spin splitting of defects in SiC

Andrey Anisimov, Breev Ilya, Baranov Pavel

Ioffe Institute, Russia, Saint-Petersburg, Politechnicheskaya st., 26
E-mail: aan0100@gmail.com
http://www.ioffe.ru/labmsc/en/main.html

Atomic-scale defects in bulk and nanocrystalline SiC are promising for quantum information processing, photonics and sensing. Breakthrough quantum properties have recently been discovered for a family of uniaxially oriented silicon vacancy-related colour centres with S = 3/2 in the ground and excited states in a hexagonal 4H-SiC, 6H-SiC and rhombic 15R-SiC crystalline matrix. It was demonstrated that these centres exhibit unique characteristics such as optical spin alignment up to the temperatures of 250°C. Silicon vacancy-related colour centres with half-integer ground spin state (S=3/2) have recently been proposed to form the basis for quantum spintronics, sensorics, and quantum information processing because of the unique properties of their electron spins, which can be optically polarized and readout even at room temperature by means of a standard optically-detected magnetic resonance (ODMR) technique.

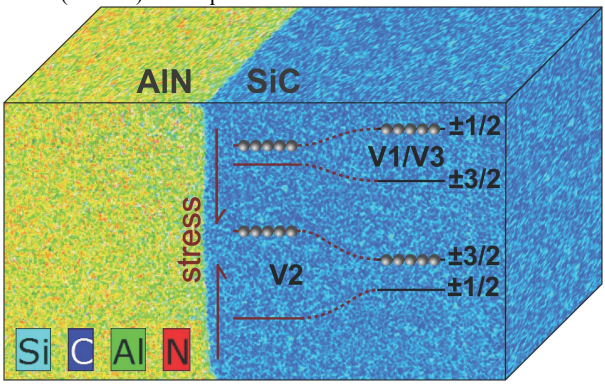

Figure. 1. Color-coded chemical element distributions obtained by EDXS across the AlN/6H-SiC heterointerface. The lines schematically represent the spatial distribution (not to scale) of the zero-field splitting in the V1/V3 and V2 V˜ (Si) centers in 6H-SiC near the heterointerface and in the bulk. The solid circles show the preferentially populated spin states under optical pumping.

For the first time, experimental results on the effect of mechanical stresses on the spin structure of spin centers in silicon carbide are presented. The influence of local mechanical strains on the splitting of D in a zero magnetic field is established. This study will expand the understanding of the properties of defects that are promising for applications in quantum devices.

The study was carried out with a grant from the Russian Science Foundation (project № 20-12-00216)

Multinuclear measurements on a 0.5T clinical scanner

Nikolay V. Anisimov[1], Arina A. Tarasova[2], Ivan A. Usanov[2], Olga S. Pavlova[1,2], Mikhail V. Gulyaev[1]

[1]Faculty of Fundamental Medicine, Lomonosov Moscow State University, 119991, Russia
[2]Faculty of Physics, Lomonosov Moscow State University, 119991, Moscow, Russia
E-mail: anisimovnv@mail.ru

Introduction

Typical clinical scanners are focused on the detection of proton (^{1}H), since living tissues are based on hydrogen-containing components - water, fat, organic compounds. These tissues also contain other chemical elements. Therefore, detection of nuclei other than protons provides additional diagnostic material. It is also of interest for technological applications - food analysis, material diagnostics, etc. Therefore, it is useful to identify the possibilities of a clinical scanner for multi-nuclear applications. In this paper, we present a short review of the results obtained for our 0.5T clinical MR scanner Bruker Tomikon S50.

^{19}F MRS & MRI

At the first stage, we adapted our scanner for fluorine (^{19}F) MRI. Favorable factors for this were that the frequency bands of the transmitter (10-100 MHz) and the transmit/receive (T/R) switch (12-32 MHz), as well as the tuning range of the receiving coils, are sufficient to detect both protons (21.1 MHz) and fluorine (19.8 MHz).

We mainly detected perfluorocarbons. In particular, we measured the relaxation characteristics of a number of compounds that are of interest as contrast agents, studied the dynamics of excretion of the drug Perftoran® ($C_{22}F_{41}N$) from the body of rat. In addition, experiments were carried out on ^{19}F MRI to visualize the passage in the human gastrointestinal tract of ingested capsules filled with fluorine-containing substances – Perftoran® and perfluorotributylamine ($C_{12}F_{27}N$) [1]. Interesting results have been obtained in experiments on ^{19}F MRI of human lungs using perfluorocyclobutane (C_4F_8) gas [2].

Detection of heavy nuclei: ^{2}H, ^{11}B, ^{13}C, ^{14}N, ^{17}O, ^{23}Na, ^{29}Si, ^{31}P, ^{35}Cl

In addition to the registration of ^{1}H and ^{19}F nuclei, our clinical scanner was used to detect the heavy nuclei - ^{2}H, ^{11}B, ^{13}C, ^{14}N, ^{17}O, ^{23}Na, ^{29}Si, ^{31}P, ^{35}Cl [1]. The last nucleus was detected by the NQR method (zero field) at a frequency of 28 MHz from powdered potassium chlorate ($KClO_3$). The Larmor frequencies of the remaining heavy nuclei were in the range of 1.5–8.5 MHz. The measurements were carried out mainly by NMR spectroscopy on samples of different volumes (1 cm^3 - 0.5 L), so a separate coil was made for each of them.

We tried to obtain the ^{1}H and ^{31}P spectra of the human head and muscle, respectively. But their informativeness is small due to the low SNR and resolution.

We also conducted test MR scans with the detection of nuclei: ^{2}H, ^{11}B, ^{13}C, ^{23}Na and ^{31}P from samples of D_2O, $B(OCH_3)_3$, $^{13}CD_3OD$, NaCl, H_3PO_4, respectively.

Polarization transfer (DEPT, INEPT) from ^{19}F and ^{1}H to ^{13}C

We carried out not only the recording of routine spectra of heavy nuclei, but also experiments on double resonance, using the second transmitting channel of the scanner [1]. To detect ^{13}C NMR from isotopically unenriched samples (with a natural content of this isotope), polarization transfer methods were used from nuclei with a high gyromagnetic ratio γ to nuclei with a low γ - DEPT and INEPT. We demonstrated the polarization transfer from ^{19}F to ^{13}C for perfluorodecalin ($C_{10}F_{18}$) – the main component of Perftoran®. Polarization transfer from ^{1}H to ^{13}C nuclei was obtained for acetone (C_2H_6CO) and ethanol (C_2H_5OH), including its aqueous solutions. The measurements of the latter were carried out as the isotopic analysis

of alcohol-containing products in order to identify the material (grapes, grain, cane, etc.) from which the alcohol was produced.

Simultaneous detection of nuclei with different γ: $^{1}H/^{19}F$, $^{13}C/^{23}Na$

Demonstration experiments were also carried out on the simultaneous detection of nuclei with different gyromagnetic ratios, and the difference in their Larmor frequencies exceeds the sampling rate (BW) [3]. In one experiment, signals from the ^{1}H (21.1 MHz) and ^{19}F (19.8 MHz) nuclei for isoflurane ($C_3F_3H_2ClO$) were simultaneously recorded, in the other, from the ^{13}C (5.3 MHz) and ^{23}Na (5.6 MHz) nuclei for a solution of bicarbonate of soda, isotopically enriched in ^{13}C - $NaH^{13}CO_3$. In both cases, due to the undersampling effect, an artificial spectra 2 kHz wide were recorded, which displayed the peaks from different nuclei.

The methodological significance of these experiments is to demonstrate that for the simultaneous detection of nuclei with different gyromagnetic ratios, a weak polarizing field is a favorable factor, and the low speed of the analog-to-digital converter is not an obstacle.

Hardware and RF interference problems

Apart from connecting homemade coils, no other modification of our scanner was carried out. Therefore, conditions for detecting heavy nuclei whose Larmor frequencies lie outside the passband of the transmitter and the T/R switch are not optimal. The correction of their AFC can optimize these conditions and increase SNR. In particular, for ^{23}Na MRI it can be increased by 2–3 times for tissues with T_2 >12 ms and more significantly for short T_2 [4].

A serious problem in detecting heavy nuclei was external RF interference. It occurs at frequencies below 10 MHz, and therefore is imperceptible during the detection of protons and fluorine [4]. This interference is most likely anthropogenic, since its activity depends on the time of day. At maximum activity, its intensity is two orders of magnitude higher than thermal noise. Its average frequency drifts at a rate of up to 0.1 kHz/min, which prevents interference suppression during signal accumulation and limits the measurement time. These factors were taken into account when planning experiment to detect heavy nuclei.

^{23}Na MRI

Our greatest attention was paid to ^{23}Na MRI. We first scanned individual segments of the human body to compose a whole body image from the segment images [5]. In this study, we applied 2D GRE method without slice selection, and used a 4-turn square loop as transceiver coil. For detecting individual human organs, we reconfigured branded receive-only coils, optimized for recording ^{1}H signals (21.1 MHz) from various human organs, to operate at a ^{23}Na NMR frequency of 5.6 MHz, and converted them into transceiver coils.

Using the 3D GRE method (TR/TE=47/12 ms, FA=70°, voxel size=6×6×6 mm^3, scan time=25 min), ^{23}Na MRI of individual organs and their volume reconstructions were built. Figure1 shows examples of MRI of different human organs obtained using different coils.

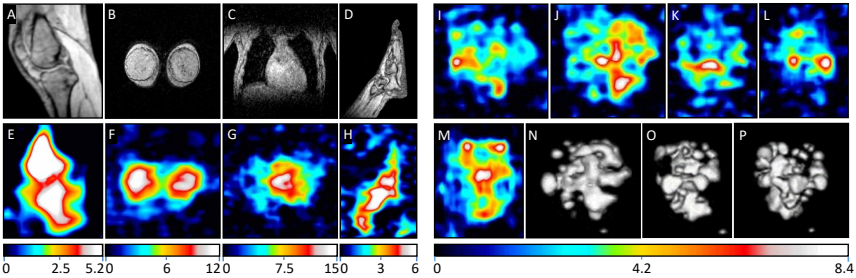

Figure 1 ^{1}H and ^{23}Na MRI of different human organs: ^{1}H (A-D) and ^{23}Na (E-O)

For assignment of anatomical structures on ^{23}Na images E (knee, sagittal), F (breast, coronal), G (heart, coronal), H (foot, sagittal), corresponding ^{1}H images are shown: A-D. The right panel shows MRI of the head - separate slices: I, J (sagittal), K, L (coronal), M (axial), as well as volume reconstruction – 3D rendering at different azimuthal angles: -90°(N), 0°(O), 10°(P). The brightness scale corresponds to the SNR values. However, it must be admitted that the detail of our ^{23}Na MR images is insufficient for diagnosis.

That's why we have been focusing on technological applications - ^{23}Na MRI of inanimate objects (in particular, food) as well as euthanized animals. This may be of interest for the morphology of animals, the measurement of sodium (salt) content in their organs. Note that at the moment it is difficult to find articles where ^{23}Na MRI of fish are presented as anatomical images. First we tried to obtain images of anatomical specimens of fish preserved in alcohol and formalin solutions. However, our attempts were not successful. We conducted experiments proving that sodium is washed out of the body of dead fish within a few days, and for ^{23}Na MRI decided to use thawed fish, fresh if possible, and live fish in the future.

Using the 3D GRE method with the above parameters we obtained MRI of euthanized and thawed fish of different classes (according to the biological classification) – Figure 2.

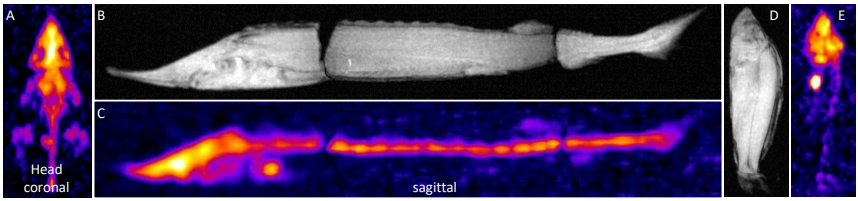

Figure 2 ^{1}H (B,D) and ^{23}Na (A,C,E) MRI (3D MIP) of fishes: sturgeon (A,B,C); carp (D,E)

In all the fish we studied, the sodium signal from the head is stronger than from the body, which, as we found out, is explained by a higher concentration of sodium ions and a longer transverse relaxation time. For herring, these differences are 3.7 and 1.8 times, respectively. In the heads of fresh (just euthanized) fish, gills, eyes, organs of the inner ear, and olfactory sacs are reliably identified. In chilled fish, sodium is reliably determined only in the eyes, in the organs of the inner ear it is revealed fragmentarily, and in the gills and olfactory sacs it is not detected at all.

Conclusion

On a clinical relatively low-field MR scanner, even without significant modification, a wide range of multinuclear studies can be successfully carried out, the results of which can be used as a starting point for their further conduct on advanced high-field equipment.

Acknowledgements

This work is supported by Russian Foundation for Basic Research (grant No. 19-29-10015), the Interdisciplinary Scientific and Educational Schools of Moscow University «Molecular Technologies of the Living Systems and Synthetic Biology» and «Photonic and quantum technologies. Digital medicine».

References

1. N. V. Anisimov, et al. - Appl. Magn. Reson., 50, 17-27 (2019).
2. O. S. Pavlova, et al. - Magn. Res. Med., 84(4), 2111-2123 (2020).
3. N. V. Anisimov, et al. - Appl. Magn. Reson., 49, 523-532 (2018).
4. N. V. Anisimov, et al. - Electromagn. waves and electronic syst., 26(5), 50-59 (2021).
5. N. V. Anisimov, et al. - Appl. Magn. Reson., 50, 1149-1161 (2019).

The stability of beta amyloid fibrils studied by molecular dynamics simulation

Antonova N.A., Komolkin A.V.

St.Petersburg State University, 7-9 Universitetskaya Emb., 199034, St.Petersburg, Russia
E-mail: st054868@student.spbu.ru

Introduction

The presumed cause of Alzheimer's disease is associated with the formation of protein fibrils of amyloid-β (Aβ). This disease is attracting increased attention due to their complex origin and medical importance. One of the ways to study the formation and destabilization of fibrils is the molecular dynamics method.

The purpose of this work was to investigate the structure and dynamics of beta amyloid fibrils in water solution, in saline and in double concentrated NaCl solution using molecular dynamics simulation.

Model systems

The initial fibril configuration was taken from the 2BEG [1] pattern in the Protein Data Bank [2]. The structure consists of the Aβ(17-42) fragment. The parameters of the simulation were taken from the OPLS-AA [3]. The model of water was chosen SPC/E [4]. The Jmol [5] program was used to build model systems. Modeling was carried out in the AKMD [6] program.

Two model systems were created. In one of them, the fibril consists of 5 peptide molecules (system I), in the another, the fibril consists of 10 peptide molecules (system II, fig. 1). Each fibril was surrounded by water molecules so that it did not interact with itself through periodic boundary conditions. The dimensions of the model cells turned out to be about 71 Å for the system I and about 92 Å for the system II. Total size of the systems was about 35000 and 80000 atoms respectively. Both systems were simulated in NpT ensemble at a temperature of 298 K and a pressure of 1 atm. during 0.2 μs.

Also similar systems in which the described fibrils are in saline and in double concentrated NaCl solution were created. They were simulated under the same conditions during 0.2 μs.

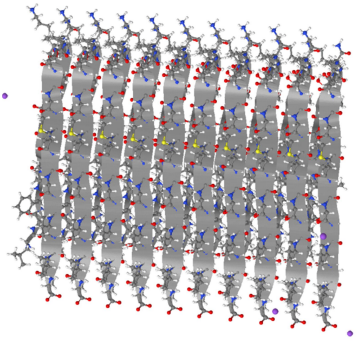

Figure 1. The fibril in the system II at the initial time of the simulation

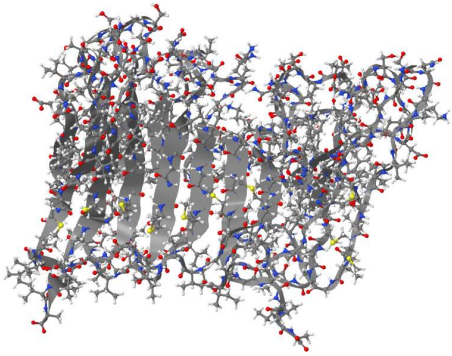

Figure 2. The fibril in the system II after 0.2 μs of the simulation

Results analysis

In all simulated systems, the fibril behaves like a single structure. This fact confirms the correctness of the constructed model.

The fibril remains stable due to hydrogen bonds between β-sheets. During the simulation, the fibrils in each of the systems largely retained its structure (Fig. 2), complete destabilization of the fibrils was not observed. The calculation of hydrogen bonds in the systems showed that the number of intra- and intermolecular bonds in the fibrils during the entire simulation time is the same within the error limits and is equal to 15±3. This means that the systems are stable.

Radial distribution functions analysis showed that in some peptide molecules the position of the inflection changed and the ends of the β-sheets shifted relative to each other (Fig. 3-4).

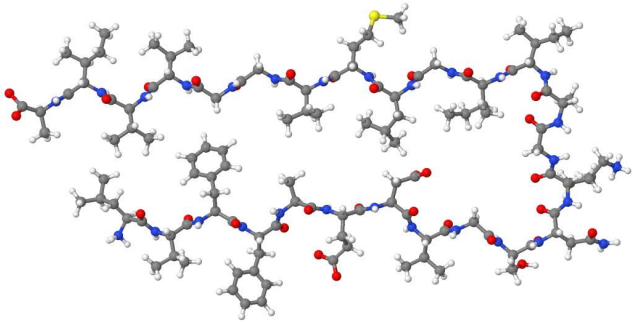

Figure 3. Initial molecule of Aβ(17-42)

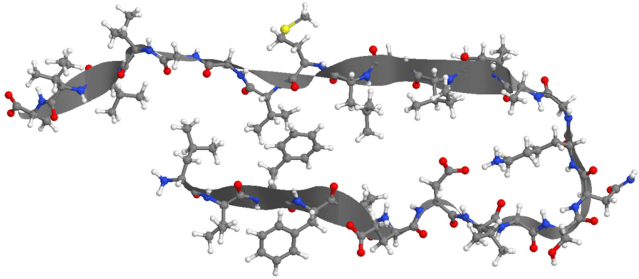

Figure 4. One of the molecules of Aβ(17-42) after 0.2 μs of the simulation

Conclusion

Simulation of the fibrils in water, in saline and in double concentrated NaCl solution showed that the chosen computer model is correct. Under given conditions, the studied systems are stable. The number of hydrogen bonds per molecule remains the same within the error limits throughout the entire simulation time. There is also a change in the position of the inflection and a shift in the ends of the β-sheets.

Acknowledgements

Research was carried out using computational resources provided by Resource Center "Computer Center of SPbU" (http://cc.spbu.ru).

References

1. Luhrs, T., Ritter, C., Adrian, M., Riek-Loher, D., Bohrmann, B., Dobeli, H., Schubert, D., Riek, R. 3D structure of Alzheimer's amyloid-{beta}(1-42) fibrils. – *Proc. Nat. Acad. Sci. USA,* **2005**, v.102: 17342-17347
2. RCSB PDB: Homepage. URL: https://www.rcsb.org/ (accessed 28.02.2020)
3. William L. Jorgensen Research Group — OPLS-AA. URL: http://zarbi.chem.yale.edu/oplsaam.html (accessed 05.03.2021)
4. Berendsen H., Grigera J., Stratsmaa T. The missing term in effective pair potentials. – *J. Phys. Chem.* **1987**, v.191, No.24, 6269–6271
5. Jmol: an open-source browser-based HTML5 viewer and stand-alone Java viewer for chemical structures in 3D. URL: http://jmol.sourceforge.net/ (accessed 05.03.2021)
6. Комолкин А. В., Шеляпина М. Г. Метод молекулярной динамики: Учеб.-метод. пособие – Спб.: Изд-во «Соло», 2007. – 72с., ил.

The new pulse sequence for Time Domain NMR for diamagnetic solids

Alexander Bogaychuk[1,2], Timur Farhutdinov[1]

[1]Institute of Physics, Kazan Federal University, Kazan, 420008, Russia
[2] Tatarstan Academy of Sciences, Kazan, 420111, Russia
E-mail: aleksandr.bogaychuk@gmail.com

Multi-dimensional correlation experiments are ubiquitous in low-field Time Domain NMR studies of molecular structure and dynamics. The T_1-T_2 [1] is one of the most used and informative technique. The spin-spin relaxation time T_2 is sensitive to slow molecular motions, whereas the spin-lattice relaxation time T_1 to fast motions at frequencies close to Larmor's frequency ω_0 [2]. But using of the classic T_1-T_2 pulse sequence can distort the data obtained in the case of solids. Inversion is unsuitable in highly coupled systems where quantitative inversion is not easily [3], and multi-pulse sequences can lead to a spin-locking effect, which leads to the measurement of some effective spin-spin relaxation time T_{2eff} [4].

The theory of the effective spin-spin relaxation time T_{2eff} for pulse sequences with narrowing the spectral line in a solid with the approximation of considering pulses as δ-functions was presented in article [5]. A feature of the T_{2eff} is the dependence not only on the correlation times τ_c, but also on the maximum spacing between pulses τ_{2eff}. Simulation shows that spin-spin relaxation time T_{2eff} and the spin-lattice relaxation time in rotating frame $T_{1\rho}$ with parameter $\omega_1=1/\tau_{2eff}$ are correlated. It makes possible for a comprehensive analysis of T_2 and T_{2eff} distributions, which is effective in assessing molecular motions at frequencies of the order of Hz and kHz.

The effectiveness of the T_2-T_{2eff} correlation method in comparison with the T_1-T_2 method was verified on RF cable samples with removed cores before and after 50 cycles of thermal cycling in the temperature range from 77 to 373 K. Both methods indicate an increase in correlation times due to changes in the crosslink density in samples, but the T_2-T_{2eff} method demonstrates a better efficiency in separating components with close T_2 values.

References

1. Y.-Q. Song, L. Venkataramanan, M. Hurlimann, M. Flaum,P. Frulla, C. Straley. T1-T2 correlation spectra obtained using a fast two-dimensional laplace inversion - Journal of Magnetic Resonance 154 (2) (2002) 261-268.
2. R. R. Ernst, A. Wokaun, G. Bodenhausen. Principles of Nuclear Magnetic Resonance in One and Two Dimensions – Oxford University Press, New York, 1990.
3. D. Besghini, M. Mauri, R. Simonutti. Time domain NMR in polymer science: From the laboratory to the industry - Applied Sciences 9 (9) (2019) 1801.
4. A. V. Bogaychuk, I. G. Mershiev, N. Y. Sinyavsky, G. S. Kupriyanova. Special features of the transverse relaxation time distributions of NMR-protons for different measurement methods - Russian Physics Journal 61 (4) (2018) 801-803.
5. W. Grunder, H. Schmiedel, D. Freude. Eine neue method zur messung von korrelationszeiten mit hilfe von nmrimpulsverfahren - Annalen der Physik 482 (4) (1972) 409-416.

Some comments concerning the MRI impact and development

Carlos Cabal Mirabal[1,2]

1. Cuban Neuroscience Center.
2. Medical Biophysics Center University of Oriente, Cuba
E. mail: carlos.cabal@cneuroedu.cu; carlos.cabal@quimica.unlp.edu.ar

MRI potential has been demonstrated during decades in several science and technology branches. The principal challenges in development of new MR hardware are discuses [1-4]. Physical, technological, biomedical, economic and commercial reasons are presented. The greater emphasis of the new technologies should promote superior and easier access to MRI studies conducting to earlier diagnostic of the diseases, disorders and anomalies. MRI physics- technological opportunities for the new development are mentioned. Further scientific networks are desirable to development these technologies are remarked.
Nowadays MRI technology development have two eyes of the same face. These two view-points, delineated below are strongly connected to each other:

The first one, in search of to improve the MR potentials: the increase of the spatial, spectral and time resolutions, the SNR and CNR rising, the reduction of the imaging time, in resume, the enlargement of the structural and functional information obtained from the subject. Likewise, it is imperative to enrich the quantitative information obtained from the experiments, even having the same MRI main parameters.

The second, and no less important viewpoint, is related to the patient comfort and access to the MRI examination, which is a cardinal issue depending on several factors, such as health policy, the density of machines per habitants, the cost of a scan, among others. These factors strong determine the real impact of MRI. Access to the MR examination decides how early diagnosis can be made a diagnostic and how effective therapy can be for higher incidence diseases such as stroke, the tumors, etc. In addition, access is crucial for prevention in healthcare. In this sense, physics and technological developments are reducing the MRI equipment requirements, and besides for the examination rooms and the experience of the operators. However, the access is not changing fast enough.

Many efforts are being doing both directions. Let mention only the some development directions [5-14]:

- Integration design of the main magnetic field with the gradient, RF and shim coils are a successful way to avoid many restrictions. Some original magnetic system on the base of array of permanent magnet most be mentioned.
- New coils configurations. Non linear gradients introducing a non-bijective relationship in space codification, a new paradigms, named Parallel Acquisition Technique with Localized gradients (Patloc) and Steering Resonance Over Object (STEREO),
- New algorithms for the images reconstruction and it post processing using the artificial intelligence, learning machine, big data, etc.
- New materials in particular Metamaterial to increase the SNR. These news materials can impact, even more, attenuating others MRI challenges like the Eddy currents and the diverse internal interactions between the prevailing electromagnetic fields.
- Novel array of local coils including RF (transmission and reception); gradient coils and shim local coils. For instance, the *Integrated Parallel Reception Excitation and Shim coil* (iPRES).
- Non Faraday base sensor of the MR signal.
- New electronics. Quantum devises and technology.
- Magnetization transfer as well as Hyper polarize substance.
- Multi nucleus MR,

- New pulse sequence according to the new hardware, the images reconstruction algorithm and informatic capabilities.

New developments of low-cost MRI machines are appearing [13, 14]. However, its keys features must to be improved for more versatile and superior examination attributes: additional pulse sequences, diversification of body parts, less scanning time, etc. Despite these and others unmentioned achievements, access remains a cardinal unresolved question to consider intensely.

Some of these ideas are discussed in more detail in the framework of this presentation.

References.

1. S. Kathiravanand, J. Kanakaraj "A Review on Potential Issues and Challenges in MR Imaging" The Scientific World Journal Volume 2013, Article ID783715,10 pages http://dx.doi.org/10.1155/2013/783715
2. A. Nowogrodzki, "The Strongest Scanners", Nature, 2018 VOL 563, p.24- 26
3. M. Sarracanie, N. Salameh "Low-Field MRI: How Low Can We Go? A Fresh View on an Old Debate" 2020, Front. Phys. 8:172. doi: 10.3389/fphy.2020.00172
4. C. Cabal "The sense of development of MRI". 18 International Youth School Conference Spinus 2021. Proceedings, Saint Petersburg, Russia, March April, 2021, p. 91-92
5. Yu. Bunkov, Supermagnonics, 14 International Youth School Conference Spinus 2021. Proceedings, Saint Petersburg, Russia, April, 2017, p. 26
6. C. Z. Cooley, M.W. Haskell, S. F. Cauley, C. Sappo, C. D. Lapierre, et all "Design of sparse Halbach magnet arrays for portable MRI using a genetic algorithm"; IEEE Trans Magn. 2018 January; 54(1): .doi:10.1109/TMAG.2017.2751001.
7. G. Schultz "Magnetic Resonance Imaging with Nonlinear Gradient fields" Springer, 2013
8. M. Poole, "Improved Equipment and Techniques for Dynamic Shimming in High Field MRI" The University of Nottingham for the degree of Doctor of Philosophy, August 2007
9. A. V. Shchelokova, C. A.T. van den Berg, D. A. Dobrykh, S. B. Glybovski, M. A. Zubkov, E. A. Brui et all "Volumetric wireless coil based on periodically coupled split-loop resonators for clinical wrist imaging" Magn. Reson. Med. 2018;1–12 DOI: 10.1002/mrm.27140
10. H. Chen, L. Guo, M. Li, A. Destruel, C. Liu, E. Weber, F. Liu and S. Crozier "Metamaterial-inspired Radiofrequency (RF) Shield with Reduced Specific Absorption Rate (SAR) and Improved Transmit Efficiency for UHF MRI"; IEEE Transactions on Biomedical Engineering: DOI 10.1109/TBME.2020.3022884,
11. J. P. Stockmanna, L. L. Walda "In vivo B0 field shimming methods for MRI at 7T" Neuroimage. 2018 March; 168: 71–87. doi: 10.1016/j.neuroimage.2017.06.013.
12. A. Alipour, A. C. Seifert, B. N. Delman, P. M. Robson, R. Shrivastava, et all "Improvement of magnetic resonance imaging using a wireless radiofrequency resonator array" Nature, Scientific Reports | (2021) 11:23034 | https://doi.org/10.1038/s41598-021-02533-3
13. T. Kimura, Y. Geya, Y.Terada, K. Kose, T. Haishi, H. Gemma, and Y. Sekozawa "Development of a mobile magnetic resonance imaging system for outdoor tree measurements" Review of Scientific Instruments 82, 053704 (2011); doi: 10.1063/1.3589854 View online: http://dx.doi.org/10.1063/1.3589854
14. Y. Liu, Alex, T. L. Leong, Y. Zhao, L. Xiao, H. K. F. Mak , A. C. On Tsang, G. K. K. Lau, G. K. K. Leu, Ed X. Wu "A low-cost and shielding-free ultra-low-field brain MRI scanner" Nature Communications | https://doi.org/10.1038/s41467-021-27317-1

Proton Magnetic Relaxation in human urine

Juan Carlos García Naranjo[2], Néstor Juan Rodríguez De la Cruz[1], Manuel Arsenio Lores Guevara[2], , Haydée Cruz Vadell[3], Fabián Tamayo Delgado[2], Indira Caballero Martínez[2], Manuel Noda Guerra[2]

[1]Escuela de Física. Facultad de Ciencias. Universidad Autónoma de Santo Domingo. Santo Domingo,República Dominicana.
[2]Laboratorio de Relajación Magnética Nuclear. Centro de Biofísica Médica. Universidad de Oriente. Santiago de Cuba. Cuba.
[3]Facultad de Medicina No. 1. Instituto Superior de Ciencias Médicas. Santiago de Cuba. Cuba.
Email: lores@uo.edu.cu
http://www.uo.edu.cu

Introduction

The human urine contains water, ions and macromolecules [1]; including information about several diseases [1, 2]. Different research methods have been used to investigate human urine [3-6], including magnetic resonance spectroscopy [7,8] and relaxation [1, 2]. Nevertheless, a low amount of samples (around 5) have been regularly used and mainly the longitudinal proton magnetic relaxation time (T_1) has been utilized.

In this work we have used proton magnetic relaxation to characterize human urine increasing the number of samples and employing T_1, the transverse proton magnetic relaxation time (T_2) and the water self-diffusion coefficient (D).

Materials and Methods

Fifty human urine samples were obtained from voluntary healthy individuals. For the measurement of T_1, T_2 and D, a LapNMR console (Tecmag, Houston, USA) was used coupled to a permanent magnet (B_0 = 0.095 T, ν_0 = 4.03 MHz). Saturation Recovery and Carr-Purcell-Meiboon-Gill (*CPMG*) pulse sequences were employed to measure the mentioned parameters [9, 10]. All the experiments were performed at 293 K.

Results and discussion

Table 1 summarizes the values of T_1, T_2 and D obtained in human urine samples from healthy individuals.

Table 1. Values of T_1, T_2 and D in 50 samples of human urine from healthy individuals.

Sample	T_1 (ms)	T_2 (ms)	D (10^{-9} m^2/s)
Human urine from healthy individuals	2659±240	2218±100	1.77±0.09

The values of T_1 and D in table 1 are very similar to those obtained in water samples in the same experimental conditions [11]. The minor value obtained for T_2 is due to the diffusion of the water protons in the small magnetic field gradient at the magnet used for the experiment, thus provoking this value corresponds with one effective T_2 value. This result support previous conclusions which suggest that human urine could be considered mainly as a water sample from the proton magnetic relaxation point of view. Then, we can stay that the proton magnetic relaxation will be characterized by the following equations [11]:

$$\begin{aligned} R_1 &= R_1^{rot} + R_1^{Dif} \\ R_2 &= R_2^{rot} + R_2^{Dif} \end{aligned} \qquad (1)$$

$$R_1^{Rot} = \frac{3}{10}\left(\frac{\mu_0}{4\pi}\right)^2 \frac{\gamma^4\hbar^2}{b^6}\left[\frac{\tau_C}{1+(\omega_0\tau_C)^2} + \frac{4\tau_C}{1+4(\omega_0\tau_C)^2}\right]$$
$$R_2^{Rot} = \frac{3}{20}\left(\frac{\mu_0}{4\pi}\right)^2 \frac{\gamma^4\hbar^2}{b^6}\left[3\tau_C + \frac{5\tau_C}{1+(\omega_0\tau_C)^2} + \frac{2\tau_C}{1+4(\omega_0\tau_C)^2}\right] \quad (2)$$

$$R_1^{Dif} = R_2^{Dif} = \left(\frac{\mu_0}{4\pi}\right)^2 \frac{3\pi^2\gamma^4\hbar^2 N_0^j}{kT}\eta \quad (3)$$

Here $R_1=1/T_1$, $R_2=1/T_2$, γ is the gyromagnetic ratio of the ^1H, $\hbar$ is the Planck constant divided by 2π, μ_0 is the magnetic permeability of the vacuum, k is the Boltzmann constant and *b* is the inter proton distance inside the water molecule. ω_0 is the frequency of resonance of the ^1H and τ_c is the effective correlation time of the spin pair interacting at a fixed distance *b*. Moreover, N_0^j is the number of water molecules per cm^3 diffusing around the relaxing ^1H, *D* is the diffusion coefficient and *r* the inter proton distance for the dipolar interaction modulated by diffusion. In equations 2 and 3 a homonuclear interaction between spin pairs with *I=1/2* (*I* is the quantum number of the interacting nucleus) has been considered, with the interacting nuclei embedded inside a spherical molecule which rotate and diffuse in a continuous medium of dynamic viscosity η at the absolute temperature *T*.

A statistically significant correlation was found between T_2 and the albumin concentration (C) in the 50 samples of human urine from healthy individuals (r=-0.817351, P<0.01, 99 % of confidence). This can be explained considering that an increase of C will increase the values of η and τ_C in equations 2 and 3 according to the Debye and Mooney models [12]. This correlation is observed also in figure 1 where is showed the behavior of R_2 ($1/T_2$) versus C in samples of human urine from healthy individuals doped with albumin.

This is a very important result because it supports a potential application of T_2 for the diagnostic of pathological states in diseases where C is increased.

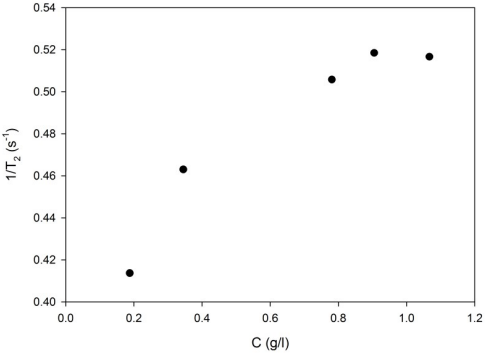

Figure 1. R_2 ($1/T_2$) versus C in samples of human urine from healthy individuals, doped with albumin.

Conclusions

A more detailed and extensive characterization of human urine from healthy individuals has been performed, which indicates that human urine can be considered as water

from the proton magnetic resonance point of view. On the other hand, a moderatly strong correlation between the transverse proton magnetic relaxation time and the albumin concentration was found supporting the posibility for development of medical applications based on magnetic relaxation applications.

Acknowledgements

This work has been supported by the Belgian Development Cooperation through VLIR-UOS. The authors also wish to thank the MRI Centre of the University of New Brunswick in Canada, for the support received for the completion of this work.

References:

1. R. Azoury, S. Abrashkin, J. Weininger, A. Iaina. – Magn. Reson.Imaging, A6, 49 (1988).
2. A. Alanen, P. Nummi, M. Kormano, K. Irjala. -Acta Radilógica, A28 (1987)
3. W.G. Robertson, D.S. Scurr, L.M. Bridge.- J. Cryst. Growth, A53, 182 (1981).
4. P.G.Werness, H. Bergert, L.H. Smith. J. Cryst. Growth, A53, 166 (1981).
5. A. Hodgkinson. -Invest. Ural. A18, 123 (1980).
6. C.E.Dent, D.J Sutor. -Lancet 2:775-778; 1971
7. S. Connor,J. Everett, J.K. Nicholson. – Magn. Reson. Med. A4, 461 (1987).
8. J.K. Nicholson, P. M. O'flynn, P. J. Sadler. -Biochem. J. A 217, 365 (1984).
9. M. Lores, C. Cabal. –Appl. Magn. Reson., 28(1), 79-84 (2005).
10. M, A. Lores Guevara, J.C. García-Naranjo, Y. Mengana, J. Pereira. -Advances in Biological Chemistry, A4, 388 (2014). doi: 10.4236/abc.2014.46044.
11. N. Bloembergen, E. M. PurceH, R. V. Pound. Phys. Rev. **A73**, 679 (1948).
12. M. A Lores-Guevara, C.A. Cabal, O. Nascimento, A. M. Gennaro.-Appl. Magn. Reson. A30, 121 (2006).

Formation of AHAHA⁻ anionic clusters via out-protonation of DMAN proton sponge by phosphoric acid

Edem R. Chakalov[1], *Valeria V. Mulloyarova*[1], *Alexander S. Antonov*[1] *and Peter M. Tolstoy*[1]

[1]*Institute of Chemistry, Saint Petersburg State University, Saint Petersburg, Russia*
E-mail: st086266@student.spbu.ru

Introduction

It is a common knowledge that the phenomenon of hydrogen bonding is ubiquitous. The mutual influence of short strong H-bonds with the bridging protons delocalized between two heavy atoms in complexes involving several coupled H-bonds (so-called cooperative effects) is attracting a great attention and is being extensively studied in connection to various problems in modern chemical bond theory and reactivity [1], biochemistry and enzyme catalysis [2], applied electrochemistry [3].

Phosphorous-containing acids (phosphonic, phosphinic, phosphoric) possess the strong POH proton donating functionality and P=O proton acceptor. Some of us shown previously by spectroscopic methods that they form exceedingly robust H-bonds in self-associates in solid, liquid and gas phase [4] (Fig. 1). Much less is known about the formation of $(AH)_nA^-$ complexes (homoconjugated anions) of these acids with their conjugate bases. To the best of our knowledge, there is only one paper published in 2001, in which the cooperativity of H-bonds in homoconjugated anions of two R_2POOH acids – dimethylphosphoric (R = MeO) and dimethylphosphinic (R = Me) is discussed [5].

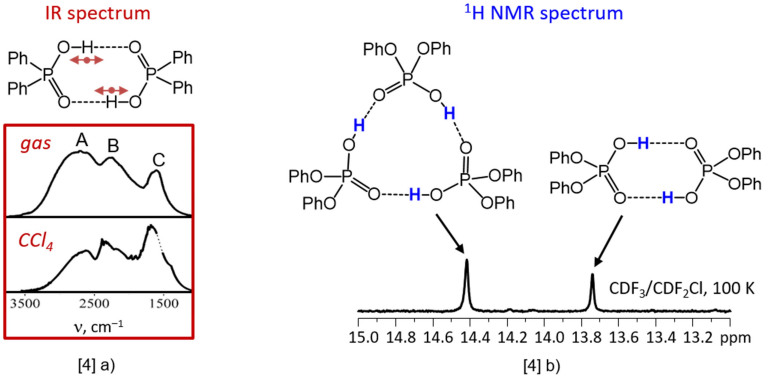

Figure 1. Examples of POOH-containing acids self-associates.

Methods and objects

NMR spectroscopy is one of the most informative methods to study H-bonded complexes. To measure NMR parameters (isotropic chemical shifts and spin-spin coupling constants) correlated with the bridging proton position the low-temperature NMR is often used in order to increase the lifetime of the complexes and to observe their separated signals due to the slow proton and molecular exchange regime [6]. Obtained correlational dependencies might then be used to interpret NMR spectra in terms of H-bond geometry and strength and to study the cooperativity effects by using H/D isotope effects on geometry as a weak perturbation of the system [7].

We have studied 1 : 1 and 1 : 3 complexes of 1,8-bis(dimethylamino)naphthalene (DMAN, a well-known organic base with exceedingly high thermodynamic basicity and very

low kinetic basicity in NMR time scale [8]) with several R_2POOH acids (Fig. 2) by low-temperature ^1H and $^{31}P\{^1H\}$ NMR spectroscopy (solvent: liquefied freon CDF_3/CDF_2Cl mixture, temperature down to 100 K).

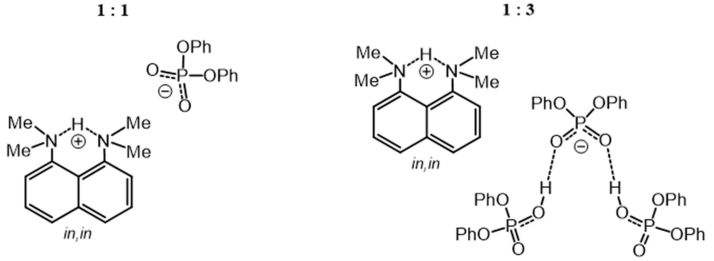

Figure 2. Schematic representation of the complexes discussed in this work.

Results and discussion

As an example, in Fig. 3 we show the low-field part of ^1H spectrum of non-deuterated sample with diphenylphosphoric acid $(PhO)_2POOH$ at 120 K.

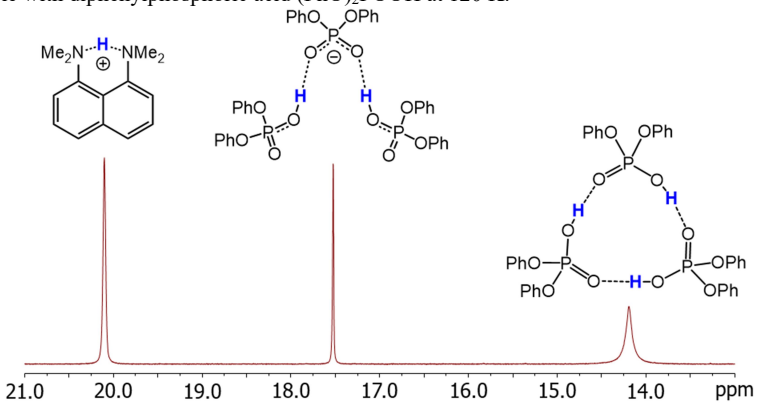

Figure 3. Low-field part of ^1H spectrum of the sample discussed in this work.

The structure of the homoconjugated anion, $(AH)_2A^-$, with two equivalent H-bond, $(PO–H\cdots OP)^-$, is fluxional and characterized by a very fast degenerate transfer of all bridging protons without dissociation of the complex via six elementary steps, similar to what was previously found for homoconjugated anions of carboxylic acids [9]. An anticooperative coupling of H-bonds, i.e. mutual weakening (lengthening) of them due the opposite directions of the electronic polarization at central POO^- moiety was confirmed by positive H/D isotope effect (low-field shift for the bridging proton signal in the half-deuterated HD form) and quantum-chemical (DFT) calculations (potential energy surface for the two protonation pathways).

Finally, we propose a model mechanism for the acid-base interaction leading to the formation of the ionic pairs $(AH)_2A^-/DMAN\text{-}H^+$ (Fig. 4). The proton transfer to the DMAN molecule proceeds via rotational interconversion (steps ① → ② and ⑤ → ⑥) of one of the dimethylamino groups [10] with a formation of an elusive short-lived intermediate states ③, ④ and ⑤ along the protonation pathway.

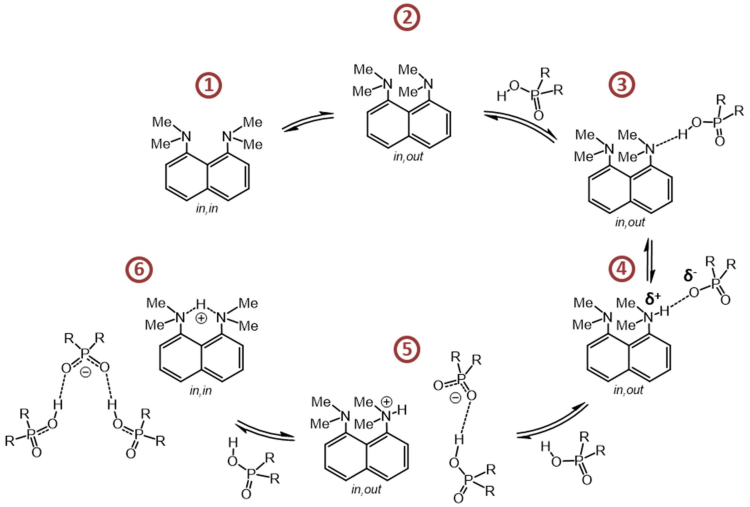

Figure 4. A model mechanism of the acid-base interaction leading to the formation of the $(AH)_2A^-$/DMAN-H^+ ion pair.

Acknowledgements

This work was supported by the Russian Science Foundation (project № 18-13-00050).

References

1. S. J. Grabowski. – Chem. Rev., 111(4), 2597–2625. (2011);
2. (a) W. W. Cleland, M. M. Kreevoy. – Science, 264, 1887–1890 (1994). (b) P. A. Frey, S. A. Whitt, J. B. Tobin. – Science, 264, 1927–1930 (1994).
3. Rath, R., P. Kumar, L. Unnikrishnan, S. Mohanty, S. K. Nayak. – Polym. Rev., 60(2), 267–317 (2019).
4. (a) R. E. Asfin, G. S. Denisov, K. G. Tokhadze, – J. Mol. Struct., 790, 11–17 (2006). (b) V. V. Mulloyarova, I. S. Giba, M. A. Kostin, G. S. Denisov, I. G. Shenderovich, P. M. Tolstoy – Phys. Chem. Chem. Phys., 20, 4901–4910 (2018). (c) R. E. Asfin, G. S. Denisov, D. N. Poplevchenkov, K. G. Tokhadze, T. V. Velikanova. – Polish J. Chem., 76, 1223–1231 (2002).
5. C. Detering, P. M. Tolstoy, N. S. Golubev, G. S. Denisov, H. H. Limbach. – Doklady Phys. Chem., 379(1–3), 191–193 (2001).
6. N. S. Golubev., S. N. Smirnov, V. A. Gindin, G. S. Denisov, H. Benedict, H. H. Limbach. – J. Am. Chem. Soc., 116, 12055–12056 (1996).
7. P. Schah-Mohammedi, I. G. Shenderovich, C. Detering, H. H. Limbach, P. M. Tolstoy, S. N. Smirnov, G. S. Denisov, N. S. Golubev. – J. Am. Chem. Soc., 122(51), 12878–12879 (2000).
8. F. Hibbert. – J. Chem. Soc., Perkin Trans., 2, 1862–1866 (1974).
9. P. M. Tolstoy, P. Schah-Mohammedi, S. N. Smirnov, N. S. Golubev, G. S. Denisov, H. H. Limbach. – J. Am. Chem. Soc., 126, 5621–5634 (2004).
10. (a) A. Szemik-Hojniak, J. M. Zwier, W. J. Buma, R. Bursi, J. H. van der Waals. – J. Am. Chem. Soc., 120, 4840–4844 (1998). (b) V. A. Ozeryanskii, A. F. Pozharskii, A. S. Antonov, A. Filarowski. – Org. Biomol. Chem., 12, 2360–2369 (2014).

Development and study of novel pervaporation mixed matrix membranes based on polyphenylene oxide modified with graphene oxide for dehydration of ethylene glycol

Anastasia Chepeleva[1], Vladislav Liamin[1], Anton Mazur[1], Anna Kuzminova[1], Anastasia Penkova[1], Mariia Dmitrenko[1]

[1]St. Petersburg State University, 7/9 Universitetskaya nab., 199034 Saint Petersburg, Russia
E-mail: chepeleva1999@yandex.ru

Introduction

Pervaporation as a sustainable process is one of the promising membrane methods for separating liquid mixtures of low molecular weight substances, and it may be an alternative to traditional separation methods due to its advantages such as energy efficiency, economy, environmental friendliness and compact equipment. Due to the rapid development of this method and its active application for various industrial fields, the development of highly efficient membranes with improved characteristics is required. In this work for pervaporation dehydration of an industrial important substance - ethylene glycol, novel membranes based on poly(2,6-dimethyl-1,4-phenylene oxide) (PPO) with improved characteristics were developed by the modification with graphene oxide (GO) nanoparticles,.

Membrane investigation

The optimal preparation conditions of PPO/GO (0.1-0.9 wt.%) composites and two types (dense and supported) of membranes based on them were developed. The effect of the modification with GO on membrane structure was studied by Fourier-transform infrared (FTIR) and nuclear magnetic resonance (NMR) spectroscopies, scanning electron (SEM) and atomic force (AFM) microscopies. The physicochemical properties of developed membranes were investigated by thermogravimetric analysis (TGA), swelling experiments, and contact angle measurements. Transport characteristics of PPO-based membranes were tested in pervaporation separation of a mixture of ethylene glycol-water in a wide concentration range (10-90 wt.% water).

Results

It was demonstrated that the introduction of even low content of GO (till 0.9 wt.%) into PPO matrix led to the improved permeability of modified membranes maintaining high selectivity in dehydration of ethylene glycol. These were related to the changes in the structure (the formation of a more amorphous and rougher structure) and physicochemical properties (surface hydrophilization and increased swelling) confirmed by various analysis methods.

Acknowledgements

This research was funded by the Russian Science Foundation, grant number 21-73-00043. The experimental work was facilitated by the equipment from the Resource Centers for Nanotechnology, Magnetic Resonance, X-ray Diffraction Studies, Cryogenic Department, Thermogravimetric and Calorimetric Research Centre, Chemical Analysis and Materials Research Centre, and Centre "Nanofabrication of Photoactive Materials (Nanophotonics)" at the St. Petersburg State University.

The investigation of SAPO-11 structure by the combination of solid-state ^{27}Al, ^{29}Si, ^{31}P NMR spectroscopy and DFT calculations

Natalia E. Cherepanova[1,2], Ilya V. Yakovlev[1,2], Irina A. Shamanaeva, Olga B. Lapina[1,2]

[1]Novosibirsk State University, Pirogova 2, 630090, Novosibirsk, Russia
[2]Boreskov Institute of Catalysis, pr. Lavrentieva 5, 630090, Novosibirsk, Russia E-mail: n.cherepanova@g.nsu.ru

Intriduction

Nowadays, microporous silicoaluminophosphates are widely used as catalysts in n-paraffin isomerization, N_2O decomposition and n-octane hydroisomerization [1]. Silicoaluminophosphates (Fig. 1) are obtained by the inclusion of Si atoms in the aluminophosphates ($AlPO_4$-n) structure, the variation of the Si atoms inclusion mechanism in the aluminophosphate structure directly influences on their chemical properties such as acidity, catalytic activity and ion-exchange. The formation mechanism of silicon centers in crystalline silicoaluminophosphates SAPO-n is a current research problem.

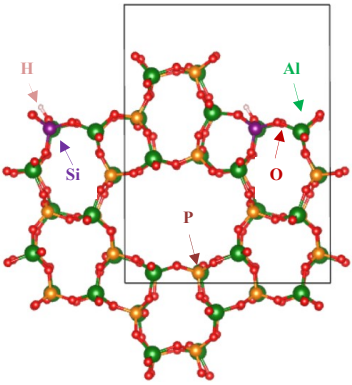

Figure 1. The SAPO-11 structure

The purpose of this work is to investigate the formation mechanisms of SAPO-11 silicon centers using the combination of solid-state ^{27}Al, ^{29}Si, ^{31}P NMR spectroscopy and DFT calculations. The combination of these techniques will allow to trace the temperature dependence of SAPO-11 silicon centers formation.

Materials and methods

The study object was crystalline silicoalumophosphate SAPO-11 which was obtained by template hydrothermal synthesis and calcined at different temperatures.

DFT (Density Functional Theory) calculations were performed to study the structure of SAPO-11 in the CASTEP software package [2]. The GIPAW method (Gauge Including Projector Augmented Waves) [3] was used to calculate the ^{27}Al, ^{29}Si, ^{31}P NMR parameters of the SAPO-11 structure.

Results and discussion

Modern solid-state NMR spectroscopy makes it possible to determine the local environment of the nuclei included in the SAPO-11 structure at the molecular level. The series of SAPO-11 ^{27}Al, ^{29}Si, ^{31}P MAS NMR spectra was obtained. The ^{31}P MAS NMR spectra of calcined SAPO-11 (Fig. 2) were characterized by the superposition of at least 2 lines whose position was about -31 ppm and -24 ppm (Fig. 3). It should be noted that the lines for

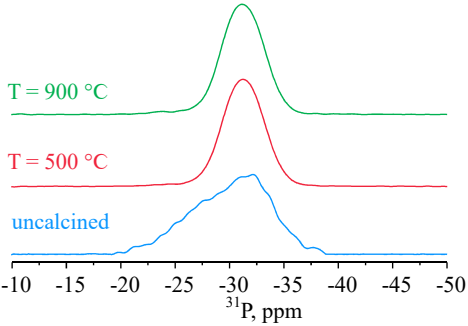

Figure 2. The ^{31}P MAS NMR spectra of SAPO-11

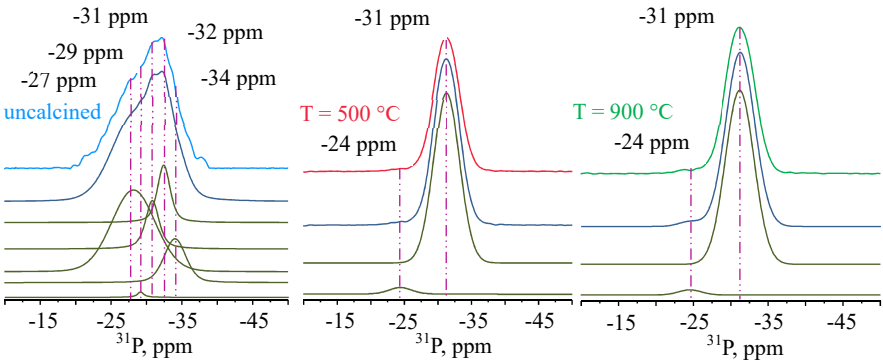

Figure 3. The simulation of SAPO-11 ^{31}P MAS NMR spectra

uncalcined SAPO-11 were broader than for calcined samples.

^{27}Al nucleus that has spin 5/2 is quadrupole, and thus, the second-order quadrupolar interaction broadening made the analysis of ^{27}Al MAS NMR spectra much more difficult. Additional experiments were required to determine the NMR parameters of quadrupole nuclei. MQMAS technique (Fig. 4) (MQMAS – Multiple Quantum Magic Angle Spinning) was used in this case, which made it possible to determine the line positions of the ^{27}Al MAS NMR spectra of SAPO-11.

^{27}Al MAS NMR spectra of SAPO-11 consisted from the superposition of at least 3 lines in the range characteristic of tetrahedrally coordinated aluminum atoms. The observed additional line for the uncalcined SAPO-11 with the isotropic chemical shift of about 6 ppm, which could be attributed to the pentacoordinated aluminum appeared as a result of the one water molecule coordination with the tetrahedrally coordinated aluminum atom.

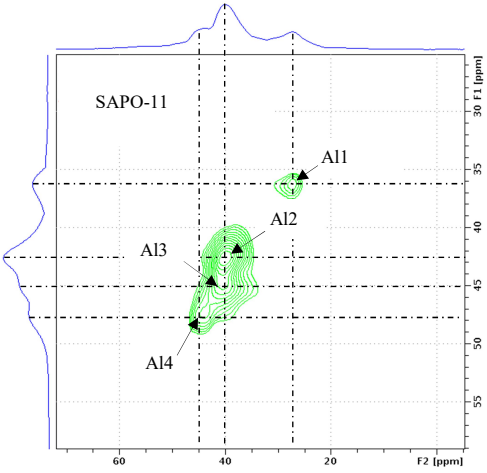

Figure 4. The ^{27}Al 3QMAS spectrum of SAPO-11

The comparison of ^{27}Al and ^{31}P MAS NMR spectra allowed to establish the changes in the SAPO-11 structure that occurred when the template was removed during sample calcination. The most informative method for the study of SAPO-11 system was ^{29}Si MAS NMR spectroscopy. ^{29}Si MAS NMR spectra were obtained for samples enriched with the ^{29}Si isotope (80% enrichment). The temperature dependence of silicon centers formation was traced by ^{29}Si MAS NMR spectroscopy for SAPO-11. It should be noted the calcined samples were characterized by the lines which allowed to attribute to the silicoaluminophosphate centers of the type Q^0 [Si(4Al)], Q^1 [Si(3Al,1Si)], Q^2 [Si(2Al,2Si)], Q^3 [Si(1Al,3Si)], respectively. The line Q^2 [Si(2Al,2Si)] was

absent for the uncalcined SAPO-11. DFT calculations were performed for detailed study of the SAPO-11 silicon centers formation.

Initially, the quantum chemical calculations of NMR parameters for the $AlPO_4$-11 structure were performed. It was determined that the $AlPO_4$-11 structure contained 3 non-equivalent aluminum centers with the following characteristic ^{27}Al NMR parameters: δ_{iso} = 38 ppm, C_Q = 2 MHz, η_Q = 0.85; δ_{iso} = 39 ppm, C_Q = 2 MHz, η_Q = 0.97; δ_{iso} = 22 ppm, C_Q = -0.6 MHz, η_Q = 0.36.

Next, the influence of the Si atoms substitution in the aluminophosphate structure on

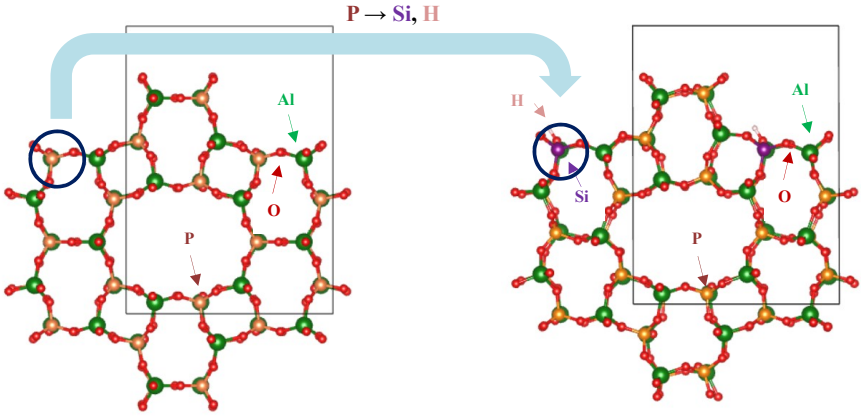

Figure 5. The $AlPO_4$-11 (on the left) and SAPO-11 (on the right) structures

the NMR parameters was considered. It was determined that the presence of one Si atom in the first coordination sphere of the Al atom changed ^{27}Al NMR parameters as followed: it increased the quadrupole constant of C_Q in 2-5 times and it changed the isotropic value of CS δ_{iso} by 5-20 ppm. The Figure 5 showed one example of a phosphorus atom substitution for a silicon atom and a proton ($P \rightarrow Si, H^+$).

Acknowledgements

This work was supported by the Ministry of Science and Higher Education of the Russian Federation within the governmental order for Boreskov Institute of Catalysis (project AAAA-A21-121011390054-1).

References

1. C. Baerlocher, L.B. McCusker, D.H. Olson, Atlas of Zeolite Framework Types, 6th Edition, 2007.
2. C.J. Pickard, F. Mauri, All-electron magnetic response with pseudopotentials: NMR chemical shifts, Phys. Rev. B - Condens. Matter Mater. Phys. (2001). https://doi.org/10.1103/physrevb.63.245101.
3. S.J. Clark, M.D. Segall, C.J. Pickard, P.J. Hasnip, M.I.J. Probert, K. Refson, M.C. Payne, First principles methods using CASTEP, Zeitschrift Fur Krist. (2005). https://doi.org/10.1524/zkri.220.5.567.65075.

NMR study of hydrogen bonding in mesogenic ionic liquids

Sergey V. Dvinskikh[1,2]

[1]Department of Chemistry, KTH Royal Institute of Technology, Stockholm, Sweden,
[2]Laboratory of Bio-NMR, St. Petersburg State University, St. Petersburg, Russia
E-mail: sergeid@kth.se

Elucidating the hydrogen bonding (HB) contribution to intermolecular interactions in imidazolium-based ionic liquids (ILs) has been a topic of a large number of experimental and computational studies [1]. It is also generally recognized that the occurrence and stability of the liquid-crystalline phase in mesogenic ILs are strongly related to a balance between hydrogen bonding, electrostatic interactions, and dispersion forces. We have recently demonstrated a profound role of HB in mesophase stabilization in ionic liquid crystals (ILCs) [2-6]. Indeed, the temperature range of the smectic phase is strongly correlated with the HB ability of counterions [3]. In the present study, the HB interactions in imidazolium-based mesogenic ILs are examined and compared in solid, isotropic liquid, and liquid crystalline states as well in ILs nanoconfined in porous solids.

Proton chemical shift (CS) in high-resolution NMR spectra provides a sensitive diagnostic tool for HB, also informing on the strength and extent of this interaction [7]. Our results in the isotropic phase of ILCs indicated that the ^{1}H CS in the imidazolium group increases in the anion sequence BF_4<I<Br<Cl, in the order of increasing hydrogen-bonding ability of anions. Such a trend essentially reproduces the tendency reported for conventional non-mesogenic ILs [7]. Accessibility of the HB sites can be also influenced by the position of the polar group within the cation and by the structure and size of substituting moieties. However, we found that the proton CS in the imidazolium ring is only slightly dependent on the structure of substitution units and location of the polar group as long as aprotic nature of the material is preserved. The HB strength is, counterintuitively, similar for cations with terminal and central position of the charged moiety. Likewise, the presence of two charged groups in the dicationic IL has a negligible effect. Thus, possible steric constraints do not alter the potential for H-bonding; the polar groups are well exposed for cation-anion association and formation of HB of these materials. In the isotropic liquid phase, this behavior can be attributed to high conformation freedom and mobility of flexible cations. On the other hand, the layered assembly in smectic phases can impose substantial constraints on cation conformational dynamics and alignment of functional groups [2-5,8].

To achieve ^{1}H chemical resolution in mesophase, MAS NMR was applied. For all materials, a small decrease of proton CS for the HB sites is observed at the transition from isotropic to smectic phase. This effect suggests decreasing potential for HB within the layered structure in SmA. The change is small for the salts with low-coordinating BF_4 anion but is more significant in the case of the strongly coordinating halogen anions. A comparably small decrease of CS is also observed for the cations with the central location of the charged moiety. Hence, also in the smectic phase, the charged group location has no large impact on the possibility of cation-anion association via HB. This justifies the concept of ionic sublayers which form in smectic ILCs irrespective of whether the charged group is in a terminal or central position in the cation structure.

When ILs are nanoconfined in porous silica, the cation-anion HB is locally disrupted by anion H-bonding to the solid interface where, for example, the surface hydroxyl group may serve as hydrogen-bonding donor centers. The observed significant upfield shift of imidazolium protons was attributed to a decrease of the cation-anion interaction due to an

increasing anion/surface hydrogen bond strength. The proximity of cations and anions to the solid surfaces was probed using a solid-state heteronuclear correlation NMR spectroscopy.

An important finding of our study is that HB strength decreases only slightly on the transition from isotropic to mesophase despite the strong molecular ordering and layered assembly in the smectic phase. The HB is not disrupted owing to the formation of an ionic sublayer where anions can approach polar groups. This dynamic ionic sub-layer forms irrespective of the structural position of the charged group in cation.

References

1. P. A. Hunt, C.R. Ashworth, R. P. Matthews. – Chem. Soc. Rev., 44, 1257 (2015).
2. J. Dai, B. B. Kharkov, S. V. Dvinskikh. – Crystals, 9, 18 (2019).
3. J. Dai, D. Majhi, B. B. Kharkov, S. V. Dvinskikh. – Crystals, 9, 495 (2019).
4. D. Majhi, J. Dai, A. V. Komolkin, S. V. Dvinskikh. – PCCP. 22, 13408 (2020).
5. D. Majhi, A. V. Komolkin, S. V. Dvinskikh. – Int. J. Mol. Sci., 21, 5024 (2020).
6. S. V. Dvinskikh. – Liq. Cryst. 47, 1975 (2020).
7. T. Cremer, et al. – Chem. Eur. J., 16, 9018 (2010).
8. D. Majhi, S. V. Dvinskikh. – Sci. Rep., 11, 5985 (2021).

NMR ^{133}Cs IN $CsPbBr_3$+Bi perovskites crystals

Andrey N. Gavrilenko[1], Alexei V. Emeline[2], Anna V. Shurukhina[2], Ecaterina V. Schmidt[1], Vadim L. Matukhin[1].

[1]Kazan State Power Engineering University, Kazan, 420066, Russia
[2]St. Petersburg State University, St. Petersburg, 198504, Russia
E-mail: ang_2000@mail.ru

Introduction

Complex lead halides $APbX_3$ (where A is a monovalent organic or inorganic cation and X is a halogen anion) with a perovskite structure exhibit truly unique electronic and optical characteristics, and their use as photoactive materials in solar cells can be considered a real breakthrough in the field of solar energy conversion [1, 2]. In this paper, we present the results of the study of perovskite $CsPbBr_3$+Bi crystals by ^{133}Cs NMR.

Methods

^{133}Cs NMR spectroscopy was carried out on a Bruker AVANCE III HD 400 NMR spectrometer (B = 9.4 T) equipped with a 4 mm double -resonance (H/X) Bruker magic-angle spinning (MAS) probe. MAS NMR spectra were acquired at natural abundance using a Bloch-decay experiment with a 10.0 μs π/2 pulse, 16 co-added transients, recycle delay of 1 second, and a spinning frequency of 9 kHz. Non – spinning ^{133}Cs NMR spectra were acquired using a Hahn echo experiment using similar experimental parameters as noted above.

Results

The ^{133}Cs isotope has a relatively small quadrupole moment and low hyromagnetic ratio. Due to specific dependencies chemical and quadrupole shifts of the central component of the spectrum NMR from Larmor frequency and to increase the signal-to-noise ratio. Simultaneous measurement of the EFG and CS tensors is expedient to be carried out in strong magnetic field. In this case, the parameters of the first tensor are determined from the orientation dependences of the quadrupole splits. The relatively small value of the quadrupole interaction ^{133}Cs nuclei made it possible to record the entire spectrum (7 lines, I=7/2) for each magnetically nonequivalent cesium ion at the corresponding values field sweeps. An example of the ^{133}Cs NMR spectrum at room temperature is shown in Figure 1 and its NMR chemical shifts is shown in Figure 2.

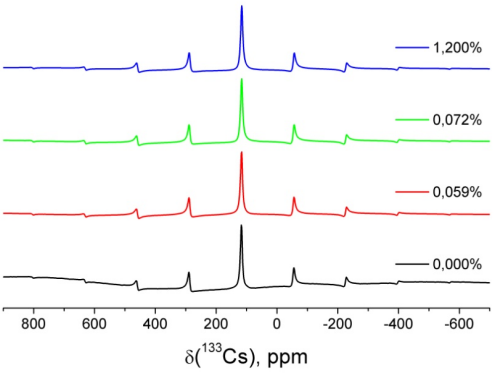

Figure 1. ^{133}Cs NMR spectra for $CsPbBr_3$+Bi at 9.398 T with a magic-angle spinning frequency of 9 kHz. The amount of Bi is indicated as a percentage in the figure.

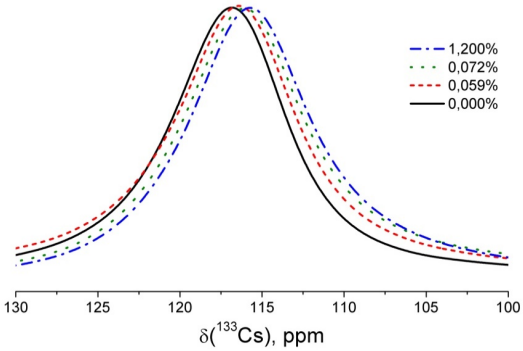

Figure 2. ^{133}Cs NMR chemical shifts for $CsPbBr_3$+Bi at 9.398 T with a magic-angle spinning frequency of 9 kHz. The amount of Bi is indicated as a percentage in the figure.

Conclusions

The obtained results of the study of the ^{133}Cs NMR spectra indicate the efficiency of the Bi doping process, i.e., the impurity is regularly incorporated into the crystal lattice of the $CsPbBr_3$ compound.

References

1. Q. Xu, D. Yang, J. Lv, Y. Y. Sun, L. Zhang, Perovskite Solar Absorbers: Materials by Design. *Small Methods*. – 2, 1700316. (2018).
2. B. R. Sutherland, E. H. Sargent. Perovskite Photonic Sources. *Nat. Photonics*. – 10, 295−302 (2016).

Magnetic properties of $Li_3V_2(PO_4)_3$/C and $Li_3V_2(PO_4)_3/Li_3PO_4$ composites: ESR measurements

Tatiana Gavrilova, Sergey Khantimerov, Ivan Yatsyk, Nail Suleimanov[1]

[1]*Zavoisky Physical-Technical Institute, Federal Research Center Kazan Scientific Center of RAS, Kazan 420029, Russia*
E-mail: tatyana.gavrilova@gmail.com

Introduction

The interest in alternative energy sources has been increasing every year over the past two decades. Among different energy alternatives, rechargeable batteries are the most popular energy storage devices. Currently, one can see the exciting developments in new positive electrode (cathode) materials for these batteries. Among them the monoclinic $Li_3V_2(PO_4)_3$ with promising electrochemical properties including excellent cycling stability, high theoretical capacity, low synthetic cost, improved safety characteristic, and low environmental impact emerges as a highly suitable candidate for using in lithium ion batteries. The possible changes in the valence state of the transition element in lithium oxides during the intercalation/deintercalation process can directly affect the transport properties of electrode materials and can be directly investigated using the electron spin resonance method.

Research objects

The investigated $Li_3V_2(PO_4)_3/Li_3PO_4$ (LVPO/LPO) solid solution was obtained by the thermal hydrolysis method with the subsequent annealing in Ar atmosphere [1]. The crystal structure of $Li_3V_2(PO_4)_3$ phase belongs to the monoclinic space group $P2_1/n$ (#14) with unit cell parameters a=8.606(1) Å, b=8.587(4) Å, c=12.032(1) Å, α=ϒ=90°, β=90.554°(1), V=889.1(2) Å^3. The crystal structure of Li_3PO_4 phase belongs to the orthorhombic space group *Pnma* (#62), a=6.146 Å, b=10.453 Å, c=4.913 Å, α= β =ϒ=90°, V=315.64 Å^3 [5]. In comparison, the mesoporous sample of $Li_3V_2(PO_4)_3$/C (LVPO/C) was synthesized by the soft-template method [2]. The unit cell parameters for $Li_3V_2(PO_4)_3$/C material are a = 8.6095 Å, b = 8.6041 Å, c = 12.0560 Å and β= 90.490°and its cell volume is estimated to be 893.044 Å^3 (space group $P2_1/n$) [2].

Magnetic properties investigations

Magnetization

The magnetization of LVPO/LPO and LVPO/C samples as a function of temperature (M-T curve) was measured in magnetic field H=0.1 T in FC regime (Figure 1 a). At high temperatures the inverse magnetic susceptibility is linear and can be well fitted by the Curie-Weiss law $\chi = C/(T - \theta_{CW})$, where C is the Curie constant and θ_{CW} - Curie-Weiss temperature. The high temperature approximation of the experimental data by the Curie-Weiss law gives the negative values of the Curie-Weiss temperature θ_{CW} = -68 K and θ_{CW} = -22 K for LVPO/LPO and LVPO/C, respectively, that suggests the antiferromagnetic nature of the exchange interactions between spins in the investigated samples. Higher absolute value of the Curie-Weiss temperature in LVPO/LPO indicates stronger magnetic interactions in this sample compared to another. The obtained from the Curie constants effective magnetic moment is equal to 3.9 μ_B for LVPO/LPO and 2.59 μ_B for LVPO/C, respectively. At the same time the theoretically estimated effective magnetic moment for V^{3+} magnetic ions ($3d^2$, S=1) is μ_{theor} = 3.9 μ_B, that confirms the valence state of the vanadium ions as V^{3+}. The ZFC-FC splitting (Figure 1b) was observed below T_{split}=120 K only in LVPO/LPO that proves the above-mentioned suggestion about the presence of more significant short-range magnetic correlations in LVPO/LPO compared to LVPO/C [1, 2]. Obviously, magnetic correlations in

the LVPO/LPO sample can lead to the existence of ferromagnetically ordered regions due to the antisite cation exchange, namely the occupation of transition metals sites by Li and vice versa, which may further affect the transport properties.

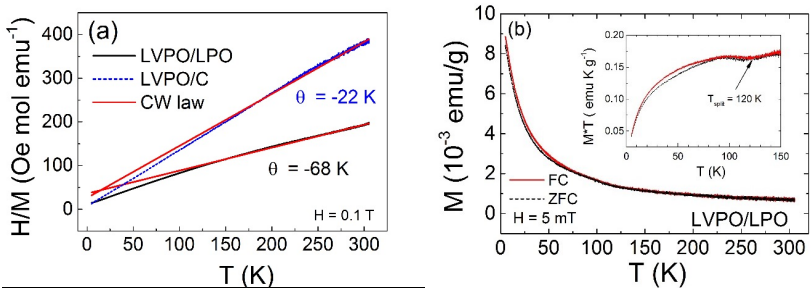

Figure 1. (a) Temperature dependencies of the inverse magnetic susceptibility H/M measured in FC regime; grey solid lines correspond to the Curie-Weiss law. (b) Temperature dependence of magnetization measured in FC, ZFC regimes; inset shows the low temperature data in representation M·T vs. T in more detail.

Electron spin resonance

Magnetic resonance spectra were measured using ER 200 SRC (EMX/plus) spectrometer (Bruker) at the frequency of 9.4 GHz with a Temperature Controller ITC503S (Oxford instruments) in the temperature range from 5 to 100 K with an interval of 5 K. Electron spin resonance measurements of as-prepared LVPO/C powder and LVPO/C electrode upon fully charging up to 4.6 V and fully discharging up to 2.5 V were performed in order to investigate the changes in the local coordination of vanadium ions and to check their valence states during the cycling of LVPO/C cell. In the as-prepared LVPO/C V^{3+} ions have d-electronic configuration $3d^2$ and ground state ^3F with spin $S = 1$. For such ions with an even number of electrons in the respective electronic shells singlet ground-state levels may result such that no ESR is observable. Indeed, we did not observe the ESR signal in as-prepared $Li_3V_2(PO_4)_3$ samples which would be expected for vanadium ions in [3+] valence state. At the same time using low temperatures we were able to resolve a weak resonance signal in the ESR spectra of as-prepared compound (Figure 2 a). Approximation of these spectra yielded the best fit of experimental data for the powder spectrum corresponding to paramagnetic centers with effective spin $S = 1/2$ and anisotropic g-factor. Obtained anisotropic g-factor $g_\perp = 1.972$, $g_\parallel = 1.933$ (at T=100 K) is close to the g-factor of V^{4+} ions in tetragonally distorted VO_6 octahedra. We suggest that ESR spectra of the as-prepared compound corresponds to V^{4+} ions. The presence of V^{4+} ions in the initial samples of LVPO/C can be associated with small lithium non-stoichiometry.

Typical ESR spectra of delithiated (obtained by the full charge of an electrochemical cell) LVPO/C can be approximated, as in the previous case, by the powder spectrum, corresponding to the paramagnetic centers with effective spin $S = 1/2$ and anisotropic g-factor (Figure 2 a). We suggest that vanadium ions in the delithiated sample can change their valency state from [3+] to [4+/5+] during charging. It should be noted that V^{5+} ion has no electrons in 3d electron shell and therefore this ion is ESR silent. It should be noted that ESR signal discussed above was not observed in the ESR spectra of relithiated (obtained after one full charge/discharge cycle) LVPO/C which has the same composition as as-prepared LVPO/C (Figure 2 b). This fact indicates that vanadium ions giving rise to the ESR signal in the as-prepared samples change their valence state during the cycling of LVPO/C cell. The reduction

of all vanadium ions to the valence state [3+] after the first charge/discharge cycle corresponds to reversible intercalation of all lithium ions to the $Li_3V_2(PO_4)_3$. Thereby, the host structure of $Li_3V_2(PO_4)_3$ samples allows to use its maximum capacity during the first charge/discharge cycle. ESR measurements of as-prepared LVPO/LPO composite also suggest the presence of a small amount of V^{4+} ions ($3d^1$, S=1/2). It is about 10 percent of total vanadium ions for LVPO/LPO [1], while for LVPO/C it is about 1.5-2% [2].

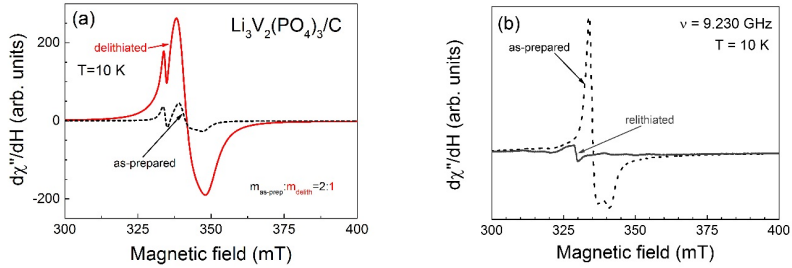

Figure 2. (a) ESR spectra of the as-prepared (dashed line) and the fully delithiated (solid line) samples of $Li_3V_2(PO_4)_3$/C normalized to the integral intensity of the reper. Inset shows the relative integral intensity of the ESR signal for as-prepared and delithiated samples; (b) ESR spectra of the as-prepared (dashed line) and the relithiated (solid line) samples of $Li_3V_2(PO_4)_3$/C normalized to the mass.

Conclusions

Magnetic properties of $Li_3V_2(PO_4)_3$/C and $Li_3V_2(PO_4)_3/Li_3PO_4$ composite materials were investigated using magnetometry and electron spin resonance methods. As-prepared phase of $Li_3V_2(PO_4)_3$/C demonstrates the paramagnetic properties due to the presence of the low amount of V^{4+} ions ($3d^1$, S=1/2) because of non-stoichiometry of the sample. ESR measurements were performed on LVPO/C sample after Li deintercalation and intercalation processes. It is known that lithium ions and electrons have to move simultaneously in the host structure of cathodic material during intercalation/deintercalation processes. The complete reduction of vanadium ions to the initial valence state V^{3+} after the first charge/discharge cycle was determined indicating the reversible intercalation of all lithium ions to the structure during the first delithiation/lithiation cycle in the investigated $Li_3V_2(PO_4)_3$/C composite and good kinetics of lithium/sodium transport in $Li_3V_2(PO_4)_3$.

Investigations of electrochemical properties of $Li_3V_2(PO_4)_3/Li_3PO_4$ composite are in progress, and we suppose that more significant short-range magnetic correlations in $Li_3V_2(PO_4)_3/Li_3PO_4$ compared to $Li_3V_2(PO_4)_3$/C can improve them.

Acknowledgements

This work is supported by the Russian Science Foundation (grant #19-79-10216).

References

1. T. Gavrilova, S. Khantimerov, M. Cherosov, R. Batulin, N. Lyadov, I. Yatsyk, Y. Deeva, D. Turkin, T. Chupakhina, N. Suleimanov. – Magnetochemistry, 7, 64 1 – 9 (2021).
2. T.P. Gavrilova, S.M. Khantimerov, R.R. Fatykhov, I.V. Yatsyk, M.A. Cherosov, H.S. Lee, R. Vishwanathan, K. Saravanan, N.M. Suleimanov. - Solid State Communications, 323, 114108 1 – 6 (2021).

Magnetic and crystal structure of Tb-doped $BiFeO_3$

N.E. Gervits[1], A.V. Tkachev[1], A.V. Gunbin[1], S.V. Zhurenko[1], A.A. Gippius[1,2], A.O. Makarova[3], V.S. Pokatilov[3]

[1]Lebedev Physical Institute, Russian Academy of Sciences, 119991, Moscow, Russia
[2]Lomonosov Moscow State University, 119991, Moscow, Russia
[3]MIREA-Russian Technological University (MIREA), 119454, Moscow, Russia
E-mail: ngervits@gmail.com

Introduction

One of the main tasks in the study of multiferroics based on bismuth orthoferrite is the search for the most suitable for industrial application dopant and the required degree of doping. The optimal composition is supposed to modify the spatial spin-modulated structure (SSMS) characteristic of the parent $BiFeO_3$ compound and realize the potential of the magnetoelectric effect of the material [1, 2].

The samples and characterization

In this work, samples of bismuth orthoferrite doped with Tb in the A position with x = {1.5%, 5%, 16%} obtained by solid-phase synthesis were studied. X-ray analysis showed that most of the samples possess the rhombohedral *R3c* structure.

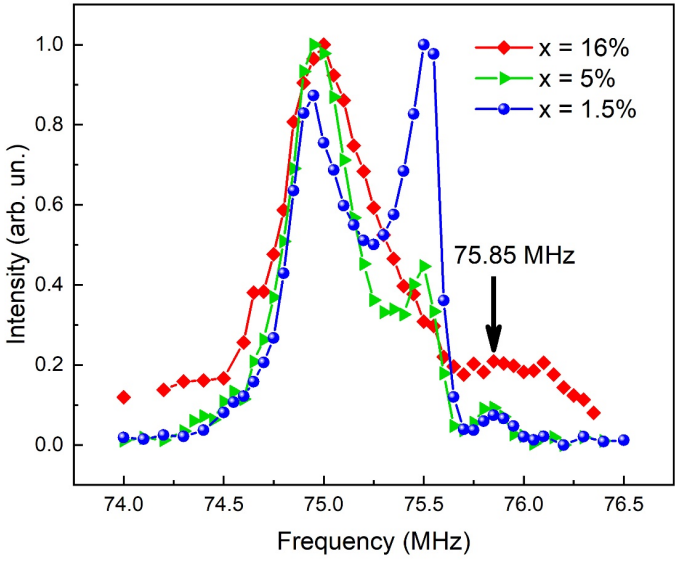

Figure 1. $Bi_{1-x}Tb_xFeO_3$ ^{57}Fe ZF NMR spectra

NMR spectroscopy data

All samples were studied using ^{57}Fe NMR spectroscopy in zero field at 4.2 K (Fig. 1). It was found that, in the substitution range of 1.5–5%, SSMS provides a different response strongly dependent on the amplitude of the applied RF pulses up to a change in the type of anisotropy. In general, small degrees (1.5; 3%) of doping result in the anharmonicity parameter *m* being reduced compared to parent bismuth ferrite.

However, when studying a sample with a substitution of 8.5%, it was found that the the above effect almost disappears and “easy plane” type anisotropy with *m* almost equal to 1 is observed, which indicates the degeneration of the SSMS into almost a collinear structure.

To the right of the main spectrum, at a frequency of 75.85 MHz, an additional low-intensity high-frequency line was detected. A similar phenomenon was previously observed when bismuth was replaced by La and Sr and can be associated with Fe atoms in the immediate vicinity of the corresponding ligands [3, 4].

Acknowledgments

V.S. Pokatilov and A.O. Makarova appreciate the support of the RFBR grant No. 20-02-00795.

References

1. Nair, S.G., Satapathy, J. & Kumar, N.P. Influence of synthesis, dopants, and structure on electrical properties of bismuth ferrite (BiFeO3). *Appl. Phys. A* **126,** 836 (2020).
2. Ghosh, A., Trujillo, D.P., Choi, H. *et al.* Electronic and Magnetic Properties of Lanthanum and Strontium Doped Bismuth Ferrite: A First-Principles Study. *Sci Rep* **9,** 194 (2019).
3. N.E. Gervits, A.V. Tkachev, S.V. Zhurenko, A.V. Gunbin, V.S. Pokatilov, A.A. Gippius, Zero-field 57Fe NMR in BiFeO3 based compounds: Problems, solutions, and application to Bi1-xSrxFeO3, Solid State Communications **344**, 114682 (2022).
4. V.S. Pokatilov, A.O. Makarova, A.A. Gippius, A.V. Tkachev, S.V. Zhurenko, A.N. Bagdinova, N.E. Gervits, Evolution of spatial spin-modulated structure with La doping in Bi1-yLayFeO3 multiferroics, *J. Magn. Magn. Mat* **517**, 167341 (2021)

Influence of the structure of hard segments on crystallinity and phase separation of thermoplastic polyurethanes on the basis of poly(butylene adipate) as it's seen by solid echo Time-Domain NMR

Marina Gorbunova[1], *Leonid Grunin*[2], *Maria Ivanova*[2], *Arina Imamutdinova*[3]

[1]*Institute of Problems of Chemical Physics Russian Academy of Sciences, Semenov Prospect 1, Chernogolovka, Russia*
[2]*Volga State University of Technology, Yoshkar-Ola, Mari El, Russia*
[3]*Lomonosov Moscow State University, Leninskie Gory 1, Moscow, Russia*
E-mail: zav@icp.ac.ru

In this work, we probe the influence of hard segments structure on the crystallinity and polymer chains dynamics of semi-crystalline thermoplastic polyurethanes based on poly(butylene adipate).

These thermoplastic polyurethanes are the simplest example of multi-block ones with shape memory effect. The main focus is placed onto the analysis of ratios between crystalline and amorphous phases of polyurethane samples by solid echo TD-NMR relaxometry. Via the Abragamian-Gaussian-Weibullian-Monoexponential model well applicable to magnetization decays in experiments to study spin-spin relaxation, it is possible to estimate of the total crystallinity and mobilities of crystalline and amorphous fractions. Together with other methods such as DSC and FTIR, it has been shown that the hard segment chemical structure determines the efficiency of hydrogen bonds between urethane groups, as well as the crystallization kinetics and stability of phase separation. The role of the polyurethane mesophase in crystallizing of soft segments is discussed for the first time. Thus, TD-NMR relaxometry in combination with DSC and FTIR spectroscopy has proven itself as the express method to probe the structure formation processes of thermoplastic polyurethanes. The analysis and prediction of properties of these crystallized materials are important for industries and medicine.

Acknowledgements

This work was performed in accordance with the state task, state registration No. AAA-A19-119032690060-9.

TD-NMR techniques for characterization of wood and cellulose

M. Ivanova, L. Grunin, V. Schiraya

Volga State University of Technology, Lenin sq. 3, Yoshkar-Ola, Russian Federation
E-mail: manyunya1107@gmail.com, mobilenmr@hotmail.com, vscnew@gmail.com
https://cellulose-research.com/

The study of features of the supramolecular structure, porous system, and sorption capacity of wood and cellulose is necessary to predict the performance properties of final products based on them. The influence of water on the structure of wood and cellulose is reflected in the physicochemical and mechanical properties of finished products during their operation under different temperature and humidity conditions. The most common method for studying the interaction of water with lignocellulosic materials is currently the analysis of sorption isotherms, which makes it possible to evaluate the integral water absorption depending on the air relative humidity, and to judge the adsorption and thermodynamic parameters, as well as indirectly the structure by the proposed models [1, 2]. However, this time-consuming method requires thorough sample preparation and high demands on conditions in an experimental laboratory. In addition to IR and Raman spectroscopy, X-ray and neutron scattering, NMR methods in high (spectroscopy) and low (relaxometry) fields are used to study the structure of wood and cellulose. Besides assessing the hygroscopic properties and structural parameters like crystallinity and sizes of crystalline and amorphous domains, NMR methods in low fields are applied to characterize the state of water in porous spaces of lignocellulosic materials.

The talk is focused on description of existing methods, discussing the new findings as well as assembling in once package of express methods for estimation of structural parameters and physicochemical properties of wood and cellulose via TD-NMR techniques.

By simulation the water adsorption in a slit-like pore of cellulose, we find out that adsorbate forms three fractions with fundamentally different adsorption potentials. This conclusion is confirmed by the presence of three components in the decays in CPMG experiment [3] with the ultrashort echo time (2τ=60 μs): at its lower values, the signals contain an undesirable contribution from surface cellulose molecules, and with the increase of 2τ, the resolution of relaxation decay from strongly bound water decreases.

These water fractions are not characterized by rapid exchange, so there is the clear separation of their contributions. The envelope of echo signals amplitudes is well described by the sum of three exponential functions (Fig. 1):

$$CPMG(t) = A_1 \exp(-t/T_{21}) + A_2 \exp(-t/T_{22}) + A_3 \exp(-t/T_{23}). \quad (1)$$

Based on the difference in molecular mobilities (or T_2), we assume that molecules of the first water fraction (~80-120 μs) are strongly bound to the surface of cellulose pores walls, and the second (~350-900 μs) and third (~8-20 ms) ones are sorbed predominantly on strongly bound water in meso- and macropores, respectively. In this case it is respected the well-known thesis that movements of water molecules in adsorption layers become freer as they move away from the adsorbent surface compared to the mobility of strongly bound water.

To estimate the transverse dimensions of cellulose crystallites, we use the equation that characterizes the diffusion path of propagation of nonequilibrium spin polarization [4] from the center of crystalline formations to their surface, or from regions with low relaxation rate to that with higher relaxation rate, in the experiment to measure T_1:

$$\langle l_{cr}^2 \rangle = 6 D_{cr} \tau, \quad (2)$$

where D_{cr} is the spin diffusion coefficient inside crystallites, τ is the average magnetization transfer time.

It is assumed that the spin diffusion coefficient in cellulose crystallites is constant (since it depends solely on crystallite geometry). There is the unambiguous correlation between the magnetization transfer time τ and the spin-lattice relaxation time T_1 of cellulose solid phase. Both parameters describe the process of spatial alignment of inhomogeneous spin polarization in systems of localized magnetic moments. Taking into account the assumption of proportionality between τ and T_1, as well as the Eq. (2), sizes of cellulose crystalline aggregates can be determined as:

$$l_{cr} = q\sqrt{T_1}, \tag{3}$$

where q is the coefficient obtained using the calibration procedure on samples with known structural parameters.

For the practical implementation of this dependence, it is necessary to consider that the measured spin-lattice relaxation time of cellulose T_{1meas} cannot be less than T_{1am} of its amorphous part, and also the crystallite size is limited from below by the size of indivisible fibrillar formations, denoting which by y_0 (Eq. (4)) can be used to approximate experimental data (Fig. 2):

$$l_{cr} = q\sqrt{T_{1meas} - T_{1am}} + y_0. \tag{4}$$

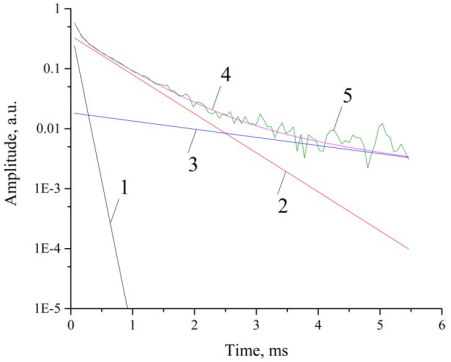

Figure 1. Fitting of CPMG data of microcrystalline cellulose with absolute water content of 6.35%: 1 – the first water fraction, 2 – the second water fraction, 3 – the third water fraction, 4 – the sum of curves 1, 2 and 3; 5 – the experimental curve

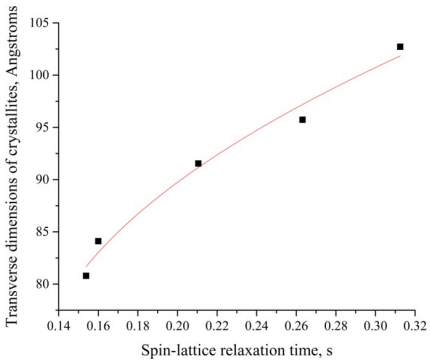

Figure 2. Transverse dimensions of cotton cellulose crystallites vs. spin-lattice relaxation times of its solid phase

According to the data in Fig. 2, cotton cellulose is characterized by: q=75 Å/c$^{0.5}$, T_{1am}=0.128 c, y_0=69.6 Å.

The relationship between transverse dimension of cellulose crystallite (in nm) and its crystallinity is shown as [1]:

$$l_{cr} = \frac{1.2}{1-\sqrt{k}}. \tag{5}$$

The model (5) formed the basis for calculating the sizes of crystallites plotted along the y-axis in Fig. 2. So it becomes easy to practically estimate its crystallinity from the measured T_1:

$$k = (1 - \frac{1.2}{q\sqrt{T_1}})^2. \quad (6)$$

Fast, accurate and reliable estimation of structural and sorption parameters of wood and cellulose by TD-NMR techniques confirms that are well-applicable to use, for instance, in online monitoring. In particular, the observed separation of water fraction contributions to CPMG decays is of great practical importance. From the amplitudes of these components, it is possible to determine from which sample pores water was completely or partially removed during the drying process, and also whether the additional cycle is required. And, as a result, the choice of optimal parameters for various drying modes, its control and regulation can be carried out. Measurements of cellulose crystallites sizes are necessary to choose the reasonable conditions for the synthesis of new smart materials for medical and environmental applications.

References

1. Grunin, Yu.B. Microstructure of cellulose: NMR Relaxation Study / Yu.B. Grunin [et al.] // Polymer Science, Ser. A. – 2012. – Vol. 54. – No. 3. – P. 201-208.
2. Grunin, Yu.B. Thermodynamics of adsorption in a cellulose-water system / Yu.B. Grunin [et al.] // Russian Journal of Physical Chemistry. – 2020. – Vol. 94. – No. 4. – P. 704-708.
3. Meiboom, S. Modified Spin-Echo Method for Measuring Nuclear Relaxation Times / S. Meiboom, D. Gill // Review of Scientific Instruments. – 1958. – V. 29. – № 8. – P. 688-691.
4. McBrierty, V. J. NMR Spectroscopy of Polymers in the Solid State / V. J. McBrierty // Comprehensive Polymer Science and Supplements. – 1989. – Ch. 19. – P. 397-428.

Improving fetal MRI at 3T with compact metasurface-based pad

Anna Kalugina[1], Viktor Puchnin[1], Evgeniy Koreshin[1], Aleksander Efimtcev[1,2], Irina Mashchenko[2], Wyger Brink[3], and Alena Shchelokova[1]

[1]School of Physics and Engineering, ITMO University, Saint Petersburg, 197101, Russia
[2]Department of Radiology, Federal Almazov North-West Medical Research Center, Saint Petersburg, Russia
[3] Department of Radiology, C.J. Gorter Center for High-Field MRI, Leiden University Medical Center, The Netherlands

Introduction

The interest of the scientific and medical community in 3 T MRI of the fetus continues to grow [1]. Mainly because 3 T scanners, in contrast to 1.5 T, provide almost two times higher signal-to-noise ratio (SNR), providing more precise fetal depiction with reduced scan time. 3 T fetal MRI has an advantage over 1.5 T in the diagnostics of the fetus' brain, bones, cartilage, and abdominal organs. In addition, MRI at 3 T has an advantage in fetuses with a gestational age of fewer than 18 weeks because of better image resolution and in angiography because of better background suppression. However, at a higher magnetic field strength, radiofrequency (RF) wavelength becomes comparable with the abdominal sizes, leading to the constructive and destructive interference of the standing waves [2]. As a result, local areas of brightening or dark occur (so-called dielectric artifact), especially at the last months of pregnancy or in females with multiple fetuses, which can significantly degrade the quality of diagnostics. Passive shimming with dielectric pads, consisting of a suspension of ceramic powder and heavy water, have been introduced to increase the RF magnetic field in low-transmit efficiency regions for abdominal [3] and fetal [4] imaging. However, the main drawback of the dielectric pads is their weight of up to 2-4 kilograms, which significantly affects the patient's comfort. In addition, the described composition of dielectric pads tends to rapidly degrade in terms of dielectric properties, which requires a frequent replacement of pads in clinics.

Recently, an ultralight and compact metasurface to improve abdominal imaging at 3 T was proposed [5]. The proposed metasurface does not content from any fast-degrading component. Here, we study the optimized metasurface-based pad for a realistic pregnant woman model and compare its performance with the state-of-the-art dielectric pad and with a case with no pad at all. The effect of the metasurface-based pad on improving fetal MRI was estimated by the value of the transverse RF magnetic field (B_1^+) inhomogeneity level in the fetus' body and brain and the value of maximum local specific absorption rate (SAR).

Methods

All numerical simulations were performed in CST Microwave Studio 2021. A voxel model (BMI=28 kg/m^2) generated from an MRI of a pregnant woman in the ninth mount was used [6]. A whole-body birdcage coil tuned and matched at 123 MHz (Larmor frequency of 3 T MRI) was used to excite the RF magnetic field. Three cases were compared: (1) only a birdcage coil with a voxelized female model, (2) a birdcage coil with a dielectric pad (size=300×250 mm^2, ε=248) or (3) a metasurface-based pad placed on the top of the model near the fetus (Fig.1 a-c). Both structures were centered on the center of the fetus' body. The metasurface was designed as an array of 15×15 flat metal crosses of dimensions 20×20 mm^2 connected by capacitors (30pF).

For each case, the mean value of the B_1^+ field amplitude normalized by 1 W of the accepted power and the relative standard deviation (RSD) in the fetal body were calculated. The SAR was evaluated in terms of the whole-body SAR (SAR_{wb}) equal to 2 W/kg according

to the recommendations of the International Electrotechnical Commission [7]. Moreover, the SAR results were normalized to the average B_1^+ magnitude in the region of interest (ROI), i.e., the entire fetus.

Results

Figure 1 (d-i) demonstrated the numerically calculated B_1^+ maps in the axial and sagittal planes. Table 1 summarizes the obtained amplitude and RSD values calculated in the fetus's body or brain volume. One can observe the B_1^+-field inhomogeneity in the ROI for the reference case (Figure 1 (d)). Adding the dielectric pad and the metasurface-based pad improves the B_1^+ in ROIs (Figure 1 (e-f), (h-i)) for almost all cases, confirmed by the decrease in RSD. The exception is the case for the entire fetus ROI with the dielectric pad; in this case, RSD slightly increased from 21% to 22.8%, while the metasurface-based pad RSD was reduced to 18.2%. At the same time, the transmit efficiency was improved by 1.3-fold for both cases.

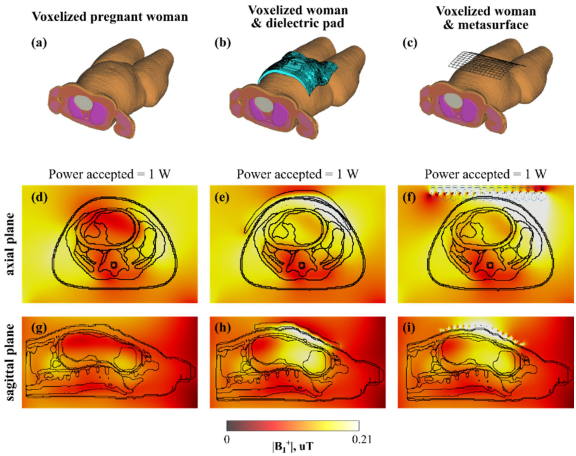

Figure 1. A voxelized model of a pregnant woman without (a) and with (b) a dielectric pad and (c) a metasurface-based pad. Numerically calculated B_1^+ maps in axial (d-f) and sagittal (g-i) planes.

Table 1. Simulation results for different cases, where RSD – relative standard deviation, $|B_1^+|$ - mean B_1^+ value in the ROI.

Setup			fetus brain		entire fetus	
	properties	size, cm^2	RSD	$\|B_1^+\|$, uT	RSD	$\|B_1^+\|$, uT
Birdcage coil	n/a	n/a	17,0%	0,16	21,0%	0,14
Dielectric pad	$\varepsilon = 248$	30×25	8,2%	0,22	22,8%	0,18
Metasurface	cap = 30 pF	30×30	9,8%	0,20	18,2%	0,18

Figure 2 illustrates simulated SAR_{10g} maps. For all cases, a decrease in SAR_{wb} was observed. Specifically, the SAR_{wb} was reduced by 1.6-fold for the cases when the entire fetus ROI was considered.

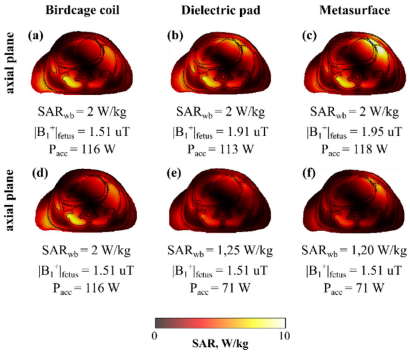

Figure 2. Numerically calculated SAR_{10g} maps in axial planes for a voxel model placed inside a body birdcage coil without (a,d) and with (b,e) dielectric pad or (c,f) metasurface-based pad centered on the entire fetus. SAR_{10g} maps were normalized to SARwb = 2 W/kg (a-c) or to the same mean value B_1^+ (d-f).

Discussion and conclusion

In this study, we demonstrated a comparison of a dielectric pad and a metasurface-based pad to increase the amplitude and uniformity of the B_1^+ field in the fetus' brain and body. Numerical simulation results have shown that a metasurface-based pad can improve the B_1^+ homogeneity and reduce SAR in pregnant women at the ninth month of gestation, similar to a state-of-the-art high-permittivity dielectric pad. However, the metasurface advantages are that it could be constructed from cheap materials making the structure ultralight and flexible. Future studies will include investigating the metasurface impact on pregnant women of other gestation ages (the third and seventh months) and experimental studies with volunteers. The authors have already received approval from the local ethic committee of Federal Almazov North-West Medical Research Center (Saint Petersburg, Russia).

Acknowledgments

This work was supported by the Ministry of Education and Science of the Russian Federation (075-15-2021-592).

References

1. Weisstanner C, Gruber GM, Brugger PC, Mitter C, Diogo MC, Kasprian G, Prayer D. Fetal MRI at 3T-ready for routine use? Br J Radiol. 2017 Jan;90(1069):20160362.
2. Collins CM et al. Central brightening due to constructive interference with, without, and despite dielectric resonance. J Magn Reson Imaging 2005; 21: 192–6.
3. De Heer et al. Increasing signal homogeneity and image quality in abdominal imaging at 3 T with very high permittivity materials. Magn Reson Med. 2012; 68(4): 1317-1324.
4. van Gemert et al. A simulation study on the effect of optimized high permittivity materials on fetal imaging at 3T. Magn Reson Med. 2019; 82(5): 1822-1831.
5. Vorobyev V et al. Improving B1+ homogeneity in abdominal imaging at 3 T with light, flexible, and compact metasurface. Magn Reson Med. 2021; Volume 87, pages 496-508
6. International Electrotechnical Commission. IEC 60601- 2- 33
7. Abaci Turk E et al. Individual variation in simulated fetal SAR assessed in multiple body models. Magn Reson Med. 2020; 83:1418-1428.

The ^{3}He gas self-diffusion in oriented Al_2O_3 aerogels at 77 K

Denis Kan,[1] Vyacheslav Kuzmin,[1] Kajum Safiullin,[1] Murat Tagirov[1,2]

[1]*Institute of Physics, Kazan Federal University, 420008 Kazan, Russia*
[2]*Tatarstan Academy of Sciences, 420111 Kazan, Russia*
E-mail: dkdnskan@gmail.com

Introduction

Nowadays, porous media are used in a wide range of industries and scientific researches. For example, porous materials are used as filters, thermal insulation, substrate for studying properties of quantum liquids. It is also possible to fill the pores with various substances to give them certain properties. Chaotic aerogel and oriented aerogels are unique materials that consist of nanometer fibers. Various nanostructures, especially aerogels, are also widely used to study the properties of ^{3}He and ^{4}He quantum liquids at ultralow temperatures. In addition, interest in the study of the superfluidity of ^{3}He in oriented aerogels has recently greatly increased due to the discovery of polar phases in oriented aerogels [1].

Gas diffusion in porous media

At present, there are many methods for studying the structure and properties of porous media. One of the best probe for porous structures studies at low temperatures is ^{3}He due to its rather long intrinsic relaxation times. The ^{3}He can act as a probe gas for a number of reasons. It is a monatomic gas with a nuclear spin I=1/2 and the ^{3}He nuclei are very sensitive to the magnetic properties of the medium, which makes it possible to characterize a porous medium by measuring the spin-lattice relaxation of ^{3}He nuclear magnetization. The ^{3}He has the smallest size (atomic radius 0.32 Å) compared to other molecules, it is chemically inert. The most important parameter for the theoretical description of the superfluidity of ^{3}He is the mean free path, which can be determined from studying the self-diffusion of atoms using nuclear magnetic resonance with an applied gradient. By using NMR method with applied magnetic field gradients it is possible to study gas diffusion in porous media, which allows to assess the structure of a porous medium, its degree of anisotropy, pore sizes, connectivity, and other characteristics.

Our research team develops the methods for studying porous media in moderate magnetic fields (up to 0.8 T) using liquid or gaseous ^{3}He at low temperatures (1.5 - 4.2 K) [2]. The purpose of this work is to study the possibilities of the ^{3}He NMR method to characterize structure of oriented aerogels of different porosity in strong magnetic fields and at higher temperatures.

Experimental results

The Al_2O_3 oriented aerogels consisting of parallel long filaments are used as samples. The filaments of diameter ~8 nm located at a distances of 15–100 nm from each other, depending on the density of the aerogels. The aerogel sample with the lowest density has porosity of 97.9%.

The results of the gaseous ^{3}He nuclei relaxation times T_1 and T_2 measurements in the aerogels by pulsed NMR at a frequency of 118.82 MHz in a magnetic field of 3.65 T and a temperature 77 K will be discussed. The ^{3}He diffusion coefficients were measured at 77 K at a pressure range from 97 to 973 mbar by using CPMG pulse sequence with applied constant magnetic field gradient, when the Knudsen and molecular diffusion regimes are realized [3]. From the dependence of the values of the diffusion coefficients for different portions of the gas, the Knudsen mean free path of ^{3}He atoms perpendicular to the filaments in the Al_2O_3 aerogel was obtained. The Knudsen mean free path is used to characterize a porous

medium. The obtained mean free paths is in a good agreement with calculated geometrical mean free paths in aerogel with porosity of 97.9%.

These studies can be further used to assess the applicability of the ^{3}He NMR method for porous nanostructures studies in strong magnetic fields at room temperature, which will involve the novel method PAMP (polarization of atoms in a magnetized plasma) method of ^{3}He hyperpolarization. To conclude, we demonstrate that ^{3}He gas diffusion at high magnetic fields is a good probe for studying structures of nanoporous media by NMR method.

Acknowledgements

This work was financially supported by the Russian Science Foundation (grant #20-42-09023).

References

1. Dmitriev V. Polar Phase of Superfluid 3He in Anisotropic Aerogel / V.V. Dmitriev, A.A. Senin, A.A. Soldatov, A.N. Yudin // Phys. Rev. Lett. 115, 165304 (2015)
2. Stanislavovas A. The 3He nuclear magnetic relaxation in nematically ordered Al2O3 aerogels: effects of 4He and nitrogen pre-plating / A. Stanislavovas, V. Kuzmin, K. Safiullin, E. Alakshin, A. Klochkov, M. Kutuzov, M. Tagirov // J. Phys.: Condens. Matter 33 195805 (2021)
3. Nacher P.-J. NMR measurements of hyperpolarized 3He gas diffusion in high porosity silica aerogels / Pierre-Jean Nacher, Geneviève Tastevin // J. Chem. Phys. 123, 064506 (2005)

Quantum-chemical investigation of factors driving the extremal value of ^{1}H NMR chemical shift for central symmetric hydrogen bonds

Kaplanskiy M.V., Tolstoy P.M., Tupikina E.Yu.

Institute of Chemistry, Saint Petersburg State University, Russia
E-mail: mark2402@mail.ru

Introduction

It is well known that ^{1}H NMR chemical shift δ_H follow the bell-shaped curve during the proton transfer: upon the strengthening of a hydrogen bond δ_H moves downfield, reaches its extremal value for quasi-symmetric (strongest) complexes, and moving upfield for complexes with a proton transfer.[1] However, the electronic factors driving such a behavior are still an issue. In this work we investigate the evolution of eigenvalues of chemical shielding tensor σ_H (Fig. 1a) and features of outer electronic shells of hydrogen-bonded complexes along the proton transfer coordinate by means of quantum chemistry.

Model systems

As model complexes we consider a set of small symmetric complexes with FHF, OHO, NHN hydrogen bonds (Fig. 1b). The behavior of proton chemical shift δ_H along the proton transfer coordinate for these systems were investigated extensively by both computational and experimental techniques.[2–4]

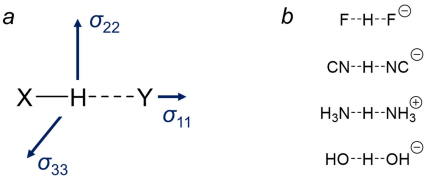

Figure 1. a – Directions of principal axes of σ_H tensor for XHY hydrogen bond (X, Y – various atoms); b – complexes investigated in this work.

Methods

Computations were performed using Gaussian16 software package. Geometries of studied complexes were calculated using hybrid methods of density functional theory (B3LYP) and triple-ζ basis set (6-311++G(d,p)). Quasi-adiabatic proton transfer was modelled by using a modredundant scheme. NMR parameters were calculated using GIAO approach and B3LYP functional along with pcSseg-3 basis set.

Acknowledgements

This work was supported by Russian Science Foundation grant №18-13-00050.

References

1. Grabowski, S. J. (Ed.), Hydrogen bonding: new insights (Vol. 3), Springer, 2006.
2. Limbach, H. H., Tolstoy, P. M., Pérez-Hernández, N., Guo, J., Shenderovich, I. G., & Denisov, G. S., Isr. J. Chem. 2009, 49(2), 199.
3. Tupikina, E. Yu., Sigalov, M., Shenderovich, I. G., Mulloyarova, V. V., Denisov, G. S., & Tolstoy, P. M., J. Chem. Phys. 2019, 150(11), 114305.
4. Tupikina, E. Yu., Denisov, G. S., Melikova, S. M., Kucherov, S. Yu., & Tolstoy, P. M., J. Mol. Struct. 2018, 1164, 129.

Computational aspects of carbon–lithium spin-spin coupling constants

Valerii V. Karpov[1], Elena Yu. Tupikina[1], Alexander S. Antonov[1]

[1]Institute of Chemistry, Saint Petersburg State University, Saint Petersburg, Russia
E-mail: v.karpov@spbu.ru

Introduction

Organolithium reagents have proven to be an indispensable tool in modern synthetic chemistry. They are widely used in metalation reactions [1] and can be utilized as initiators in polymerization [2]. As is often the case in organometallic chemistry, their usage requires a deep understanding of their aggregation behaviour, since it strongly affects reactivity of organolithium species. Most of reactions take place in solution and one of the most informative methods of aggregation investigation in solvent is NMR spectroscopy. Based on multiplicity and values of spin-spin coupling constant between carbon and lithium – $^1J_{CLi}$, one can distinguish organolithium aggregates, for example, a monomer from a dimer. But it usually happens that signals are poorly resolved or every multiplet component cannot be observed, thus, spin-spin coupling constant remains the sole aggregation descriptor. For the foregoing reasons, calculated data can substantially simplify experimental spectra interpretation. That is why in this work we discuss the algorithm of building an effective computational scheme that allows to obtain a value of $^1J_{CLi}$ with high accuracy.

Simulated set of organolithiums

In order to achieve it, we consider a set of model organolithium species (Fig. 1), which includes various organolithium reagents with special agents that affect aggregation, namely N,N,N,N-tetramethylethylenediamine (TMEDA), N,N,N,N,N-pentamethyldiethylenetriamine (PMDTA), and tetrahydrofuran (THF). This benchmark set consists of phenyllithium monomer with PMDTA, monomer of secondary butyllithium with PMDTA, monomers of 1- and 2-lithionaphthalenes with PMDTA, a phenyllithium dimer with two TMEDA molecules, and a methyllithium tetramer with for THF molecules. Spin-spin coupling constants are available from experimental spectra for all above-mentioned species.

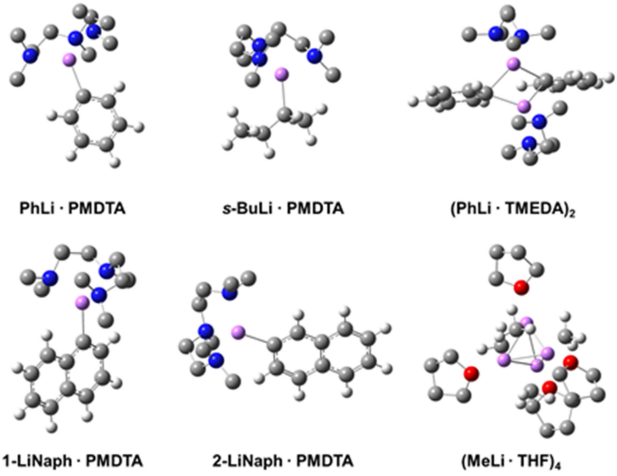

Figure 1. The studied organolithium systems. Ligands' hydrogens are omitted for clarity

We emphasise that this set covers various organolithium reagents, since it is composed of species with different aggregation numbers, aromatic and aliphatic organolithiums, with one and two conjugated aromatic rings, and with nitrogen and oxygen as ligand bonding atoms.

Computational details

The calculations were carried out using Gaussian16 software package.

Optimized geometries were obtained on B3LYP-D3/def2-TZVP level of theory with tight criteria for both geometry optimization and self-consistent field single-point calculation. In order to account solvent effects, Conductor-like Polarizable Continuum Model (CPCM) was implemented for species in corresponding solvents (tetrahydrofuran or diethyl ether). To saturate the first coordination sphere of lithium, we added special ligands that control the aggregation. All structures obtained were checked on the absence of imaginary frequencies. These structures were utilized to calculate NMR properties of interest.

Spin-spin coupling constants were calculated using the GIAO approximation. For the purpose of comparing the calculated and experimental data, constants obtained were rounded down according to experimental resolution.

In our results, we present performance of different basis sets of extensive use in carbon-lithium indirect spin-spin coupling constant. Beneficial effect of polarization functions and disturbing effect of diffuse functions is of interest. Also, we state about the implicit solvation impact diminishing with increasing aggregation number.

Acknowledgements

This work was financially supported by the RSF grant 21-73-10040. The calculations were performed in the Computer Center of Saint-Petersburg University Research Park (www.cc.spbu.ru).

References

1. L. Zhang, G. J. Lovinger, E. K. Edelstein, A. A. Szymaniak, M. P. Chierchia, J. P. Morken. – *Science*., **351**, 70–74 (2016).
2. S. Carlotti, P. Desbois, C. Billouard, A. Deffieux. – *Polym. Int*., **55**, 1126–1131 (2006).

^{2}H NMR study of structure, hydrogen bond dynamics and phase transition in a model ionic liquid electrolyte

Alexander E. Khudozhitkov[1,2], *Daniil I. Kolokolov*[1,2]

[1] *Boreskov Institute of Catalysis, Siberian Branch of Russian Academy of Sciences, Prospekt Akademika Lavrentieva 5, Novosibirsk 630090, Russia*
[2] *Novosibirsk State University, Pirogova Street 2, Novosibirsk 630090, Russia*
E-mail: alexandr.khudozhitkov@gmail.com

^{2}H NMR method is a versatile tool that allows probing dynamics and phase behaviour in solid state. This method has been successfully utilized in various systems ranging from zeolites to proton conductors and polymers. Recently, we have developed a robust approach for gaining access to the structure and dynamics in liquid, supercooled and crystallized protic ionic liquids (PILs) by using the solid state ^{2}H NMR line shape and spin relaxation analysis. Herein, we exploit this approach to perform a comprehensive solid state ^{2}H NMR study of the PIL over a broad temperature range of 133-436 K, delivering information about the structure, hydrogen bond dynamics and phase transition in the model ionic liquid electrolyte.

The PIL under consideration is triethylammonium (TEA) bis(trifluoromethanesulfonyl)imide (NTf_2) [TEA][NTf_2]. NTf_2 is the most frequently used anion due to its ability to form only weak hydrogen bonds within the cation-anion pair, thus creating opportunity for the cations to migrate on its own and not only within an ionic pair. Moreover, PILs based on 3-alkyl ammonium cations were recently shown to provide good transport and stability properties for the Li ions. In the same time, knowledge about the microscopic structure and dynamics in similar PILs remains often unknown even for the model electrolytes such as the [TEA][NTf_2].

Deuterium is located in the N-D group of [TEA] cation so we can directly follow the dynamics of hydrogen bond between cation and anion. ^{2}H NMR spectra line shape at 133-223 K consists of two Pake doublets with notably different deuterium quadrupole coupling constants (DQCC) Q_{Ia} = 172 – 175 kHz and Q_{Ib} = 144 – 145 kHz, accompanied by asymmetry parameters, η, ranging between 0 – 0.04. It indicates at two possible ways of hydrogen bond formation. The smaller DQCC refers to the stronger hydrogen bond (ND···N) between the ND bond and the central nitrogen atom of the NTf_2 anion, whereas the higher value could be assigned to one of the four possible hydrogen bonds (ND···O) with the oxygen atoms of the two sulfonyl groups of the anion (Fig. 1).

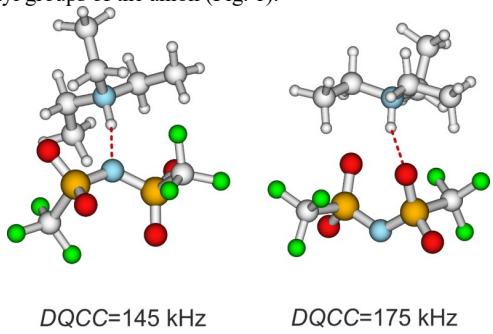

Figure 1. Two measured DQCCs: the $^+$N-D···N$^-$ interaction can be related to the small DQQC, whereas the $^+$N-D···O$^-$ interaction results in a larger DQCC.

In the 233-283 K temperature region there appears the Lorentzian signal in the spectrum originating from the isotropic liquid phase. The intensity of isotropic signal p_{II} increases with the temperature as the melting through the dynamically heterogeneous state occurs. This melting transition is governed by two sets of thermodynamic parameters. For the initial process below 238 K $\Delta H_1^{\Theta} = 110 \pm 20$ kJ mol^{-1}, close to the second melting transition we obtained $\Delta H_2^{\Theta} = 22 \pm 5$ kJ mol^{-1}, indicating that less energy is required to reach the second melting transition.

In order to probe motional behavior of [TEA][NTf_2] we measured the deuteron spin-lattice $(T_1)_D$ and spin-spin $(T_2)_D$ relaxation times of the N–D molecular vector for the isotropic and anisotropic components (Fig. 2a). From fitting the temperature dependence of spin relaxation times, we determine the geometry, activation barriers and rates of motions exhibited by the [TEA] cation.

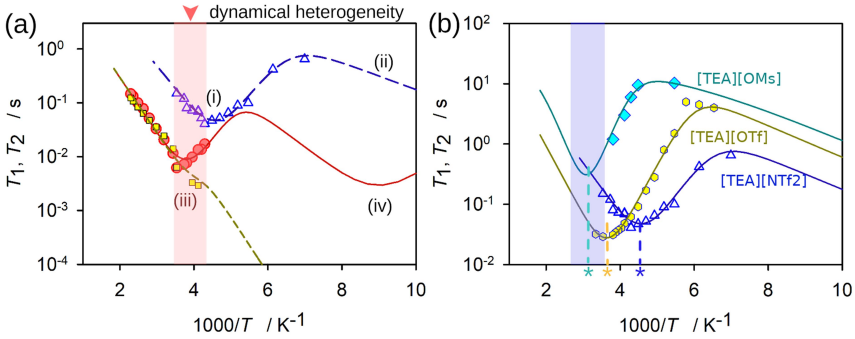

*Figure 2. (a) ^{2}H NMR spin relaxation temperature dependences: experimental T_1 (△) for anisotropic state I; experimental T_1 (●) and T_2 (□) for isotropic mobile state II. (b) Comparison of the relaxation in anisotropic state with (♦) [TEA][OMs] and (○) [TEA][OTf] PILs. The * symbol indicates the characteristic minimum for the ND bond torsion librational motion where $\omega\tau \sim 1$. Simulations are given in lines. All experimental data was measured at 61.4 MHz resonance frequency.*

We compare our results with previously reported data regarding ionic liquids with anions of varying strength: [TEA][OTf] and [TEA][OMs] (Fig. 2b). Our results prove that the stronger hydrogen bonds between cation and anion lead to the lower enthalpy change between solid and liquid state, higher activation barrier of tumbling motion and lower amplitude of librational motion.

Finally, we relate the DQCCs for the PILs [TEA][NTf_2], [TEA][OTf] and [TEA][OMs] versus correlation times τ_{ND}, here expressed by the T_1 minima, viscosities as well as spectroscopic properties such as intra and intermolecular IR vibrational frequencies ν_{NH} and ν_{NO}. Throughout, the increasing cation-anion interaction strength in the order [NTf_2] < [OTf] < [OMs] as given by the decreasing values of the DQQCs are reflected in all structural and dynamical properties. These structure property relations are almost linear which underlines that NMR DQCCs and IR frequencies describe the locality and directionality of hydrogen bonding in similar way.

Acknowledgements

This work has been supported by the Russian Science Foundation (grant № 21-13-00047).

Improving fMRI at 1.5T with high permittivity materials

Vladislav Koloskov[1], Mikhail Zubkov[1], Georgiy Solomakha[1], Viktor Puchnin[1] and Alena Shchelokova[1]

[1]School of Physics and Engineering, ITMO University, Saint-Petersburg, Russia
E-mail: vladislav.koloskov@metalab.ifmo.ru

Introduction

Functional magnetic resonance imaging (fMRI) is a modern non-invasive, widely used imaging method for mapping brain functions. It requires a sequence of magnetic resonance (MR) images captured in time during specific patient activities [1]. It was previously investigated that high permittivity materials (HPMs) can improve the quality of brain MR imaging [2-5]. Specifically, HPMs have been shown to enhance transmit efficiency (B_1^+) and receive sensitivity (B_1^-), leading to a significant increase in the signal-to-noise ratio (SNR) of the image. In this work, we propose and demonstrate the positive impact of HPMs on fMRI at 1.5 T via numerical simulations.

Methods

We considered six setups during the numerical simulations: (1) phantom without (Fig. 1a), (2) with uniform and (3) single-side HPMs' blocks placement with the hole-body birdcage coil in transmitting regime; (4) phantom without, (5) with uniform (Fig. 1b) and (6) single-side (Fig. 1c) HPMs' blocks placement with the head coil in receive regime. 16-leg high-pass birdcage transmit coil with a 350 mm diameter, and 650 mm long with a circularly polarized transmission field was included in the numerical model and matched to the working frequency at 63.8 MHz. A head phantom also used in further fMRI simulations is built as a set of 43 elliptical slices (3 mm thick each), with relative permittivity ε=38, conductivity σ=0.5 S/m. The receive-only 6-channel loop coil array was tuned and matched to the 63.8 MHz. A match of -10 for S_{ii} and of -10 to -16 dB for S_{ij} was achieved for all the coil elements. HPMs based on BaTiO3 were simulated as blocks with permittivity ε=4500, tan δ=0.1, and dimensions of 57×71×13 mm^3. It was previously shown that such HPMs' blocks improve receive performance of wrist coil at 1.5 T [6].

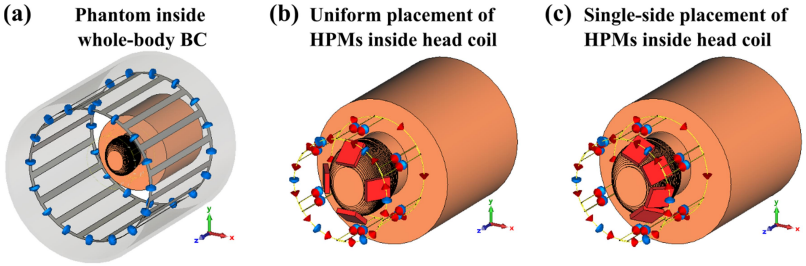

Figure 1. Examples of the numerical setups used in simulations: phantom inside whole-body birdcage coil (a); uniform (b) and single-side (c) HPMs' blocks placement around the head phantom together with a local head coil.

All electromagnetic calculations were performed in CST Studio Suite 2021 (Darmstadt, Germany); SNR and its gain calculations were performed with in-house scripts based on Eq. 21 from [7] in MATLAB (The MathWorks Inc, Natick, MA). fMRI simulations were performed using the STANCE MATLAB toolbox [8], while its postprocessing was done

with the Statistical Parametric Mapping (SPM) toolbox (The Wellcome Centre for Human Neuroimaging, UCL Queen Square Institute of Neurology, London, UK). The numerically calculated B_1^+ field distributions were normalized to 1W of total power accepted by the birdcage coil. The fMRI time series simulating finger-tapping tasks were simulated at different SNR values with its spatial distributions provided by CST simulations. The time series were then analyzed in SPM (with a family-wise error threshold of 0.05) and compared against the ground truth to calculate the false-negative activation rate.

Results

B_1^+ field maps for three setups (1-3) are shown in Fig. 2a-c. Localization of the magnetic field with HPMs' blocks led to an 8% gain in the region of interest indicated with white circles in Figure 2 for both cases. Figure 3 shows the SNR for a base setup (4) and gain maps for setups with pads (5, 6). Placing HPMs' blocks near the region of interest increased the SNR by 20%, as demonstrated in Fig. 3d and 3e.

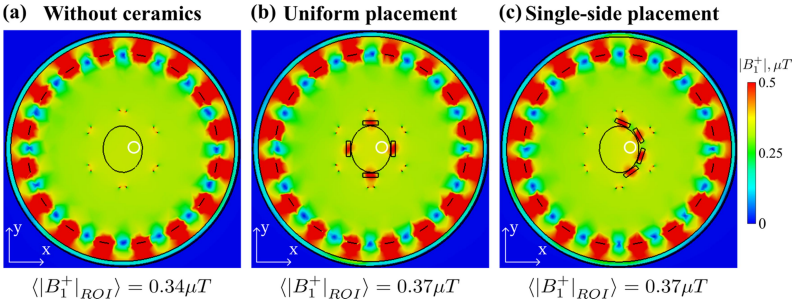

Figure 2. Numerically calculated B_1^+ maps for phantom and detuned receive coil placed in the whole-body birdcage coil without (a), with uniform (b) and single-side (c) HPMs' blocks placement. B_1^+ maps were normed on 1 W of accepted power. For each case mean B_1^+ field value was calculated in the region of interest (ROI) indicated with white circles.

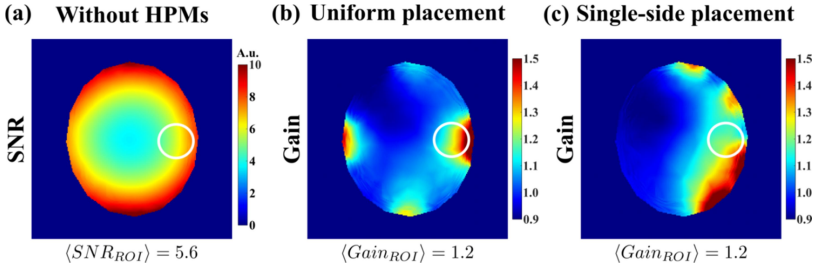

Figure 3. Numerically calculated SNR map for the reference case (a), gain maps for uniform (b), and single-side HPMs' blocks placement (c). For each case mean value was calculated in the region of interest indicated with white circles.

Figure 4 shows the results of the fMRI simulation. The number of detected activations increased by 32% and by 40% (Fig. 4a), whereas the number of undetected activations decreased by 3,5% and 4% (Fig. 4b) for uniform and single-side placement, respectively, in comparison to setup without them for max SNR value. The false-positive rate was 0% for all SNR values.

Discussion and conclusion

In this work, we demonstrated that HPMs could be used to increase transmit efficiency, receive sensitivity, and consequently, the number of activations in the human brain at 1.5T. Numerical simulations have shown a 1.4-fold increase in the amount of brain activation during functional MRI and a 4% drop in false-negative rate compared to the basic setup (1). Therefore, the accuracy of real examination can be improved, which is significant for pre-surgical planning. In the future, we plan to perform experimental phantom and *in-vivo* investigations.

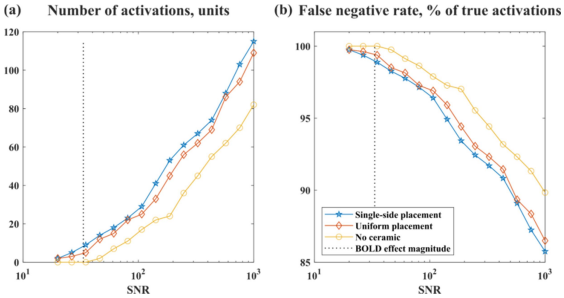

Figure 4. Statistical data acquired from fMRI simulations: number of detected activations in ROI (a) and false-negative rate (b).

Acknowledgements

The work was carried out with the support of a grant from the President of the Russian Federation for scientific school НШ-2359.2022.4. VK acknowledges the RPMA grant of the School of Physics and Engineering of ITMO University.

References

1. Rogers, B. P., Morgan, V. L., Newton, A. T., and Gore, J. C., *Assessing functional connectivity in the human brain by fMRI*, Magn. Reson. Imag., 25 1347 –1357 (2007)
2. Rupprecht S, Sica CT, Chen W, Lanagan MT, Yang QX. *Improvements of transmit efficiency and receive sensitivity with ultrahigh dielectric constant (uHDC) ceramics at 1.5 T and 3 T.* Magn Reson Med. 2018;79:2842–2851.
3. Vaidya, Manushka V et al. *Improved detection of fMRI activation in the cerebellum at 7T with dielectric pads extending the imaging region of a commercial head coil.* Journal of magnetic resonance imaging: JMRI vol. 48,2 (2018): 431-440.
4. Lakshmanan, K, Carluccio, G, Walczyk, J, et al. *Improved whole-brain SNR with an integrated high-permittivity material in a head array at 7T.* Magn Reson Med. 2021; 86: 1167– 1174.
5. Teeuwisse, W.M., Brink, W.M., Haines, K.N. and Webb, A.G. (2012), *Simulations of high permittivity materials for 7 T neuroimaging and evaluation of a new barium titanate-based dielectric.* Magn. Reson. Med., 67: 912-918.
6. I. Zivkovic, W. Teeuwisse, A. Slobozhanyuk, E. Nenasheva, A. Webb *High permittivity ceramics improve the transmit field and receive efficiency of a commercial extremity coil at 1.5 tesla* J Magn Reson, 299 (2019), pp. 59-65
7. P. B. Roemer; W. A. Edelstein; C. E. Hayes; S. P. Souza; O. M. Mueller (1990). *The NMR phased array., 16(2), 192–225.*
8. Jason E. Hill, Xiangyu Liu, Brian Nutter, and Sunanda Mitra *A task-related and resting state realistic fMRI simulator for fMRI data validation*, Proc. SPIE 10133, Medical Imaging 2017: Image Processing, 101332N

The NMR Chemical Shift of a Helium-3 Atom as a Probe for Aromatic and Antiaromatic compounds

Korostelev V.O.[1], Tupikina E.Yu[1]

[1]Institute of Chemistry, Saint Petersburg State University, Saint Petersburg, Russia
E-mail: vladfromlive@yandex.ru

Introduction

The electronic shell structure of molecules plays a crucial role in the bond formation, non-covalent interactions, general reactivity, and prediction of chemical and physical properties. Aromaticity, as a feature of electronic shell has represented one of the most significant fundamental concepts in modern chemistry [1]. Nowadays, its determination is not limited to the molecules obeying the [4n + 2] Huckel rule, but extended to those satisfying other criteria — structural, electronic, magnetic and energetic indices should be noted to determine the aromatic nature of a molecule comprehensively.

Numerous theoretical ways to visualize electronic structure features exist. Most commonly used are functions as molecular electrostatic potential (MESP) [2,3], electron localization function (ELF) [4,5] and electron density (ED) [6] and many others [7].

Another way to visualize electronic shell features is to use test molecules, which form weak non-covalent bonds with the investigated molecule. The main idea is to probe its outer electronic shell properties and thus propose its properties [8], nucleus-independent chemical shift (NICS) methods have similar ideas [9]. The disadvantage of these methods is a considerably strong structure deformation of the investigated molecule by the probe particle. Using low-perturbing probes is experimentally difficult and computationally challenging, as the description of a weak interaction at high level of theory requires significant computational resources.

During the last decade, a number of publications were devoted to the study of van der Waals complexes of various molecules and ions with helium atom [10–12]. Theoretical investigation of van der Waals complexes of a helium atom with neutral halogen atoms showed, that the energy of complex He + Hal (Hal = F, Cl, Br) is negligibly small and significant changes in electron density of both molecules do not occur [10].

Helium atom 3He was considered as a probe, whose NMR chemical shift, δHe, and interaction energy with investigated molecules (fullerenes, nanotubes, graphene) was used to describe their electronic features [13]. The δHe for helium atoms encapsulated into fullerene cages was also measured experimentally [14].

Goal and idea

It was already shown, that it is possible using the helium probe for studying the various features of electronic shells, especially direction of lone pair localization [15–17]. In this work, we are focused on developing and testing of a quantum mechanical approach for constructing a 3D map of the outer electronic shell of aromatic, antiaromatic and nonaromatic molecules. The main idea is using helium atom ^{3}He as a probe particle for visualization of aromaticity and antiaromaticity.

The key feature of our work is the transition to spectroscopically observable parameters, namely, to ^{3}He NMR chemical shifts, and linking the observables to the main features of the probed electronic shell.

Methods

Quantum mechanical calculations were carried out using Gaussian16 software and computational resources were provided by Computer Center of Saint-Petersburg University Research Park. For isolated molecules, the geometry optimization was performed at

mp2/def2-tzvp level with tight convergence criteria. Molecular electrostatic potential (MESP) and Electron Localization Function (ELF) were calculated from Gaussian wavefunction files in MultiWFN wavefunction analysis program [18]. The calculations were performed in a two-dimensional Cartesian grid of points, the 3He was placed at 1 Å above the plane of cyclic compounds. The size of the grid was 3.0×3.0 Å (4.0×4.0 Å for bigger complexes) with step 0.1 Å in each direction. The NMR shielding of helium atom 3He was calculated at B3LYP/6-31g. NMR shieldings were converted into chemical shifts δHe using the shielding value of a free helium atom (σref = 59.7969 ppm) calculated at the same level of theory. Data treatment was carried out in MatLab R2016b package.

Results

In this report, we present the test results of the concept – using the ^{3}He helium atom as a probing particle for investigation aromaticity phenomena. We were not limited only by aromatic and antiaromatic compounds. We compared 4np- and (4n+2)p-electron flat systems. You can see the benzene – the aromatic system probed by ^{3}He (Fig. 1) and antiaromatic system – cyclobutadiene (Fig. 2).

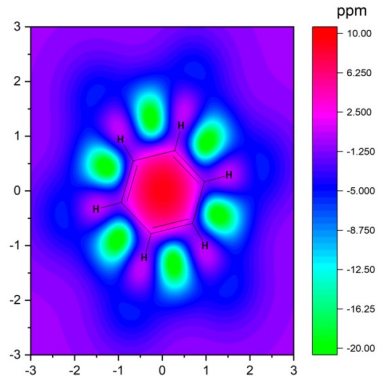

Figure 1. Chemical shift of ^{3}He atom δ_{He} in plane above aromatic system – benzene.

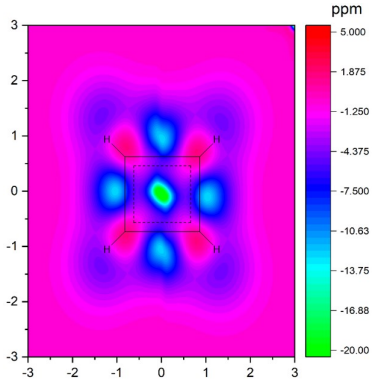

Figure 2. Chemical shift of ^{3}He atom δ_{He} in plane above antiaromatic system – cyclobutadiene.

Acknowledgements

This work was supported by RFBR grant 20-03-00231.

References

1. A. T. Balaban, P. R. Schleyer, and H. S. Rzepa. – *Chem. Rev.*, **105**, 3436 (2005).
2. N. Mohan, C. H. Suresh, A. Kumar, and S. R. Gadre. – *Phys. Chem. Chem. Phys.*, **15**, 18401 (2013).
3. X. Kou, Y. Huang, Y. Yang. – *J. Hazard. Mater.* **420**, 126623 (2021).
4. P. Fuentealba and J. C. Santos. – *Curr. Org. Chem.* **15**, 3619 (2011).
5. K. Ota, R. Kinjo. – RSC Adv. **11**, 592 (2021).
6. D. Chen, D. W. Szczepanik, J. Zhu, and M. Solà,. – *Chem. – A Eur. J.* **26**, 12964 (2020).
7. M. M. Edim, O. C. Enudi, B. B. Asuquo, H. Louis, E. A. Bisong, J. A. Agwupuye, A. G. Chioma, J. O. Odey, I. Joseph, and F. I. Bassey. – *Heliyon* **7**, e06138 (2021).

8. N. H. Martin, D. M. Loveless, and D. C. Wade. – *J. Mol. Graph. Model.* **23**, 285 (2004).
9. R. Báez-Grez, L. Ruiz, R. Pino-Rios, and W. Tiznado. – RSC Adv. **8**, 13446 (2018).
10. J. Wei, S. Zhuo, and G. Ju. – *Chem. Phys.* **270**, 31 (2001).
11. A. Wada, A. Kikkawa, T. Sugiyama, and K. Hiraoka. – *Int. J. Mass Spectrom.* **267**, 284 (2007).
12. Y. Ajili, K. Hammami, N. E. Jaidane, M. Lanza, Y. N. Kalugina, F. Lique, and M. Hochlaf. – *Phys. Chem. Chem. Phys.* **15**, 10062 (2013).
13. T. Kupka, M. Stachów, L. Stobiński, and J. Kaminský. – *Magn. Reson. Chem.* **51**, 463 (2013).
14. T. Sternfeld, M. Saunders, R. J. Cross, and M. Rabinovitz. – *Angew. Chemie Int. Ed.* **42**, 3136 (2003).
15. E. Y. Tupikina, A. A. Efimova, G. S. Denisov, and P. M. Tolstoy. – *J. Phys. Chem. A* **121**, 9654 (2017).
16. E. Y. Tupikina, A. A. Efimova, G. S. Denisov, and P. M. Tolstoy. – *J. Comput. Chem.* **39**, 2459 (2018).
17. E. Y. Tupikina, K. G. Tokhadze, G. S. Denisov, and P. M. Tolstoy. – *J.* Comput. Chem. **41**, 1194 (2020).
18. T. Lu and F. Chen. – *J. Comput. Chem*. **33**, 580 (2012).

Synthesis and NMR relaxometry studies of self-assembling nanoclusters of SPIONs conjugated with bioactive ligands

Anna Kosogornova[1], Boris Nikolaev[2], Ludmila Yakovleva[2], Vyacheslav Fedorov[1], Anton Mazur[3], Maxim Shevtsov[2]

[1]Saint Petersburg State Institute of Technology, Saint Petersburg, Russia
[2]Institute of Cytology of the Russian Academy of Sciences (RAS), Saint Petersburg, Russia
[3]Saint Petersburg State University, Saint Petersburg, Russia
E-mail: akosogornova@mail.ru

Introduction

Superparamagnetic iron oxide nanoparticles (SPIONs) conjugated with specific recognition molecules (e.g., antibodies, peptides, aptamers) provide a promising strategy for targeted drug delivery with an immediate carrier monitoring by noninvasive magnetic resonance imaging (MRI) [1]. The MRI visualization of such hybrid specific nanocarriers strongly depends on the contrast efficacy of magnetic conjugate. Herein, we offer multicore construction on the base of monodomen SPIONs connected with ligands of various functionality which have high contrast efficiency registered in standard tomographic modes.

SPIONs were prepared as magnetic nanoparticles by coprecipitation from salt solutions Fe^{+2}/Fe^{+3} at pH ~10, t=80°C. Colloid stabilization of magnetic nanosuspension was achieved by addition of biocompatible neutral dextran (Dx) or carboxymethyldextran (CMDx) (MW 10000-2000). After ultrasonic processing, the fine suspension was separated on permanent magnet and purified by dialysis. The resulting magnetic suspension consisted of multicore nanoclusters with average hydrodynamic diameter ~100 nm was recorded by dynamic light scattering (DLS) measurement on Malvern ZetasizerPro (Malvern Panalytical Ltd., UK). The suspension was modified with antigen-specific ligands via carbodiimide-mediated NH_2 and COOH coupling. T1 and $T2^*$ relaxation times of water protons in nanosuspensions were estimated employing low-field resonance spectrometer Spinsolve Ultra (Magritek) at 60 MHz [2]. Magnetic characteristics were evaluated by magnetic resonance relaxometry in suspension and MRI of phantom gel samples loaded by the nanocarrier. Influence of magnetic field on relaxation rate was accounted for in limits of fast diffusional model in strong field gradient.

Results and Discussion

The relaxation times of CMDx-SPIONs were measured using the NMR inversion-recovery method. Based on the obtained data, a graph of the linear dependence of -ln(1-Mz/Mo) on t was plotted (Fig. 1). The tangent of the slope was used to evaluate the relaxation time T1. $T2^*$ were estimated by measuring the width of proton resonance at low concentrated suspensions in H_2O by relation $T2^* = (\pi\Delta\nu(Hz))^{-1}$ and so $T2^*$=14,7 msec.

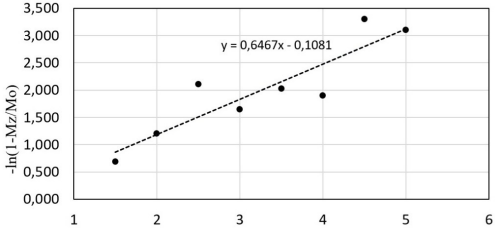

Figure 1. Plot of log scaled SPIONs magnetization in dependence on time t between 180° and 90° impulses in inversion-recovery mode in low field at resonance frequency of 60 MHz.

The relaxation times of novel conjugated SPIONs in 2% agar-agar gel were measured by MRI. CMDx-SPIONs have been modified with the following ligands: anti-GD2 monoclonal antibody specific to disiogangliosis expressed in neuroectodermal tumors; anti-LAM antibody against the surface antigen lipoarabinomannan of *M. tuberculosis*; anti-CD11b antibody detecting macrophages; TKD is 14-mer oligomerization domain peptide of the 70 kDa heat shock protein Hsp70; isotype IgG1 antibodies (control). TKD peptide and anti-GD2 antibodies were used as fluorescein isothiocyanate (FITC) labeled substrates. Binding of these labelled molecules to targets was assessed by confocal microscopy on tumor and normal cell cultures.

The prepared phantom samples were made by forming three layers of suspension of different Dx-SPIONs concentration with interlayers of pure agar-agar. The MR scans were obtained on a Bruker 400 MHz WB Avance III spectrometer (Bruker, Germany) in the RARE-T1+T2 mode. Axial T1- and T2-weighted images were acquired. The common protocols for MRI study of phantoms made possible to obtain the relaxation times T1 and T2. T1/ T2 ratios were calculated and showed in Table 1.

Table 1. Spin-lattice (T1), spin-spin (T2) relaxation times and their ratios in SPIONs phantom layers.

Layer name	T1, sec	T2, msec	T1/ T2
Dx-SPIONs 0.2 mM	1.7	15.1	112.6
Agar-agar without SPIONs	2.1	23.9	87.9
Dx-SPIONs 0.5 mM	1.5	9.7	154.6
Agar-agar without SPIONs	1.9	21.0	90.5
Dx-SPIONs 0.7 mM	1.3	7.0	185.7
Agar-agar without SPIONs	1.8	34.7	51.9

The MRI relaxation time of diluted suspensions in low magnetic field (1.4 T) turned out to be longer than values detected in MR scanner, which can be explained by the different resonant frequency of NMR relaxometry (60 MHz) and MRI spectrometry (400 MHz). These differences are supported by the theory [3, 4]. In brief, for most materials we observed T1 increase although T2 did not significantly change with an increase of the field strength. This can be explained by reviewing the principles underlying dipole-dipole interactions, the primary mechanism responsible for T1 and T2 relaxation rates for ^{1}H nuclei.

The relaxation times of conjugated SPIONs in phantom agar-agar gels were measured by MRI. After functionalization of the surface, the particles did not lose their contrast efficacy, due to the fact that the superparamagnetic core is protected by carboxymethyldextran. Based on the known concentration of each conjugate (0.5 mM) and the obtained spin-spin relaxation times T2, the relative relaxivities r2 were calculated. The values of relaxivities for some commercial contrast agents are also presented (Fig. 2).

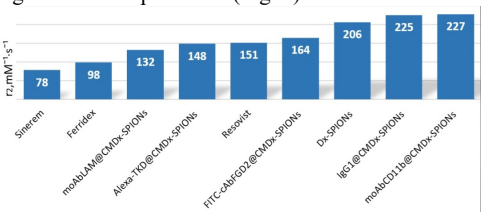

Figure 2. Relaxivity r2 of conjugated CMDx-SPIONs in relation to standard contrast agents.

The values of relaxivities of magnetic conjugates were higher than commercial contrast agents such as Sinerem and Feridex. The high relaxivity of conjugated SPIONs was attributed to multicore densily packed monocrystalline iron oxide nanoparticles in whole cluster shell. Multicore cluster generate intense nonhomogeneous magnetic field of dipole character. The sum magnetic dipole moment creates the large dephasing zone with loss of time memory in proton precision. The size and chemical structure of coating less affect the relaxation rate of protons in vicinity of conjugated SPIONs construct. Therefore, we observed close values relaxivity of different magnetic species obtained from TKD, IgG1, and anti-CD11 antibodies bioligands. Signal intensity of MR images (darkening spot in T2-weighted mode) conjugated SPIONs nanoclusters correlates with measured T2, T2* in defined contrast regions.

Conclusion

Research results evidence that engineered functionalized SPIONs have high relaxivity and retain superparamagnetic properties. Formation of multicore nanoaggregate yields enhancement of induced relaxivity and increase in T2 – negative contrast image. The synthesized bioactive conjugates of TKD, IgG1, and anti-CD11 antibody with iron oxide magnetic nanoparticles obtained by covalent coupling to carboxylmethyldextran coat can be used as a negative contrast agent in MRI studies and have the potential of targeted nanocarrier for medical applications.

Acknowledgments

Authors thank Dr. D. Bobkov and Dr. N. Yudintceva for cell experiments. This research was funded by Russian Foundation for Basic Research project № 19-58-55001. The MR studies were performed at the Resource Center of Saint-Petersburg State University.

References

1. G. Lin, D. Makarov, O. G. Schmidt. Magnetic sensing platform technologies for biomedical applications. *Lab on a Chip*, 17(11), 1884–1912 (2017).
2. M. Grootveld, B. Percival, M. Gibson, Y. Osman, M. Edgar, M. Molinari, M.L. Mather, F. Casanova, P. B. Wilson. Progress in Low-Field Benchtop NMR Spectroscopy in Chemical and Biochemical Analysis. *Analytica Chimica Acta*, 1067, 11-30 (2019).
3. J. Mitchell, T.C. Chandrasekera, M.L. Johns, L.F. Gladden, E. J. Fordham. Nuclear magnetic resonance relaxation and diffusion in the presence of internal gradients: The effect of magnetic field strength. *Physical Review E*, 81(2), 026101(19) (2010).
4. J.-P. Korb, R. G. Bryant. Magnetic field dependence of proton spin-lattice relaxation times. *Magnetic Resonance in Medicine*, 48(1), 21–26 (2002).
5. N. Yudintceva, N. Mikhailova, D. Bobkov, L. Yakovleva, B. Nikolaev, D. Krasavina, A. Muraviov, T. Vinogradova, P. Yablonskiy, I. Samusenko, V. Ryzhov, V. Deriglazov, Y. Marchenko, G. Multhoff, A.P. Klapproth, W.B. Li, B. Nayak, A. Sonawane, M. Shevtsov. Evaluation of the Biodistribution of Mesenchymal Stem Cells in a Pre-clinical Renal Tuberculosis Model by Non-linear Magnetic Response Measurements. *Frontiers in physics*, 9, 625622 (2021).

Investigation by ^{1}H NMR spectroscopy of the composition of the reaction mixture at the production of hybrid ion-conducting membranes based on polyvinyl alcohol

Olga S. Lezova[1], Stanislav I. Selivanov[1,2], Olga A. Shilova[1], Alexandra G. Ivanova[1]

[1] Institute of Silicate Chemistry of the Russian Academy of Sciences, Makarova embankment, 2, 199034, Saint-Petersburg, Russia
[2] Institute of Chemistry, State University of Saint-Petersburg, University prospect 26, 198504, Saint-Petersburg, Russia
E-mails: [1]os-zar@mail.ru; [2]nmr.group.spbu@gmaill.com

Introduction

The development of a competitive ion-conducting membrane material for a hydrogen-air solid polymer fuel cell (SPFC) is quite an urgent task. Currently, a significant number of foreign and domestic scientific groups are engaged in the development of ion-conducting hybrid membranes based on various polymer materials – sulfonated or phosphorylated aromatic and aliphatic polymers [1, 2]. The use of nuclear magnetic resonance (NMR) spectroscopy in the study of a membrane material makes it possible to determine its composition, structure and mechanism of formation [3].

Earlier, using liquid-phase NMR ^{1}H spectroscopy, we investigated the composition and structure of new ion-conducting hybrid membranes based on polyvinyl alcohol (PVA) crosslinked with furfural (FUR), modified by aminosulfonic acid (ASA) and tetraethoxysilane (TEOS) in an organic medium – dimethyl sulfoxide (DMSO) [4]. In the NMR ^{1}H spectra of hybrid membranes, in addition to the broadened signals of protons of the CH- and CH_2-groups of PVA, the broadening of which is because of the decrease in the segmental mobility of the PVA chains, probably during their cross-linking of the FUR, and triplet signals of protons $^{14}NH_4^+$, the appearance of additional $^{14}NH_4^+$ triplets shifted relative to the main triplet in both high and low fields is observed. The appearance of additional signals of $^{14}NH_4^+$ triplets is probably due to the intermolecular interaction between ammonium ions and the PVA chain and/or between ammonium ions and the TEOS hydrolysis product. A significant decrease in the intensity of the proton signals of PVA OH- groups indicates their interaction with ASA, FUR and TEOS. However, in the NMR ^{1}H spectra of hybrid membranes, no signals of FUR protons and TEOS hydrolysis products were detected.

In this regard, the purpose of this work was to study the changes in the composition of the reaction mixture over time, from the beginning to the end of the multi-stage chemical process of interaction of PVS with its modifying components – ASA, FUR and TEOS, necessary to obtain an ion-conducting hybrid membrane by the method of liquid-phase ^{1}H NMR spectroscopy.

Experiments and results

DMSO was used as a solvent in the synthesis of the membrane material. The synthesis of hybrid ion-conducting membrane material can be divided into 3 stages. The first stage is the interaction of the PVS with the ASA. A suspension of ASA weighing 0.5 g was added to a 10% solution of PVA. After 8 hours of stirring on a magnetic stirrer of the reaction mixture solution at a temperature of 80 °C, a sample was taken for the analysis of its composition. In the ^{1}H NMR spectrum of the PVA-ASA reaction mixture (Fig. **1**), signals of protons of the CH_2-, CH- and OH-groups of PVA are observed with an integral intensity ratio of 2:1:1 in regions 1.2 – 1.6, 3.7 – 4.0 and 4.2 – 4.7 ppm., respectively. The characteristic triplet signal of the $^{14}NH^+_4$ group at 7.1 ppm. probably indicates the interaction of sulfogroups of ASA with OH groups of PVA with the formation of $-OSO_2ONH_4^+$-groups in the polymer chain. At the

same time, there are no signals from ASAs that have not chemically reacted with PVA such as an expanded signal at about 9.6 ppm., the appearance of which is usually due to the intermolecular exchange of protons of the ASA sulfogroup ($HO\text{-}SO_2NH_2$) and water, and a narrow signal at 5.8 ppm. corresponding to the rapid exchange of protons of the amino group of ASA with protons of the sulfogroup of the same acid with the formation, or NH_3^+-groups of ASA (zwitter ion – $SO_3NH_3^+$), or in the opposite direction of NH_2 groups ($HOSO_2NH_2$).

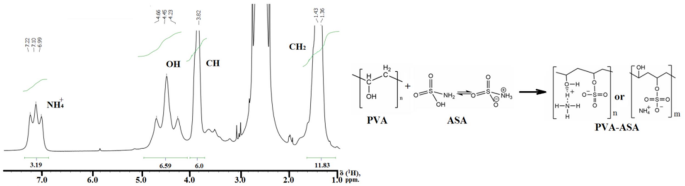

Figure 1. ^{1}H NMR spectrum of the PVA-ASA reaction mixture after 8 hours of stirring at 80 °C and schematic picture of PVA and ASA structurs and their interaction product PVA-ASA.

The second stage is the interaction of the PVA-ASA with the FUR: 0.9 ml of FUR was added to the solution of the reaction mixture containing PVA-ASA. After 12 hours of stirring on a magnetic stirrer of the reaction mixture solution at a temperature of 80 ° C, a sample was taken for the analysis of its composition. In the ^{1}H NMR spectrum of the PVA-ASA-FUR reaction mixture (Fig. **2**), in addition to the disappearance of three signals related to the protons of the OH groups of PVA, and the broadening of the signals of protons of the CH- and CH_2- groups associated with a decrease in the segmental mobility of the PVA chains, the triplet signal of protons $^{14}NH_4^+$ ASA in the region of 7.1 ppm. is preserved.

At the same time, the proton signals of the FUR are observed in the form of two different sets: the first of them includes narrow signals of the FUR that did not react with the PVA, and the second – broadened signals shifted to the high field region of NMR ^{1}H spectrum. They are situated at 5.58 (1), 6.43 (2, 3), and 7.62 (4) ppm., corresponding to the result of the interaction of FUR with OH-groups of PVA. These widenings can be explained by a decrease in the mobility of the furan cycle during its interaction with OH-groups of PVA. As a result, there are FUR crosslinking of two polymer chains through their OH groups and/or FUR crosslinking of adjacent OH-groups of one polymer chain. Narrow signals of the protons of the FUR, which did not react with the PVA, are observed at 6.8 (3*), 7.5 (2*), 8.1 (4*), 9.6 (1*) ppm. and have a lower intensity (~20% of the total quantity of FUR). The ^{1}H NMR spectrum of the PVA-ASA-FUR the reaction mixture also contains two doublet ($^3J_{H\text{-}H}$ = 8.0 Hz) signals at 7.55 and 7.56 ppm. belonging to the catalyst – p-toluene sulfonic acid.

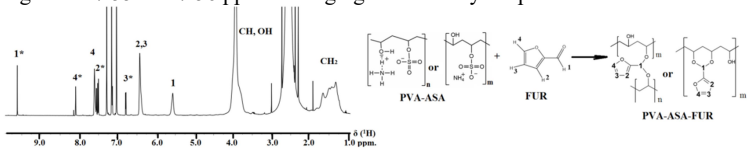

Figure 2. ^{1}H NMR spectrum of a reaction mixture containing PVA-ASA-FUR after 12 hours of mixing at a temperature of 80 °C and schematic picture of the PVA-ASA and FUR structures and their interaction product PVA-ASA-FUR

The third stage is the interaction of PVA-ASA-FUR with TEOS. 0.15 ml TEOS was added to the solution of the reaction mixture containing PVA-ASA-FUR. After 4 hours of stirring on a magnetic stirrer of the reaction mixture solution at room temperature, a sample was taken for its analysis. Analysis of the ^{1}H NMR spectrum of the reaction mixture (Fig. **3**)

shows the presence of broadened signals of OH-, CH- and CH_2-group protons, a triplet signal of $^{14}NH_4^+$-group protons at 7.1 m.d. with a characteristic constant of 51 Hz, as well as the signals of the protons of the FUR that reacted and did not react with the PVA. The intensity of the signals of the free, unbound polymer FUR has decreased even more. In the ^{1}H NMR spectrum, the appearance of narrow, intense signals of ethyl alcohol protons is observed: a triplet signal of protons at 1.05 ppm. (CH_3), a quartet signal of 3.44 ppm. (CH_2) and broad signal at 3.97 ppm. from OH- protons. The formation of ethanol molecules probably indicates the interaction of TEOS with OH groups of PVA.

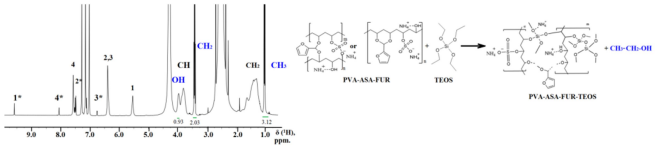

Figure 3. ^{1}H NMR spectrum of the PVA-ASA-FUR-TEOS reaction mixture after 4 hour. Schematic representation of PVA-ASA-FUR and TEOS mixture and their interaction product PVA-ASA-FUR-TEOS is shown on the right.

Conclusion

Based on the analysis of the 1H NMR spectra of the composition of the reaction mixture from the beginning to the end of the multi-stage chemical process of interaction of PVA with ASA, FUR and TEOS, the following conclusions can be drawn: 1) a gradual decrease in the intensity of the proton signals of OH-groups of PVA from one stage of chemical synthesis to another – when added to the PVA at the first stage – ASA, at the second stage – FUR and at the third stage – TEOS, indicate the interaction of OH-groups of PVA with its modifiers – ASA, FUR and TEOS; 2) ASA fully reacts with PVA; 3) the appearance of two different sets of proton signals of the furan ring of FUR indicates that not the entire volume of FUR has time to react with OH-groups of PVA during the synthesis of membrane material; 4) the appearance of ethyl alcohol proton signals when added to the reaction mixture of PVA-ASA-FUR and TEOS probably indicate the interaction of OH-groups of PVS with TEOS; 5) in the 1H NMR spectra of the reaction mixture of PVA-ASA-FUR-TEOS, no proton signals of additional triplets of 14NH4+ groups were detected, which were previously observed in the 1H NMR spectra of the finished membrane material dissolved in DMSO-d6.

Further investigation using solid-state NMR spectroscopy (SSNMR) will make it possible to more accurately determine the structure of the resulting hybrid membranes.

Acknowledgments

NMR experiments were carried out on the basis of the Engineering Center of SPbSTI (TU) on the AVANCE III-400 AG spectrometer (Bruker) with an operating frequency of 400 MHz. The work was carried out within the framework of the state task of the ICS RAS in the field of fundamental scientific research and partially with the financial support of the RFBR grant, project A-20-03-00938.

References

1. I.A. Stenina et al. J. Applied Polymer Sc., 2021, 138(27), № 50644.
2. Q. Liu, Z. Li, D. Wang, Z. Li et al. Metal Organic Frameworks Modified Proton Exchange Membranes for Fuel Cells. Frontiers in Chemistry, 2020, 8, № 694; DOI: 10.3389/fchem.2020.00694
3. K. Saalwachter et al. NMR methods for characterization of synthetic and natural Polymers, 2019, pp. 1-22; DOI: 10.1039/9781788016483-3
4. O.S. Lezova et al. International journal of hydrogen energy, 2022, 47(7), 4846–4853.

Development and investigation of pervaporation membranes based on polydimethylsiloxane-block-polyphenylene oxide copolymer

Vladislav P. Liamin[1], Anastasia D. Chepeleva[1], Anna I. Kuzminova[1], Anton S. Mazur[1], Anastasia V. Penkova[1], Mariia E. Dmitrenko[1]

[1]St. Petersburg State University, 7/9 Universitetskaya nab., St. Petersburg 199034, Russia
E-mail: lyamin.vlad.322@gmail.com

Introduction

Nowadays pollution problems are becoming more urgent. Therefore, investigations in the field of membrane separation processes have become topical due to their advantageous features, namely, waste-free, environmentally friendly, low-energy and compact equipment. One of the most promising methods for separation of liquid mixtures with low molecular components is pervaporation, which allows easily and effectively separating azeotropic mixtures, mixtures of close-boiling and thermally unstable substances, mixtures of isomers. The rapid development of this method requires the creation of novel membranes with tailored characteristics for more efficient separation.

A promising way to create more productive membranes is mixing of polymer features in block copolymers. In this work, poly(2,6-dimethyl-1,4-phenylene oxide) (PPO) and polydimethylsiloxane (PDMS) polymers were combined in block copolymer (PPO-b-PDMS), which was used as membrane matrix for the development of novel high-effective membranes for pervaporation dehydration of alcohols.

Membrane investigation

The optimal composition and conditions for preparation membranes based on PPO-b-PDMS copolymer were developed. The structural features of the developed membranes were studied by nuclear magnetic resonance (NMR) and Fourier-transform infrared spectroscopic (FTIR) analysis methods. The membrane inner and surface morphology was investigated by scanning electron (SEM) and atomic-force (AFM) microscopies. Transport characteristics of the membranes were evaluated in pervaporation dehydration of ethanol in a wide concentration range (5-90 wt.% water).

Results

The formation of the PPO-b-PDMS copolymer was confirmed by spectroscopic methods. And the preparation of the membranes based on PPO-b-PDMS copolymer led to the significant improvement of the permeability compared to pristine PPO membrane in pervaporation dehydration of ethanol.

Acknowledgements

This work is supported by the Russian Science Foundation (grant №21-73-00043). The experimental work was facilitated by the equipment from the Resource Centers for Nanotechnology, Magnetic Resonance, X-ray Diffraction Studies, Cryogenic Department, Thermogravimetric and Calorimetric Research Centre, Chemical Analysis and Materials Research Centre, and Centre "Nanofabrication of Photoactive Materials (Nanophotonics)" at the St. Petersburg State University.

Preliminary studies of the helium-3 hyperpolarization method in magnetized plasma

Makarchenko A.S.[1], Safiullin K.R. [1], Kuzmin V.V.[1], Tagirov M.S.[1,2]

[1]Institute of Physics, Kazan Federal University, 420008 Kazan, Russia
[2] Tatarstan Academy of Sciences, 420111 Kazan, Russia
E-mail: Makarchenko46@gmail.com

Introduction

Hyperpolarized noble gases, such as ^{3}He and ^{129}Xe, are widely used in physics for high-precision magnetometry, for detecting and polarizing neutrons, studying a porous media at room temperatures, and also for MRI studies in medicine. Today, the production of a hyperpolarized gas requires either the use of ultra-low temperatures and high magnetic fields, or the use of sophisticated equipment for optical polarization at room temperature. This greatly limits the possibilities of hyperpolarized gases applications.

New helium-3 nuclei hyperpolarization method

In 2018, a group of European scientists presented a new method of helium-3 polarization at room temperature in a magnetized plasma - polarization of atoms in a magnetized plasma (PAMP). In order to polarize helium-3 nuclei by this method, it is necessary to place helium-3 plasma in a strong magnetic field under certain conditions. The PAMP method significantly simplifies and reduces the cost of obtaining hyperpolarized helium-3, and with the further development of this method, it can become an alternative to the ordinary methods used to obtain hyperpolarized helium-3. To date, the maximum value of the polarization of helium-3 nuclei by this method is 9±5% [1]. In 2021, our research team obtained hyperpolarized helium-3 using the PAMP method under slightly different experimental conditions if compared with the original PAMP article. The description of this work is given in the article [2]. This article also describes the equipment for the production and cleaning of experimental glass cells and helium gas to ppm-level purity, which is also used in the experiments described below.

Performed experiments

Within the frame of this work, the polarization experiments were carried out on the helium-3 nuclei in a specially prepared polarization cell. It consists of a part for gas polarization which is connected by a thin capillary with a smaller part for NMR signal recording. The polarization cell was pre-cleaned and filled at room temperature with 10 millibars of high purity helium-3. During the polarization experiments, the optical spectra of the helium plasma were recorded to control its purity during the polarization experiments. From these spectra, it became clear that there is some amount of oxygen in the plasma, which concentration correlates with the temperature of the polarization cell. The measurement of the polarization was carried out on a home-made pulsed NMR spectrometer [3]. The dependences of the rate of the polarization process and the magnitude of the maximum polarization of helium-3 nuclei on the RF power supplied to the RF gas discharge circuit were measured. The dependences of the polarization value and signal growth rates on the temperature-, such as oxygen concentration in the polarization cell, were also measured. Current achievements of this work will be reported.

Acknowledgements

This work was financially supported by the Russian Science Foundation (grant #19-72- 10061).

References

1. Maul A. et al. Nuclear hyperpolarization of He3 by magnetized plasmas //Physical Review A. - 2018. - T. 98. - no. 6. - S. 063405
2. Makarchenko A.S. et al. Cryogenic Purification of Helium and its Use for Preparing Polarization Cells and Carrying Out Non-Optical Polarization of 3He Nuclei //Instruments and Experimental Techniques. - 2021. - T. 64. - No. 6. - P. 911-916
3. Kuzmin V.V. et al. The home-built high-field multifunctional pulsed NMR spectrometer //Magnetic Resonance in Solids. Electronic Journal. – 2019. – T.21. – №. 1. – C. 4-4.

Coarse Resonance search for the CIERMag Digital Magnetic Resonance Spectrometer (DMRS)

Julia Marcolan [1] *and Alberto Tannús*[1]

[1]*University of São Paulo, Institute of Physics of São Carlos, São Carlos, SP, Brazil.*
E-mail: juliamarcolan@usp.br

Introduction

Techniques that use Magnetic Resonance (MR) like Imaging (MRI) and Spectroscopy (MRS) are powerful because they allow the investigation of molecular structures and biochemical profile of tissues helping e.g., the identification of disease. In addition to the wide applicability, MR is a non-invasive technique and does not offer any danger to the sample or patient.

However, according to a review conducted by the *Centro de Imagens e Espectroscopia por Ressonância Magnética* (CIERMag), current MR commercial equipment do not facilitate the development of new MR Methods. The open-source tools have many useful features but at the same time, they have many problems related to code structure and poorly developed graphical interfaces. On the other hand, commercial equipment has other difficulties, although they are practical to use in most applications, they are very restricted for modifications [1].

In an attempt to solve this problem, the CIERMag team has developed a Digital Magnetic Resonance Spectrometer (DMRS) based on a holistic approach that synthesizes all hardware subsystems residing in a single FPGA; all critical signals are restricted to transmission within the FPGA reducing timing mismatch of the necessary signal. The DMRS includes a software background to support the development of new Methods including an Integrated Development Environment (IDE) based on Python Magnetic Resonance Framework (PyMR) [1] the ToRM Console for acquisition, organization, visualization, and storage of the data [2], the "F language", with its own compiler and a Language Server Protocol (LSP), and plugins that allow the use of the Eclipse and Spyder resources in F code, including syntax highlighting. F is a primitive language created for MR pulse sequence development, it is intended to be a robust language with reusable structures for its specialized applications.

This abstract describes the development of the Method *FindResonance* used for DMRS calibration. The purpose of this Method is to find the system coarse resonance frequency. The experiments were performed in a 0.54 T homemade permanent magnet using the ^{1}H nucleus. For these conditions, the coarse resonance frequency found was 23256.3 kHz. Compared with commercial MR spectrometers, CIERMag's DMRS is inexpensive and the structure for MR sequence development is a good alternative to the conventional standard equipment. This arrangement allows new techniques and new MR Methods to be developed, in addition to being easy to use. It can represent an advantage for research and development of MR techniques.

Methods

The Method FindResonance was developed using the proprietary and primitive F-Language to help in the DMRS calibration. The F-language was developed for programming pulse sequences used in MR experiments and has several features that facilitate the development of new techniques. An important feature of this language is the possibility of having a pictorial view of the pulse sequence that is under development, to make the sequence programmer closer to the experiment. In addition to the pulse sequence in the F-language, the Methods are also composed of validation and processing scripts that are python scripts.

FindResonance was developed to search for the system's coarse resonance frequency, it sends one RF pulse and acquires one FID at each repetition time. Each RF pulse used to

excite the sample operates with a different excitation frequency, the same used for the receiver. A group of frequency offset was previously calculated in the validation script, for each RF pulse the excitation frequency is composed of the base spectrometer frequency plus the pre-calculated offset. In its turn, the spectrometer base frequency is composed of the Larmor Frequency plus the offset.

The processing protocol is responsible for processing the acquired data, in the Find Resonance maximum intensity from the FIDs in the acquired data was calculated. The Method scans the frequencies around the Larmor frequency to find the resonance frequency. The experiments were done in a homemade permanent magnet with 0.54 T (precisely 0.5463145 T) intensity showing in Figure 1. The sample chosen for the experiments was $1\ cm^3$ from mineral oil, and considering the Hydrogen nucleus with gyromagnetic ratio equal to 42577.48 kHz/T. A 20 degree flip angle with a 15 μs duration was used in the experiment. The scans was were done using a bandwidth of 10 kHz and using 100 steps, i.e., using an increment of 0.1 kHz in the offset of each RF pulse.

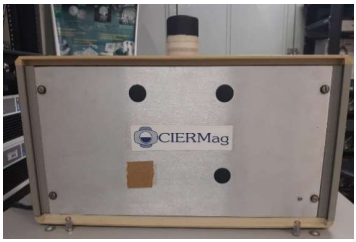

Figure 1. 0.5463145 T CIERMag permanent magnet.

Using the Larmor relation, when w_0 is the resonance frequency, B_0 is the field strength and γ is the Hydrogen gyromagnetic ratio

$$w_0 = \gamma B_0,$$

It was expected to found a coarse resonance around 23260.69 kHz.

Results and discussion

Using the method described in the above sections it was possible to find the value of 23256.3 kHz and an offset of – 4.7 kHz. Figure 2 shows the Fourier transform from a FID signal acquired using a sequence with a single RF pulse which offset was correct to the found value.

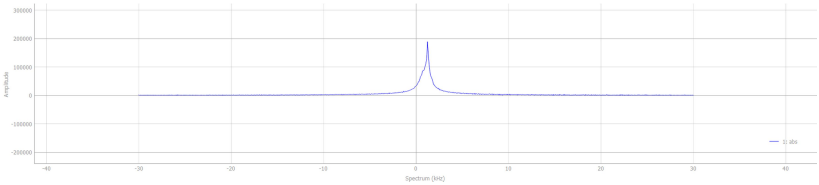

Figure 2. Fourier transform from a FID acquired with one pulse sequence using the offset, of - 4.7 KHz, found by the Find Resonance sequence.

On the other hand, in Figure 3 the resulting Fourier transform offset was manually corrected to – 3.4 kHz. For this offset, the resonance frequency is 23257.29 kHz.

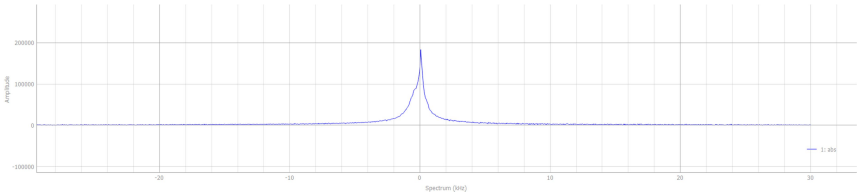

Figure 3. Fourier transform from a FID acquired with one pulse sequence using the offset, of - 3.4 KHz, adjusted manually.

Conclusion

Comparing Figure 1 and Figure 2 it is possible to notice that using the offset calculated by the Find Resonance the spectrum is not centralized in the zero position. The difference between the offset calculated by the FindResonance and the manually adjusted offset was 1.3 kHz; Based on these values, it is possible to conclude that the Method chosen cannot find an accurate fine resonance frequency, it only can be used to find the coarse resonance frequency.

The DMRS introduces a new way to create MR experiments that give to the sequence designer the control over the complete experiment including hardware control. Designing standard MR methods compatible with this new approach is extremely important to construct the basis for the development of new techniques. In addition, it carries on the didactic function to help new developers to understand the DMRS functionalities. CIERMag's DMRS is a good alternative to conventional standard MR equipment. This arrangement allows new techniques and new Methods to be developed. It can represent an advantage for the research and development of MR techniques.

Acknowledgements

This work is supported by the National Council for Scientific and Technological Development (CNPq).

References

1. Pizetta, D. C. (2019). *PyMR: a framework for programming magnetic resonance systems* [Universidade de São Paulo].
2. Silva, D. M. D. D. da. (2014). Desenvolvimento de console multiplataforma para aquisição, organização e visualização de dados do espectrômetro digital de RM do CIERMag: ToRM Console [Universidade de São Paulo].

Do 5-HT Receptor Ligands Modulate the Phase Behavior of Complex Lipid Bilayers?

Guzel Musabirova[1,2], Oskar Engberg[1], Ankur Gupta[3], Debsankar Saha Roy[3], Sudipta Maiti[3], Daniel Huster[1,3].

1Institute for Medical Physics and Biophysics, University of Leipzig, D-0410, Leipzig, Germany
2Institute of Physics, Kazan (Volga Region) Federal University, 420008 Kazan, Russian Federation
3Department of Chemical Sciences, Tata Institute of Fundamental Research, Mumbai 400 005, India
E-mail: guzel.musabirova@bk.ru
https://kpfu.ru/main?p_id=42585

Introduction

It is well known that in heterogeneous mixtures lipids tend to form different lipid phases (L_d and L_o). Lipid rafts are special areas (microdomains) of the plasma membrane enriched with glycosphingolipids and cholesterol. These sites coordinate cellular processes, affect membrane fluidity, serve as organizing centers for the assembly of signaling molecules, regulate the movement of membrane proteins, receptors, and also regulate neurotransmission. Lipid rafts are more structured and packed more densely than the surrounding lipid bilayer. One of the main differences between lipid rafts and plasma membrane is their lipid composition. Studies have shown that lipid rafts contain 3-5 times more cholesterol than the surrounding lipid bilayer. In addition, lipid rafts are enriched with sphingolipids - for example, sphingomyelin, the content of which in lipid rafts is usually 50% higher than that in the plasma membrane. ^{2}H NMR spectroscopy is very suitable method for studying in detail the biophysical properties of membranes with different coexisting lipid phases. Individual lipids can be deuterated and their phase behavior in a mixture is investigated.

Serotonin or 5-hydroxytryptamine (5-HT) is a hormone and neurotransmitter. Only about 5% of serotonin is synthesized in the brain, and most of it, about 80-90%, is in the intestine. Serotonin is involved in the formation and regulation of various physiological parameters of the body. Also diminished activity of serotonin pathways plays a causal role in the pathophysiology of depression. Serotonin usually acts on its target G-protein coupled receptor. However, in recent studies, Engberg A. et.al [1] discovered drastic restructuring of phases in a model membrane mimicking the outer plasma membrane leaflet, which was induced when 5-HT is added to the membranes at a 9 mol% concentration relative to the lipids. In this work, it was decided to check whether serotonergic drug (Aripiprazole, BRL-54443, BW723C 86, CP-135807) contain the same pharmacophore group (fig. 1) as serotonin modulate the phase behavior of complex lipid bilayers.

The effect(s) of the incorporation of small molecules on membrane mechanics has been widely studied; for example, statins [2], sorafenib and regorafenib [3], bile acids [4], salicylates [5], etc. It is assumed that the introduction of small molecules is able to modulate the properties of the lipid bilayer, changing its fluidity, thickness, and permeability. Various membrane proteins are embedded in the lipid membrane, the activity of which depends on the properties of the lipid bilayer. Thus, small molecules, without directly binding to the protein, can influence them through modulation of the lipid environment. Studying the interactions of small molecules with the lipid membrane will help explain the possible protein malfunctioning, physiological reactions, and eventually adverse side effects.

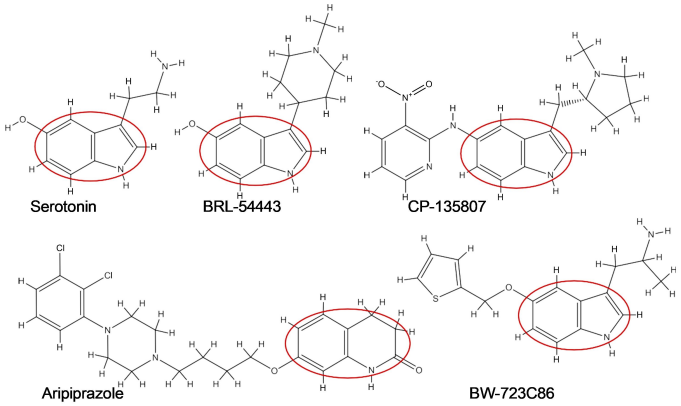

Figure 1. Chemical structure of serotonin, BRL-54443, BW-723C86, CP-135807 and Aripirpazole. In the red circle is the common pharmacophore group.

Materials

In current research was studied the interaction of BRL (BRL-54443), BW (BW-723C86), CP (CP-135807) and Ari (Aripiprazole) with lipids mixture containing cholesterol. The following lipids were used: POPC (1-palmitoyl-2-oleoyl-sn-glycero-3-phosphocholine) and PSM (N-palmitoyl-Derythro-sphingosylphosphorylcholine) and their sn-1 chain perdeuterated analogs POPC-d31 and PSM-d31. MLVs were prepared according to the method described by O. Engberg [1] in lipid molar ratio POPC/PSM/Chol/drug as 4/4/2/1. Lipids mixture was hydrated to 50 wt% using an aqueous buffer (20 mM K2PO4, 100 mM NaCl, 0.1 mM EGTA, pH 7.4). All measurements have been done on NMR spectrometer Bruker 750 Avance I with temperature range 20 to 50 °C with 10 °C steps.

Results

It was found that at 20°C and 30°C, two domains are observed in all lipid mixtures, one of which is more ordered (Lo), and one of the more disordered (Ld). It is noteworthy that for samples that do not contain serotonin-type preparations, the separation of lipids into phases under the same conditions is not observed. Numerical line shape simulations were carried out as described in [1] for more clear 20°C spectra. This complex analysis allows comparing the effects of the individual serotonergic drugs on the order parameters and projected chain lengths of the POPC-d31 and PSM-d31 palmitoyl chains in both the more disordered and more ordered domains.

The order parameters POPC- d31 in the Ld phase in the presence of serotonergic drugs almost did not change. However, there is a noticeable increase in them in the Lo phase and the strongest change is observed in the presence of Ari, followed by CP, BW, BRL. Also, a detailed analysis of the 2H NMR spectra of PSM- d31 showed the following picture: the order parameters of the Lo phase in the presence of serotonergic drugs did not change significantly, whereas the Ld phase showed very strong decreases.

The relative contribution of POPC- d31 and PSM- d31 the different phases are shown on the fig. 2. From 60% to 70% POPC- d31 in Ld phase was observed when for PSM- d31 was found opposite situation: 70-80% in Lo phase.

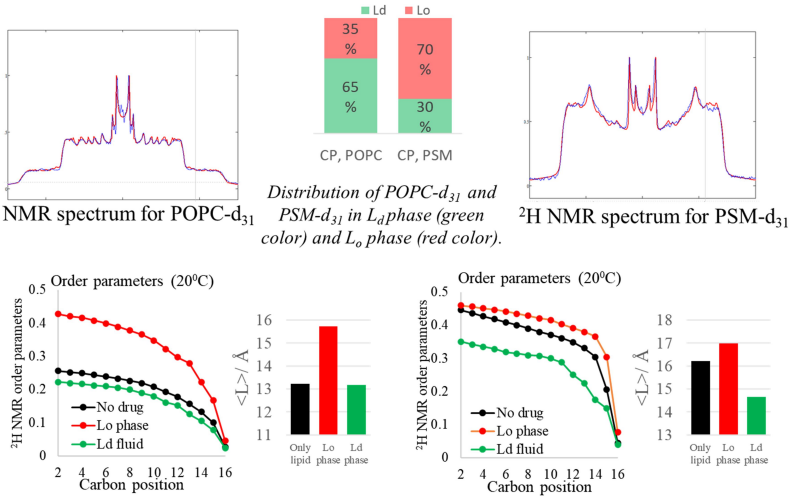

^{2}H NMR spectrum for POPC-d$_{31}$

Distribution of POPC-d_{31} and PSM-d_{31} in L_d phase (green color) and L_o phase (red color).

^{2}H NMR spectrum for PSM-d$_{31}$

Figure 2. ^{2}H NMR order parameter profiles, spectra, and numerical lineshape simulations of POPC/PSM/Chol 4/4/2 membranes in the presence and absence of CP at a lipid/drug molar ratio of 10:1 at a temperature of 20°C. Left panels show data for POPC- d_{31} and right panels the data for PSM- d_{31}. The inserts present the projected chain lengths <L> for POPC- d_{31} and PSM-d_{31} in the absence (black bars) and in the presence of CP for both phases (colored bars). In the ^{2}H NMR spectra, the red lines indicate the original spectra and the blue lines the best fit numerical lineshape simulations.

We found that aripiprazole, BRL-54443, BW723C 86 and CP-135807 modulate the phase behavior of complex membrane models. This could potentially affect the function of membrane proteins that do not interact with these small molecules leading to alterations in the function of these molecules as a basis for side effects of these drugs.

References

1. Engberg O. et al. Serotonin Alters the Phase Equilibrium of a Ternary Mixture of Phospholipids and Cholesterol // Front. Physiol. 2020. Vol. 11.
2. Galiullina L.F. et al. Interaction of statins with phospholipid bilayers studied by solid-state NMR spectroscopy. // Biochim. Biophys. acta. Biomembr. Netherlands, 2019. Vol. 1861, № 3. P. 584–593.
3. Haralampiev I. et al. The interaction of sorafenib and regorafenib with membranes is modulated by their lipid composition // Biochim. Biophys. Acta - Biomembr. 2016. Vol. 1858, № 11. P. 2871–2881.
4. Evans E., Rawicz W., Hofmann. A.F. Lipid bilayer expansion and mechanical disruption in solutions of water-soluble bile acid. 80th ed. Bile Acids Gastroenterol. Basic Clin. Adv., 1995. 59–68 p.
5. Zhou Y., Raphael R.M. Effect of Salicylate on the Elasticity, Bending Stiffness, and Strength of SOPC Membranes // Biophys. J. 2005. Vol. 89, № 3. P. 1789–1801.

Radiofrequency safety assessment of a volumetric wireless coil for MRI of wrist joint at 3 T

Nasonov Aleksei, Alena Schelokova[1], Ekaterina Brui[1]

[1]Faculty of Physics, ITMO University, Kronverkskiy pr. 49, 197101 St. Petersburg, Russia
E-mail: aleksei.nasonov@metalab.ifmol.ru

Introduction

Recently, a new concept of a dedicated metamaterial-inspired wireless coil has been proposed for a 1.5 T wrist MRI [1]. The wireless coil was based on an array of coupled split-loop resonators that focuses transmit and receive capabilities of a whole-body "birdcage coil" (BC) within the region of interest. This concept provided more than twice higher signal-to-noise ratio (SNR) in comparison to a 4-channel receive array, and a dramatic decrease in the maximum local specific absorption rate (SAR) of a BC, allowing the safe utilization of efficient SAR-demanding pulse sequences [2]. Meanwhile, 3 T MRI is advantageous in joint diseases studies [3], however, SAR becomes a more critical issue than at 1.5 T. That is why, it is interesting to transfer the proposed concept to 3 T MRI. This work numerically investigates RF safety characteristics of 3 T wireless coil for wrist MRI. As the instabilities of RF safety may cause heating of the patient's body, we thoroughly study their robustness to the possible breakdowns.

Methods

Electromagnetic simulations

All calculations were performed in CST Studio Suite 2020. A whole-body high pass BC tuned and matched to 124 MHz was used for excitation. It consisted of 16 copper legs (length - 650 mm, diameter - 700 mm) with an RF shield (diameter - 826 mm, length - 1250 mm). Previously proposed numerical model of the wireless coil for 1.5 T [1] was adapted for 3 T by tuning its lower frequency volumetric mode to 124 MHz. To do this, the distributed capacitance was adjusted by changing the substrate (Arlon 255C with ε=2.55, dielectric loss tgδ=0.0018, thickness - 2 mm) and changing of copper strips size. Thus, the wireless coil consists of two dielectric substrates with the size of 244×124×2 mm^3 with overlapped copper strips (118×3 mm^2 on one side and 42.5×3 mm^2 on the opposite side) connected by copper tubes of 280 mm (Fig. 1 A). The voxel model "Gustav" from the CST library positioned in a prone "superman" position was used to evaluate the coil performance in the presence of a human body. Electromagnetic fields distributions were simulated for two setups when the RF field was excited by: 1) the BC, and 2) a system of coupled BC and wireless coil. RF magnetic field (B_1^+) and SAR were calculated for 1 W of accepted power. RF safety was calculated as a ratio of the root mean squared value (RMS) of B_1^+ divided by the square root of the maximum local SAR or whole-body SAR. RF safety robustness study included considering of the breakage of one of the wires and inaccurate coil positioning (5° rotation).

Prototyping and B1$^+$ mapping experiments

A prototype of the wireless coil was assembled and a plastic case was designed and printed on a 3D printer. To obtain experimental B1$^+$ maps, a double-flip-angle method [4] was used. MR studies were conducted using 3 T Siemens MAGNETOM Trio clinical scanner. B1$^+$ maps were acquired for a homogeneous phantom composed of water, salt, and agarose, and for a hand of a healthy volunteer. A reference voltage used by the scanner to create a 180° flip angle was recorded to estimate the increase of transmit efficiency provided by the wireless coil.

Results

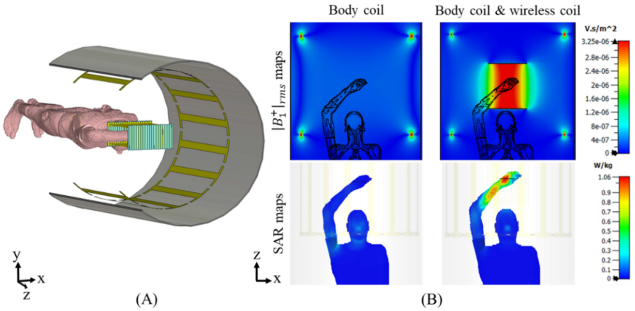

Figure 1. (A) Numerical model of a wireless coil placed inside a birdcage coil together with a voxelized human body model in a "superman" position. (B) The $B1^+$ maps without and with the wireless coil (top panel). SAR maps normalized to 1 W of accepted power (bottom panel).

When the wireless coil was placed into the BC, a strong coupling was observed, and the resonance of the BC was splited. Thus, in this RF setup, the mode located at 120.21 MHz was considered. Figure 1 B shows the $|B1^+|_{RMS}$ magnetic field and SAR maps for 1 W of accepted power for both RF setups. Numerical values of local and whole-body SAR and $B1^+$ in the region of interest are presented in Figure 2 A together with the calculated RF safety. Figure 2 B shows the $B1^+$ field and SAR distributions for the case when the wireless coil is rotated by 5°. Due to the decrease in the focusing ability, the $B1^+$ field and maximum local SAR values were decreased. As a result, local RF safety raised. Weaker focusing led to the decrease of transmit efficiency and to the decrease of the whole-body RF safety characteristic (Fig. 2 A). Dependence of the local and total RF safety characteristics on the numerical position of wire considered as unsoldered (marked in Figure 3 A) is presented in Figure 3 B. It turns out that the breakage of the central wires leads to a decrease in the whole-body RF safety, while local RF safety is increased. The breakage of the side wires leads to an opposite effect.

Case	BC	BC + WLC	BC + WLC 5° deviation	Unit
$\|B_1^+\|_{rms}$	0.355	3.169	2.860	μT
$psSAR_{10g}$	0.23	1.054	0.737	W/Kg
$wbSAR$	0.007	0.012	0.011	W/Kg
$\|B_1^+\|_{rms}/\sqrt{psSAR_{10g}}$	0.75	3.086	3.332	$\mu T/\sqrt{W/Kg}$
$\|B_1^+\|_{rms}/\sqrt{wbSAR}$	4.27	28.645	26.693	$\mu T/\sqrt{W/Kg}$

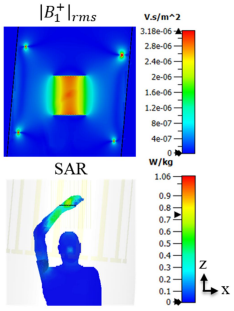

Figure 2. (A) Magnetic field B_1^+, SAR and RF safety data for different cases. (B) B_1^+ magnetic field and SAR for inaccurate positioning case.

Experimental $B1^+$ maps obtained with and without a prototype of the wireless coil (Fig. 4 A) are presented in Figure 4 B (phantom) and Figure 4 C (in-vivo). The recorded reference voltage for BC was 431.6 V, and 54.7 V while using the wireless coil together with BC.

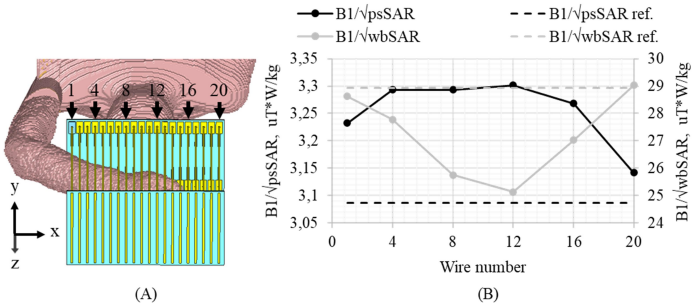

Figure 3. Numbers and position of wires that were broken (A), RF safety graphs for different breakages (B). "Ref." - the reference case of the model, not affected by breakdowns.

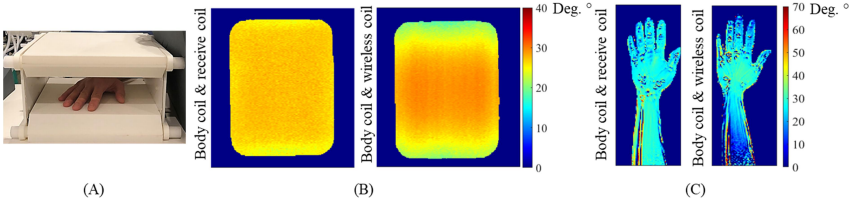

Figure 4. (A) Photo of the wireless coil prototype. Experimentally measured $B1^+$ maps for phantom (B) and volunteer (C).

Discussion and Conclusion

In the present work, we have demonstrated that a concept of a metamaterial-inspired wireless coil may be successfully transferred to a 3 T MRI. Numerical simulations have shown that the B_1^+ field and RF safety of a whole-body BC can be drastically improved using this coil as a secondary inductively coupled element. The numerically predicted increase in the B_1^+ field (8.9-fold) was in a good agreement with the reduction of RF pulse voltage (7.9-fold) provided by the use of the wireless coil. In the study of a possible breakdown, a 12 % drop of the whole-body RF safety and 17 % decrease of the B_1^+ field amplitude was noticed. However, these changes are not significant compared with the use of BC alone. The increase in whole-body RF safety changed from 6.7 to 5.9 times. A slight error in coil positioning resulted in a 10 % efficiency drop and an 8 % decrease in whole-body RF safety. Thus, the coil characteristics are robust for the minor imperfections of the experimental setup that may occur during actual scanning. Due to a high RF safety, the wireless coil may be potentially helpful for increasing the safety of MR scanning of patients with implants.

Acknowledgments

The work was carried out with the support of a grant from the President of the Russian Federation for scientific school НШ-2359.2022.4.

References

1. Shchelokova A. V. et al. Magn Reson Med. 2018; 80(4):1726-1737.
2. Brui E. A. et al. MAGMA, 2021; 34(6):929-938.
3. Wieners G. et al. Eur. Radiol. 2007; 17(8):2176-82.
4. Cunningham C. H. et al. Magn Reson Med. 2006; 55(6):1326-33.

NMR resonance assignments of NAD-dependent formate dehydrogenase

Polina A. Nikiforova[1], Sofia S. Mariasina[1], Vladimir I. Tishkov[1], Vladimir I. Polshakov[1]

[1]Lomonosov Moscow State University, Moscow, Russia
E-mail: mikevazovski23@gmail.com

Introduction

Staphylococcus aureus is a facultative anaerobic bacterium and multifaceted causative agent of clinical infections [1]. Furthermore it forms functionally heterogeneous bacterial communities called biofilms. The high resistance of biofilm-embedded cells requires new inhibitors. Previous studies demonstrated an upregulation of NAD-dependent formate dehydrogenase (FDH) in *Staphylococcus aureus* biofilms. In this regard FDH appears to be one of the most promising target [2,3].

Formate dehydrogenase

FDH is an enzyme that catalyze oxidation of formate ion to carbon dioxide with the coupled reduction of NAD^+ to NADH:

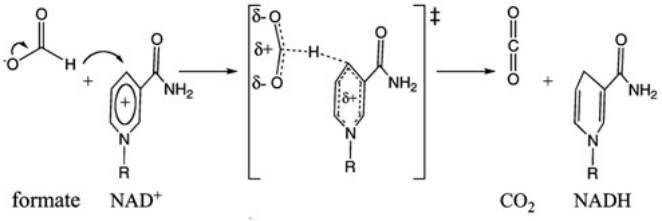

Figure 1. FDH-catalyzed hydride-transfer reaction

NMR screening detects binding of ligands to a protein, rather than inhibition of protein function that is provides binding assay. NMR screening is performed by protein observation and further protein-ligand observation. The chemical shifts of protein resonances depend sensitively on the local environment of the respective nuclei. After ligand binding the local environment changes and protein residues consequently experience chemical shift perturbations due to direct cotact with the ligand or conformational changes. For perturbations detecting one must assign protein resonances to their position in the amino acid sequence. Thus the assignment seems to be a first step towards ligand screening. Recently FDH crystal structure was obtained that facilitates assignment procedure.

Figure 2. Crystal structure of sa-FDH dimer (PDB ID 6TTB)

Sa-FDH protein samples

FDH is a homodimer with molecular weight 84 kDa. Such size recquires deuteration for the slowdown of transverse relaxation that is expression in D_2O. Just before NMR experiment amide deuterium should be replaced by protium through H_2O exchange. However such exchange is hampered in case of high-structured protein, especially in the beta-sheets due to the strong hydrogen-bonds formation. That's why culture medium containes 50% H_2O (with ^{13}C, ^{15}N, ^{2}D isotope enrichment of carbon sources). Finally it is worth noting FDH thermostability which allows experiments up to 45°C.

Sa-FDH 2D and 3D NMR spectra

In this work for assignment 2D (HNQC) and 3D NMR spectra (HNCO, HN(CA)CO, HNCA, HN(CO)CA, HNCACB and CBCA(CO)NH) are used (all in trosy-version for high quality [4]). In HSQC case magnetization is transferred from hydrogen to attached ^{15}N nuclei via the J-coupling. The chemical shift is evolved on the nitrogen and the magnetisation is then transferred back to the hydrogen for detection. In 3D spectra cases magnetisation is passed from ^{1}H to ^{15}N and then selectively to the carbonyl ^{13}C via the $^{15}N^{H}$–^{13}C J-coupling. Magnetisation is then passed back via ^{15}N to ^{1}H for detection. The chemical shift is evolved on all three nuclei resulting in a three-dimensional spectrum.

Sa-FDH NMR assignment

NMRFAM-Sparky is usual tool for assignment procedure. ^{1}H, ^{15}N, ^{13}C axes synchronize with each other. Next for each HSQC amide signal one maps it to J-coupling signal between:

- HNCO previous amino acid carbonyl and HN(CA)CO current amino acid carbonyl
- HN(CO)CA previous amino acid α-carbon and HNCA current amino acid α-carbon
- CBCA(CO)NH previous amino acid β-carbon and HNCACB current amino acid β-carbon

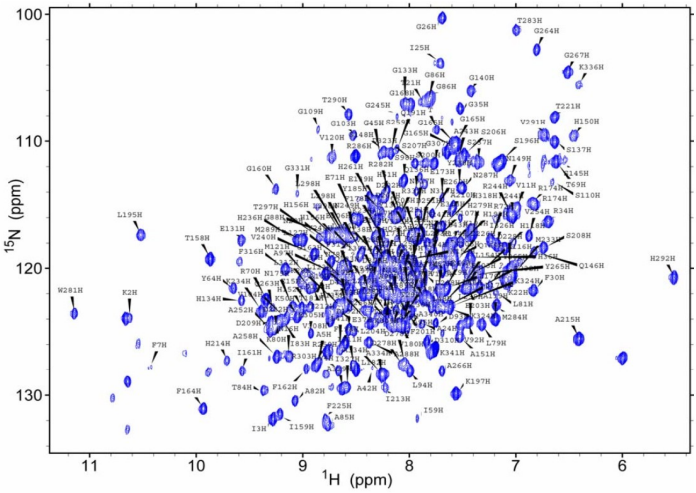

Figure 3. ^{15}N-^{1}H TROSY spectrum of saFDH.

Automated assignment programs such as PINE [5] can facilitate this process but still require manual verification. Next secondary structure verification according to the chemical shifts is assessed on the basis of executed assignment by means of Talos+ program [6].

Acknowledgements

This research is supported by the Russian Science Foundation (grant 19-14-00115).

References

1. Lowy FD. Staphylococcus aureus infections. *N Engl J Med*. 1998 Aug 20;339(8):520-32.
2. Leibig M, Liebeke M, Mader D, Lalk M, Peschel A, Götz F. Pyruvate formate lyase acts as a formate supplier for metabolic processes during anaerobiosis in Staphylococcus aureus. *J Bacteriol*. 2011 Feb;193(4):952-62.
3. Savin SS, Tishkov VI. Assessment of Formate Dehydrogenase Stress Stability In vivo using Inactivation by Hydrogen Peroxide. *Acta Naturae*. 2010;2(1):97-102.
4. Zhu, Guang, et al. "Protein dynamics measurements by TROSY-based NMR experiments." (2000): 423-426.
5. Lee, W., Bahrami, A., Dashti, H. T., Eghbalnia, H. R., Tonelli, M., Westler, W. M., & Markley, J. L.(2019). I-PINE web server: an integrative probabilistic NMR assignment system for proteins. *Journal of Biomolecular NMR*, 73(5), 213-222.
6. Shen, Y., Delaglio, F., Cornilescu, G. *et al.* TALOS+: a hybrid method for predicting protein backbone torsion angles from NMR chemical shifts. *J Biomol NMR* **44,** 213–223 (2009).

^{1}H and ^{19}F MRI of the lungs in clinical and preclinical studies

Olga S. Pavlova[1,2], Nikolay V. Anisimov[1], Mikhail V. Gulyaev[1], Yury A. Pirogov[2]

[1]Faculty of Fundamental Medicine, Lomonosov Moscow State University, 119991, Russia
[2]Faculty of Physics, Lomonosov Moscow State University, 119991, Moscow, Russia
E-mail: ofleurp@mail.ru

Introduction

Potentially, MRI is an ideal facility for diagnostic of lung diseases, since it is highly informative and does not use any harmful ionizing radiation. Thus, MRI is a good alternative method to computed tomography (CT), which is the most commonly used for diagnostic of lung diseases [1]. It is especially significant for pediatric studies and for systematic long-term observations.

However, conventional (proton, ^{1}H) pulmonary MRI is complicated by low proton density and magnetic susceptibility artefacts [2]. Therefore, for structural imaging of the lungs, it is preferable to use ultra-fast pulses sequences [3]. To enhance diagnostic of lung diseases, structural images of the lungs can be supplemented with functional information, which can be obtained by special MRI techniques based on the inhaled contrast gas imaging – for example, using inert fluorinated gas in ^{19}F MRI [4].

This paper presents modern MRI methods aimed for diagnostic of lung diseases. The prospects of such approaches for preclinical studies of small laboratory animals in strong magnetic fields and human clinical studies in weak fields are demonstrated.

^{1}H and ^{19}F MRI of rat lungs at 7 Tesla

The magnetic susceptibility artifacts increase with magnetic field strength, which leads to the reduction in T_2^* (<<1 ms). However, the use of the 3D UTE pulse sequence [5], which provides ultra-short TE (up to 20 μs), made it possible to visualize fibrotic changes in rat lungs in ^{1}H MRI (Fig. 1). The effectiveness of 3D UTE for the detection of ventilation disorders in the fibrosis zone was also shown using the fluorinated gas octafluorocyclobutane (OFCB, C_4F_8) in ^{19}F MRI (Fig. 1). OFCB has high density (8.82 kg/m^3) and 8 magnetically equivalent ^{19}F nuclei which form strong MR signal.

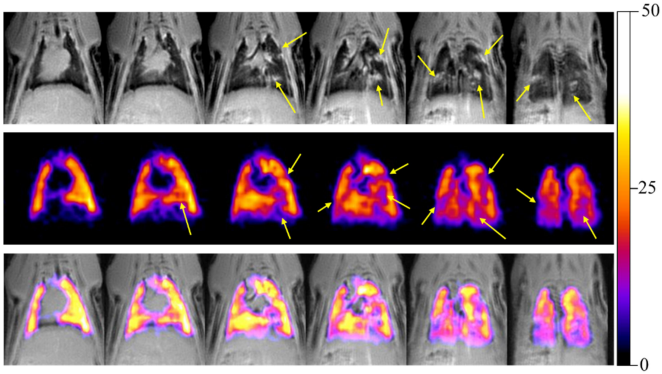

Figure 1. MRI of a rat with lung fibrosis – selected slices in coronal projection. Top row: ^{1}H MRI; Middle row: ^{19}F SNR maps; Bottom row: sum of ^{1}H and ^{19}F MRI. The arrows points to fibrotic changes in lungs. The color scale corresponds to SNR values in ^{19}F MR images

^{1}H and ^{19}F MRI of human lungs at 0.5 Tesla

In our experiments on clinical 0.5T MR scanner we took into account that for ^{1}H and ^{19}F pulmonary MRI the conventional pulse sequences can be used as the low magnetic fields provide higher T_2^* (1-3 ms). Some of the obtained results demonstrating the comparison of healthy and post-COVID lungs are shown in Fig. 2.

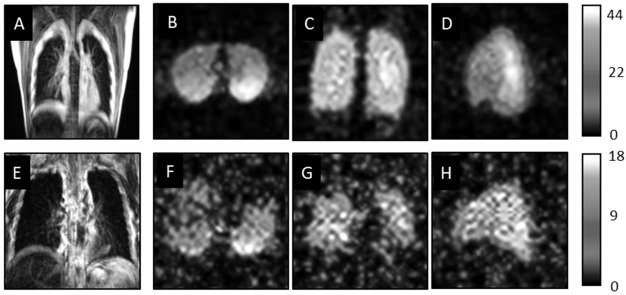

Figure 2. MRI of a healthy (upper row) and a post-COVID (bottom row) volunteers. A,E: ^{1}H MRI (Z-project-Standard Deviation). B-H: non slice-selective ^{19}F MRI in axial (B,F), coronal (C,G), and sagittal (D,H) projections. The grey scales corresponds to SNR in ^{19}F MRI

The potential of OFCB as a contrast gas for lung imaging is associated also with its long T_1 (~56 ms), that is especially important for low field MRI. It also makes OFCB an effective marker for oxygenation measurements that provides information about lung perfusion and gas exchange. Using OFCB, we obtained 3D lung images, calculated T_1 maps, studied the wash-in/-out dynamics of the gas flow during single respiratory cycle. It provided functional information on lung ventilation and perfusion.

We have also implemented ^{1}H MRI PREFUL (phase resolved functional lung imaging [6]) method for functional diagnostics of lungs. This method is based on collecting a series of lung images obtained with high time resolution (< 500 ms per image). The signal inside the lungs varies due to two factors – respiration and blood supply, since both of them affect the concentration of paramagnetic oxygen inside the lungs. The PREFUL technique makes it possible to separate these two processes and calculate maps of lung ventilation and perfusion.

Conclusions

^{1}H and ^{19}F MRI are useful for revealing not only structural fibrotic changes in lungs of small laboratory animals, but also for functional diagnostic of ventilation and perfusion in human lungs. The use of OFCB in ^{19}F MRI is especially effective at low magnetic field.

Acknowledgements

This work is supported by Russian Science Foundation grant #21-75-10038, the Interdisciplinary Scientific and Educational Schools of Moscow University «Molecular Technologies of the Living Systems and Synthetic Biology» and «Photonic and quantum technologies. Digital medicine».

References

1. L. P. Lavelle, et al. – *Diagn. Interv. Radiol.*, 23(2), 106-111 (2017).
2. J. F. Schenck. – *Med. Phys.*, 23, 815-850 (1996).
3. K. Bae, et al. – *Eur. Radiol.*, 29(5), 2253-2262 (2019).
4. M. J. Couch, et al. - *J. Magn. Reson. Imaging*, 49, 343–354 (2019).
5. G. Bauman, et al. – *Magn. Reson. Med.*, 73, 555–564 (2015).
6. A. Voskrebenzev, et al. – *Magn. Reson. Med.,* 79, 2306–2314 (2018).

Characterization of spin properties of organomineral aggregates

Alina A. Pichugina[1], Larisa V. Tsyro[1]

[1]Institute of Natural and Technical Sciences, Surgut State University, Lenina avenue 1, Surgut, Russian Federation
E-mail: alina.com9@mail.ru
http://www.surgu.ru

Introduction

Organo-mineral aggregates are chemically complex substances, because they include various organic and inorganic compounds [1]. Such aggregates include gall, urinary and salivary stones [2]. The process of formation of an organomineral aggregate is complex and debatable, because there is still no exact description of the occurrence of such neoplasms in the body. The authors of [3, 4] believe that the formation of organomineral aggregates is associated with such factors as the environment, nutrition, consumption of various drugs, etc. In the article [5], the process of formation of organomineral aggregates was considered, associated with the appearance in the human body of paramagnetic and radical particles, which have a negative attention to the work of the body and cause the appearance of various negative neoplasms.

Currently, there are many physicochemical methods for the analysis of organomineral aggregates, such as X-ray phase analysis, IR-Fourier spectroscopy, X-ray fluorescence analysis, atomic absorption spectroscopy, nuclear magnetic resonance, electron paramagnetic resonance [6, 7]. However, to study biological systems containing one or more unpaired electrons, the most applicable method is electron paramagnetic resonance. This method makes it possible to identify the presence of paramagnetic ions and radical particles, which are involved in the formation of organomineral aggregates.

Therefore, the purpose of this work was to establish paramagnetic particles in organomineral aggregates.

Research Methods

The objects of the study were gallstones (cholesterol, pigment and mixed types) removed from patients in the Tomsk region.

EPR spectra of the samples were obtained on a JOEL-FA200 spectrometer, under the following shooting conditions: t = 25 °C, microwave frequency ~ 9.4 GHz, modulation frequency 100 kHz, sensitivity $7 \cdot 10^9$ spin / 0.1 mT, maximum magnetic field sweep 500 mT, modulation width 1 mT, field sweep time 4 min. The sample was analyzed in a quartz ampoule 5 mm in diameter.

Results

As can be seen from Figure 1, paramagnetic particles are present in the studied samples of organomineral aggregates, as indicated by characteristic signals in the EPR spectrum. The types and amounts of such paramagnetic particles are different. This suggests that during the formation of an organomineral aggregate in the human body, various biological and chemical processes take place. Thus, in all EPR spectra of the studied samples, there is a narrow signal with a g-factor equal to 2,003, which corresponds to the presence of a free radical in the organomineral aggregate. In addition to free radicals, you can see a signal consisting of six lines (Fig. 1c). This type of signal corresponds to the Mn^{2+} ion, which has five unpaired electrons, with a nuclear spin of 5/2. However, the authors of [8] believe that this type of signal can also be attributed to Mn^{4+} ions. In the sample shown in Fig. 1a, a more detailed examination reveals a sextet related to Mn^{2+} ions. Also, in all the EPR spectra of the

studied objects, a broad signal of different intensity was observed in the g-factor region of 4,19. This signal can be attributed to the center of the high-spin state of iron – Fe^{3+}, with a nuclear spin of 5/2. In addition to the signals described above, the EPR spectrum shown in Fig. 1b, two signals are observed in the region of g-factors 2,4 – 2.1 and 2,05. These types of signals can be attributed to the paramagnetic centers of divalent copper ions - Cu^{2+}. Thus, the authors of [9] noted that the paramagnetic center of divalent copper ions can give one signal consisting of two peaks with $g_{\parallel} \sim 2{,}37$ and $g_{\perp} \sim 2{,}05$, which are poorly resolved or not resolved at all, which causes their merging into one wide signal in the EPR spectrum. Such types of signals indicate that copper ions in organomineral aggregates exist as isolated mononuclear bioorganic complexes with four nitrogen atoms in the coordination sphere. Such complexes can be formed by the interaction of copper ions with groups of C–N- or C–H-amino acids.

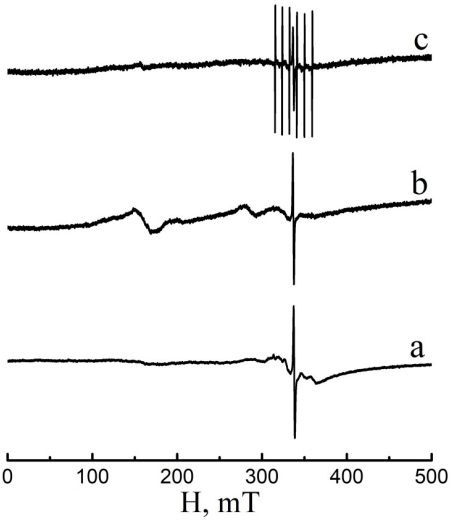

Figure 1. Examples of EPR spectra of organomineral aggregates

To understand the processes of formation/association of organomineral aggregates, they were dissolved in such solvents as C_6H_6 and CS_2. When organomineral aggregates are dissolved in benzene, a colloidal system is formed, in which the particle size can reach about 250 nm. The dissolution of organomineral aggregates in carbon disulfide leads to almost complete dissolution of the studied samples, as evidenced by the particle size, which is 10–15 nm. This behavior is due to the fact that carbon disulfide is able to form complexes with the paramagnetic centers of the organomineral aggregate.

To confirm that the processes of associate formation of organomineral aggregates proceed with the participation of paramagnetic particles, the EPR spectra of these solutions and precipitates from dissolution were recorded (Fig. 2).

As can be seen from Fig. 2, in all the given EPR spectra there is a narrow signal in the g-factor region of 2,003, which is characteristic of free radicals. Thus, the total number of paramagnetic centers in the solution "organomineral aggregate - benzene" is $1{,}8 \cdot 10^{20}$ spin/g, and in the solution "organomineral aggregate - carbon disulfide" the total number of paramagnetic centers is $1{,}6 \cdot 10^{18}$ spin/g. Figure 2, c shows the EPR spectrum of the sediment of an organomineral aggregate that has not dissolved in benzene. It can be seen from the

presented EPR spectrum that, in addition to free radicals, there is a broad unresolved line in the region of the g factor 2,4–2,1, which corresponds to the paramagnetic Cu^{2+} centers. The total number of paramagnetic centers in the precipitate is $3{,}2 \cdot 10^{20}$ spin/g.

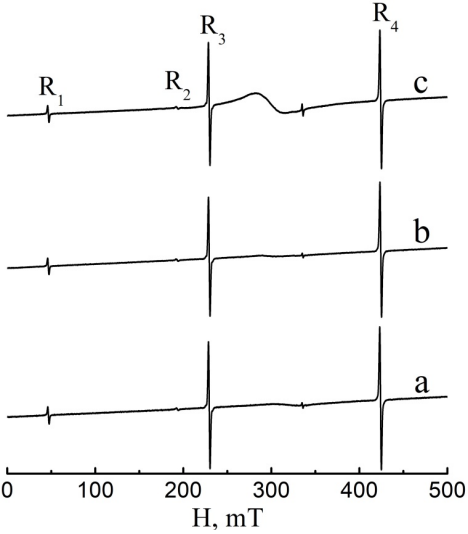

Figure 2. EPR spectra of solutions and sediments of organomineral aggregates: a – in benzene; b – in carbon disulfide; c – precipitate after dissolution in benzene

Summing up the work done, we can conclude that the formation of organomineral aggregates in the human body occurs with the participation of paramagnetic particles of various types. It can also be assumed that for the dissolution of such aggregates, it is necessary to use drugs that have a structure similar to carbon disulfide.

References

1. S. Pramanik, S. Ghosh, A. Ray, R. Mukherjee, A. K. Mukherjee. – *Z. Kristallogr.*, **231** (2), 97-105 (2016).
2. O. A. Golovanova, O. V. Frank-Kamenetskay, Yu. O. Punin. – *Russian Journal of General Chemistry*, **81**, 1392-1406 (2011).
3. V. K. Singh, B. S. Jaswal, J. Sharma, P. K. Rai. – Biophysical Reviews, 12, 647-668 (2020).
4. A. Di Ciaula, DQH Wang, P. Portincasa. – *Curr Opin Gastroenterol.*, **34** (2), 71-80 (2018).
5. F. G. Unger, L. V. Tsyro, A. A. Pichugina, D. A. Afanasiev, S. A. Kiselev. – *Herald of the Bauman Moscow State Tech. Univ.*, **84** (2), 107-122 (2016).
6. A. A. Pichugina, L. V. Tsyro, F. G. Unger. – *Journal of Applied Spectroscopy*, **84** (6), 1024-1029 (2018).
7. D. Y. Lu, X.-L. Gao, Y. Chi, H.-G. Wang, X. Yang, T. Qiao. – *Journal of Trace Elements in Medicine and Biology*, **60**, 126494 (2020).
8. V.V. Pantyushov, O.M. Zhigalina, D.N. Khemelin, I.A. Kokorin, W.E. Trommer, Y.N. Degtuarev, A.I. Kokorin. – *Applied Magnetic Resonance*., doi.org/10.1007/s00723-021-01360-z, (2021).
9. T. Sanikidze, M. Shengelia, E. Chikvaidze, S. Kiparoidze, N. Gogebashvili, P. Kuppusamy. – *Current. Topics in Biophisics.*, **37**, 1-8 (2014).

The method of electron spin resonance in the evaluation of spin properties of scale and precipitation of natural waters

Alina A. Pichugina[1], Larisa V. Tsyro[1], Felix G. Unger[2]

[1]Institute of Natural and Technical Sciences, Surgut State University, Lenina avenue 1, Surgut, Russian Federation
[2] Chemical Faculty, National Research Tomsk State University, Lenina avenue, 36, Tomsk, Russian Federation
E-mail: tsyro_lv@surgu.ru
http://www.surgu.ru

Introduction

Scale deposits are solid formations that form when water is heated on the walls of heating appliances. In natural conditions, precipitation occurs during the evaporation of water. The formation of such deposits is associated with the presence of hardness salts in the water. Deposits can be of the carbonate type – these are calcium and magnesium carbonates; sulfate type – this is calcium sulfate; silicate type – these are silicic acid compounds of calcium, magnesium, iron, aluminum.

Scales are a weak conductor of heat, greatly reduce the thermal conductivity of boilers and cause unproductive fuel consumption, and also contribute to the intensive course of corrosion processes [1,2].

Scale formation is a complex physical and chemical process, the study of which is the possibility of solving the problem of hard water.

It is believed that scale is formed as a result of water heating due to the decomposition of calcium and magnesium bicarbonates into carbon dioxide and insoluble sediment. The physical structure of the resulting solid precipitates can be different – from an amorphous powder to a solid crystalline formation [3, 4].

It turned out that the scale and precipitation of water systems are characterized by an abnormally high concentration of unpaired electrons. This raises many debatable questions and requires in-depth research, because. compounds with unpaired electrons (free radicals) can hardly be attributed to electrolytic salts, which fit perfectly into the physicochemical laws of dissolution.

Research Methods

A dry sample, previously grounded into powder, was spilled into the ampoule tested for intensity, which was placed in the ESR spectrometer resonator (microwave field $\lambda = 3.2$ cm). The shooting spectrum conditions: the electromagnet field was changed in the range of 60-520 mT; the time of the magnetic field sweep was 42 s; the amplitude of the RF modulation was 0.25 mT; the sensitivity was selected. The sample resonant absorption of the microwave energy was recorded by an amplitude-digital converter on a computer. The obtained spectra were processed using a program that includes integration and calculation of the area under the integral curve. The area was measured in abstract units, which were then converted to the concentration of spin centers (SC). By the spin center (SC) we mean any particle, such as atomic or molecular system, among the spin orbitals (described by the wave function square), where there is such orbital (or there are such orbitals), which are inhabited by a single electron.

Results

Using the electron spin resonance (ESR) method, we undertook a study of the spin nature of scales obtained by prolonged heating of tap water from different regions of Tomsk and the Tomsk region, as well as the city of Vladivostok. For analysis, scale was taken, which

is formed directly in the heating system, namely in the distiller. For comparative analysis, scale samples obtained from filtered tap water and sediments obtained from water systems during freezing cleaning were also studied. Since frozen water is a structure in which there are regions with pure ice and regions with coagulated initial particles of the dispersed phase, during defrosting, particles larger than in the initial water are formed, which are capable of precipitation (sediments) [5].

Under the spin center we mean – any particle – such an atomic or molecular system in which there are electron shells that are not completely filled (an atom – there is no such thing for our system, free radicals, radical ions, transition metals, molecules in the triplet state). For the precipitates under consideration, these are transition metals, molecules in the triplet state.

Figure 1 shows typical ESR spectra of scales and sediments that have fallen out of the water during the freezing process. The position of the peaks of the ruby rods R_2 and R_3 on the spectra is characterized by the following g-factors: $g(R_2) = 2{,}6416$, $g(R_3) = 1{,}4844$, which were obtained by testing the instrument using a sample of Mn** in MgO with a known g-factor. Samples obtained without removal of soluble salts showed lower signal intensity.

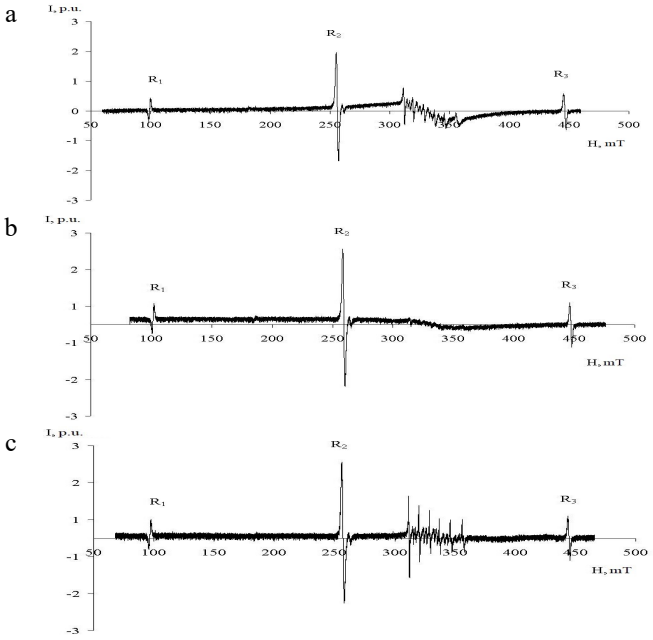

Figure 1. ESR spectra of scales from water: a – Cheremoshniki district; b – st. A. Ivanova; c – sediment obtained as a result of water purification from the Kirov region by freezing

The ESR spectra of scales and deposits are similar, which indicates the presence of SCs of the same nature in the studied samples. All the spectra obtained have a complex structure; in all cases, superposition of lines is observed.

In some spectra, 6 allowed lines are observed in the area between the peaks of the R_2 and R_3 ruby rods; sextet of hyperfine structure of atoms with nuclear spin 5/2.

Integration of the obtained differential curves indicates the presence of a broad line in all the studied samples, the area under which is quite large, which determines the high content

of SC. Note that for all the spectra obtained, the background was subtracted, which is due to the SC impurities in the materials from which the instrument's resonator and ampoule are made.

Comparative analysis of the table data showed that both in scales and in sediments obtained from filtered water, the concentration of SC is significantly lower than in samples obtained from unfiltered water. The concentration of SC was found to be high for scales formed directly in heating systems (distiller).

Table. The concentration of spin centers in scale and sediment samples obtained in the process of water freezing

Scale from water samples	$C_{SC} \cdot 10^{-20}$, spin/sm^3		
	1 area*	2 area*	amount
Tomsk, st. A. Ivanova	0,30	3,15	3,45
Tomsk, st. A. Ivanova, distiller	0,87	1,61	2,48
Vladivostok	0,33	1,07	1,40
Vladivostok, filter	0,34	0,92	1,26
Tomsk, Cheremoshniki district	0,78	5,90	6,68
Sediment from water samples	$C_{SC} \cdot 10^{-20}$, spin/cm^3		
	1 area*	2 area*	amount
Tomsk, Kirovsky district	0,33	2,08	2,41
Tomsk, Kirovsky district, filter	0,15	0,16	0,31
Tomsk, Akademgorodok	0,54	1,08	1,62
* 1 area – the area between R_1 and R_2; 2 area – the area between R_2 and R_3			

Taking into account the experimental fact that precipitation of "hardness salts" falling out of water systems has a spin nature, it can be stated that the formation of SC occurs in aqueous media with increasing temperature due to the formation of doublet states of thermally destructible dimers of radicals, because there are practically no SC in the water itself. Since SC are spin-uncompensated particles, in an aqueous medium, which is a diamagnet with fully compensated spin pairs, molecules with an unpaired electron and water molecules do not exchange interaction, and electronic repulsion leads to SC repulsion, that is, rejection from the water environment. Molecules containing SC are concentrated on the bottom, walls of the vessel, or on the surface of water, depending on their density, which is observed in experiments.

Ignoring broad lines in the ESR spectrum, the local intensity of which is small and sometimes barely noticeable, actually reflects a significant intensity of unpaired electrons in the substance under study, and therefore leads to errors in the interpretation of the spectrum. Only complete integration of the differential signal leads to a picture of a clear quantitative image of the total spin properties of the sample under study.

References

1. A. N. Shpagina, N. V. Kupriyanov, N. P. Dankov. – Water sector of Russia, 39 (3), 25-34 (2001).
2. P. R. Traube, A. G. Baranova. – Chemistry and microbiology of water (in Russian). – M.: Higher school, 1985.
3. M. I. Shahporonov. – Mechanisms of fast processes in liquids. Textbook for universities (in Russian). – M.: Higher school, 1980.
4. M. I. Shahporonov. – Introduction to the modern theory of solutions (in Russian). – M.: Higher school, 1976.
5. N. L. Lavrik. – Chemistry of Sustainable Development, 11, 863-867 (2003).

Application of NMR diffusometry for diffusion studies in plasticized polymeric membranes of ion-selective sensors

Nadezhda V. Pokhvishcheva[1], Andrey V. Kalinichev[1], Alexandr V. Ievlev[2], Maria A. Peshkova[1]

[1]Institute of Chemistry, Saint Petersburg State University, 26 Universitetskii prospect, 198504, Petergof, St. Petersburg, Russia
[2]Department of Nuclear Physics Research Methods, Saint Petersburg State University, 7/9, Universitetskaya nab., 199034, Saint Petersburg, Russia
E-mail: n.v.pokhvishcheva@gmail.com

Introduction

NMR diffusometry is a powerful tool for studying molecular mobility in various environments, and for determining diffusion coefficients for both neutral and charged species [1, 2]. In addition, this method makes it possible to understand the nature and number of molecules and ions involved in transport processes in a particular medium We report here on a new application area of NMR diffusometry, namely, plasticized polymeric membranes of ion-selective sensors.

There are two main types of such sensors: ion-selective electrodes (ISEs) and bulk optodes (ISOs). Typically, they are made of hydrophobic matrix components, e.g. polyvinyl chloride (PVC) or polymethyl methacrylate (PMMA), doped with a plasticizer (ether or esters) and a hydrophobic sensing chemistry. They sense ionic and neutral analytes in aqueous media. The response of ISEs and ISOs is determined by heterogeneous equilibria between the sample and the hydrophobic polymeric phase (sensor membrane); therefore, these sensors provide non-destructive analysis. The latter, along with ease of signal acquisition, a wide range of available analytes, and high selectivity, make ion-selective sensors promising analytical tools.

The response of ion-selective sensors is closely related to transport phenomena in both the aqueous and polymeric phases. For example, the signal of ion-selective optical sensors (optodes) is based on the following ion-exchange equilibrium [3]:

$$I^{+(aq)} + CH^{+(m)} + L^{(m)} \leftrightarrow IL^{+(m)} + C^{(m)} + H^{+(aq)}$$

where L is a neutral ligand capable of selective binding with the solution cation I^+; C is a hydrophobic pH-indicator; (aq), (m) denote aqueous and membrane phase, respectively. To obtain a stable signal, this equilibrium must be established throughout the entire sensor phase, which is essentially a 2-20 μm thick viscous polymeric film. Obviously, the sensor response time will be determined by the diffusion coefficients of all species involved in the process. In the case of ISEs, the diffusion rate is also responsible for the sensor detection limits, since the latter are determined by the transmembrane ion fluxes to/from electrode inner solution [4]. The transport of water microdroplets, and, in turn, their diffusion coefficients in the polymeric sensing phase regulate the rate of co-extraction of the solution electrolyte by the sensor membrane; and determine the signal stability of redox-sensitive polymeric sensors [5]. Chronopotentiometry with ion-selective membranes can be used to estimate the diffusion coefficients of charged carriers and their dissociation degree in the polymeric phase from the specific conductivity of the latter [6]. However, chronopotentiometry deals with the average diffusion coefficients of mobile charged species, meaning that the corresponding estimates may contain a significant error. The use of a different method for measuring diffusion coefficients would significantly benefit the accuracy of electrochemical studies.

The above also applies to a relatively new and highly promising type of sensors: polymeric membranes containing ionic liquids. The use of ILs in sensors has been extensively studied over the past decade, mainly due to their multifunctional performance. ILs can serve

as active sensor components, at the same time plasticizing the polymeric sensing phase [7]. The ionic liquids being used as plasticizers change the viscosity and polarity of the polymeric phase as compared to the traditional plasticizers. Therefore, the ILs can heavily affect the ionic distribution coefficients, the stability of ion-ligand complexes and the association/dissociation of ionic pairs in the sensing phase. Meanwhile, extensive NMR investigation of the transport and electrolytic properties of pure ILs and their mixtures with liquid solvents is being carried out [2, 8] providing the prerequisites for the successful study of ILs in the composition of the polymeric sensor phase.

Experimental results

One of the most commonly used ionic liquid 1 hexyl-3-methyl-1*H*-imidazol-3-ium bis[(trifluoromethyl)sulfonyl]amide ([C_6Meim][NTf_2]) was studied as a plasticizing component in binary bis(2-ethylhexyl)sebacate (DOS) ester-IL mixtures to plasticize PVC membranes. Its quantity was varied relative to the conventional DOS plasticizer: 26.9, 41.9 and 45.4 wt.% of [C_6Meim][NTf_2] in plasticizing mixture. The diffusion coefficients were estimated by means of pulsed field gradient stimulated echo with bipolar gradient (PFG STEb technique). ^{1}H and ^{19}F spectra of the membrane with 45.4 wt.% of IL in the plasticizing mixture recorded at different values of the gradient amplitude are shown in Fig. 1.

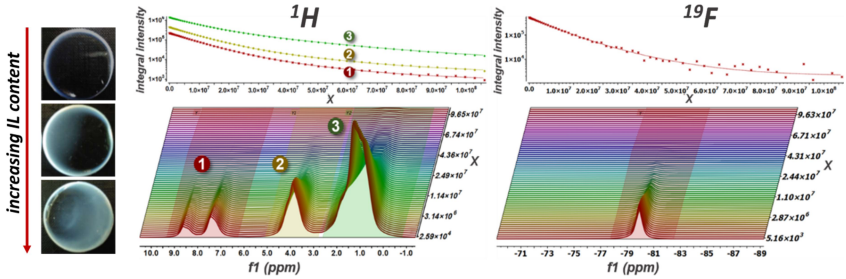

Figure 1. ^{1}H and ^{19}F spectra of the membrane with 45.4 wt.% of IL in the plasticizing mixture at different values of the gradient amplitude. Insets: the respective experimental (symbols) and fitted (lines) dependences of the integral intensity on the square of gradient amplitude (x). The photographs show PVC membranes doped with IL.

It was found that spectral lines for all the samples are strongly broadened due to the presence of PVC-DOS matrix. A double peak between 6 and 9 ppm characteristic for the protons of imidazole ring of IL cation, was observed in ^{1}H spectra. The intensity of this peak grows with an increase of IL load in the membrane. The remaining peaks overlap with the peaks of the plasticizer protons (3-5.5 ppm and -1-3 ppm). ^{19}F peak (-76 to -83 ppm) can be readily attributed to the fluorine-containing IL anion. In agreement with theoretical considerations, the integral intensity of this peak linearly increased with increasing IL content.

The respective dependences of the intensity on the gradient amplitude were fitted with modified Stejscal-Tanner equation: a superposition of the two decaying exponents.

$$I(x) = I_1 \exp(-D_1 x) + I_2 \exp(-D_2 x)\ ;\ \text{with}\ \ x = \gamma^2 G^2 \delta^2 \left(\Delta - \frac{\delta}{3}\right)$$

with D: the diffusion coefficient, I: the integral intensity, γ: the gyromagnetic ratio, G: the gradient amplitude, δ: the equivalent duration of the gradient pulses, and Δ: the time interval between the gradient pulses. Each of the obtained exponents contained a “fast”

component with a higher value of the fitting parameter D_1, and a "slower" impact with a lower value of D_2. The D_1 values obtained from the ^{1}H and ^{19}F spectra differ from each other and can be attributed to the diffusion coefficients of imidazolium cation and fluorine-containing anion, respectively. The "fast" component and the corresponding diffusion coefficient D_1 values required for successful fitting of $I(x)$ dependences for all three peaks in ^{1}H spectra (6-9 ppm, 3-5.5 ppm and -1-3 ppm, Fig. 1) coincided within the limits of error. The values of diffusion coefficients are shown in Fig. 2, along with the data obtained from chronopotentiometry (blue symbols). Diffusion coefficients D_2 for the second ("slow") component obtained for both cation and anion (green symbols in Fig. 2), are equal within the margin of error and are almost an order of magnitude lower than the ionic diffusion coefficients (red symbols). This result may indicate that some amount of the IL diffuse in a form of an ion pair.

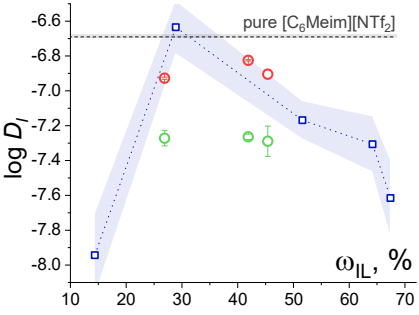

Figure 2. Dependence of mean diffusion coefficient (D_1) of charge carriers in the membrane vs. IL content. Blue: D_1 from chronopotentiometry; red and green: D_1 from NMR diffusometry for ionic species and ion pair, respectively. Grey line – D_1 for pure IL.

The mean values of ionic diffusion coefficients obtained by NMR are in good agreement with the values estimated using chronopotentiometry. Both methods suggest the non-monotonic dependence of the diffusion coefficient versus IL content in the polymeric phase: the mean D_1 goes through a maximum between 20 and 40 wt.% of IL in the plasticizing mixture. The value of mean diffusion coefficient, found for the membranes with ca. 30 wt.% of IL in the plasticizing mixture, reaches $2.3 \cdot 10^{-7}$ cm^2/s, which is slightly higher than our estimate for pure IL (ca. $2 \cdot 10^{-7}$ cm^2/s).

Based on the obtained results, we can conclude that NMR diffusometry is a functional instrument for exploration of transport phenomena in polymeric ion-selective membranes. By varying the relative content of IL in the polymeric phase, one can tune the properties of sensing PVC membranes, namely, their viscosity and polarity. The observed dependences pave the way for further explanation of the effect of ILs on the response of polymeric ion-selective sensors.

Acknowledgements

This work was funded by the Russian Science Foundation, project number 20-73-10033.

References

1. W.S Price. – *Concepts Magn. Reson.*, *10*, 197–237 (1998)
2. T Umecky, Y Saito, H. Matsumoto. – *ECS Trans*., 25, 23–29 (2019)
3. E. Bakker, P. Bühlmann, E. Pretsch. – *Chem. Rev*., 97, 3083-3132 (1997)
4. Z. Szigeti, T. Vigassy, E. Bakker, E. Pretsch. – *Electroanalysis*, 18, 1254-1265 (2006)
5. A.P. Thoma, A. Viviani-Nauer, S. Arvanitis, W.E. Morf, W. Simon. – *Anal. Chem*., 49, 1567–1572 (1977)
6. K.N. Mikhelson, V.M. Lutov, K. Sulko, O.K. Stefanova. – *Sov. Electrochem*., 24, 1369 (1988)
7. N. V. Shvedene, D. V. Chernyshov, I. V. Pletnev. – *Russ. Chem. J*., LII, 80–91 (2008)
8. H. Tokuda, S. Tsuzuki, M.A.B.H. Susan, K. Hayamizu, M. Watanabe. – *J. Phys. Chem. B*, 110, 19593–19600 (2006)

Regio-isomers of 2,5,6,7,8-pentaaryl-1*H*-azepino[3,2,1-*ij*]quinazoline-1,3(2*H*)-dione containing various aryl substituents in the azepine ring: structures determination using NMR methods

Julia A. Pronina[1], *Darya D. Komolova*[2], *Alexander V. Stepakov*[2], *Stanislav I. Selivanov*[2]

[1]*Saint-Petersburg State Institute of Technology (Technical University), Moskovsky prospect 26, 190013, Saint-Petersburg, Russia*
[2]*Institute of Chemistry, State University of Saint-Petersburg, University prospect 26, 198504, Saint-Petersburg, Russia*
E-mails: [1]*pronina.iuli05@ yandex.ru;* [2]*nmr.group.spbu@gmaill.com*

Introduction

At present, the development of NMR approaches to simplify and facilitate the analysis of complex ^{1}H NMR spectra in solution of individual chemical compounds and/or their multicomponent mixtures is one of the main practical directions. They are associated with the success of NMR spectroscopy in the structural and conformational analysis of both large bioorganic molecules [1] and relatively small molecules [2, 3] and/or mixtures thereof [4, 5]. All the developed NMR-methodologies can be broadly classified into two groups: (**a**) the experimental techniques to derive additional information for subsequent analyses of complex ^{1}H spectra and (**b**) methods to simplify the complexity of the spectra amenable for easy analyses [6].

*In practice, to solve specific problems of ^{1}H NMR spectrum analysis a set of auxiliary methods belonging to both (**a**) and (**b**) groups is used. At the same time, the preference (at least at the initial stage) is given to those of them that have passed many-sided practical testing and/or are the most accessible and inexpensive. However, this cannot always guarantee their efficiency, which was previously demonstrated in the analysis of other complex proton spectra obtained even for structurally close compounds. In such cases, it is necessary to collect information from the results of applying several homo- and heteronuclear experiments and draw final and unambiguous conclusions about the identification of signals based on a comparison of these results with each other. Moreover, you also need take into account all the possibilities and limitations of each of the experiments used.*

*In this work we used some different NMR methods to analyze a mixture of some structurally similar regio-isomers of 1*H*-azepino[3,2,1-*ij*]quinazoline-1,3(2*H*)-dione (**3**) formed as a result of the palladium-catalyzed reaction 3-phenylquinazolin-2,4(1*H*,3*H*)-dione (**1**) with 1-methoxy-4-(phenylethynyl)benzene (**2**) because these isomers cannot be isolated from the reaction mixture and studied individually (Figure **1**).*

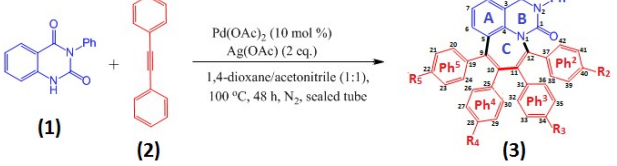

Regio-isomers	(3a)	(3b)	(3c)	(3d)
R^2	OMe	H	H	OMe
R^3	H	OMe	OMe	H
R^4	H	H	OMe	OMe
R^5	OMe	OMe	H	H

*Figure **1**. Sheme of reaction and structures of regio-isomers (**3a**), (**3b**), (**3c**) and (**3d**) (Numbering of rings and some atoms are shown by figures).*

It should be noted that the studied compounds (**3**) may be of interest as fluorescent systems for materials science research [7].

Experiments and results

This report presents the results of studying the ^{1}H NMR spectrum of a mixture of two regio-isomers (**3**) in order to prove the structure of each of them. In the aromatic region of this spectrum, there are multiplet signals of 10 phenyl rings, four of which have a methoxy group in the para-position. Thus, the proton spectrum in the region 6.5–7.2 ppm contains 46 proton signals that must be identified both in terms of belonging to one of the isomers, and by belonging to a certain position in each of them. The structural similarity of regio-isomers, as well as the slight difference in their populations P_i (P_1:P_2 ≈ 56:44) make the task of complete identification rather difficult. Therefore, additional methods for simplifying the ^{1}H spectrum were used with the help of the J-COSY, COSY-90, NOESY, HSQC, HMBC, and COLOC experiments. Figure **2** shows fragments of the first two of them used to analyze the easy-to-identify signals of protons H6, H7, and H8. Each of them has a "doubled" multiplet structure, which are easily detected in both J-COSY (Fig. **2a**) and COSY-90 (Fig. **2b**) spectra due to the simultaneous decomposition into chemical shifts of individual multiplets in the first case and change in the position of cross peaks along two frequency coordinates in the second case.

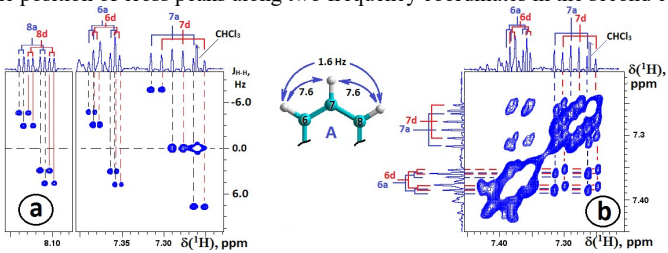

*Figure 2. Fragments of spectra **a)** J-COSY and **b)** COSY-90 for mixture of two regio-isomers of (**3**) in $CDCl_3$, which help us to determine multiplete structure of proton signals H6, H7 and H8. Signals for main and minor regio-isomers are depicted with blue and red color, respectively.*

These results were used to establish the ownership of all other signals. For example, the spatial interaction (NOE) between the H6 proton and the doublet signal of one of the ortho-protons (at 6.87 ppm) proves (Fig. **3a**) that the Ph^5 ring in the main isomer is para-substituted (R_5 = OMe). The presence of cross-peak (20,24/26,30) between the ortho-protons (at 6.97 ppm) of the unsubstituted Ph^5 ring (R_5 = H) in the minor isomer and the ortho-protons (at 6.75 ppm) of the adjacent substituted Ph^4 ring (R_4 = OMe) gives strong there are reasons to believe that the main and minor regio-isomers differ from each other due to the replacement of the Ph^5 and Ph^4 rings with each other. At the same time, in the proton spectrum of main and minor isomers almost identical values of chemical shifts of ortho- and meta-protons of the second substituted and unsubstituted ring are observed, as well as complete coincidence of the corresponding chemical shifts of ^{13}C nuclei (Fig. **3c**) at 131.05 ppm for the ortho-carbons of the para-substituted rings and at 130.64 ppm for the unsubstituted rings. In addition, one should take into account the absence in the NOESY spectrum of cross peaks between the signals of the H8 proton at 8.12 ppm and the ortho-protons of the unsubstituted rings of the main region-isomer, which are in the region of 6.78–6.85 ppm, and the presence of a cross peak between the signals of the H8 protons and ortho-protons of the para-substituted rings of the main and minor regio-isomers at 6.92 ppm (see Fig. **3a** and **3b**). Only one possibility satisfies all these experimental requirements (see the table in Fig. **1**): the main regio-isomer is (**3a**), and the minor one is (**3d**).

The conclusion made about of the isomer structures is in good agreement with all other data, including differences in the chemical shifts of both protonated and quaternary ^{13}C atoms.

The most significant of them can be considered the simultaneous "opposite" change in $\Delta\delta(^{1}H)$ and $\Delta\delta(^{13}C)$ for

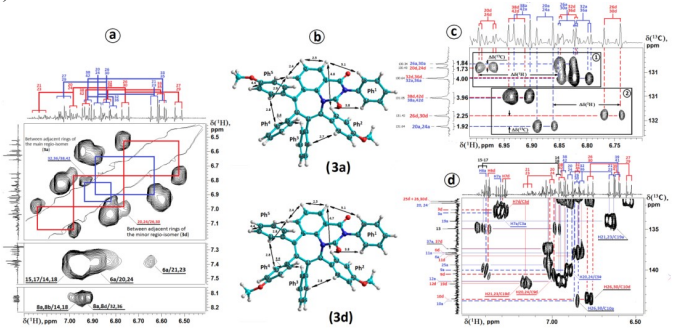

*Figure 3. Fragments of spectra **a)** NOESY, **c)** HSQC and **d)** HMBC for mixture in $CDCl_3$ of two regio-isomers **(3a)** and **(3d)**, which are shown in **b)** by using MM2 structure optimization (arrows indicate interproton distances in Å). All signals in 1D and 2D spectra for main **(3a)** and minor **(3d)** regio-isomers are depicted with blue and red color, respectively. In ^{1}H NMR spectrum of **a)** through space interactions (NOEs) between protons are shown by blue and red solid lines for each isomer.*

the *ortho*-positions of these nuclei in the rings Ph^4 and Ph^5 during the transition from regio-isomer (**3a**) to isomer (**3d**). Chemical shift changes of proton and carbon signals for these isomers are shown in rectangles "**1**" and "**2**" for pairs of ^{1}H-^{13}C nuclei *ortho*-located in Ph^4 and Ph^5 group, relatively (Fig. **3c**). Moreover, the NOESY spectrum (Fig. **3a**) demonstrates cross peaks between the signals of *ortho*-protons H32,36 and H38,42, confirming the proximity of adjacent rings Ph^2, Ph^3 in isomer (**3a**).

Conclusion

Using various homo- and heteronuclear NMR experiments (J-COSY, COSY-90, NOESY, HSQC, HMBC and COLOC), a complete identification of signals in the ^{1}H and ^{13}C NMR spectra was made for a mixture of two regio-isomers of 2,5,6,7,8-pentaaryl-1*H*-azepino[3,2,1-*ij*]quinazoline-1,3(2*H*)-dione containing various aryl substituents in the azepine ring and their ratio (56:44) was determined with an accuracy of no more than ± 2%. An analysis of all the NMR-data, including scalar and through space dipole-dipole interactions, made it possible to obtain a reliable proof of structures of both regio-isomers without usual separation from the mixture.

Acknowledgments

NMR experiments were performed on spectrometer DPX-300 (Bruker) in the Resource Center "Magnetic Resonance Research Centre" of the Saint-Petersburg State University.

References

1. D. P. Frueh. Progress in NMR Spectroscopy 2014, 78, 47–75.
2. W.F. Reynolds, R.G. Enriquez. J. Nat. Prod., 2002, 65, 221–244.
3. M. Jaeger, R.L.E.G. Aspers. Ann. Rep. NMR Sp-py, 2012, 77, ch. 3, 115–258.
4. M. Tiainen, P. Soininen, R. Laatikainen. J. Magn. Reson., 2014, 242(1), 67–78.
5. A. Verma, B. Baishya. J. Magn. Reson., 2016, 266(1), 51–58.
6. B. Baishya, U.R. Prabhu, N. Suryaprakash. Ann. Rep. NMR Sp-py, 2009, 67, ch. 4, 331–423.
7. H.-R. Pan, X.-R. Wang, C.-X. Yan et al. Org. Biomol. Chem., 2011, 9, 2166–2174.

Demonstration of the targeted breast MRI concept at 1.5 T

Viktor Puchnin[1], Anna Hurshkainen[1], Georgiy Solomakha[1], Anton Nikulin[2], Aigerim Jandaliyeva[1], Alexander Efimtcev[1,3], Anna Andreychenko[1,4] and Alena Shchelokova[1]

[1] Faculty of Physics, School of Physics and Engineering, ITMO University, Saint Petersburg, Russian Federation
[2] Department for Biomedical Magnetic Resonance, University of Tübingen, Tübingen, Germany
[3] Department of Radiology, Federal Almazov North-West Medical Research Center, Saint Petersburg, Russian Federation
[4] Research and Practical Clinical Center of Diagnostics and Telemedicine Technologies, Department of Health Care of Moscow, Moscow, Russian Federation
E-mail: viktor.puchnin@metalab.ifmo.ru

Introduction

The targeted breast magnetic resonance imaging (MRI) concept based on a high-permittivity ceramic resonator [1,2] or an array of strongly coupled split-loop resonators [3,4] could be potentially used for breast cancer screening purposes. Such an opportunity arises from the fact that targeted MRI allows one to focus the imaging ability of magnetic resonance (MR) scanner on the breast, which entails improving the quality of the MR images obtained without specialized dedicated coils up to the level achieved with these additional local coils. These resonators inductively couple to the whole-body birdcage coil focusing its magnetic flux in the region of interest (ROI), thus improving the birdcage coil's transmit efficiency and receive performance. In addition, improving the RF safety provided by these wireless devices can reduce signal acquisition time and safe in vivo application of energy-intensive sequences with high-amplitude RF pulses [5,6] necessary to provide various specialized functional contrasts. This work demonstrates a quadrature metamaterial-inspired wireless coil for bilateral breast imaging and studies its efficiency and diagnostic capabilities via numerical simulations and in vivo experiments at 1.5 T.

Methods

All numerical studies were conducted in CST Microwave Studio 2021. We used a whole-body birdcage coil tuned and matched the operating frequency of 63.68 MHz (1.5 T) to excite the electromagnetic field. The coil was loaded with a voxelized female model. Two setups were compared: birdcage coil without (Fig.1 a) and with (Fig.1 b) a wireless breast coil based on metamaterials. The wireless coil consisted of a pair of two volumetric resonators: an array of split-ring resonators and a Helmholtz resonator. The first type includes 10 split-rings resonators (160×135 mm^2) containing two parallel telescopic brass tubes connected by two capacitors at their ends. The capacitors are implemented as the copper strips printed on the top and bottom layers of the dielectric substrate (Rogers RO4250B material) with ε=3.5, tan δ=0.0004. Each Helmholtz resonator consists of connected pair of three turns of copper wire forming three loops. Both types of volumetric resonators were tuned to 63.68 MHz. The considered structures have orthogonal linear polarizations of the RF magnetic field. The combined coil allows obtaining quadrature polarization. MRI experiments were performed on a 1.5 T Siemens MAGNETOM Espree clinical system at Federal Almazov North-West Medical Research Centre with a healthy volunteer. To estimate the effectiveness of the wireless breast coil in terms of the signal-to-noise (SNR), we acquired the reference images using the spine coil (Spine matrix coil, Siemens). All MR experiments with wireless coil were performed only after a precise RF power calibration procedure, ensuring that input power was within RF safety limits. In the case of using a clinical coil, the signal transmission was carried out by a birdcage coil and reception by S1-S2 segments of the spinal coil. The signal was

received and transmitted using a birdcage coil when using a quadrature wireless coil. MR images were acquired using a T1-weighted, 3D GRE sequence: flip angle=12^0, TR/TE=10.5/4.8 ms, voxel size=0.8×0.8×0.8 mm^3, acquisition matrix=224×224×256 pixels.

Results

Figure 1 shows the distributions of the transmitting RF magnetic field component B_1^+ and specific absorption rate (SAR) averaged over 10g ($SAR_{av.10g}$) without and with the proposed wireless coil, correspondingly. The B_1^+-field and SAR distributions were normalized to 1 W of the total accepted power. The strong localization of the B_1^+ field in the breast area in the presence of the resonator led to a 9.7-fold enhancement in transmit efficiency (Fig. 1 c, d). At the same time, the local maximum of $SAR_{av.10g}$ in the body model is 3 times higher in the presence of the resonator (Fig.1 e, f). However, the maximum local $SAR_{av.10g}$ for the same B_1^+=0.3μT in the ROI becomes 32 times lower with the wireless coil since the required power was reduced from 1W to 0.011W. It means that the proposed wireless breast coil makes MR examination safer than with the birdcage coil used alone in terms of SAR.

The results of in vivo scanning are presented in Fig. 2. In the case of using a wireless breast coil, the transmit efficiency increased by 7.7 times. The strong localization of the B_1 field in the ROI also led to a 2.5-fold higher SNR in comparison with the spinal coil.

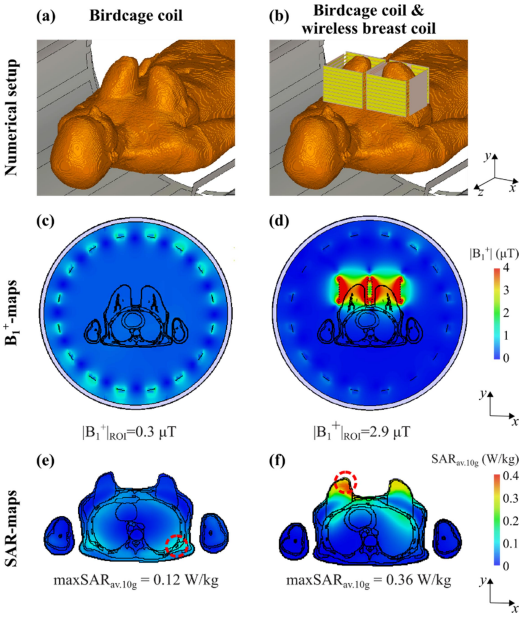

Figure 1. (a,b) Schematic view of the numerical setups for a female voxel model placed inside the birdcage coil without (left) and with (middle and right panels) the wireless coil. (c,d) Numerically calculated B_1^+ maps (in the transverse plane). The mean value of the B_1^+-field was calculated in the breast area. (e,f) Numerically calculated $SAR_{av.10g}$ maps.

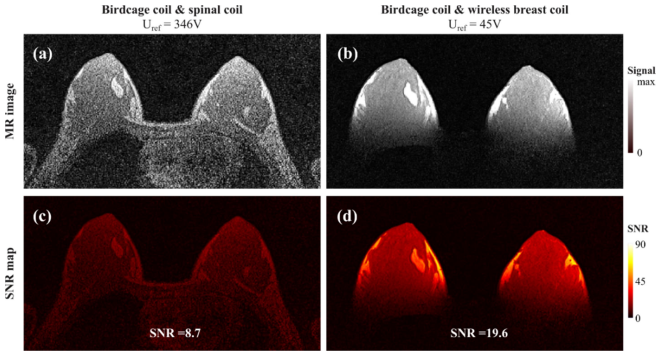

Figure 2. In vivo MR images (top row) and SNR maps (bottom row) for two setups: the birdcage coil used in transmit mode and spinal coil used for receiving MR signal (a,c) and the birdcage coil combined with wireless breast coil used in both regimes (b,d).

Discussion and conclusion.

The proposed wireless coil made it possible to increase transmit efficiency greater than previously presented designs based on high-permittivity ceramics and metamaterial-inspired structures [1-3]. This is due to using a quadrature-polarized structure that induces an RF magnetic field rotating similarly to the field in the birdcage coil. Since the metamaterial-inspired wireless coils are much cheaper and easier to manufacture than commercially available coils, the usage of such devices can make targeted MRI much more accessible to a wide range of people. In addition, wireless coils can be used without software modification and with most types of MR scanners, including on outdated models. The limitation of the proposed design is the inhomogeneity of the B_1^+ field across the breast. Another drawback is the absence of a signal from the axillary region essential for diagnosis. The usage of advanced pulse sequences and extension of the resonant element's dimensions can improve the quality of the obtained MR images by increasing the uniformity of the transmitting RF magnetic field and field of view correspondingly.

Acknowledgments

This work was supported by the grant of the Russian Science Foundation (Project № 18-75-10088).

References

1. A. Shchelokova et al., “Ceramic resonators for targeted clinical magnetic resonance imaging of the breast”, Nat Commun 11, 3840, 2020.
2. Viacheslav Ivanov et al., “Coupled very-high permittivity dielectric resonators for clinical MRI”, Appl. Phys. Lett. 117, 103701, 2020
3. Viktor Puchnin, et al., “Metamaterial inspired wireless coil for clinical breast imaging”, Journal of Magnetic Resonance, 322:106877, 2021
4. Viktor Puchnin et al., “Comparison of different wireless coils for 1.5 T bilateral breast MRI”, 1, 012116, 2021
5. Sebastian Bickelhaupt et al., “Fast and Noninvasive Characterization of Suspicious Lesions Detected at Breast Cancer X-Ray Screening: Capability of Diffusion-weighted MR Imaging with MIPs”, Radiology, 278, 3: 689-697, 2016
6. Zhang, S. et al., “CEST-Dixon for human breast lesion characterization at 3 T: A preliminary study”, Magn. Reson. Med, 80: 895-903, 2018.

Methodology for determination of contrast agent relaxivity using MRI

Israel Reyes Molina[1], Armando J. Hernandez Rodriguez[1], Carlos A. Cabal Mirabal[1], Evelio R. González Dalmau [1]

[1]Magnetic Resonance Imaging Department, Cuban Centre for Neuroscience, Havana, Cuba
E-mail: israel@cneuro.edu.cu

Introduction

The MRI represent a powerful method because its non-invasiveness, high spatial resolution and contrast and the possibility to obtain quantitative information regarding dynamic processes. However, it has a relatively low sensitivity. The use of exogenous contrast agents (CA) (paramagnetic and superparamagnetic) makes possible to partially overcome this disadvantage.

The efficiency of the CA can be characterized by the relaxivity (longitudinal r1 and transverse r2). Higher relaxivity allow the greatest contrast enhancement. Moreover, higher relaxivity permit lower dose at same the contrast concentration, lowering the CA toxicity[1].

Generally, the relaxivity is measured by NMR relaxometers, yet, there is an increasing trend to use MRI scanners for this purpose [2,3]. This approach has the advantage that the CA characterization is carried out under the same equipment (field strength, RF coil configuration, pulse sequences, etc.) where they will be employed. Nevertheless, several sources of errors need to be taken into account such as: 1) Different contribution on the MR signal of the relaxation rates ($\frac{1}{T_{1,2}}$), and diffusion coefficient ($\vec{D}$) to image weighting. 2) Minimum TR and TE values attainable by the scanner, 3) Signal-to-noise ratio (SNR), 4) RF field homogeneity, 5) Susceptibility effects 6) Sample temperature stability among others.

In this work these restrictions are briefly discussed and taken into account in a methodology for relaxivities determination by MRI.

Relaxivity dependence.

The observed relaxation rate depends linearly of CA concentration, assuming a fast exchange between the inner sphere of the paramagnetic or superparamagnetic center (P/S-magnetic) and the free water:

$$\left(\frac{1}{T_{1,2}}\right)_{obs} = \left(\frac{1}{T_{1,2}}\right)_{dia} + r_{1,2}[\mathrm{C}A] \qquad (1)$$

Here, the first term of the right member corresponds to the relaxation rate of the diamagnetic states. The second member correspond to the P/S-magnetic contribution, being [CA] the concentration and $r_{1,2}$ the relaxivity. Relaxivities $r_{1,2}$ depends on field strength, correlation times of the magnetic interactions and temperature. The linear relationship expressed by equation is more complex in vivo [4].

MRI experimental setup.

Relaxation time calibration using phantom. To validate a methodology a phantom consisting of CA solutions with known T_1 and T_2 values (previously determined by NMR relaxometry) at different concentrations is necessary. The T_1 and T_2 of the solution should match with the relaxation times range of the tissues under examination.

Pulse sequences for relaxation times determination. Relaxation times are determined using spin-echo sequences (SE) for T_1, T_2 and inversion-recovery spin-echo sequences (IR-SE) for T_1. The main reason behind its widely extended use lies in its precision [5].

The general signal equation for each pixel in a MR image in a SE can be expressed as:

$$S(\mathrm{x},\mathrm{y}) = S_0(\mathrm{x},\mathrm{y})(1 - A(\mathrm{x},\mathrm{y})e^{-\frac{TR}{T_1(\mathrm{x},\mathrm{y})}})e^{-\frac{TE}{T_2(\mathrm{x},\mathrm{y})}}e^{-\vec{b}\bullet\vec{D}} \quad (2)$$

As no diffusion sensitizing gradient is applied, the last exponential factor can be discarded. The parameters TR and TE can then be adjusted to separate the contribution of each relaxation time.The T_1 measurement error is affected by the minimum TE and TR attainable by the MRI equipment. For T_1 measure TR is varied while keeping TE minimum. For a T_2 measurement TE is varied and TR is chosen as to fulfil $TR \approx 5T_1$, minimizing T_1 weighting.

In the case of the IR-SE method the expression (2) become to be the formula (3):

$$S(\mathrm{x},\mathrm{y}) = S_0(\mathrm{x},\mathrm{y})(1 - A(\mathrm{x},\mathrm{y})\,\mathrm{e}^{-\frac{TI}{T_1(\mathrm{x},\mathrm{y})}}) \quad (3)$$

Where $A(\mathrm{x},\mathrm{y}) = 1 - \cos\theta(\mathrm{x},\mathrm{y})$, TI is the inversion time and θ(x,y) is the inversion angle. This parameter is introduced to take into account the imperfections in the 180 degrees pulse as a consequence of the RF inhomogeneity.

Some experimental restrictions:

- **RF field inhomogeneity:** The RF map of a homogeneous phantom make possible the RF inhomogeneity compensation. If two images are acquired, with flip angles related by $\theta_2 = 2\theta_1$, and the flip angle distribution is obtained by a S_2/S_1 signal ratio:

$$\theta(\mathrm{x},\mathrm{y}) = \gamma\int_0^{t_p} B_1(\mathrm{x},\mathrm{y})\,\mathrm{d}\,\tau = \arccos\left(\frac{S_2(\mathrm{x},\mathrm{y})}{2S_1(\mathrm{x},\mathrm{y})}\right) \quad (4)$$

- **Signal to Noise Ratio (SNR):** Likewise, SNR can be determined and controlled using a homogenous phantom. Measuring the mean value of the signal in a region of interest (ROI) in the phantom and the standard deviation of the signal in a ROI in the background, the SNR can be calculated as:

$$SNR = 0.655\frac{mean(\mathrm{S}_{phantom})}{std(\mathrm{S}_{background})} \quad (5)$$

- **Susceptibility effects** A ROIs in the CA samples should be selected away from its boundaries where anisotropy of susceptibilities and partial volume effects are accentuated. The different samples of the CA must be placed at a distance of at least one diameter away from each other to diminish the mutual influences of the adjacent samples.

- **Temperature.** The temperature must be monitored throughout the duration of the experiment.

Software Workflow

The methodology was implemented as a MATLAB 2014a toolbox. The procedure to calculate the relaxivities using MR images encompass several sequential steps enumerated below:

1. Automatic handling of raw DICOM files
2. Region of Interests (ROI) selection corresponding to images of CA sample solutions.
3. Calculation of mean and standard deviation from each ROI at the different time points.
4. Estimation of relaxation times using Levenberg-Marquardt algorithm.

5. Determination of relaxivities through linear regression.

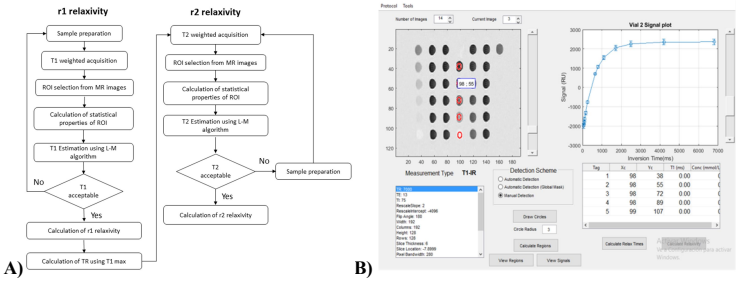

Figure 1 A) Algorithmic depiction of the steps involved in the determination of the relaxivity r_1 and r_2. B) Toolbox GUI with different visualization capabilities.

References

1. M. Rohrer, H. Bauer, J. Mintorovitch, M. Requardt, and H. J. Weinmann, "Comparison of magnetic properties of MRI contrast media solutions at different magnetic field strengths," *Invest. Radiol.*, vol. 40, no. 11, pp. 715–724, 2005, doi: 10.1097/01.rli.0000184756.66360.d3.
2. S. Arsalani *et al.*, "Aqueous paramagnetic solutions for MRI phantoms at 3 T: A detailed study on relaxivities," *Invest. Radiol.*, vol. 275, no. 3, pp. 2108–2121, 2017, doi: 10.3906/elk-1602-123.
3. G. Knobloch *et al.*, "Relaxivity of Ferumoxytol at 1.5 T and 3.0 T," *Invest. Radiol.*, vol. 53, no. 5, pp. 257–263, 2018, doi: 10.1097/RLI.0000000000000434.
4. M. M. J. Modo and J. W. M. Bulte, *Molecular and cellular MR imaging*. CRC Press, 2007.
5. R. W. Brown, Y.-C. N. Cheng, E. M. Haacke, M. R. Thompson, and R. Venkatesan, *Magnetic resonance imaging: physical principles and sequence design*. John Wiley & Sons, 2014.

Experiments with ultra-cold atomic hydrogen

Semakin Aleksei, Otto Hanski, Janne Ahokas, Sergey Vasiliev

Wihuri Physical Laboratory, Physics and Astronomy department, University of Turku, 20014 Turku, Finland
E-mail: assema@utu.fi
http://hturku.utu.fi

Introduction

Experimental studies of properties of H are always of prime importance because of the possibility to calculate them theoretically from the first principles. As it is the simplest of atoms, H has played a key role in revealing and testing fundamental laws of physics. Studies of optical spectra led to Bohr theory of the atom. The discovery of Lamb shift [1] provided foundations of Quantum Electrodynamics (QED). The H maser [2] served for many decades as the frequency standard. Being the lightest of atoms hydrogen has an advantage in view of possible experimental studies of quantum effects. Experiments with gravitational states of ultracold neutrons opened a new way for studies of fundamental properties of matter and gravity [3], and similar experiments are suggested for atomic hydrogen and antihydrogen [4, 5]. Recent developments in production and cooling of antihydrogen in CERN demonstrate that such experiments are realistic in the nearest future. Although, there is no reason to expect that gravitational properties of antimatter differ substantially from that of the matter, observation of even a small difference would have a strong impact on our fundamental understanding of nature.

Gravitational Quantum States(GQS)

Earth gravity and quantum reflection from the surface created a vertical angular potential. According to quantum mechanics of atomic motion in a such potential, there are stationary states with characteristic energies of ~1 peV localized at the distance of a few tens of microns from the surface. GQS were first observed at ILL in Grenoble when measuring transmission of ultra-cold neutrons (UCN) through a gap between reflective and absorbing plates [6, 7]. Later experiments on Gravitational Resonance Spectroscopy (GRS) of UCN provided the first values of the energy intervals between low-lying states [8]. Since the masses of H and neutron are almost equal, they should have similar GQS.

In contrast to neutrons, atoms have non-zero polarizability and van der Waals/Casimir-Polder interaction with surfaces. This attractive interaction is responsible for quantum reflection of atoms. Theory predicts small shifts of the GQS energy levels dependent on the actual details of the interaction. Accurate measurements of the GQS energies and comparison with theory may reveal existence of unknown short-range forces (SRF) acting at the characteristic distance of several tens of microns [9]. For H on liquid helium the interaction is much weaker than on solids and the shifts are smallest [10], which makes the H-He system most sensitive for the search of the SRF. Several constraints on possible effects beyond the SM were made from neutron GRS, which reached the resolution of 10^{-14} eV [11]. Due to the high reflectivity of helium surface, hydrogen atoms have longest life-time in the GQS which yields the best resolution and sensitivity to the SRF effects.

The 50-100 Hz linewidths of transitions in GRS experiments with neutrons were determined by the 50 ms flight time of the 6 m/s neutron beam through the 30 cm wide interaction region. In our experiments H atoms will be two orders of magnitude slower and the interaction time will increase accordingly. We also suggest an experiment with H atoms trapped above the reflecting surface in radial direction. In this case, the life-time of the GQS due to non-ideal quantum reflection or sticking to the surface will limit the GRS resolution. The lifetime of H in GQS on liquid helium is expected to be in the range 1-10 s [12, 13], leading to

sub-Hz linewidths of GRS transitions. Another advantage of H over neutrons is a much higher phase space density available. Several orders of magnitude larger particle fluxes can be obtained for ultra-cold H atoms than for UCN [14]. This will improve the signal-to-noise ratio in GRS and further enhance the resolution.

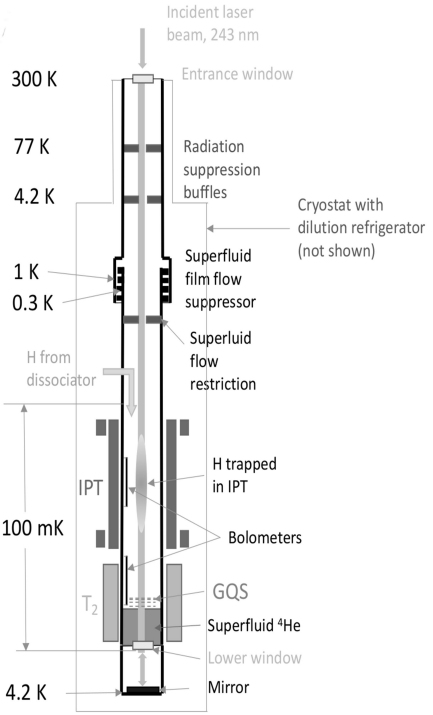

Figure 1. Scheme of precision 1S-2S spectroscopy and observation of GQS

Precision spectroscopy of H

An essential limitation of any spectroscopy is the presence of velocity dispersion of the atoms. Since the advent of tuneable lasers and methods of Doppler-free spectroscopy in the 1970s, the optical spectroscopy of H has been renewed. Consequently, the frequency of the 1S-2S interval is now known with a fractional accuracy better than 10-14 [15].

Trapping and evaporative cooling of atomic hydrogen by the MIT group [16] to temperatures below 1 mK offered a chance for high precision spectroscopy. The density of atoms was so large that the frequency shift caused by atomic collisions (so-called clock shift) rendered the measurements of the two-photon 1S-2S transition comparatively imprecise. In addition, the UV laser system used had a relatively large spectral width and low power.

Reaching a natural linewidth NLW of ~1.3 Hz for the 1S-2S transition is an ambitious goal for ultrahigh-resolution spectroscopy. Progress in the laser technology allows nowadays reaching the laser linewidth close to 1 Hz [17, 18]. Using such a state-of-the-art light source for studies of ultra-slow atoms, we will push the 1S-2S H spectroscopy to the NLW level. The total estimated uncertainty due to systematic effects was estimated to be at the level of 0.02 Hz for atoms at 1 mK. Since we are planning to work at much lower temperatures with large

numbers of atoms, this level seems plausible to be reached. The absolute accuracy will be limited by the precision of the frequency standard available for the project. For our location in Turku the best solution is to use a GPS clock and an active local reference (Cs or hydrogen maser) using a frequency comb for laser locking. Accuracy of approaching 10-15 can be reached using such a system.

Acknowledgements

This work is supported by the Culture Foundation Varsinais-Suomi Regional Fund (grant #85211894), Antti ja Jenny Wihuri Foundation, academy of Finland grant No. 317141.

References

1. W.E. Lamb et al, Fine structure of the hydrogen atom, Phys. Rev. **79** (1950) 549;
2. D. Kleppner et al, Theory of the hydrogen maser, Phys. Rev. **126,** 603 (1962);
3. V.V. Nesvizhevsky et al, Nature **415** (2002) 297;
4. GBAR Collaboration, CERN: https://home.cern/science/experiments/gbar ;
5. S. Vasiliev et al., Hyperfine Interactions, **240**, 14 (2019);
6. V. V. Nesvizhevsky et. al., Quantum states of neutrons in the Earth's gravitational field, Nature 415, 297 (2002);
7. V.V. Nesvizhevsky et al., Measurement of quantum states of neutrons in the Earth's gravitational field, Phys. Rev. D 67, 102002 (2003);
8. G. Cronenberg, Acoustic Rabi oscillations between gravitational quantum states and impact on symmetron dark energy, Nature Physics 14, 1022 (2018);
9. A. Yu. Voronin, P. Froelich, and V. V. Nesvizhevsky, Gravitational quantum states of Antihydrogen, Phys. Rev. A 83, 032903 (2011);
10. P.-P. Crepin et al., Quantum reflection of antihydrogen from a liquid helium film, Europhys. Lett. 119, 33001 (2017);
11. G. Cronenberg, Acoustic Rabi oscillations between gravitational quantum states and impact on symmetron dark energy, Nature Physics 14, 1022 (2018);
12. P.-P. Crepin et al., Quantum reflection of antihydrogen from a liquid helium film, Europhys. Lett. 119, 33001 (2017);
13. I. A. Yu et al., Evidence for Universal Quantum Reflection of Hydrogen from Liquid ^{4}He, Phys. Rev. Lett. 71, 1589 (1993);
14. S. Vasiliev et al., Gravitational and matter-wave spectroscopy of atomic hydrogen at ultra-low energies, Hyperfine Interact., 240, 14 (2019)
15. A. Matveev et al., Precision Measurement of the Hydrogen 1S-2S Frequency via a 920-km Fiber Link Phys. Rev. Lett 110, 230801 (2013);
16. D. G. Fried et al., Bose-Einstein condensation of atomic hydrogen, Phys. Rev. Lett. 81, 3811 (1998);
17. J. Alnis et al, Subhertz linewidth diode lasers by stabilization to vibrationally and thermally compensated ultralow-expansion glass Fabry-Pérot cavities, Phys. Rev. A 77, 053809 (2008);
18. N. Kolachevsky et al, Low phase noise diode laser oscillator for 1S–2S spectroscopy in atomic hydrogen, Opt. Lett. 36, 4299 (2011);

Study of structural features $Cu_{1-X}Pd_XFeS_2$ compounds

Iliya G. Sevastianov[1], Andrey N. Gavrilenko[1], Vadim L. Matukhin[1], Alexander A. Rodionov[2], Ecaterina V. Schmidt[1], Jiri Navratil[3]

[1]Kazan State Power Engineering University, Krasnoselskaya, 51, Kazan 420066, Russian Federation
[2]Kazan Federal University, Kremlyovskaya, 18, Kazan 420008, Russian Federation
[3]Institute of Physics of the Czech Academy of Sciences Cukrovarnicka 10/112, 16200, Praha 6, Czech Republic
E-mail: ang_2000@mail.ru

Introduction

The study of thermoelectric materials has been of interest recently. In [1] it was proposed to use magnetic semiconductors. The $CuFeS_2$ semiconductor compound belongs to this type of compounds. The possibility of increasing the efficiency of such thermoelectrics by dilute doping has been shown [2,3]. Thermoelectric and transport properties of samples of the $Cu_{1-X}Pd_XFeS_2$ structure (x=0-0.1) were shown in [4]. In this paper, we present the results of a study of a series compounds $Cu_{1-X}Pd_XFeS_2$(x=0, 0.01, 0.02) in comparison with the structure of $Cu_{1.02}Fe_{0.98}S_2$ by NMR $^{63.65}$Cu in the local field and EPR methods.

Experiment

Polycrystalline samples with the nominal composition of $Cu_{1-X}Pd_XFeS_2$ (x=0, 0.01, 0.02) were synthesized from a mixture of pure elements obtained from Sigma-Aldrich, including Cu (4 N shots), Pd (4 N powder), Fe (4 N granular) and S (5 powder). The synthesis of the samples is described in Ref. [4].

The spectral parameters of $^{63.65}$Cu NMR in a local field in samples were measured on a Tecmag Redstone multi-pulse NQR/NMR spectrometer. Measurement of the NMR line shape was performed using quadrature detection by recording spin echo signals with step-by-step passage of the frequency range and signal accumulation.

The EPR spectra of 4 samples $Cu_{1-X}Pd_XFeS_2$ (x = 0, 0.01, 0.02) and $Cu_{1.02}Fe_{0.98}S_2$ were studied on a Bruker stationary X-ray spectrometer ESP-300 in the temperature range 15 - 300 K. The masses of the samples were approximately the same.

Results and discussion

The results of the EPR experiments are presented in Figures 1 and 2. The behavior of the spectra of samples of the composition $Cu_{1-X}Pd_XFeS_2$ (x = 0, 0.01, 0.02) is compared with the spectra of the sample $Cu_{1.02}Fe_{0.98}S_2$.

A distinctive feature of the $CuFeS_2$ sample is the presence of an intense EPR signal with a wide anisotropic line shape over the entire range of the studied temperatures, presumably having a ferromagnetic nature. Also, in the temperature range of 100 – 130 K, there is a rapid change in the signal parameters, which indicates the possible presence of a structural phase transition.

A distinctive feature of the EPR spectra of the $Cu_{1.02}Fe_{0.98}S_2$ sample is the almost complete absence of an intense signal of ferromagnetic nature in the entire range of temperatures studied. At low temperatures, a signal with a g-factor of g = 2.08 is clearly visible, its intensity and the shape of the line change as it heats up to room temperature.

$^{63.65}$Cu NMR spectra of the $Cu_{1.02}Fe_{0.98}S_2$ sample (Figure 3) have a structure similar to that of the $Cu_{1-X}Pd_XFeS_2$ (x=0, 0.01, 0.02) and $CuFeS_2$ samples – each line of the chalcopyrite spectrum on the high-frequency side is complemented by a wide line of smaller amplitude, and the main lines of chalcopyrite are widened, not symmetrical and slightly shifted to the high-frequency region of the spectrum. The main feature of the spectrum of the sample

$Cu_{1.02}Fe_{0.98}S_2$ is the closest correspondence to the spectrum of chalcopyrite, i.e. the above-mentioned effects of broadening and displacement of lines are minimal in the studied group of samples.

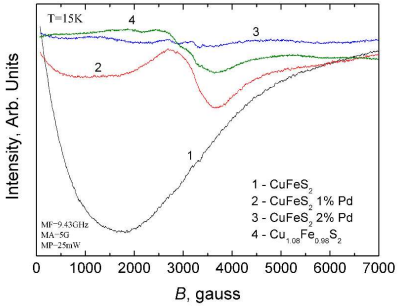

Figure 1. Measured EPR spectra at the temperature 15 K of $CuFeS_2$ (1), $Cu_{0.99}Pd_{0.01}FeS_2$ (2), $Cu_{0.98}Pd_{0.02}FeS_2$ (3) and $Cu_{1.02}Fe_{0.98}S_2$ (4) samples

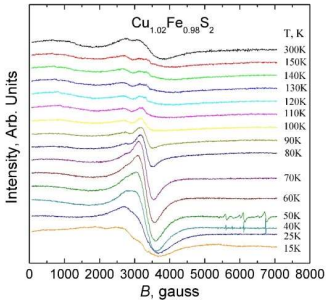

Figure 2. Measured EPR spectra at the temperatures 15-300 K of $Cu_{1.02}Fe_{0.98}S_2$ sample

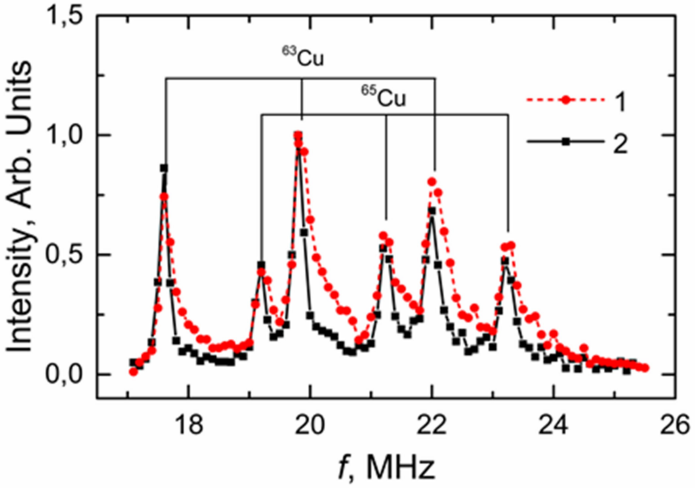

Figure 3. Measured $^{63,65}Cu$ NMR spectra at the temperatures 77 K of $CuFeS_2$ (1) sample and $Cu_{1.02}Fe_{0.98}S_2$ sample (2)

Conclusions

EPR and NMR studies of the features of the $Cu_{1.02}Fe_{0.98}S_2$ sample show its lower defect compared to the composition of $CuFeS_2$ and the effect of this structure on the spectra is similar to samples of the $Cu_{0.99}Pd_{0.01}FeS_2$ structure.

The results of EPR and NMR studies also show that the composition of $CuFeS_2$ is not a stoichiometric composition of chalcopyrite, but is a stoichiometric chalcopyrite with structural defects.

A rapid change in the shape of the EPR spectrum was detected in the temperature range of 100 K-130 K in the $CuFeS_2$ sample, which presumably corresponds to a possible structural phase transition. We have previously shown that natural chalcopyrite does not have a phase transition. All these results may also indicate that the $CuFeS_2$ formula is not stoichiometric for chalcopyrite.

The broadening of the NMR resonance lines may be the result of an increase in the number of defects in the crystal lattice of the compound, leading to a larger spread of EFG on the resonant copper nuclei. Such defects can be Fe_{Cu}^{2+} antisite (AS) defects. The formation of such defects is caused by the formation of the PdS phase in the chalcopyrite matrix, with increasing nominal content of Pd.

Acknowledgements

EPR measurements were supported by subsidy allocated to Kazan Federal University for the state assignment No. 0671-2020-0051.

References

1. N. Tsujii. – *J. Electron. Mater.,* **42**, 1974 (2013).
2. H. Takaki, K. Kobayashi, M. Shimono, N. Kobayashi, K. Hirose, N. Tsujii, and T. Mori. – *Mater. Today Phys*., **3**, 85 (2017).
3. H. Takaki, K. Kobayashi, M. Shimono, N. Kobayashi, K. Hirose, N. Tsujii, and T. Mori. – *Appl. Phys. Lett*., **110**, 072107 (2017).
4. J. Navratil, J. Kasparova, T. Plechacek, L. Benes, Z. Olmrova-Zmrhalova, V. Kucek, and C. Drasar. – *J. Electron. Mater*., **48,** (2019).

The local orientational mobility of collapsed and swollen lysine-based dendrimer with double histidine insertions

Oleg V. Shavykin[1,2,3], Valeriy V. Bezrodnyi[1,2], Emil I. Fatullaev[2], Sofia E. Mikhtaniuk[2], Anatoly A. Darinskii[4], Igor M. Neelov[1,2], Nadezhda N. Sheveleva[1] and Denis A. Markelov[1]

1St. Petersburg State University, 7/9 Universitetskaya nab., 199034 St. Petersburg, Russia
2St. Petersburg National Research University of Information Technologies, Mechanics and Optics (ITMO University), Kronverkskiy pr. 49, 197101 St. Petersburg, Russia
3Tver State University, Zhelyabova St., 33, 170100 Tver, Russia
4 Institute of Macromolecular Compounds RAS, Bolshoi pr.31, 199004, St.Petersburg, Russia
E-mail: kupala-89@mail.ru

Introduction

The novel peptide dendrimers Lys2Lys, Lys2Arg and LysHis with double lysine (2Lys) and double arginine (2Arg) and double histidine (2His) inserts were recently synthesized and studied by us [1-7]. Their properties as nanocontainers for gene delivery were studied also [8,9]. Here we present results of investigation of relaxation processes in swollen and collapsed dendrimer with linear histidine inserts using NMR experiment and molecular dynamics simulation. We used MD method described by us earlier [10-13] and functions described in other simulations using BD [14-15] and SCF approaches [16-17].

Local Orientational Mobility

We calculated the relaxation properties of NMR active groups in computer simulations, using the procedure described in detail in [18]. The autocorrelation functions of the H-H vector rotation process were calculated. Using a linear combination of Fourier transforms, we obtained the frequency dependence of the spin-lattice relaxation rate $1/T_{1H}$ over a wide temperature range. At the same time, the experiment was also carried out for different temperatures, but only at the device frequency, which is a constant characteristic. Having chosen the points corresponding to this frequency from the simulation results, we compared the temperature dependences obtained from the simulation and the NMR experiment (see Figure 1). The local mobility in a swollen dendrimer is similar to that in a dendrimer with linear arginine inserts [3,4]. At the same time, the mobility of the side groups becomes slower in the collapsed dendrimer.

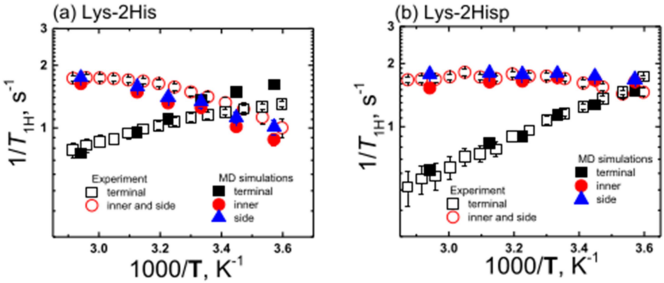

Figure 1. ^1H NMR spin-lattice relaxation rate, $1/T_{1H}$, as a function of inverse temperature 1000/T for the inner, side, and terminal CH_2 groups at the fixed frequency $\omega_H/2\pi$ = 500 MHz from the simulation and experimental data for (a) Lys-2His and (b) Lys-2Hisp.

We also calculated the mobility of H-H groups and spacers in different subgenerations. It was shown that for the swollen dendrimer, the mobility increases with distance from the

dendrimer core, which was previously observed for the lysine dendrimer. This is due to the fact that the role of rotation as a whole as a contribution to mobility dominates in the nucleus. In the collapsed dendrimer, in each subgeneration, the mobility is close to the rotation as a whole (because the contribution of rotation as a whole dominates here). A similar study of mobility in swollen and collapsed dendrimers was previously carried out for PPI dendrimers [19].

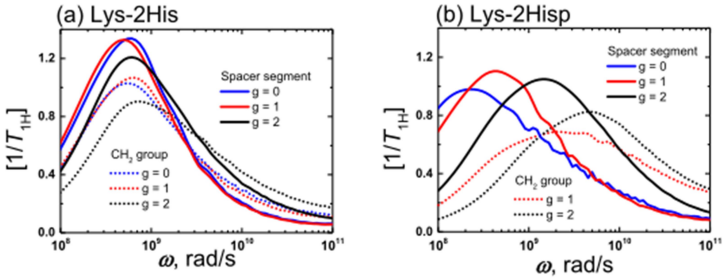

Figure 2. Frequency dependencies of [1/T_{1H}] for the SSs and inner CH_2 groups with different dendrimer layers g beginning from the dendrimer core for the Lys-2His (a) and Lys-2Hisp (b) dendrimers at 310 K.

Acknowledgements

This work is supported by RFBR grant 20-53-12036. The research is carried out using the equipment of the shared research facilities of HPC computing resources at Lomonosov Moscow State University[20], Computer Resources Center of Saint Petersburg State University and the HybriLIT heterogeneous platform (JINR LIT).

References

1. Sheveleva, N.N.; Markelov, D.A.; Vovk, M.A.; Mikhailova, M.E.; Tarasenko, I.I.; Neelov, I.M.; Lahderanta, E. NMR studies of excluded volume interactions in peptide dendrimers. Sci. Rep. 2018, 8, 8916.
2. Mikhtaniuk S.E., Bezrodniy V.V., Shavykin O.V., Neelov I.M., Sheveleva N.N., Penkova A.V., Markelov D.A. Comparison of Structure and Local Dynamics of Two Peptide Dendrimers with the Same Backbone but with Different Side Groups in Their Spacers//Polymers, 2020, 12, No. 8, 1657
3. Sheveleva, N. N.; Markelov, D. A.; Vovk, M. A.; Mikhailova, M. E.; Tarasenko, I. I.; Tolstoy, P. M.; Neelov, I. M.; Lähderanta, E. Lysine-Based Dendrimer with Double Arginine Residues. RSC Adv. 2019, 9, 18018−18026.
4. Bezrodnyi, V. V.; Shavykin, O. V.; Mikhtaniuk, S. E.; Neelov, I. M.; Sheveleva, N. N.; Markelov, D. A. Why the Orientational Mobility in Arginine and Lysine Spacers of Peptide Dendrimers Designed for Gene Delivery Is Different? Int. J. Mol. Sci. 2020, 21, 9749.
5. Sheveleva, N. N.; Markelov, D. A.; Vovk, M. A.; Tarasenko, I. I.; Mikhailova, M. E.; Ilyash, M. Y.; Neelov, I. M.; Lahderanta, E. Stable Deuterium Labeling of Histidine-Rich Lysine-Based Dendrimers. Molecules 2019, 24, 2481.
6. Bezrodnyi V.V., Mikhtaniuk S.E., O. V. Shavykin, I. M. Neelov, N. N. Sheveleva, D. A. Markelov Size and Structure of Empty and Filled Nanocontainer Based on Peptide Dendrimer with Histidine Spacers at Different pH // Molecules 2021, 26, 6552.

7. Sheveleva N.N., Bezrodnyi V.V., Mikhtaniuk S.E., Shavykin O.V., Neelov I.M., Tarasenko I.I., Vovk M.A., Mikhailova M.E., Penkova A.V., Markelov D.A. Local Orientational Mobility of Collapsed Dendrimers, Macromolecules, 2021, 54, 23
8. Gorzkiewicz, M., Konopka, M., Janaszewska, A., Tarasenko I.I., Sheveleva N.N. Neelov I.M., Klajnert-Maculewicz, B. Application of new lysine-based peptide dendrimers D3K2 and D3G2 for gene delivery: Specific cytotoxicity to cancer cells and transfection in vitro, Bioorganic Chemistry 2020, 95, 103504.
9. Gorzkiewicz, M.; Kopeć , O.; Janaszewska, A.; Konopka, M.; Pędziwiatr-Werbicka, E.; Tarasenko, I. I.; Bezrodnyi, V. V.; Neelov, I. M.; Klajnert-Maculewicz, B. Poly(Lysine) Dendrimers Form Complexes with SiRNA and Provide Its Efficient Uptake by Myeloid Cells. Int. J. Mol. Sci. 2020, 21, 3138.
10. Darinskii, A.A., Zarembo, A., Balabaev, N.K., Sundholm, F. Anisotropy of diffusion in a liquid crystalline system of semi-flexible polymer chains, Physical Chemistry Chemical Physics, 2003, 5(11), 2410–2416.
11. Ennari, J., Neelov I. Sundholm, F. Simulation of a PEO based solid polyelectrolyte, comparison of the CMM and the Ewald summation method, Polymer, 2000, 41(6), 2149.
12. Neelov, I.M., Shavykin, O.V., Ilyash, M.Y., Bezrodnyi V.V., Mikhtaniuk S.E., Darinskii, A.A., Leermakers, F.A.M Application of high-performance computing for comparison of two highly branched lysine molecules of different topology, Supercomputing Frontiers and Innovations, 2018, 5 (3), 60-64
13. Falkovich, S.G., Darinskii, A.A. Mechanism of shear deformation of a coiled myosin coil: Computer simulation. Polymer Science - Series A, 2010, 52(6), 662–670.
14. Shavykin, O.V., Mikhailov, I.V., Darinskii, A.A., Neelov I.M., Leermakers, F.A.M. Effect of an asymmetry of branching on structural characteristics of dendrimers revealed by Brownian dynamics simulations, Polymer, 2018, 146, 256-266
15. Darinskii, A.A., Gotlib Y.Y., Lyulin A.V., Neelov I.M. The spectrum of relaxation time for the normal modes of a freely jointed chain consisting of rigid elements in an orienting quadrupole field. Theory and computer modeling, Polymer science, 1992, 34 (1), 11-15
16. Okrugin, B., Ilyash, M., Markelov, D., Lysine dendrigraft nanocontainers. Influence o topology. Pharmaceutics, 2018, 10(3), 129
17. Shavykin, O.V., Neelov I.M., Borisov, O.V., Darinskii, A.A., Leermakers, F.A.M SCF Theory of Uniformly Charged Dendrimers: Impact of Asymmetry of Branching, Generation Number, and Salt Concentration, Macromolecules, 2020, 53 (17), 7298.
18. Markelov, D. A.; Falkovich, S. G.; Neelov, I. M.; Ilyash, M. Y.; Matveev, V. V.; Lähderanta, E.; Ingman, P.; Darinskii, A. A. Molecular Dynamics Simulation of Spin−Lattice NMR Relaxation in Poly-L- Lysine Dendrimers: Manifestation of the Semiflexibility Effect. Phys. Chem. Chem. Phys. 2015, 17, 3214−3226.
19. Gupta, S.; Biswas, P. Orientational Relaxation of Poly(Propylene Imine) Dendrimers at Different PH. J. Phys. Chem. B 2020, 124, 4193− 4202.
20. Sadovnichy, V.; Tikhonravov, A.; Voevodin, V.; Opanasenko, V. “Lomonosov”: Supercomputing at Moscow State University. In Contemporary High Performance Computing: From Petascale toward Exascale; Chapman and Hall/CRC: Boca Raton, FL, USA, 2013; pp. 283–307

A purely spatial diffusion of H atoms in solid normal and para-hydrogen films

Sergei Sheludiakov[1], David M. Lee[2], Vladimir V. Khmelenko[2], Yu. A. Dmitriev[3], Jarno Järvinen[4], Janne Ahokas[4], Sergey Vasiliev[4]

[1]Department of Physics and Astronomy, University of Pittsburgh, PA 15260
[2]Institute for Quantum Science and Engineering, Department of Physics and Astronomy, Texas A&M University, College Station, TX, 77843, US
[3]Ioffe Institute, 26 Politekhnicheskaya, St. Petersburg 194021, Russian Federation
[4]Department of Physics and Astronomy, University of Turku, 20014 Turku, Finland
E-mail: ses276@pitt.edu

Introduction

Hydrogen is the lightest and simplest among the elements. Along with solid helium and molecular hydrogen isotopes, hydrogen atoms embedded in solid H_2 represent a class of so-called quantum crystals, the only solid-state systems where atomic and molecular diffusion does not freeze even at temperatures below 1 K [1].

Helium atoms diffuse through the lattice by interchanging their positions with the adjacent atoms. On the contrary, the H atom diffusion in solid H_2 at $T<1$ K proceeds through a repetition of the most elementary chemical reaction $H+H_2=H_2+H$ when a single H atom interchanges position with an H atom of the neighboring H_2 molecule without a vacancy formation. The diffusion of H atoms in solid H_2 is conventionally detected and probed through their recombination back to H_2 molecules using electron-spin resonance (ESR).

In this process, two hydrogen atoms first approach each other to occupy neighboring lattice sites and then recombine. As a result, the H atom diffusion rates obtained in recombination measurements are biased by the slower H atom diffusion at small H-H distances and do not provide a pure tunneling rate when H atoms move through the H_2 matrix potential far from other unpaired hydrogen atoms. Due to a stronger van-der-Waals interaction and a completely different diffusion mechanism, the H atom diffusion in solid H_2 proceeds much slower as compared with that of ^{3}He atoms in solid ^{4}He. This makes measurements of a pure H atom spatial diffusion in solid H_2 a much more challenging task.

Experimental techniques

We created samples of H atoms in solid H_2 films in two stages:

1) we deposited a thin film of solid molecular para-H2 onto a cold (<1 K) surface of a quartz microbalance, which served also as a mirror of a 128-GHz Fabry-Perot resonator [2].

2) we dissociated part of the molecules in the film by running an RF discharge in the miniature helical resonator located nearby. The ESR study was performed using a cryogenic 128-GHz heterodyne spectrometer which is optimized for reaching highest sensitivity at very low (in the pW range) excitation powers.

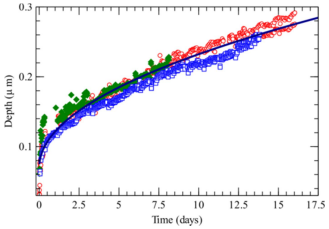

Figure 1. Pure-spatial diffusion of H-atom rich layer into the bulk of solid H_2 films.

Results

We carried out the first measurement of a pure H atom spatial diffusion in solid H_2 at T=0.7 K. We made two different measurements of H atom diffusion in the same experiment: the one based on H atom recombination and the other on H atom diffusion based on their propagation into the film bulk (Fig. 1). In our experiments, we stimulated the H atom diffusion with phonons created in the H_2 film by running an rf discharge above the top surface of our H_2 samples.

We observed a two order-of-magnitude faster pure H atom spatial diffusion rate as compared to that obtained from the H atom recombination. These results provide the first direct measurement of the pure spatial diffusion rate of H atoms in solid H_2, the only solid-state system besides solid $^3He - ^4He$ mixtures where the atomic diffusion does not vanish at temperatures below 1 K.

References

1. Y. Kagan, J. Low Temp. Phys. 87, 525-569 (1992)
2. S. Sheludiakov, D.M. Lee, V. V. Khmelenko, J. Järvinen, J. Ahokas, and S. Vasiliev, Rev. Sci. Instrum. 91, 063901-063901(9) (2020).
3. S. Sheludiakov, D.M. Lee, V. V. Khmelenko, J. Järvinen, J. Ahokas, and S. Vasiliev, Phys. Rev. Lett, 126, 195301-195301(5) (2021).

Diffusion ordered spectroscopy (DOSY NMR) for solutions of biocompatible compounds with similar structure but different mass

Valeriya Shpotya[1], Alexander Perepukhov[1], Alexander Maksimychev[1]

[1]Moscow Institute of Physics and Technology (National Research University), Russia
E-mail: shpotya.valeriya@yandex.ru

Introduction

Biocompatible materials with a high degree of organization are rapidly being employed in medicine, and mass synthesis is the limiting stage in their use. Simplified synthesis methods allow for the faster and simpler production of the desired substance, but the amount of contaminants rises too. Because of the strong overlap of the corresponding spectrum signals, it might be difficult to identify contaminants from the target molecule using NMR spectra. The diffusion experiment of the DOSY NMR [1] is one method for resolving the percentage of signals per component. Among its benefits is the simplicity of usage in the context of routine sample analysis using NMR spectroscopy techniques.

Processing of the DOSY experiment

Despite the fact that the diffusion research method based on the application of gradient magnetic fields was created in the 1960s [2, 3], the problem of processing its data is still not completely solved. The theoretical dependence of signal intensity I on value proportional to square of gradient value Z is as follows:

$$I = \sum a_i \cdot \exp(-D_i Z),$$

where a_i is an amplitude of the signal of the i-th component, and D_i is its self-diffusion coefficient. Thus, using the experimental data, information about the self-diffusion coefficients of the components and the proportions of signals from the corresponding components of the mixture may be obtained. At the same time, the problem of identifying an unknown number of exponents with particular weights is poorly conditioned, and the results of processing diffusion tests do not contain information about component fractions in many standard software programs for processing NMR spectra.

Experiments can be processed in several ways, including approximation by the sum of one, two, or three exponents (i.e., an upper bound on the number of components in the mixture is assumed during processing), approximation by a piecewise linear function for data on a logarithmic scale, and application of the inverse Laplace transform to the data. Each approach has benefits and disadvantages that must be carefully considered in regard to the systems under examination.

When the self-diffusion coefficients of the components differ by less than an order of magnitude, the inaccuracy in identifying the characteristics rises. At the same time, it is precisely such systems that are frequently of interest for study, thus it is critical to define the techniques of processing the DOSY spectra that are appropriate for such cases, as well as the limits of their application.

Calibration of DOSY results for PEG mixtures

Spectra for PEG mixtures of various weights were collected to analyze the behavior of various DOSY processing techniques (1kDa, 2kDa, 4kDa, 8kDa). The primary criterion for selecting the object of research was its purity, which was defined as the lack of components that were comparable in composition and structure but differed in size (and, accordingly, the coefficient of self-diffusion). PEG mixtures with varying polymer mass ratios, as well as

varying mass fraction ratios in the final solution, were investigated. Furthermore, systems with varying numbers of components were explored.

As a result, we evaluated the error in identifying characteristics using various processing techniques, the effect of component mass ratio on the accuracy of estimating their fractions, and identified the major causes of error in diffusion experiment data.

The findings of this study may be useful in the future for the analysis of block copolymer/homopolymer type systems, where the signals of components in the proton spectrum are poorly resolved and distort the evaluation of the block copolymer's characteristics when used without taking into account the presence of other components.

References

1. W. Hiller. – *Macromolecular Chemistry and Physics*, **220**, 17, 1-13 (2019).
2. E. Stejskal, J. Tanner. – *The Journal of Chemical Physics*, **42**, 288-292 (1965).
3. P. Stilbs. Diffusion and Electrophoretic NMR. – De Gruyter, Berlin, 2019.

Heat exchange impact on NMR logging while drilling

Oleg A. Shushakov [1,2], Oleg B. Bocharov[3], Radu Coman[4], Holger F. Thern[4]

[1]Institute of Chemical Kinetics and Combustion SB RAS, 3, Institutskaya St., 630090 Novosibirsk, Russia
[2]Novosibirsk State University, 1, Pirogova St., 630090 Novosibirsk, Russia
E-mail: oleg.shushakov@bakerhughes.com
[3]Baker Hughes Russia, Novosibirsk Technology Center, 4a, Kutateladze St., 630090 Novosibirsk, Russia4[2]Baker Hughes,, Celle Technology Center, 1 Baker-Hughes Strasse, 29221 Celle, Germany

Introduction

Temperature affects nuclear magnetic resonance measurements in the well. Both nuclear spin magnetization and NMR signal are inversely proportional to absolute temperature (Curie-Langevin law). In the magnetic field $\mathbf{B_0}$ a macroscopic magnetization $\mathbf{M}_0(\mathbf{r})$ of a unit volume in thermal equilibrium state is described by the equation:

$$\mathbf{M_0}(\mathbf{r}) = n(\mathbf{r})\frac{\gamma^2\hbar^2}{3kT}S(S+1)\cdot\mathbf{B_0},$$

where $n(\mathbf{r})$ is the number of magnetic nuclei per unit volume, γ is gyromagnetic ratio for protons, S=1/2 is the nuclear spin (for protons), $\hbar$ and k are Planck and Boltzmann constants, respectively, and T is an absolute formation temperature.

Modern wells are very long and have considerable temperature differences in length. In both wireline NMR logging and NMR logging while drilling (LWD) the measured mud temperature on signed level used as a proxy temperature of NMR sensitive volume situated in several centimetres deep into formation from borehole surface. In NMR LWD the temperature of mud and formation could be different in contrast to wireline NMR logging. This can reduce the accuracy of determined by NMR porosities. In MMR LWD temperature correction is not yet in standard use [1].

For NMR logging while drilling temperature correction, we have to estimate the temperature in the NMR sensitive volume, which is situated in several centimeters from borehole wall deep into formation [2].

A heat conduction with mud filtration model

A heat conduction equation considering mud invasion is $\frac{\partial T}{\partial t} = div\left(D_T \cdot gradT - \vec{v}\cdot T\right)$, where $\vec{v}$ is mud filtration rate. In cylindrical coordinate frame for constant radial flux $\vec{v} = \frac{v_0 \cdot a}{r}\cdot\vec{e}_r$ (v_0= const is the filtration flow rate at r=a, a is the borehole radius, $\vec{e}_r$ is the unit vector along radius r). For dimensionless τ_T= $D_T\, t/a^2$ and ρ=r/a, and β=$v_0 a/2D_T$

$$\frac{\partial T}{\partial \tau_T} = \frac{\partial^2 T}{\partial \rho^2} + \frac{1-2\beta}{\rho}\cdot\frac{\partial T}{\partial \rho},$$

For constant initial and boundary conditions $\begin{cases} T(\tau_T, 1) = T_1 \\ T(0,\rho) = T_0 \end{cases}$, the solution for $\rho > 1$ and $\tau_T > 0$ is

$$\frac{T-T_0}{T_1-T_0} = 1 + \frac{2\rho^\beta}{\pi}\int_0^\infty exp(-\tau_T u^2)\cdot\frac{J_\beta(u\rho)\cdot Y_\beta(u) - Y_\beta(u\rho)\cdot J_\beta(u)}{J_\beta^2(u) + Y_\beta^2(u)}\cdot\frac{du}{u}$$

(where J_β and Y_β are Bessel and Neumann functions). The convection parameter β, obtained from filtration problem with the initial and boundary conditions for a pressure P of the type: $\begin{cases} P(\tau_P,1)=P_1 \\ P(0,\rho)=P_0 \end{cases}$ takes the form

$$\beta = \frac{k}{\eta}\cdot\frac{P_1-P_0}{2D_T}\left(\frac{2}{\pi}\right)^2 \int_0^\infty \frac{exp(-\tau_P u^2)\cdot du}{J_0^2(u)+Y_0^2(u)},$$

where dimensionless $\tau_P = D_P\, t/a^2$, $\rho = r/a$, and $D_P = k/(\eta\varepsilon\phi)$ is piezo-conductivity coefficient, k is permeability, η is viscosity, ϕ is porosity of movable fluid, and ε is formation compressibility.

Numerical modeling of heat conduction and mud filtration

Figure 1a) exemplifies an effect of temperature on NMR LWD echo train for clay-bound water formation with temperatures close to similar to real (figure 1b). Figure 1b) shows measured temperature in the borehole, formation temperature estimated using geothermal gradient, and temperature of NMR LWD sensitive volume calculated by our model at different borehole vertical depths. The results of fig 1 have been obtained with time of NMR measurement amounts value around 1 hour since drilled that is close to minimal for NMR LWD.

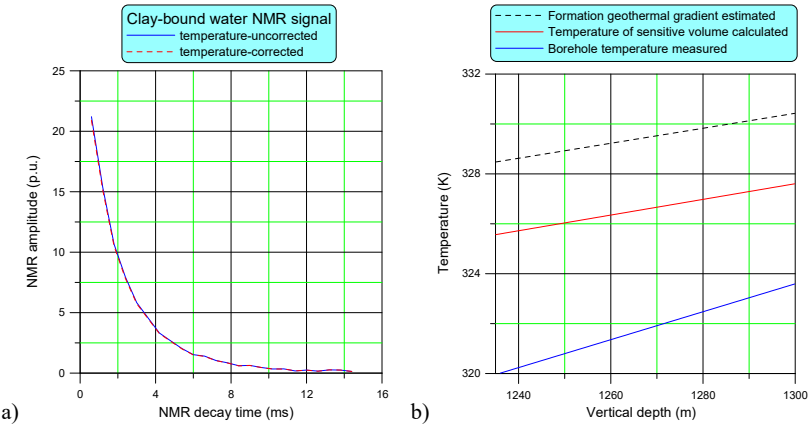

Figure 1. a) Temperature effect on NMR LWD signal at vertical depth 1235m to1300m, b) Temperature of borehole, formation, and sensitive volume vs vertical depth.

Figures 2 and 3 present the same temperatures as at the figure 1b) for the same borehole, all rig statuses (drilling and reaming), and wider vertical depth interval. For permeable layers the temperature of NMR LWD sensitive volume is equal to the temperature measured in the borehole (fig. 2). The structure at vertical depth 1500m at figure 2 is associated with drilling technology. Nevertheless, structures at 1600 and 1690 m correlates with the permeability measured versus vertical depth (fig. 3).

The parameters used for the modeling are: the borehole diameter is *8.5"*, the sensitive-volume diameter is *13.2"*, the thermal diffusivity D_T is 10^{-2} *cm*^{2}*/s*, the viscosity η is 10^{-2} *poise*, the compressibility ε is $5\cdot10^{-2}$ *Pa*$^{-1}$, ϕ=20%, the pressure difference P_1 -P_0 is *20 atm*, and geothermal gradient is 3K/100m.

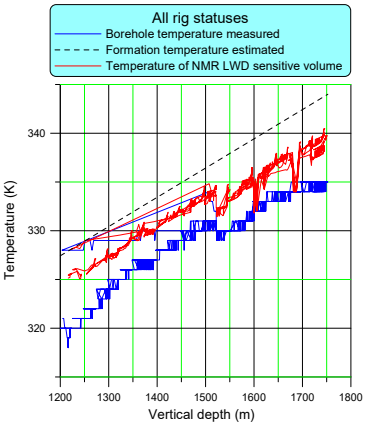

Figure 2. Temperature of borehole, formation, and sensitive volume vs vertical depth around permeable layers.

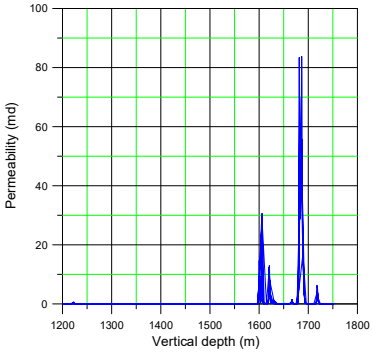

Figure 3. Permeability measured by NMR LWD versus the borehole vertical depth.

Summary

This material presents an analytical approach for NMR LWD data temperature-effect estimation. We add convective heat transfer for permeable layers. Method efficiency is illustrated on a field data for vertical well:

- the model of heat transfer with convection feels permeable layers;
- the model gives the temperature of NMR LWD sensitive module of permeable levels being close to measured temperature in a borehole.

References

1. M.G. Prammer, G.D. Goodman, S.K. Menger et al. Field test of NMR LWD device. SPWLA-EEE, Dallas, Texas, 2000.
2. R. Coman, H. Tietjen. Temperature correction in NMR logging while drilling. - SPE-185334-MS, Mumbai, India, 2017.

Investigation of mechanism of Ionic and Molecular transport in the nafion membrane by nmr

Nikita A. Slesarenko[1], Alexander V. Chernyak[1,2], Vitaly I. Volkov[1,2]

[1]Institute of Problems of Chemical Physics RAS, 142432 Chernogolovka, Russia
[2]Scientific Center in Chernogolovka RAS, 142432 Chernogolovka, Russia
E-mail: wownik007@mail.ru
https://www.icp.ac.ru

Introduction

Ionic transport in sulfonic cation (-exchange) membrane is controlled by ionogenic channels nanostructure and particularities of the cation hydration. For transport mechanism revelation an ionic interaction, mobility of water molecules and cations in different spatial scales should be investigated. NMR spectroscopy is widely applied for investigation of structure and dynamics complicated molecular systems.

Mobility and self-diffusion peculiarities of water and Li^+, Na^+, Cs^+ cations in Nafion membrane with well known ionogenic channel microstructure will be revealed by ^1H, ^7Li, ^{23}Na, ^{133}Cs spin-relaxation and pulsed field gradient (PFG) NMR techniques.

Materials

Extruded N117 (thickness 183 μm, equivalent weight (EW)=1100, Dupont, Ion Power Inc.) membranes were used for the experimental characterization of Nafion in salt (Li+, Na+, Cs+) ionic form.

Methods

High resolution NMR

High resolution of Nafion membrane ^1H, ^7Li, ^{23}Na, ^{133}Cs spectra were recorded on the AVANCE-III-500 Bruker NMR spectrometer (proton Larmor frequency is 500 MHz) in the temperature region from -40ºC to +60ºC. The 1H chemical shift was calculated relatively bulk water ^1H NMR signal (δ_{H2O}=4.30 ppm relatively TMS), chemical shift measurement error was less than 0.05 ppm.

Pulsed field gradient NMR

The self-diffusion coefficients were measured on ^1H, ^7Li, ^{23}Na, ^{133}Cs nuclei by pulsed field gradient technique at the frequencies 400.22, 155.51, 105.84, 52.48 MHz, respectively. The measurements were carried out on Bruker AVANCE-III-400 NMR spectrometer, equipped with the diff60 gradient unit. The pulsed field gradient stimulated echo sequence was used.

The evolution of spin echo signal is described by the following equation.

$$A(2\tau,\tau_1,g) = A(2\tau,\tau_{1,0})\exp(-\gamma^2 g^2 \delta^2 t_d D_s) \qquad (1)$$

where γ is gyromagnetic ratio, t_d=Δ-δ/3 is the diffusion time, and D_s is the self-diffusion coefficient, $A(2\tau, \tau_1, 0)$ is expressed by the equation

$$A(2\tau,\tau_{1,0}) = \frac{A(0)}{2\exp\left(-\frac{2\tau}{T_2}-\frac{\tau_1}{T_1}\right)},$$

$A(0)$ is the signal intensity after the first radio frequency (RF) pulse. T_1 and T_2 are the spin-lattice and spin-spin relaxation times, respectively. During measurement of echo signal evolution, τ and τ_1 are fixed, and only the dependence of A on g (diffusion decay) is analyzed.

NMR Relaxation

Spin-lattice T_1 and spin-spin T_2 nuclear relaxation times were measured using 180^o-τ-90^o and Carr-Purcell-Meiboom-Gill $(90o - \tau - n180^o)$ pulsed sequences, correspondingly. Longitudinal magnetization M_z recovery and perpendicular magnetization $M_{x,y}$ decay were approximated by exponential dependences (3) and (4), correspondingly for ^{1}H, ^{7}Li, ^{23}Na, ^{133}Cs nuclei. Spin echo attenuation of ^{23}Na and ^{133}Cs nuclei was too fast in order to detect a detailed decay curve shape.

$$\frac{(M_0 - M_z)}{2M_0} = \exp(-t / T_1) \quad (2)$$

$$M_x(t) = M_0 \cdot \exp(-t / T_2) \quad (3)$$

M_o is equilibrium nuclear magnetization

Results and discussion

Water molecule and Li^+, Na^+, Cs^+cation self-diffusion

Self-diffusion coefficients of water molecules and cations Li^+, Na^+, Cs^+ were measured. Self-diffusion coefficient temperature dependences are approximated by the Arrhenius equitation:

$$D = D_0 \cdot \exp(-E_a / RT) \quad (4)$$

where D_o is temperature independent, R is gas constant, T is absolute temperature. E_a is self-diffusion activation energy.

Activation energies of water self-diffusion in Li^+ and Na^+ membrane ionic forms increase in low temperature region below of 0^oC. Activation energies are 18.6 kJ/mole, 29.1 kJ/mole and 21.7 kJ/mole, 33.8 kJ/mole in high and low temperature regions of Li^+, Na^+ membrane ionic forms. Self-diffusion activation energies are 35.5 kJ/mole for water molecules in Cs^+ ionic form and 25.3 kJ/mole for Li^+ cation. The reason of rupture in water self-diffusion coefficients temperature dependence curves for high water content $\lambda > h$ (λ = 6.4 and 5.1 for Li^+ and Na^+ ionic forms correspondingly) is water molecule associate forming at temperature below 0^oC [1].

Spin relaxation of ^{1}H, ^{7}Li, ^{23}Na, ^{133}Cs nuclei. Water molecules and Li^+, Na^+, Cs^+ cations local motion.

^{1}H spin- relaxation, water mobility

Spin of ^{1}H nuclei is 1/2, therefore spin relaxation occurs due to proton dipole-dipole interaction modulated by water molecule mobility. In the case of exponential correlation function relaxation times described by Bloembergen, Purcell, Pound equations. The temperature dependences of the spin-lattice relaxation time $T_1(T)$ have a minimum at $\omega\tau_{av} = 0.62$, where τ_{av} is average correlation time the value of average correlation time τ_{av} in minimum $T_1(T)$ is $2.46 \cdot 10^{-10}$ sec. Water self-diffusion coefficient may be estimated from Einstein relation (5).

$$D = l^2 / 6 \cdot \tau_{av} \quad (5)$$

where l is average jumping distance.

Calculated from local mobility water self-diffusion coefficients and measured water macroscopic self-diffusion coefficients are differ no more than in 2 times well for Li^+ and Na^+ ionic forms. Keeping in mind an approximation calculation of self-diffusion from Einstein relation it is a good agreement. Therefore it may be concluded that macroscopic water self-diffusion is controlled by water molecule local motion through the continuous hydrogen bond network which forms at rather high water content (λ is 6.4 in Li^+ form and 5.1 in Na^+ form at RH=75%). For Cs^+ ionic form measured water self-diffusion coefficient is one order of mag-

nitude less compare with calculated one. Water content λ=1.5 at RH=75% in Cs^+ ionic form. Three water molecules per sulfonate group are not enough to form continuous hydrogen bond network and this network is broken. Therefore the fast local water molecule rotation (which causes spin-relaxation) is not correlated with translation jumping because rotation frequency is more fast compare to translational frequency.

^{7}Li, ^{23}Na, ^{133}Cs spin relaxation, cation mobilities.

The nuclear spins of ^7Li, ^{23}Na are *3/2*, but ^{133}Cs nuclear spin is 7/2. For these nuclei the main relaxation mechanism is quadrupole relaxation. For nuclear spin = 3/2

At high temperature magnetization kinetic curves are exponential approximated by equations (2) and (3). With temperature decreasing magnetization $1 \le (\omega\tau)^2$ and kinetic curves should be two exponential shape, but it may be not success to observe two exponential curves experimentally especially for longitude magnetization recovery.

At RH=75% T_1 *(T)* and T_2 *(T)* of ^{7}Li and ^{23}Na decrease with decreasing temperature, which indicates the fast narrowing conditions ($(\omega\tau)^2 << 1$), but for ^{133}Cs T_1 increases with decreasing temperature ($1 < (\omega\tau)^2$). In the samples equilibrated with water ^{133}Cs T_1 *(T)* shows minimum. Unfortunately it was impossible to measure T_1 of ^7Li and ^{23}Na at temperature below -40°C in order to observe these nuclei spin-relaxation minimum. Activation energies of $^7Li^+$ spin relaxation is about 20 kJ/mole that is close to Li^+ self-diffusion activation energy. Activation energies of ^{23}Na spin-relaxation and self-diffusion are also close to each other (about 20 kJ/mole) in samples equilibrated with water. Approximation of T_1 *(T)* by Gaussian function the temperature of ^{7}Li and ^{23}Na spin-relaxation times may be crudely estimated which is 233K for ^{7}Li. According to Eq. 6 in minimum $T_1\ (\omega\tau_{av})^2 \approx 1$ and $\tau_{av}=10^{-9}$sec. At this temperature Li^+ self-diffusion coefficient is $4\cdot10^{-12}$m^2/sec. From Eq.5 *l* is 0.15 nm that is closed to water hydrogen bond length. It may be supposed that Li^+ cation translation displacement is controlled by a rearrangement of hydrated water molecules hydrogen bond that explains a symbasis of water and lithium cation self-diffusion behavior. The temperature dependence T_1 *(T)* ^{133}Cs shows minimum at 20°C. In spite that ^{133}Cs nuclear spin is 7/2 we can crudely estimate the correlation time at this temperature from the relation $(\omega\tau_{av})^2 \approx 1$ and τ_{av} is $3\cdot10^{-9}$ sec. Cesium cation at this temperature is $3\cdot10^{-11}$ m^2/sec. From relation (11) *l* approximately is 0.7 nm. This value equals to average distance between neighboring sulfonate groups.

Acknowledgements

NMR measurements were performed using equipment of the Multi-User Analytical Center of the Institute of Problems of Chemical Physics RAS and Science Center in Chernogolovka RAS with the support of State Assignment of the Institute of Problems of Chemical Physics RAS (state registration No 0089-2019-0010/AAAA-A19-119071190044-3).

References

1. V.I. Volkov, A.V. Chernyak, I A. Avilova, N.A. Slesarenko, D.L. Melnikova and V.D. Skirda. Molecular and Ionic Diffusion in Ion Exchange Membranes and Biological Systems (Cells and Proteins) Studied by NMR. Membranes 2021, 11(6), 385
2. Volkov V.I., Chernyak A.V., Gnezdilov O.I., Skirda V.D. Hydration, self-diffusion and ionic conductivity of Li^+, Na^+ and Cs^+ cations in Nafion membrane studied by NMR. Solid State Ionics 2021, 364, 115627

Structure and ^{19}F MAS NMR spectra of pentafluoridozirconic acid hydrates according to NMR spectroscopy

Slobodyuk A.B., Didenko N.A.

Institute of chemistry, FEB RAS, 159, Pr. Stoletiya Vladivostoka, 159, Vladivostok, Russia
E-mail: ampy@ich.dvo.ru

Fluorozirconates are interesting objects to study by means of solid state ^{19}F NMR method. The ^{91}Zr nucleus possess extremely small magnetic moment while the electronic shell of Zr^{4+} is closed and characterizes by various hybridization states which results in various configuration polyhedra shapes which can be interconnected by various ways. The ^{19}F chemical shift range of fluorozirconates constitutes some 250 ppm suggesting that the structural information could be obtained from the spectra. The resulting correlations between the spectra and the structures could be used to investigate structure of the fluorozirconate glasses, which have perspective physical and optical properties, by means of the NMR method.

In a number of works, the relations between the structure of a fluorozirconate and its NMR spectrum were studied [1, 2].

The structures of anionic layers in crystalline hydrates of $HZrF_5{\cdot}nH_2O$ acids (n = 2, 3) are characteristic to a number to other fluorozirconate salts (F/Zr=5) with large protonated organic cations or complex octahedral cations such as $ZnZr_2F_{10}{\cdot}6H_2O$, $(C_2H_{10}N_2)Zr_2F_{10}\cdot H_2O$, $(CH_3NH_3)ZrF_5{\cdot}0.5H_2O$, $(H_3NCH_2COOH)ZrF_5\cdot 2H_2O$, and $(H_3N(CH_2)_2COOH)ZrF_5$ [3-6]. This fact and the "perfect" character of the fluoridozirconate layer constructed from equivalent almost ideal dodecahedra makes these compounds interesting model objects for studying the relation between ^{19}F NMR chemical shifts, complex anion structure and the nature of the cation. NMR studies of crystal hydrates of pentafluoridozirconic acid have not previously been performed.

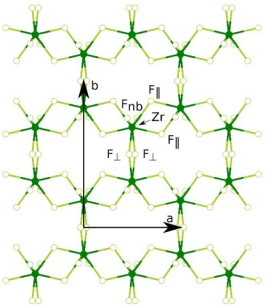

Figure 1. Anion layer in the structures of $HZrF_5{\cdot}nH_2O$ (n=2, 3) pentafluoridozirconate acids and related compounds.

The anionic layers can be represented as chains consisting from ZrF_8^{4-} dodecahedra interlinked by edges parallel to the layer plane. The chains are also linked to each other along the edges of dodecahedra which are perpendicular to the plane (Fig. 1).

The four vertices of a dodecahedron are located at short distances from its center, while the other four have longer distances. It allows one to distinguish three types of fluorine atoms with substantially differing bond lengths with the central atom in the discussed structures. The dodecahedron edges perpendicular to the layer plane contain $F_\perp$ fluorine atoms (F4 according to Marsh et al., [7]) forming two long bonds with zirconium atoms, while the edges parallel to the plane contain $F_\parallel$ (F1 and F5) fluorine linking zirconium atoms

by a nonsymmetrical bridging bond. The two non-bridging F_{nb} (F2 and F3) fluorine atoms are located at short distances from the zirconium ones. The amount of $F_{\perp}$, $F_{\parallel}$, and F_{nb} atoms accounted for one zirconium atom equals to 1, 2, and 2 respectively.

According to the previous paragraph, three types of fluorine bond exist in the structures of $HZrF_5 \cdot nH_2O$ acids. Correspondingly, three peaks are observed in ^{19}F NMR MAS spectra of the compounds (Fig. 1). The spectrum of $HZrF_5 \cdot 3H_2O$ contains signals with chemical shifts of 34.5, -9.6, and -21.8 ppm; shifts of the signals in the spectrum of the dihydrate are 17.3, -1.8 and -14.3 ppm. Considering the bond lengths of the layer structure under question, the signals can be assigned to the discussed above fluorine types F_{nb}, $F_{\parallel}$, $F_{\perp}$, respectively (Fig. 1).

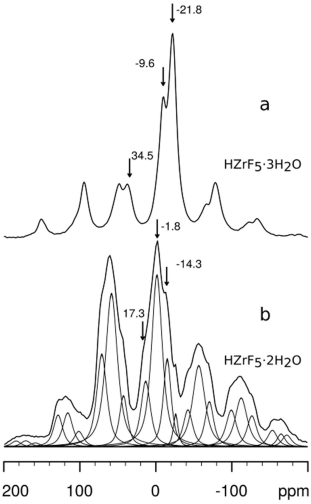

Figure 2. ^{19}F MAS NMR spectra of $HZrF_5 \cdot 3H_2O$ (a) and $HZrF_5 \cdot 2H_2O$ (b). Central signal positions are labeled, spinning (ν_{rot} = 16 kHz) sidebands are left unmarked.

Due to the overlapping of the peaks and the spinning sidebands on the spectra of $HZrF_5 \cdot 3H_2O$, we could estimate the integrated intensities only for the $HZrF_5 \cdot 2H_2O$. The ratio of the intensities (26:54:20) is similar to the one obtained for $ZnZr_2F_{10} \cdot nH_2O$ (n = 2, 4). The signal positions in the NMR spectra and the shape of the sideband envelope, despite the closeness of the layer structure of these compounds, differ substantially. The redistribution of the intensities between the central signals and the corresponding spinning sidebands indicates significant changes in the chemical shielding anisotropy of the fluorine sites which could be related to the strong dipole moment of the water molecules which leads to the large differences in the crystalline field around the complex anion. It can be noted that while the larger dispersion of chemical shifts is observed for $HZrF_5 \cdot 3H_2O$, the shielding anisotropy is greater for the $HZrF_5 \cdot 2H_2O$. It seems unexpected since the fluorine chemical shift in the coordination compounds is believed to be dominated by the paramagnetic contribution and correlates to the shielding anisotropy.

Acknowledgements

This work was supported by the RFBR fund; project no 20-03-00279.

References

1. R.E. Youngman, S. Sen, A high-resolution ^{19}F NMR spectroscopic study of barium fluorozirconate glasses and related crystals, Solid State Nucl. Magn. Reson. 27 (2005) 77–89. doi: 10.1016/j.ssnmr.2004.06.008
2. A.V. Gerasimenko, K.A. Gaivoronskaya, A.B. Slobodyuk, N.A. Didenko, Magnesium hexafluoridozirconates $MgZrF_6 \cdot 5H_2O$, $MgZrF_6 \cdot 2H_2O$, and $MgZrF_6$: structures, phase transitions, and internal mobility of water molecules, Z. Anorg. Allg. Chem. 643 (2017) 1785–1792. doi:10.1002/zaac.201700166
3. Gerasimenko A.V., Davidovich R.L., Logvinova V.B., Crystal structures of layered zirconium pentafluorides of methylammonium, glycinium, and β-alanine, J. Struct. Chem. 52 (3) (2011) 540-546 (in Russian).
4. Ben Ali A., Body M., Leblanc M., Maisonneuve V. 2D zirconium fluorides: Synthesis, structure and NMR spectroscopy // Solid State Scinces. 2011. V. 13. N. P. 394-398. 10.1016/j.solidstatesciences.2010.11.044
5. Sykora R.E., Ruf M., Albrecht-Schmitt T.E. Organically Templated Zirconium Fluorides: Hydrothermal Syntheses, Structural Relationships, and Thermal Behavior of $(C_2H_{10}N_2)Zr_2F_{10}\cdot H_2O$ and $(C_4H_{12}N_2)ZrF_6\cdot H_2O$ // J. Solid State Chem. 2001. V. 159. N. 1. P. 198-203. doi.org/10.1006/jssc.2001.9151
6. Voit E.I., Didenko N.A., Gerasimenko A.V., Slobodyuk A.B., Synthesis and complex study of the crystal hydrate $ZnZr_2F_{10}\cdot 6H_2O$, J. Fluor. Chem. 232 (2020) 109475. doi:10.1016/j.jfluchem.2020.109475
7. Marsh R.E., Noyes A.A., Structure of oxonium pentafluorozirconate dihydrate. Corrigendum, Acta Cryst. C 45 (1989) 980. doi:10.1107/S0108270188014672

Computational fluid dynamics and magnetic resonance imaging: a study of the circle of Willis blood flow

Gustavo Solcia[1] and Fernando F. Paiva[1]

[1]São Carlos Institute of Physics, University of São Paulo, PO BOX 369, 13560-970, São Carlos, Brazil
E-mail: gustavo.solcia@usp.br
https://gustavosolcia.github.io

Introduction

Computational Fluid Dynamics (CFD) based on Magnetic Resonance Imaging (MRI) helps understand the behavior of structures and dynamics in the human body. The Circle of Willis (CoW), for instance, can be thoroughly studied by combining these techniques. Its importance relies on the fact that it is a crucial structure for cerebral blood flow and has the role of compensating the flow in brain regions in the case of artery occlusion. Healthy subjects can have different CoW anatomies [1], including variations of even not having an artery connection. These anatomical variations can influence the blood flow dynamics in occlusion scenarios. The main goal of this study is to use CFD based on MRI to simulate the hemodynamic in different CoW anatomies.

Methods

From the Information eXtraction from Images (IXI) dataset [2], we selected angiographies of a healthy female with complete CoW anatomy and a healthy male with incomplete CoW anatomy. Figure 1 shows the Maximum Intensity Projection (MIP) of the selected data, and in Figure 1b is possible to notice the absence of the Right Posterior Communicating Artery (RPCoA) on the male volunteer anatomy.

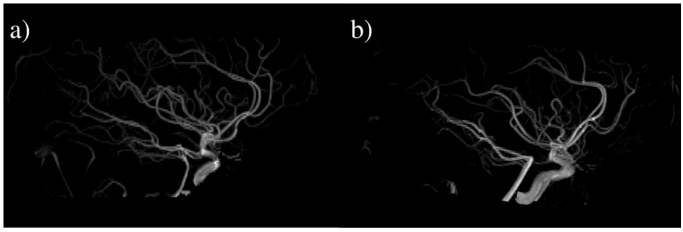

Figure 1. MIP of Time-of-Flight MRI from subjects of IXI dataset. a) Healthy female with complete CoW anatomy. b) Healthy male with incomplete CoW anatomy (absence of RPCoA).

Once the structural angiographies were selected, we applied image processing and tridimensional reconstruction steps to prepare the data for a CFD simulation. We used the non-local means [3] noise filter modified for Rician noise to improve the image homogeneity. Then, we applied three classes of Atropos segmentation [4] to select only the structure of the arteries. With the binarized image, we reconstructed the arteries with the marching cubes algorithm [5] and then applied surface smoothing with the Taubin filter [6]. Additional surface modeling was made in Blender [7] to prepare the boundaries and correct the remaining artifacts.

For the CFD simulations, we used the open-source software OpenFOAM [8] from OpenCFD Ltd. We prepared the volumetric mesh with the OpenFOAM cfMesh tool from the same distribution using a maximum cell size parameter of $6 \cdot 10^{-4}$m and three additional refinement levels for arteries walls. After the volumetric mesh creation, we applied the

simpleFoam solver for steady-state laminar flow simulations of blood with a dynamic viscosity of $3.5 \cdot 10^{-3}\ Pa \cdot s$.

Using blood flow rate values from groups of healthy female and male subjects [9] for the boundary conditions, we simulated four hemodynamic scenarios: normal flow, Basilar Artery (BA) occlusion, Right Internal Carotid Artery (RICA) occlusion, and Left Internal Carotid Artery (LICA) occlusion. With the post-processing tools from OpenFOAM, we measured the blood flow rate outcomes of each hemodynamic scenario on the Left and Right Medial Cerebral Artery branches (LMCAb and RMCAb), Anterior Cerebral Artery branches (ACAb), Posterior Cerebral Artery branches (PCAb), and on crucial arteries from the CoW such as Left and Right Posterior Communicating Artery (LPCoA and RPCoA). We estimated the percentage variation between each occlusion scenario and the normal flow condition.

Results and discussion

Table 1 shows the blood flow rate outcomes from all scenarios and their variations compared to the normal flow condition for the healthy volunteer with complete CoW. All cases show an increase in blood flow on the LPCoA and RPCoA, which might be associated with the CoW blood flow compensation functionality, shown in streamlines from Figure 2a. Also, it is possible to notice that the flow rate gap is shorter between LPCoA and RPCoA in occlusion scenarios, compensating for the lower baseline flow rate found for RPCoA, which is likely due to the additional artery connecting RICA and the medial cerebral artery present in this subject, shown in Figure 2c.

Table 1. Blood flow rate outcomes from hemodynamic scenarios for the healthy subject with complete CoW. The percentage values are relative to the normal flow condition.

Hemodynamic Scenario	LPCoA	LMCAb	ACAb	PCAb	RMCAb	RPCoA
Normal flow (ml/min)	10.7	160	112	159	153	0.99
BA Occlusion	+397%	-18%	-19%	-35%	-19%	+4788%
RICA Occlusion	+139%	-20%	-47%	-29%	-65%	+5870%
LICA Occlusion	+337%	-66%	-37%	-29%	-19%	+1279%

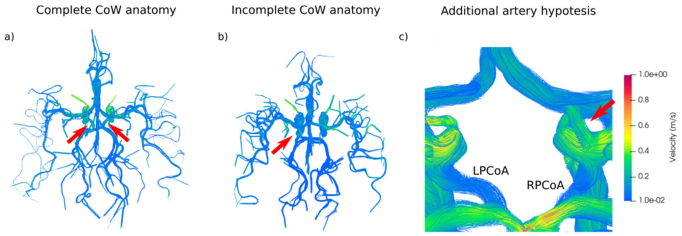

Figure 2. Representative velocity streamlines from blood flow simulations. a) BA occlusion scenario for complete CoW anatomy. Red arrow highlights LPCoA and RPCoA. b) BA occlusion scenario for incomplete CoW anatomy. c) Complete CoW anatomy on normal flow scenario with red arrow showing additional artery on the right side.

Table 2 shows the results from the subject with incomplete CoW. The blood flow on the branches is clearly more affected by the occlusion scenarios due to the absence of RPCoA. Except for the BA occlusion scenario, shown in streamlines from Figure 2b, the LPCoA

experiences a decrease in blood flow rate while an occlusion is present. Results also show a more severe reduction in the flow rate on important regions like PCAb on BA occlusion, RMCAb on RICA occlusion, and ACAb on LICA occlusion.

Table 2. Blood flow rate outcomes from hemodynamic scenarios for the healthy subject with an incomplete CoW (absence of RPCoA). The percentage values are relative to the normal flow condition.

Hemodynamic Scenario	LPCoA	LMCAb	ACAb	PCAb	RMCAb	RPCoA
Normal flow (ml/min)	28.2	136	121	165	144	-
BA Occlusion	+106%	-8%	-6%	-71%	-3%	-
RICA Occlusion	-65%	-22%	-50%	-9%	-75%	-
LICA Occlusion	-7%	-66%	-51%	-26%	-18%	-

Conclusion

We investigated the blood flow rate outcome from hemodynamic scenarios on different CoW anatomies using CFD based on MRI. For the complete anatomy, the simulations showed the CoW acting as expected in an occlusion scenario with an increased flow rate on LPCoA and RPCoA. However, for the incomplete anatomy with an absence of an RPCoA, we notice a decrease in the flow rate in regions like ACAb, PCAb, and RMCAb. In summary, the simulations indicate that an occlusion could potentially cause more damage on a healthy subject that has an incomplete CoW. Future studies will focus on patient-specific applications, in which case the flow rate data for the boundary conditions can be obtained from MRI-based techniques like arterial spin labeling and phase contrast angiography.

Acknowledgements

This work is supported by the Coordenação de Aperfeiçoamento de Pessoal de Nível Superior – Brasil (CAPES) – Finance Code 001 (grant 88887.476130/2020-00*).*

References

1. M J Krabbe-Hartkamp et al., Radiology, 207:1, 103-111, 1998.
2. Biomedical Image Analysis Group Imperial College London, Information eXtraction from Images (IXI) dataset, 2010, Available: http://www.brain-development.org/, Accessed 06 Aug 2021.
3. A. Buades, B. Coll, J. -. Morel, IEEE computer society conference on computer vision and patter recognition, v. 2, p. 60-65, 2005.
4. B. B. Avants et al., Neuroinformatics., 9(4):381-400, 2011.
5. W. E. Lorensen and H. E. Cline. *SIGGRAPH Comput. Graph.* 21, 163–169, 1987.
6. G. Taubin, *Proceedings of IEEE International Conference on Computer Vision*, pp. 852-857, 1995.
7. R. Hess, Blender Foundations: The Essential Guide to Learning Blender 2.6. Focal Press; 2010.
8. H. G. Weller et al., Computers in Physics, v. 12, n. 6, p. 620-631, 1998.
9. L. Zarrinkoob et al., Journal of Cerebral Blood Flow & Metabolism, 35, 648-654, 2015.

Structurally protected optically polarized electron spin states of defects in hexagonal Boron Nitride

Victor Soltamov[1,2], Fadis Murzakhanov[1], Georgy Mamin[1]

[1]Institute of Physics, Kazan Federal University, 420008, Kazan, Rassia
[1]Ioffe institute, 194021, Saint Petersburg, Russia
E-mail: victrosoltamov@gmail.com

Introduction

Optically addressable high spin states (S>1/2) of defects in semiconductors are one of the building blocks in the solid-state quantum technologies [1]. Widely studied in the 3D crystals, defects possessing optically addressable high spin states have recently been found in 2D material formed by atomic planes of sp2-hybridized atoms, interconnected through van der Waals forces, namely hexagonal Boron Nitride (hBN) [2,3]. One defect in the form of negatively charged boron vacancy (V_B^-) is of particular interest since its spin-triplet ground state can be addressed and readout by means of optically detected magnetic resonance at room temperature [3]. This unique property of V_B^- defect combined with the inherent two-dimensionality of hBN provides sub-nanoscale closeness of the optically active paramagnetic probe to target samples for high-resolution quantum-sensing. The latter is of special importance since hBN is the most relevant encapsulation material for 2D atomically thin heterostructures built up utilizing the lego-construction concept [4].

Exploration of two dimensional localization of defect spin in hBN

Fig. 1 represents the hBN crystal structure with boron vacancy [5]. To study and explore the spin properties of this defect we use 94 GHz pulsed EPR and EPR-related technique known as an Electron Nuclear Double Resonance (ENDOR) [6].

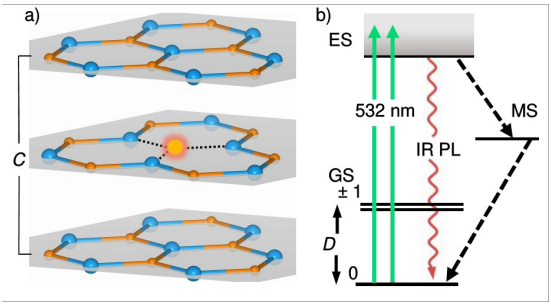

Figure 1. Schematic representation of the hBN crystal structure. Boron vacancy is shown as glowing spot. Nitrogen and boron are shown in blue and brown colors, respectively. Sp^2-hybridized Nitrogen-Boron atoms stacked parallel along the c hexagonal axis, are shown in grey. (b) V_B^- defect energy levels diagram in the absence of external static magnetic field and the scheme of optical pumping cycle of the ground state (GS) $m_S = 0$ spin sublevel. Excitation (green) transfers the system into the excited state (ES). Radiative recombination (purple) and spin-dependent nonradiative intersystem crossings decay to the GS via metastable state (MS) (dashed lines). D denotes the ZFS.

Both these methods form the basis to study the defects' structure through analysis of the hyperfine, quadrupole, and spin-spin interactions extracted from the corresponding EPR and ENDOR data [6]. The results of such studies will be presented and discussed. Namely,

reconstruction of the spin density around the defect site through analysis of isotropic and anisotropic hyperfine interactions with surrounding nuclei will be shown together with its correlation with the ENDOR data. Since nitrogen nuclei of hBN possess nuclear magnetic moment (^{14}N, I = 1) the nuclear quadrupole interaction reflecting an interaction between the ^{14}N nuclear electric quadrupole moment with the electric field gradient, is expected. We probe this interaction through ENDOR and the corresponding NQI constant to be C_q= 2.44 MHz [7].

Having all these data in hands, we are able to show that the spin density of the defect is indeed localised in the single 2D-BN layer. The latter drastically differ this defect from other optically addressable spin defects in 3D crystals, such as diamond or Silicon Carbide, and serves as a prerequisite demonstration toward atomically devices based on optically polarized spin states of defects [8].

Acknowledgements

This work has been supported by the RSF grant number 20-72-10068.

References

1. D. Awschalom, R. Hanson, J. Wrachtrup, and B.B. Zhou, Quantum technologies with optically interfaced solid-state spins. – Nat. Photonics **12**, 516. (2018).
2. A. L. Exarhos, D. A. Hopper, R. N. Patel, M. W. Doherty & L. C. Bassett, Magnetic-field-dependent quantum emission in hexagonal boron nitride at room temperature. – Nat. Commun. **10**, 222 (2019).
3. A. Gottscholl, M. Kianinia, V. Soltamov, S. Orlinskii, G. Mamin, C. Bradac, C. Kasper, K. Krambrock, A. Sperlich, M. Toth, I. Aharonovich, and V. Dyakonov. Initialization and read-out of intrinsic spin defects in a van der Waals crystal at room temperature. – Nat. Mater. **19**, 540 (2020).
4. Geim, A. K. & Grigorieva, I. V., Van der Waals heterostructures. – Nature **499**, 419 (2013).
5. F. F. Murzakhanov, B. V. Yavkin, G. V. Mamin, S. B. Orlinskii, I. E. Mumdzhi, I. N. Gracheva, B. F. Gabbasov, A. N. Smirnov, V. Yu. Davydov and V. A. Soltamov.- Creation of Negatively Charged Boron Vacancies in hexagonal Boron Nitride crystal by electron irradiation and mechanism of inhomogeneous broadening of Boron Vacancy-related spin resonance lines. – Nanomaterials **11**, 1373 (2021).
6. P. G. Baranov, H. J. von Bardeleben, F. Jelezko, J. Wrachtrup, Magnetic Resonance of Semiconductors and Their Nanostructures: Basic and Advanced Applications. – Springer Series in Material Science. Springer, Heidelberg (2017).
7. F.F. Murzakhanov, G.V. Mamin, S.B. Orlinskii, U. Gerstmann, W.G. Schmidt, T. Biktagirov, I. Aharonovich, A. Gottscholl, A. Sperlich, V. Dyakonov, and V.A. Soltamov. Electron-nuclear coherent coupling and nuclear spin readout through optically polarized V_B^- spin states in hBN. – arXiv:2112.10628 (2021).
8. A. Gottscholl, M. Diez, V. Soltamov, C. Kasper, D. Krauße, A. Sperlich, M. Kianinia, C. Bradac, I. Aharonovich and V. Dyakonov. Spin defects in hBN as promising temperature, pressure and magnetic field quantum sensors. – Nat. Commun. **12**, 4480 (2021).

DFT investigation of systems with three coupled NHN hydrogen bonds

Anna A. Titova, Elena Yu. Tupikina

Institute of Chemistry, Saint Petersburg State University, Saint Petersburg, Russia
E-mail: aatitova1210@gmail.com

Introduction

Multiple non-covalent interactions, including hydrogen bonds, playing an important role in design of supramolecular materials with properties of adaptability, ability to recover and controlled decomposition. For the development of this technologies, it is extremely important to investigate the properties of various combinations of proton-donor and proton-acceptor fragments in order to achieve the largest cooperative (mutual enhancing) effect, which can be made, for example, by means quantum chemical methods.

Many systems with a single hydrogen bond are well-studied and described thoroughly in various papers.[1,2] However, in the case of multiple hydrogen bonds, it is necessary to consider cooperative and anticooperative effects, influence of substituents and external conditions.[3–5]

Models

In this work we investigate the geometry and thermodynamic stability of a system with three NH···N hydrogen bonds – heterodimers of diaminopyridines with three hydrogen bonds in two combinations DAD-ADA and ADD-DAA (Figure 1, where D – proton donor, A – proton acceptor) – by means of quantum chemistry.

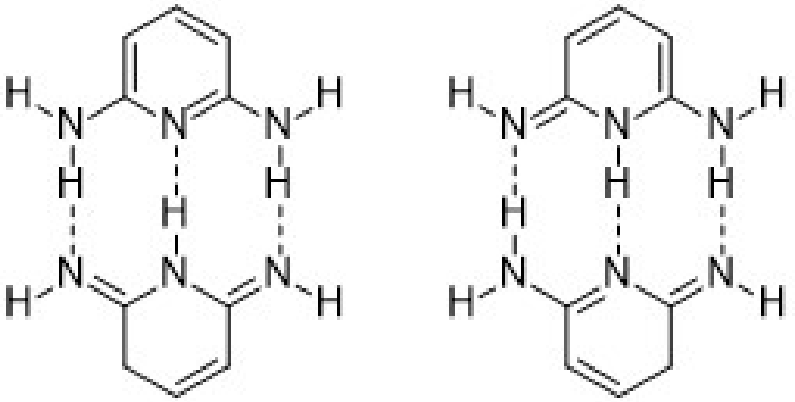

Figure 1. Investigated complexes with three hydrogen bonds DAD-ADA and ADD-DAA

Methods

Calculations were performed at B3LYP/6-311G++G(d,p) level using Gaussian16 software. Structures of studied monomers and dimers were optimized and checked for the absence of imaginary frequencies. NMR parameters were calculated at the same of level of theory using GIAO approach. QTAIM analysis were performed using MultiWFN.

References

1. Grabowski, S. J. (**2020**). Understanding Hydrogen Bonds: Theoretical and Experimental Views. Royal Society of Chemistry.
2. Gilli, G., & Gilli, P. (**2009**). The nature of the hydrogen bond: outline of a comprehensive hydrogen bond theory (Vol. 23). Oxford university press.
3. Tupikina, E. Y., Denisov, G. S., & Tolstoy, P. M. (**2019**). Anticooperativity of $FH\cdots Cl^-$ hydrogen bonds in $[(FH)_nCl]^-$ clusters (n= 1… 6). Journal of Computational Chemistry, 40(32), 2858-2867.
4. Kucherov, S. Y., Bureiko, S. F., & Denisov, G. S. (**2016**). Anticooperativity of FHF hydrogen bonds in clusters of the type $F^-\times(HF)_n$, $RF\times(HF)_n$ and $XF\times(HF)_n$, R= alkyl and X= H, Br, Cl, F. Journal of Molecular Structure, 1105, 246-255.
5. Romero-Montalvo, E., Guevara-Vela, J. M., Costales, A., Pendás, Á. M., & Rocha-Rinza, T. (**2017**). Cooperative and anticooperative effects in resonance assisted hydrogen bonds in merged structures of malondialdehyde. Physical Chemistry Chemical Physics, 19(1), 97-107.

Effect of addition of Al(NO3)3 on molecular mobility in ethylammonium nitrate. A molecular dynamics simulation study

Milosh Ubovich, Andrei V. Egorov, Vladimir. I. Chizhik

Faculty of Physics, Saint-Petersburg State University, Russia
E-mail: ubovich.milosh@yandex.ru

Introduction

At present, the interest in the study of alkylammonium nitrate protic ionic liquids (AN PILs) has grown significantly. PILs consist of ions, but, unlike "classical" salts, they are in a liquid state at a relatively low temperature (from room temperature up to about 100^{o}C). These compounds attract the attention of researchers due to their remarkable properties, such as high thermal stability, low vapor pressure, etc. PILs are used in various electrochemical applications (for example, lithium ion batteries, fuel cells, etc.). AN PILs attract the attention by an unusual combination of properties (in particular, they have a relatively low cost and low toxicity). Ethylammonium nitrate (EAN) is a typical substance among AN PILs. Mixtures of EAN (Fig. 1) and aluminum nitrate ($Al(NO_3)_3$) were chosen as the main object of the present study.

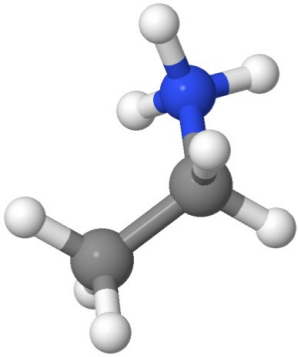

Figure 1. The schematic representation of cation ethylammonium nitrate (hydrogen – white, nitrogen – blue, carbon – grey)

An attempt was made to investigate the mechanisms of changes in molecular mobility, when adding aluminum nitrate to the EAN, by the molecular dynamics simulations. The main goal was not only to quantify the kinetic characteristics of the components in the mixture at their different ratios but also to identify the relationship between the peculiarities of the local structure that observed, when salt is added, and the processes of rotational reorientation of ions.

Simulation details and results

In the research the pure ionic liquid (EAN without additives) and mixtures containing aluminum nitrate were simulated using the MD method. The simulation was carried out in a cubic cell with periodic boundary conditions in the isothermal-isobaric ensemble at 298 K and 1 atm. employing the MDynaMix simulation package [1]. The temperature was kept constant with a Nose-Hoover thermostat [2, 3], and the pressure was maintained with a Hoover barostat [4]. The ethylammonium cation (EA^{+}) was modeled employing the potentials

described in Ref. [5, 6]. A model nitrate anion (Fig. 2) was treated as a 4-site planar structure with the central nitrogen atom and three oxygen atoms at the distance of 1.22 Å with all O-N-O angles of 120° [7]. Its intermolecular interactions were described by the sum of Coulomb and Lennard-Jones (6-12) potentials. Three different potential parameter sets, taken from Refs. [5, 8, 9], were considered. The interaction potential of the model aluminum ion was also the sum of Coulomb and Lennard-Jones (6-12) potentials, the potential parameters were described in Ref. [10]. Simulation time was 1 ns.

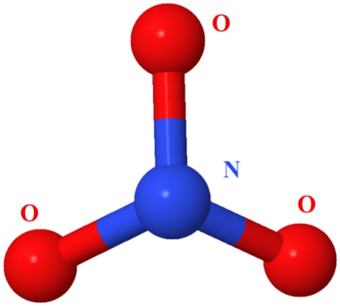

Figure 2. A schematic representation of nitrate anion

The radial distribution functions, self-diffusion coefficients, and reorientation times of the intramolecular vectors of the nitrate anion and EA^+ cation were calculated for each model systems in this research. As part of the study, it was shown that with an increase in the concentration of $Al(NO_3)_3$, the processes of reorientation of the nitrate anion and the translational motions of the components of the system under study slow down. It was demonstrated via the calculation of the radial distribution functions that the aluminum ion does not penetrate into the nearest environment of the EA^+ cation. However, the appearance of three-charged aluminum ions has a noticeable effect on the ordering of nitrate anions, including those in the environment of the EA^+ cation. This leads to the slowdown in the rotational reorientation of the nitrate anion.

It is planned to compare the results obtained with experimental NMR data (NMR diffusometry and NMR relaxation).

References

1. Lyubartsev A. P., Laaksonen A. – Comp. Phys. Comm. 2000. V. 128. No. 3. P. 565.
2. Nose S. – Mol. Phys. 1984. V. 52. No. 2. P.255.
3. Martyna G. J., Tobias D. J., Klein M. L. – J. Chem. Phys. 1994. V. 101. No. 5. P. 4177.
4. Martyna G. J., Tuckerman M. E., Tobias D. J., et al. – Mol. Phys. V. 87. No. 5. P. 1117.
5. Umebayashi Y., Chung W.-L., Mitsugi T., et al. – J. Comput. Chem. Jpn. 2008. V. 7. No. 4. P. 125.
6. Choe J., Kim K., Chang S. – Bull. Korean Chem. Soc. 2000. V. 21. P. 200.
7. Ebner C., Sansone R., Hengrasmee S., et al. – Int. J. Quant. Chem. 1999. V. 75. P. 805.
8. Megyes T., Balint S., Peter E., et al. – J. Phys. Chem. B. 2009. V. 113. No. 13. P. 4054.
9. Laaksonen A., Kovacs H. – Can. J. Chem. 1994. V. 72. P. 2278.
10. Faro T. M. C., Thim G. P., Skaf M. S. – J. Chem. Phys. 2010. V. 132. P. 11450.

Investigation of liquid-liquid phase transition in gallium alloys under nanoconfinement

Vasilev A.A. [1], Podorozhkin D.Y. [1]

[1] Faculty of Physics, Saint Petersburg State University, Saint Petersburg, Russian Federation
E-mail: Allisher93529@yandex.ru

Introduction

The study of the structural transformations in liquids is an active research field at the present time. In this regard, liquid-liquid phase transition (LLPT) in gallium alloys is of special interest due to the ability of gallium to be supercooled. Embedding such liquids in nanoporous matrices allows alloys to be supercooled to temperatures much lower than the melting temperatures, which raises expectations that LLPT can be found in liquids under nanoconfinement.

The present study has been carried out by using NMR technique, which is an instrument powerful enough for obtaining the information about the internal structure of liquids and solids through measurements of the Knight shift. The ^{71}Ga and ^{115}In NMR measurements of the Knight shift have been obtained in a ternary Ga-In-Sn alloy, embedded in porous glass, with the view to found LLPT.

Experiment

The ternary eutectic Ga-In-Sn (Ga−75at.%, In−17at.% и Sn−8at.%) alloy is embedded in the porous glass with the mean diameter of the pores 18 nm under pressure up to 10 kbar. From loaded opals the samples for NMR studies were cut in the shape of parallelepipeds 3 × 3 × 6 mm.

Studies were carried out using NMR Bruker Avance 400 pulse spectrometer at magnetic field 9.4 T.

Results

The Fig. 1 shows the evolution of the ^{71}Ga NMR spectrum. It can be seen that the high-frequency signal occurs at the temperature 234 K. One can conclude from the width of the line that this high-frequency component corresponds to a liquid phase. The relative integral intensity of the high-frequency component increases, whereas the relative integral intensity of the low-frequency component decreases upon cooling. The last one disappears at the temperature 210 K. The high-frequency signal disappears at the temperature 172 K, which corresponds to the crystallization of gallium.

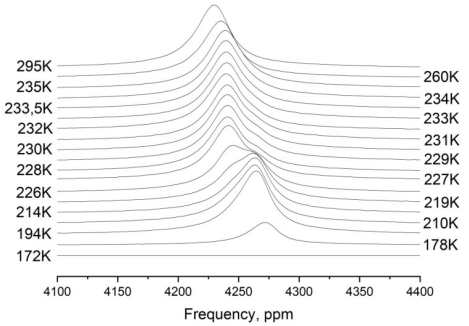

Fig. 1 The evolution of the 71Ga NMR spectrum.

The appearance of the high-frequency component in ^{71}Ga spectrum might relate to changes in relative density of an alloy. According to this assumption the high-frequency signal corresponds to the alloy region where the presence of indium is negligible.

However, it can be seen from the Fig. 2 that the high-frequency signal appears earlier than indium starts melting, which allows us to conclude that this assumption is unlikely to be plausible and the liquid-liquid phase transition might take place under conditions in question.

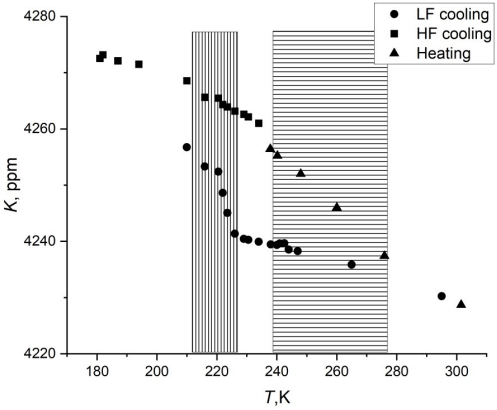

Fig. 2 The temperature dependence of the ^{71}Ga Knight shift for the full freezing-melting cycle. The bar with vertical lines – crystallization of indium, the bar with horizontal lines – melting of indium.

The Knight shift has been measured for the incomplete cycles in order to confirm the hypothesis about the liquid-liquid phase transition.

NMR studies revealed changes in behavior of the ternary Ga-In-Sn alloy in comparison with the bulk alloy. It has been found that the splitting of ^{71}Ga NMR lines in two components is followed by the gradual transformation of low-frequency signal into the high-frequency one upon cooling. A step-like splitting of the Knight shift in gallium has been detected in the alloy region where the presence of indium is negligible. The NMR measurements proved that the line splitting occurs due to LLPT under nanoconfinement within a temperature range where the coexistence of two spectral components is seen. It is worth noting that the splitting of the 71Ga NMR line was not found in a binary Ga-Sn alloy, embedded in a porous glass and porous matrices, which allows us to conclude that LLPT is sensitive to the alloy composition.

References

1. C. Tien. E.V. Chanaya, W. Wang, Y.A. Kumzerov, D. Michel. Phys. Rev. B 74, 024116 (2006).
2. Д.Ю. Нефедов, Е.В. Чарная, А.В. Усков, Д.Ю. Подорожкин, А.О. Антоненко, J. Haase, Ю.А. Кумзеров. Физика Твёрдого Тела 61, 169 (2019).
3. D.Y. Nefedov, D.Y. Podorozhkin, E.V. Charnaya, A.V. Uskov, J. Haase, Y.A. Kumzerov, A.V. Fokin. Phys. Condens. Matter 31, 255101 (2019).

The self-diffusion of 128-arm star-shaped polydimethylsiloxanes with a dendritic branching center.

Sergey G. Vasil'ev[1], Ksenia V. Panicheva[1,2]

[1]Institute of Problems of Chemical Physics, Chernogolovka 142432, Moscow Oblast, Russia
[2]Faculty of Fundamental Physical-Chemical Engineering, Lomonosov Moscow State University, GSP-1, Moscow 119991, Russia
E-mail: viesssw@mail.ru

Preparation of new materials with controllable properties which combine the advantages of various classes of soft matter attracts considerable attention of researchers. Linear polymers and colloids are the most studied classes of soft materials. These classes represent two extreme cases among possible connectivity of monomers in a macromolecule. In the first case, the molecule is a flexible chain of links, while in the second, the structure is rigid and compact (for example, spherical). Differences in architecture lead to significant differences in the dynamics of these macromolecules, and, consequently, in the physical properties of materials. Beside these, many materials have been created that occupy an intermediate position between the mentioned classes, combining the properties of colloidal particles and polymers. Combining these properties has great potential to produce new materials with the desired characteristics. Such intermediate classes include dendrimers, dense molecular brushes, nanogels, and multiarm stars.

In this work, the self-diffusion of new star-shaped 128-arm polydimethylsiloxanes (PDMS) based on a 6th carbosilane dendrimer with different arm lengths were investigated [1]. The measurements were performed using stimulated spin echo experiment on a Bruker Avance III 400 spectrometer on 1H nuclei.

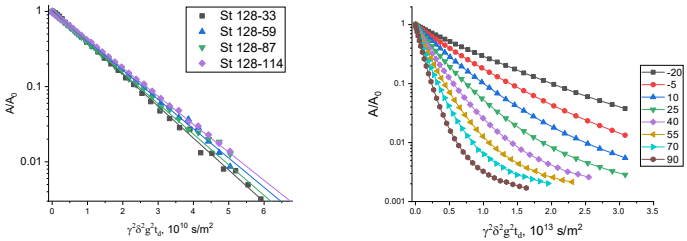

Figure 1. The diffusion decays for 128-arm star-shaped PDMS: diluted solutions in toluene for samples with different arm lengths (left) and neat stars with the arm length of 59 units at different temperatures (right).

The graph shown on the left side of Fig. 1 demonstrate the diffusion decays for samples with different arm lengths in diluted solutions of toluene (about 1 % of polymer). The shapes of the decays are exponential confirming the narrow molecular weight distributions of the investigated polymers. The hydrodynamic radii calculated using Stokes-Einstein formula give the values in the range of 4-4.6 nm. For the samples in the absence of the solvent the diffusion decays are clearly deviate from a single exponential decay as shown in the right side of Fig. 1. Intuitively the appearance of such polydispersity of the diffusing species can be explained by the formation of some aggregates or regions with different mobility. In such cases the dynamics is expected to be time dependent but the experiments with different diffusion times didn't show the changes of the diffusion decays. The liquid appears homogeneous and transparent in the absence of solvent.

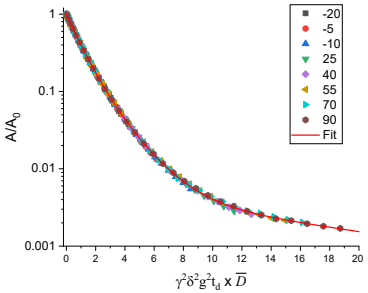

Figure 2. The diffusion decays for 128-arm star-shaped PDMS with the arm length of 59 units at different temperatures.

It was also found that the shape of the diffusion decays does not depend on temperature for the melts of 128-arm star-shaped PDMS. This is shown in Fig. 2 for one of the samples. Fig. 2 represents the data of the right side of Fig. 1 but the x axis is multiplied by the average self-diffusion coefficient determined at each temperature from the initial slope of the decay. Similar behavior is observed for other samples with different arm lengths. Similar changes of the diffusion decays were not observed for the melts of siloxane dendrimers [2] having the similar chemical composition but smaller hydrodynamic radii (0.5-1.4 nm). These data may indicate that the observed changes of the diffusion decays are related with the peculiarities of the self-diffusion of the multiarm star polymers itself and not the intermolecular interactions.

Acknowledgements

This work was done as a part of the state task (registration no. AAAA-A19-119071190017-7).

This work was supported by the Russian Foundation for Basic Research (grant 20-03-00147).

References

1. Tikhonov, P. A., Vasilenko, N. G., Gallyamov, M. O., Cherkaev, G. V., Vasil'ev, V. G., Demchenko, N. V., Buzin, M. I., Vasil'ev, S. G., Muzafarov, A. M. Molecules 26(11), 3280 (2021).
2. K. Boldyrev, A. Chernyak, I. Meshkov, A. Muzafarov, E. Tatarinova, S. Vasil'ev Soft Matter V. 16, 9712-9725 (2020)

Structural Magnetic Resonance Imaging in Alzheimer's Disease. NeuroEPO Clinical Trial

Ariel Viña-González[1], Iris Rodríguez Gil[1], Leslie Pérez Ruiz[2], Teresita Rodríguez Obaya[2], Evelio González Dalmau[1]

[1]*Cuban Center for Neuroscience, La Habana, Cuba.*
[2]*Center of Molecular Immunology, La Habana, Cuba.*
E-mail: ariel.vina@cneuro.edu.cu
https://www.researchgate.net/profile/Ariel-Vina-Gonzalez

Introduction

The structural magnetic resonance imaging (sMRI) is used in clinical investigations to follow-up brain structural changes in several diseases. Recently the Cuban Phase II/III NeuroEPO Clinical Trial was finished and sMRI was used as a biomarker of neurodegeneration as part of the A/T/N classification scheme of the disease declared by the National Institute on Aging and Alzheimer's Association (NIA-AA) [1]. Hippocampal volume (HV) is recognized as a surrogate imaging biomarker for the study of Alzheimer´s Disease (AD) and is widely used in clinical trials [2]. The propose of this research was the automatic longitudinal hippocampal volume quantification of the patients for a year to document the drug effect. The variables analyzed for this cerebral structure were the annual percent change rate (%AC) and asymmetry index (AI). The sample consist on 98 subjects diagnosed with possible mild or moderate AD, with mean ages of 73.77 ± 6.74 years. The study sample was divided in three groups: two groups treated with different initial doses (0.5 mg and 1.0 mg) and a placebo.

MRI Protocol

In this investigation was used the pulse sequences recommended by the Alzheimer's Disease Neuroimaging Initiative (ADNI) [3], adapted to the Siemens Magnetom Allegra 3.0 T scanner installed at the Cuban Center for Neuroscience (Table 1). This pulse sequence was selected to identify comorbidities during subject recruitment. The quality control of scanner performance was certified by the Cuban health regulatory entity CECMED (Centro para el Control Estatal de Medicamentos, Equipos y Dispositivos Médicos) and no hardware/software upgrades were performed during the course of the investigation. Total study time per patient was ranged from 38 to 40 min; patients were instructed to remain still, awake, with their eyes closed and in supine position. 3D sagittal sequences was acquire with axial and coronal reconstruction. T1-3D MP-RAGE was selected to perform the automatic hippocampal segmentation.

Processing Pipeline

The software used to perform the MRI processing was FreeSurfer 6.0, implemented in the high performance computer available in the laboratory. His choice was based on a previous investigation where we carried out an analysis of its usefulness for this pathology [4]. Unlike cross-sectional processing, longitudinal processing allows to follow up the subject treatment with better sensitivity to structural changes. We use the standard recon-all stream for longitudinal processing, divided in three steps and adding specific flags to the command line as are described in detail in a previous paper [5].

Table 1. Pulse sequences used

Sequence	Voxel Size (mm^3)	Time (ms)	Duration (min)	Propose
T1-3D MP-RAGE	0.8x0.8x1	TE=2.6 TR=2000 TI=900	9:19	T1-weighted structure analysis; also may be used as source of spatial information in PET imaging
T2-weighted 2D	0.5x0.5x2	TE=101 TR=8020	5:37	Discard stroke and Hippocampal subfield measurement
FLAIR 3D	0.5x0.5x1	TE=353 TR=4800 TI=1650	8:24	White matter disease, infarction, pathology. May be used in conjunction with MP-RAGE for multi-spectral tissue segmentation
T2 *	0.86x0.86x4	TE=20 TR=650	2:43	Cerebral microbleed assessment
Tractography of 12 directions	1.8x1.8x2	TR=8000 TE=86	01:54	Map brain connectivity
Resting state fMRI	3x3x3	TR=2590 TE=30	6:34	Cerebral zones activation study

This kind of processing stream creates an unbiased within-subject template space and average image using robust, inverse consistent registration. Information from this subject template is used to initialize the longitudinal image processing in several locations to increase repeatability and statistical power. The image quality control acquisition and postprocessing process was made by visual inspection to discard images non-processable due to artefacts and errors in the segmentations. Additionally, to obtain better image quality results, the geometric distortion correction and increase of signal noise ratio using adaptive Gaussian filter was used. FreeSurfer in his own algorithm made an image pre-processing step to correct the variation in intensity due to the B1 bias field. And finally for a better correspondence to the 3T magnetic field was added the <– 3T> flag to correct image intensity.

Results

No significant difference was encountered in the initial values and %AC of HV for the three groups. Analyzing the result by groups of treatment, the placebo group show the higher asymmetry and the lowest HV even when his initial average values was better that the other's group. Supporting the mild and moderate stage of disease diagnosis made by the neurologists, higher average values of HV was identified in mild subject versus moderate with significant differences around 2% (Fig. 1). The sensitivity of the method could be explained by the utilization of a higher voxel resolution of $0.8mm^3$ versus $1mm^3$ recommended by ADNI. The placebo group show a higher atrophy in left hippocampus (4.16%) versus right (2.47%).

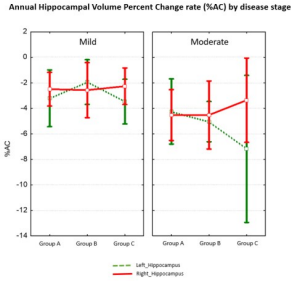

	Mean of %AC	
Stage	Left_Hipp	Right_Hipp
Mild	-2.973	-2.530
Moderate	-5.273	-4.568
T-test	$p = 0.0126$	$p = 0.0153$

Figure 2. Annual percent change rate of hippocampal volume of the three groups at baseline (identified with star symbol) and final stage.

Conclusions

The adequacy of the pulse sequences allowed an increase in the sensitivity of the measurement method. This could have allowed the differentiation of the stages of each group, demonstrating the robustness and sensitivity of the measurement method. The automatic pipeline for the longitudinal processing of brain structures and, in particular the hippocampus, was implemented for clinical studies.

Acknowledgements

To thank the Ministry of Science, Technology and Environment of the Republic of Cuba (CITMA) for the Financial Fund for Science and Innovation (FONCI).

References

1. Jack Jr, Clifford R., et al. "NIA-AA research framework: toward a biological definition of Alzheimer's disease." Alzheimer's & Dementia 14.4 (2018): 535-562.
2. Kim, Gwang-Won, et al. "A pilot study of brain morphometry following donepezil treatment in mild cognitive impairment: volume changes of cortical/subcortical regions and hippocampal subfields." Scientific reports 10.1 (2020): 1-11.
3. Jack Jr, Clifford R., et al. "The Alzheimer's disease neuroimaging initiative (ADNI): MRI methods." Journal of Magnetic Resonance Imaging: An Official Journal of the International Society for Magnetic Resonance in Medicine 27.4 (2008): 685-691.
4. Viña-González, Ariel, et al. "Volumetric measurement of the hippocampus in a series of patients with Alzheimer disease." Neurology Perspectives 1.3 (2021): 149-159.
5. Viña González, Ariel, et al. "Procesamiento longitudinal de IRM para documentar el efecto de medicamentos en ensayos clínicos." Ingeniería Electrónica, Automática y Comunicaciones 42.3 (2021): 71-81.

Application of ^{59}Co Internal Field NMR for determination of size and structure of Co nanoparticles

Ilya V. Yakovlev[1,2,3], *Jean-Baptiste d'Espinose de Lacaillerie*[3], *Olga B. Lapina*[1,2]

[1]*Novosibirsk State University, Novosibirsk, Russia*
[2]*Boreskov Institute of Catalysis, Novosibirsk, Russia*
[3]*SIMM, ESPCI Paris, Paris France*
E-mail: iv_yakovlev@catalysis.ru

Introduction

Since its first observation by Gossard and Portis in 1959 [1], ^{59}Co NMR in ferromagnetic materials (^{59}Co Internal Field NMR, ^{59}Co IF NMR) has been applied extensively to the study of Co micro- and nanostructures. This technique provides data on the distribution of the local magnetic field acting on the nuclear spins and the RF enhancement coefficient. In turn, these quantities depend on the crystalline and magnetic structure of the studied material as well as its morphology. ^{59}Co IF NMR has been applied successfully to describe the structures of various alloys and 2-dimensional layered materials due to the relatively simple dependence of the local field on the presence of guest atoms in the local environment of Co nuclei.

Co nanparticles present great interest due to their exceptional physicochemical properties in various fields of science and technology such as heterogeneous catalysis, energy storage, electromagnetic shielding etc. However, the application of ^{59}Co IF NMR to the study of Co nanoparticles remains somewhat hindered due to the complex influence of the structure, morphology, shape factor and interparticle interactions on the spectral line shapes. Thus, in order to reliably determine the influence of these factors on the ^{59}Co IF NMR spectra a careful sample design and preparation procedure is required.

In this work, we demonstrate two examples of application of ^{59}Co IF NMR to the study of small isolated Co nanoparticles supported on high surface area materials.

Temperature-dependent superparamagnetic - ferromagnetic transitions

Co nanoparticles have been supported on small multi-walled carbon nanotubes (MWCNT) with the inner diameter of roughly 4 nm by incipient wetness impregnation with subsequent reduction by hydrogen. In order to obtain a narrow Co nanoparticles size distribution, the weight fraction of Co metal was chosen to be roughly 5 wt.%. This led to formation of nanoparticles located exclusively inside the inner channels of MWCNTs, which limited the transverse size of the nanoparticles to ~4 nm as demonstrated by high-resolution TEM.

The varied-temperature ^{59}Co IF NMR experiments have demonstrated that the majority of Co nanoparticles underwent a superparamagnetic-ferromagnetic transition between room temperature and 30 K, which led to a 40-fold difference of spectral intensity. The occurrence of such transitions was confirmed using the ferromagnetic resonance (FMR) spectroscopy technique that allowed us to provide an estimate for the thermal flip time constant that determines the critical temperature (or volume) for transition into the superparamagnetic state.

Thus, we have demonstrated that ^{59}Co IF NMR is a viable bulk (as opposed to HRTEM) technique for determination of particle size distribution as first proposed by Liu et al. [2].

Epitaxy of cobalt nanoparticles on the surface of alumina supports

Two sets of samples were synthesized with different weight fractions of metallic Co supported on the surfaces of nanodisperse metastable aluminas γ-Al_2O_3 and χ-Al_2O_3. Using HRTEM and ^{59}Co IF NMR we were able to demonstrate that in the case of γ-Al_2O_3 strong metal-support interaction leads to a high degree of dispersion of Co nanoparticles over the surface of the support in the form of small (< 5 nm) nanoparticles that are mainly represented by fcc Co crystal structure. In the case of χ-Al_2O_3 we have also observed a strong metal-support interaction, but due to the morphology of the supporting surface it led to the epitaxy of Co nanoparticles in the form of larger nanoparticles predominantly having hcp crystal structure. These results are relevant in the Fischer-Tropsch synthesis process, where the activity and selectivity of Co catalysts highly depend on the structure and morphology of the nanoparticles. According to the existing literature data Co nanoparticles sized in the range of 10-15 nm and having hcp crystal structure demonstrate much higher activity and selectivity towards C_{5+} hydrocarbons.

Acknowledgements

This work is supported by the Ministry of Science and Higher Education of the Russian Federation within the governmental order for Boreskov Institute of Catalysis (project AAAA-A21-121011390054-1).

References

1. A. Gossard, A. Portis, Observation of Nuclear Resonance in a Ferromagnet, *Phys. Rev. Lett.* 3, 164-166 (**1959**)
2. Y. Liu, B. de Tymowski, F. Vigneron, I. Florea, O. Ersen, C. Meny, P. Nguyen, C. Pham, F. Luck and C. Pham-Huu, Titania-Decorated Silicon Carbide-Containing Cobalt Catalyst for Fischer–Tropsch Synthesis, *ACS Catalysis* 3, 393-404 (**2013**)

Poster Session

Diffusion of Toluene and Methanol in composopzite systeme: Poly-m-Phenyleneisophthalomide and MOF By Molecular Dynamics Simulations

Vladimir Y. Bazaykin,[1] Denis A. Markelov,[1] Andrei V. Komolkin,[1]

[1]Saint Petersburg State University, 7/9 Universitetskaya nab., St. Petersburg 199034, Russia
E-Mail: st084938@student.spbu.ru

Introduction

Purification of material is a historically actual problem. Today, the cleaning technology consists of a several inalienable elements: energy efficiency, environmental friendliness, as we mentioned earlier high degree of purity. One of the technologies that contains each of the above elements is pervaporation.

This method is utilized for difficult-to-separate liquids using a polymer membrane through which only one component of the mixture predominantly passes. To improve this process, polymeric materials are modified with metal-organic complex structures.

Organometallic frameworks (MOF's) are used by a class of hybrid materials in which metal ions are interconnected by organic molecules. MOF has a microporous structure with dimensions of several tens of nanometers and can be one-, two-, or three-dimensional.

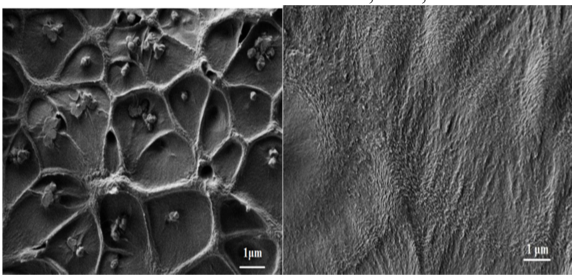

Fig. 1. SEM data of membrane cross-section with MOF (left) and without MOF (right)

Details of simulating

Using the molecular dynamics method, we have added liquid molecules (36 methanol molecules and 26 toluene molecules) to previously assembled systems: one system contained only linear chains of poly-m-phenylene isophthalomide (PFI), while the second one contained a MOF UiO-66 (NH2) nanoparticle. Liquid molecules are separated in the process of pervaporation where the simulated material is used as a separating membrane.

First, we equilibrated the systems at 800K, then slowly cooled it down to room temperature – 300K, and finally simulated 140ns at room temperature as an equilibrium trajectory.

After the systems were assembled, for its quick equilibrating, the simulation was carried out at a temperature of 800K. Trajectory length at 800K was 50 ns. Then, the system was cooled to 300 K in 100 ns. The density of the system at this temperature, $\rho \approx 1238$ kg/m3, was close to the experimental one [1]. Finally it was simulated 140ns at room temperature as an equilibrium trajectory.

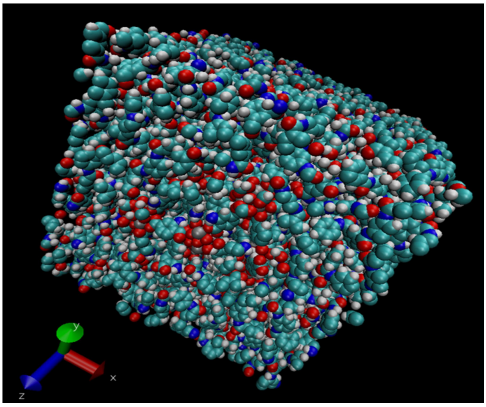

Fig. 2. Instant simulating cell configuration with MOF.

Results and discussion

We have established that follow important results:

1)The translational mobility of methanol in the system with MOF is much faster than in its absence. It can be argued that due to MOF, channels for fast diffusion are created.

2)The mobility of toluene is much slower than that of methanol in systems, both with and without MOF, the method used does not allow us to study the difference in diffusion of toluene in systems, due to the strongly slow translational mobility of toluene molecules.

3) The methanol passes through the MOF much faster than through the pure polymer, even though the toluene molecules are practically stuck.

Conclusion

Summarizing, the addition of MOF nanoparticles improves the characteristics of polymeric membranes for the separation of a mixture of toluene and methanol, since this practically does not affect the mobility of toluene through the membrane and accelerates the diffusion of methanol by several times. Our results are in good agreement with experimental data [1].

Acknowledgments

The simulations have been performed by using the Computer Resources Center of Saint Petersburg State University. .

References

1. A.V. Penkova, A.I. Kuzminova, M.E. Dmitrenko, V.A. Surkova, V.P. Liamin, D.A. Markelov, A.V. Komolkin, D.Y. Poloneeva, A.V. Laptenkova, A.A. Selyutin, A.S. Mazur, A.V. Emeline, S.Thomas, S.S. Ermakov / *Sep. Purif. Technol*., 2021, 263, 118370

Histidine-rich lysine-based dendrimer and its interaction with molecules of therapeutic tetrapeptide at two different pH

Valeriy V. Bezrodnyi[1,2], Emil I. Fatullaev[2], Sofia E. Mikhtaniuk[2], Oleg V. Shavykin[1,2,3], Igor M. Neelov[1,2], Anatoly A. Darinskii[4], Nadezhda N. Sheveleva[1] and Denis A. Markelov[1]

[1]St. Petersburg State University, 7/9 Universitetskaya nab., 199034 St. Petersburg, Russia
[2]St. Petersburg National Research University of Information Technologies, Mechanics and Optics (ITMO University), Kronverkskiy pr. 49, 197101 St. Petersburg, Russia
[3]Tver State University, Zhelyabova St., 33, 170100 Tver, Russia
[4] Institute of Macromolecular Compounds RAS, Bolshoi pr.31, 199004, St.Petersburg, Russia
E-mail: kupala-89@mail.ru

Introduction

In recent years several novel peptide dendrimers have been synthesized, studied experimentally and using MD simulation [1-7]. It has been shown that dendrimer with linear double histidine (2His) inserts have some specific features for gene delivery in comparison with Lys2Arg and Lys2Lys dendrimers with double arginine (2Arg), double lysine (2Lys) and double histidine (2His) inserts [8, 9]. In this study, we used molecular dynamics simulation to study Lys-2His dendrimers with linear histidine inserts in wide temperature range (from 280 K to 340 K) and at two pH: Lys2His with neutral histidine (His) at normal pH and Lys2Hisp with protonated histidine (Hisp) at low pH in water. We studied both single dendrimers and dendrimers with 16 therapeutics tetrapeptides molecules. We used MD method described by us earlier [10-13] and functions described in other simulations using BD [14] and SCF approaches [15-16].

Structure

We used the radius of gyration Rg to estimate the size of the Lys2His and Lys2Hisp dendrimers. It was shown (Fig. 1a) that the size of Lys2Hisp at low pH values is significantly larger than that of Lys2His at normal pH due to the higher charge of the Lys2Hisp dendrimer. A small value of the asphericity parameter α (Fig. 1b) indicates that both dendrimers have a shape close to spherical. At both pH values, the size Rg of the dendrimer and its asphericity α are not sensitive to temperature changes (see Fig. 1). The Lys-2His dendrimer has a dense and almost “dry” interior, while Lys2Hisp is swollen.

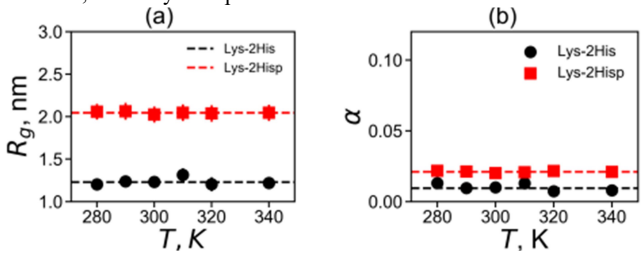

Figure 1. The temperature dependencies of (a) the mean-squared radius of gyration R_g and (b) the shape anisotropy α. All data for Lys-2His and Lys-2Hisp.

The Imidazole Pairing

In this work, we check does pairing effect strong enough to affect the properties of new peptide dendrimers. Lys-2Hisp dendrimer has a large positive charge. Counterions could penetrate into it and partly decrease the effective charge. Both dendrimers form approximately the same number of hydrogen bonds with water. At the same time there is large number of

intra-dendrimeric hydrogen bonds in collapsed Lys-2His dendrimer while they are practically absent in swollen Lys-2Hisp dendrimer. Figure 2 shows the dependence of the number of histidine-histidine pairs (yellow colour corresponds to greater number of such pairs) as function of the angle between the planes of the two histidine imidazole rings and the distance between centers of these rings. We have demonstrated that collapsed Lys-2His dendrimer forms large number of pairs between imidazole rings (with neutral His at normal pH) than swollen Lys-2Hisp (at low pH and charged Hisp groups).

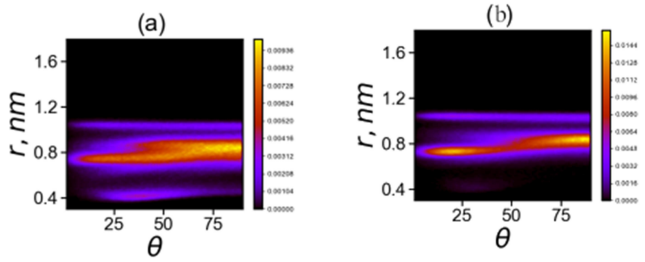

Figure 2. The number $N_{pairs}(\theta, r)$ of neighboring pairs of imidazole rings as function of angle (θ) and distance (r) between imidazole rings for (a) Lys–2His, (b)Lys– 2Hisp (b). T = 310 K.

The Interaction of Dendrimers with Therapeutic Tetrapeptide

We also considered the ability of Lys2His and Lys2Hisp dendrimers to attract oppositely charged 16 AEDG peptides. Lys-2Hisp dendrimer attracts almost all 16 peptide molecules while Lys-2His only 9 of them. For swollen Lys-2Hisp dendrimer with charged interior the value of R_g of the complex almost coincides with R_g of dendrimer, while the size of the complex of collapsed dendrimer Lys-2Hisp increases when peptide molecules mainly stay on surface of this dendrimer and do not penetrate into its neutral and “dry” core.

Table 1. The size (Rg) of dendrimers in complexes and Rg of complexes. (Two parameters s = 1.5 and 2 determine radius when peptide molecules accounted as adsorbed on dendrimer. The results practically do not depend on the value of this parameter.)

	Lys-2His		**Lys-2Hisp**	
	s=1.5	**s=2**	**s=1.5**	**s=2**
$R_{g,dendrimer}$	1.22	1.22	1.57	1.57
$R_{g,complex}$	1.46	1.47	1.63	1.63
n^{lc}	8.98	9.29	15.64	15.70

Acknowledgements

This work is supported by RFBR grant 20-53-12036. The research is carried out using the equipment of the shared research facilities of HPC computing resources at Lomonosov Moscow State University, Computer Resources Center of Saint Petersburg State University and the HybriLIT heterogeneous platform (JINR LIT) [17].

References

1. Sheveleva, N.N.; Markelov, D.A.; Vovk, M.A.; Mikhailova, M.E.; Tarasenko, I.I.; Neelov, I.M.; Lahderanta, E. NMR studies of excluded volume interactions in peptide dendrimers. Sci. Rep. 2018, 8, 8916.

2. Mikhtaniuk S.E., Bezrodniy V.V., Shavykin O.V., Neelov I.M., Sheveleva N.N., Penkova A.V., Markelov D.A. Comparison of Structure and Local Dynamics of Two Peptide Dendrimers with the Same Backbone but with Different Side Groups in Their Spacers//Polymers, 2020, 12, No. 8, 1657
3. Sheveleva, N. N.; Markelov, D. A.; Vovk, M. A.; Mikhailova, M. E.; Tarasenko, I. I.; Tolstoy, P. M.; Neelov, I. M.; Lähderanta, E. Lysine-Based Dendrimer with Double Arginine Residues. RSC Adv. 2019, 9, 18018−18026.
4. Bezrodnyi, V. V.; Shavykin, O. V.; Mikhtaniuk, S. E.; Neelov, I. M.; Sheveleva, N. N.; Markelov, D. A. Why the Orientational Mobility in Arginine and Lysine Spacers of Peptide Dendrimers Designed for Gene Delivery Is Different? Int. J. Mol. Sci. 2020, 21, 9749.
5. Sheveleva, N. N.; Markelov, D. A.; Vovk, M. A.; Tarasenko, I. I.; Mikhailova, M. E.; Ilyash, M. Y.; Neelov, I. M.; Lahderanta, E. Stable Deuterium Labeling of Histidine-Rich Lysine-Based Dendrimers. Molecules 2019, 24, 2481.
6. Bezrodnyi V.V., Mikhtaniuk S.E., O. V. Shavykin, I. M. Neelov, N. N. Sheveleva, D. A. Markelov Size and Structure of Empty and Filled Nanocontainer Based on Peptide Dendrimer with Histidine Spacers at Different pH // Molecules 2021, 26, 6552.
7. Sheveleva N.N., Bezrodnyi V.V., Mikhtaniuk S.E., Shavykin O.V., Neelov I.M., Tarasenko I.I., Vovk M.A., Mikhailova M.E., Penkova A.V., Markelov D.A. Local Orientational Mobility of Collapsed Dendrimers, Macromolecules, 2021, 54, 23
8. Gorzkiewicz, M., Konopka, M., Janaszewska, A., Tarasenko I.I., Sheveleva N.N. Neelov I.M., Klajnert-Maculewicz, B. Application of new lysine-based peptide dendrimers D3K2 and D3G2 for gene delivery: Specific cytotoxicity to cancer cells and transfection in vitro, Bioorganic Chemistry 2020, 95, 103504.
9. Gorzkiewicz, M.; Kopeć , O.; Janaszewska, A.; Konopka, M.; Pędziwiatr-Werbicka, E.; Tarasenko, I. I.; Bezrodnyi, V. V.; Neelov, I. M.; Klajnert-Maculewicz, B. Poly(Lysine) Dendrimers Form Complexes with SiRNA and Provide Its Efficient Uptake by Myeloid Cells. Int. J. Mol. Sci. 2020, 21, 3138.
10. Darinskii, A.A., Zarembo, A., Balabaev, N.K., Sundholm, F. Anisotropy of diffusion in a liquid crystalline system of semi-flexible polymer chains, Physical Chemistry Chemical Physics, 2003, 5(11), 2410–2416.
11. Ennari, J., Neelov I. Sundholm, F. Simulation of a PEO based solid polyelectrolyte, comparison of the CMM and the Ewald summation method, Polymer, 2000, 41, 2149.
12. Neelov, I.M., Shavykin, O.V., Ilyash, M.Y., Bezrodnyi V.V., Mikhtaniuk S.E., Darinskii, A.A., Leermakers, F.A.M Application of high-performance computing for comparison of two highly branched lysine molecules of different topology, Supercomputing Frontiers and Innovations, 2018, 5 (3), 60-64
13. Falkovich, S.G., Darinskii, A.A. Mechanism of shear deformation of a coiled myosin coil: Computer simulation. Polymer Science - Series A, 2010, 52(6), 662–670.
14. Shavykin, O.V., Mikhailov, I.V., Darinskii, A.A., Neelov I.M., Leermakers, F.A.M. Effect of an asymmetry of branching on structural characteristics of dendrimers revealed by Brownian dynamics simulations, Polymer, 2018, 146, 256-266
15. Okrugin, B., Ilyash, M., Markelov, D., Lysine dendrigraft nanocontainers. Influence o topology. Pharmaceutics, 2018, 10(3), 129
16. Shavykin, O.V., Neelov I.M., Borisov, O.V., Darinskii, A.A., Leermakers, F.A.M., SCF Theory of Uniformly Charged Dendrimers: Impact of Asymmetry of Branching, Generation Number, and Salt Concentration, Macromolecules, 2020, 53 (17), 7298.
17. Gh. Adam, M. Bashashin, D. Belyakov, M. Kirakosyan, M. Matveev, D. Podgainy, T. Sapozhnikova, O. Streltsova, Sh. Torosyan, M. Vala, L. Valova, A. Vorontsov, T. Zaikina, E. Zemlyanaya, M. Zuev. IT-ecosystem of the HybriLIT heterogeneous platform for high-performance computing and training of IT-specialists. Selected Papers of the 8th International Conference «Distributed Computing and Grid-technologies in Science and Education» (GRID 2018), Dubna, Russia, September 10-14, 2018, CEUR-WS.org/Vol-2267″

Structure of the amyloidogenic peptide SEM1(68-107) by NMR spectroscopy and molecular dynamics

Dmitriy S. Blokhin, Daria A. Sanchugova, Vladimir V. Klochkov

Kazan Federal University, Kremlevskaya Str., 18, 420008 Kazan, Russia
E-mail: dblohin@kpfu.ru

Introduction

The semenogelin 1 protein is secreted in the seminal vesicles. During ejaculation it is split into small peptide fragments using internal proteases. It was showed that some of these fragments (SEM1(86-107), SEM1(68-107), SEM1(49-107) and SEM1(45-107)) form amyloid fibrils, which increases the possibility of HIV infection [1].

In this work, the task was to evaluate the structural properties of the SEM1(68-107) peptide in an aqueous solution. Nuclear magnetic resonance (NMR) spectroscopy is an informative method for determining the molecule structure in solution; however, the study of a peptide consisting of 40 amino acid residues with a natural content of 13C/15N isotopes is difficult due to significant signal overlap. Therefore, the SEM1(68-107) peptide was divided into two peptides: N-terminus - SEM1(68-85); C-terminus - SEM1(86-107). The SEM1(68-85) peptide was investigated by NMR, and internuclear distances and dihedral angels were determined. Internuclear distances of SEM1(86-107) were taken from our previously published article [2]. The data (internuclear distances and dihedral angles) were used as input parameters for SEM1(68-107) peptide spatial structure calculation using the XPLOR-NH program. Next, molecular dynamics simulation of calculated SEM1(68-107) structure was carried out by Gromacs 2020 program.

Experimental section

Materials

SEM1(68-85) is a peptide of 18 amino acid residues corresponding to 68-85 amino acid residues of the human semenogelin 1 protein. Amino acid sequence of SEM1(68-85) peptide: TYHVDANDHDQSRKSQQY. The peptide was obtained by solid-phase synthesis by the method described in article Kamalov et.al. [3].

Methods

1D and 2D NMR spectra of SEM1(68-85) (1.1 mM) in aqua solution (H_2O+D_2O/ 90%+10%) were carried out on NMR spectrometer 700 MHz (Bruker, AVANCE III-700) equipped with a quadruple resonance (^{1}H, ^{13}C, ^{15}N, ^{31}P) CryoProbe at the temperature 298 K. Based on the NMR spectra it was done assignment chemical shifts of ^{1}H, ^{13}C, ^{15}N and identifies internuclear distances and dihedral angles for SEM1(68-85). Data processing was performed using the Bruker Topspin 3.6 software. All spectra were analyzed using the programs CCP-NMR [4]. No changes in the ^{1}H NMR spectra of the SEM1(68-85) peptide were observed during all NMR experiments. Based on this, we can suppose that no structural changes of the peptide occurred.

The calculation of the spatial structure SEM1(68-107) was performed using the XPLOR-NIH program [5]. We used restraints for the structure calculations: internuclear distances from SEM1(86-107) (data of article [2]); internuclear distances and dihedral angles from SEM1(68-85). Individual structures were minimized, heated to 1000 K for 6000 steps, cooled in 100 K increments to 50 K, each with 3000 steps, and finally minimized with 1000 steps of steepest descent followed by 1000 steps of conjugate gradient minimization. Thus, a total of 200 structures were generated, which were then refined in subsequent calculations

using the protein.par force field [5,6], giving more weight to the distance constraints. Finally, the lowest energy structure was retained.

Molecular dynamics simulation of SEM1(68-107) peptide was performed using GROMACS 2020 code [7]. The Charmm36 [8] and TIP3P [9] models were used for protein and water molecules, respectively. To create conditions close to physiological, Cl^- and Na^+ ions were added to the system. Next, the solvent was equilibrated around the protein in two phases: (1) NVT (constant Number of particles, Volume, and Temperature); (2) NPT (constant Number of particles, Pressure, and Temperature). After the system equilibration the final run was performed for 100 nanoseconds using same pressure, temperature, and integrator.

Results and discussions

Assignment of 1H NMR signals was performed using 2D 1H-1H TOCSY and 2D 1H-1H NOESY NMR spectra of SEM1(68-85). The obtained hydrogen chemical shifts of various amino acid residues were compared with the data from the literature [10]. The chemical shift values of H, N, Hα, Cα, C are required to obtain the dihedral angles restrictions using the TALOS+ service (https://spin.niddk.nih.gov/bax/nmrserver/talos). Chemical shifts of Cα and C were determined from spectra 2D 1H-13C HSQC, 2D 1H-13C HMBC and 2D 1H-13C HSQC-TOCSY, chemical shifts of 15N – from 2D 1H-15N HSQC. Internuclear distances were determined from NOESY spectrum analysis.

We also used the internuclear distances of SEM1(86-107) obtained in [2]. The obtained experimental restrictions of N- and C-terminuses SEM1(68-107) (internuclear distances and dihedral angles) were used as input parameters for SEM1(68-107) peptide spatial structure calculation using the XPLOR-NIH program.

To evaluate the stability of SEM1(68-107) structure obtained from XPLOR-NIH calculations, molecular dynamics simulations were run by Gromacs 2020 software. The simulation was carried out in a water cell with neutralization of the system charge using Na+ and Cl− ions. Based on the simulation results, it can be noted that N-terminus contains β-sheet throughout the entire simulation (Figure 1). The rest of the molecule is mobile and contains a large number of bends in backbone chain.

Based on the data obtained, we can conclude that the N-terminus of SEM1(68-107) contains a stable β-sheet, and we can assume that this site can play a significant role in the formation of amyloid fibrils in human sperm.

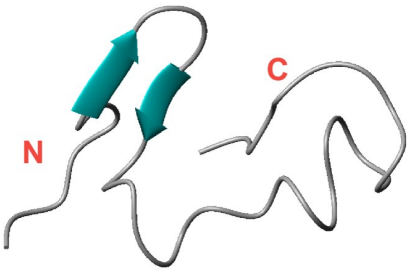

Figure 1. The spatial structure of SEM1(68-107) peptide after molecular dynamics simulation.

Acknowledgements

This work is supported by the Russian Science Foundation (D.S. Blokhin, project no. 20-73-10034).

References

1. J. Munch, et al., Semen-derived amyloid fibrils drastically enhance HIV infection. Cell, 2007, Vol. 131(6), P. 1059–1071.
2. D. Sanchugova, et al., The Structure of Fibril-Forming SEM1(86-107) Peptide Increasing the HIV Infectivity. BioNanoScience, 2021, Vol. 11, P. 182–188.
3. M. I. Kamalov, et al., Syntesis and Characterization of Polyaspartic Acid-Histidine Conjugate as an Analog of Antioxidant Enzymes. Applied Biochemistry and Microbiology, 2019, Vol. 55, P. 474-481
4. W.F. Vranken, et al., The CCPN data model for NMR spectroscopy: Development of a software pipeline. Proteins, 2005, Vol. 59, P. 687–696.
5. C. D. Schwieters, et al., The Xplor-NIH NMR molecular structure determination package. Journal of Magnetic Resonance, 2003, Vol. 160, P. 65-73.
6. C. D. Schwieters, et al., Using Xplor–NIH for NMR molecular structure determination. Prog. Nucl. Magn. Reson. Spectrosc., 2006, Vol. 48, P. 47-62.
7. S. Pronk, et al., GROMACS 4.5: a high-throughput and highly parallel open source molecular simulation toolkit. Bioinformatics, 2013, Vol. 29(7), P 845-854.
8. J. Huang, A.D. MacKerell, CHARMM36 All-Atom Additive Protein Force Field: Validation Based on Comparison to NMR Data. Journal of Computational Chemistry, 2013, Vol. 34(25), P. 2135-2145.
9. W. Jorgensen, et al., Comparison of simple potential functions for simulating liquid water. J Chem Phys, 1983, Vol. 79(2), P. 926–935.
10. K. Wuthrich, NMR of proteins and nucleic acids. New York: Wiley-VCH, 1986.

Relaxation of protons and heteronuclei in cyclosporins

Bychkova D.A., Kobchikova P.P., Efimov S.V.

Institute of Physics, Kazan Federal University, Kazan, 420008 Russia
E-mail: bychkowadascha@gmail.com

Introduction

Cyclosporins belong to a series of peptides produced by fungi, parasites of insects; most widely known is cyclosporin A (CsA) used as an immunosuppressor [1]. However, possible use of these cyclic peptides and their analogues is not limited to immunosuppression. One of the important properties of cyclosporins is their ability to penetrate through cell membranes, increasing the bioavailability of the drug. The question arises if this property is due to the hydrophobic nature of the peptide or to its ability to change the conformation in different media, or both factors work at a time [2, 3]. Nuclear magnetic relaxation is an instrument which can give insight into dynamic properties of a polypeptide chain and describe its flexibility.

Object

Variants of cyclosporin other than CsA have not been investigated at the same level. CsG can also be used to prevent allograft rejection, but most cyclosporins do not show immunosuppressive properties. In this work we studied cyclosporin variants G, E and L. The former one differs from CsA by a single amino acid replacement Abu2→Nva2 (norvaline). Other two molecules have standard amino acids instead of N-methylated ones (Mva11→Val11 in CsE and Bmt1→Hbt1 in CsL). Additional fifth NH group capable of forming intramolecular H-bond may influence the chain flexibility in CsE and CsL.Chemical formulas of the studied compounds are presented in Figure 1.

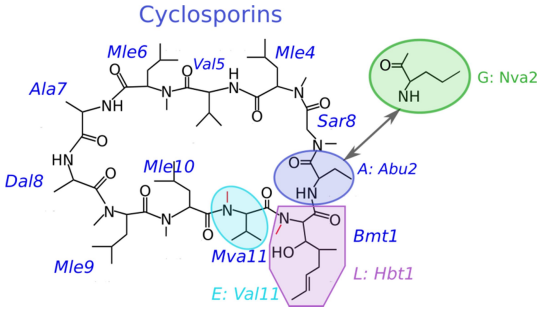

Figure 1. Structural formula of cyclosporins variants A, G, E, and L

Method

Experiments were carried out on a Bruker Avance III HD 700 and Avance II 500 NMR spectrometers. Solutions of the peptides were prepared in chloroform ($CDCl_3$) at the concentration of 1–2 mM.Proton relaxation times were measured using the inversion-recovery (for T_1) and CPMG-perfect (for T_2) pulse sequences. Relaxation times of ^{13}C and ^{15}N were obtained using pseudo-3D experiments; analysis of the data was made in the Dynamic Center of TopSpin software.

Results

Obtained spin-lattice and spin-sin relaxation times are shown in the Table 1. As cyclosporins contain only four or five NH groups, data for nitrogen are obtained only for these positions (number of amino acid residues stay to the left of the columns). Other amide protons are substituted by methyl groups, the table lists their proton relaxation times.

Table 1. Relaxation times in cyclosporins E, G and L (seconds) at 298 K, measured in field of 16.44 T (700 MHz proton resonance frequency). Inaccuracy of the estimate for relaxation times of nitrogen is given in parentheses.

CsL		**CsG**		**CsE**			
^{15}N (NH)		^{1}H (NCH_3 group)		^{15}N (NH)		^{1}H (NCH_3 group)	
T_1	T_2	T_1	T_2	T_1	T_2	T_1	T_2
1: 1.09(6)	1.21(7)	1: 0.789	0.430	2: 0.99(25)	0.96(12)	1: 0.593	0.319
2: 1.18(4)	1.03(3)	3: 0.891	0.519	5: 1.33(28)	1.03(7)	3: 0.705	0.385
5: 1.16(6)	1.15(20)			7: 0.99(19)	0.99(15)	4: 0.633	0.327
7: 1.16(3)	1.22(17)	6: 0.845	0.496	8: 1.21(8)	1.10(11)	6: 0.593	0.314
8: 1.29(7)	0.85(6)			11:1.21(10)	1.11(19)	9: 674	0.359
		10: 1.056	0.533			10: 0.810	0.443
		11: 0.874	0.455				

Evidently, relaxation times T_1 and T_2 of nitrogen nuclei almost coincide within the experimental error. Moreover, they are close to each other in different residues of the same peptide. The frequency dependence of relaxation times is very smooth and does not allow to distinguish between experimental data recorded on different spectrometers (e.g., at 50.7 and 71.0 MHz for ^{15}N). Assuming that the dipolar relaxation is prevailing for amide nitrogens, we can estimate the molecular correlation time to be nearly 0.3 ns.

In a similar way, we estimated the correlation time τ_c using the data of ^{13}C spin-lattice relaxation in CsL. Typical value of T_1 for α-carbons lies in the range from 0.35 to 0.45 s, which gives roughly $\tau_c \sim 0.2$ ns. Earlier correlation times were calculated from proton relaxation times. In this case effective distance to neighbour nuclei causing relaxation is unknown a priori, and the system of equations involving T_1 and T_2 at a time (or two values of T_1 obtained at different frequencies) should be solved to get r_{eff} and τ_c. Thus, a typical value of 0.18–0.2 ns was obtained for NCH_3 protons [4].

Further efforts will be applied to combine these data and achieve unambiguous values of correlation times. To do this, another source of relaxation of heteronuclei(chemical shift anisotropy) and possible two-mode flexibility (overall tumbling and local flexibility) should be analysed.

Acknowledgements

This work is supported by the subsidy allocated to Kazan Federal University for the state assignment in the sphere of scientific activities (no. 0671-2020-0051).

References

1. S.A. Survase, L.D. Kagliwal, U.S. Annapure et al. – Biotech. Adv., 29, 418-435 (2011).
2. C.K. Wang, J.E. Swedberg, P.J. Harvey et al. – J. Phys. Chem. B, 122, 2261-2276 (2018).
3. K.M. Corbett, L. Ford, D.B. Warren et al. – Med. Chem., 64, 13131-13151 (2021).
4. P.P. Kobchikova, S.V. Efimov, I.A. Khodov et al. – J. Mol. Liq., 336, 116244 (2021).

Inhibitors of tumor cells proliferation, fungicides and DNA complexones — *electron-rich* σ^H-1,10-phenanthrocyanines of d-elements, structural analogues and potential antagonists of NADH: ESR spectroscopy of *temperature accessible* excited electronic triplet biradical states

Viktor N. Demidov[1], *Stanislav M. Sukharzhevsky*[2], *Sofia V. Paston*[3], *Tatiana B. Pakhomova*[1], *Vladimir V. Sharoyko*[4], *Evgenia V. Bogomolova*[5], *Andrey V. Zinchenko*[1]

[1]*Department of Inorganic Chemistry, St. Petersburg State Technological Institute (Technical University), 190013, Moskovsky Ave., 24-26/49 lit. A , Saint Petersburg, Russia*
[2]*Faculty of Chemistry, St. Petersburg State University, RC "MRMI", 198504, Peterhof, Universitetskiy ave., 26, Russia*
[3]*Department of Molecular Biophysics and Polymer Physics, St. Petersburg State University, 198504, Peterhof, Universitetskiy Ave., 26, Russia*
[4]*Laboratory of Biomedical Chemistry, Institute of Chemistry, St. Petersburg State University, 198504, Peterhof, Universitetskaya ave., 26, Russia*
[5]*V.L. Komarov Botanical Institute of the Russian Academy of Sciences, 197376, St. Petersburg, Prof. Popova, 2, Russia*
E-mail: vndemidov@mail.ru

Introduction

Coordination compounds of a new structural class: chromophoric *non-innocent electron-rich* σ^H-1,10-phenanthrocyanines of d-elements, *structural* analogues and potential antagonists of NADH, were obtained for the first time by us using the original methodology of metal-assisted nondehydrogenative C(sp^2)*H* coupling of coordinated 1,10-phenanthrolines in *solutions* and *melts* [1, 2], including as one of the main intermediate stages *nucleophilic substitution of hydrogen* S_N^H.

1,10-Phenanthrocyanine complexes obtained in low temperature melts (175 - 195 ^oC), when the melts are cooled, form amorphous phases (they are in an amorphous glassy state), which, when dissolved in water or organic solvents, pass into a *semicolloidal* state when monomeric units are in equilibrium with polymer aggregates. Nanostructured aggregates of the micelle type are recorded in solutions of 1,10-phenanthrocyanines by nuclear magnetic relaxation, and metal comp-lex polymer "*grids*" - by dynamic light scattering.

Structured aggregates of 1,10-phenanthrocyanines in solutions scatter red and green laser beams. These compounds exhibit the properties of DNA complexones [3], have a cytostatic effect against tumor cells in vitro (proliferation inhibitors) and demonstrate the ability to inhibit the deve-lopment of pathogenic fungi (for example, in the case of Co(II)-containing compounds). The effe-ctiveness of the effect of 1,10-phenanthrocyanines of d-elements on biological objects depends on the nature of the complexing agent metal.

1,10-phenanthroline complexes of Zn(II) bind to DNA intercalationally [4], so that the pla-nes of 1,10-phenanthroline ligands are embedded between the turns of DNA double helices accor-ding to the type of π-stacking. The data obtained by us indicate that the more structurally complex, volumetric Zn(II) 1,10-phenanthrocyanins most likely form ionic associates with DNA [3] and are also capable of external binding with the formation of π-stacking structures by the type of external “layering”, as it is established for *electron-rich* binuclear Pd(II) 2,9-dimethyl-1,10-phenanthrocyanine.

Method of ESR spectroscopy in investigation of *electron-rich* 1,10-phe-nanthrocyanines of d-elements

Using EPR spectroscopy in the solid state and in solutions for 1,10-phenanthrocyanine com-plexes, EPR signals (g-factor in the range of values 2.01- 2.05, in some cases of a very complex form) were recorded, characterizing these compounds as substances with a non-stoichiometric (10^{-2} - 10^{-3} spins per molecule) concentration of paramagnetic centers. The nature of the formation of ESR signals in this case is complex and as the most likely scheme, we proposed to consider their oc-currence as a result of singlet-triplet $S^0 \rightarrow T_{low.}$-transitions of the compound from the basic singlet state S^0 to the temperature accessible excited electronic lower triplet biradical state $T_{low.}$ [5]. Such transitions have been studied recently for a number of organic and metal complex systems [6].

We have previously reported on studies by the ESR method of the electron-rich binuclear bridge diamagnetic Pt(II) 1,10-phenanthrocyanine $[(py)_2Pt(\mu\text{-phencyanine}^{-})Pt(py)_2]Cl_3$ (purple form) (Pt^{2+} cation: [Xe] $4f^{14}$ $5d^8$) [7]. The obtained results point to the fact that the localization of the paramagnetic spin centers in this compound is too complicated and apparently assumes the existence of the different electron-rich radical states. 1,10-Phenanthrocyanine coordination compounds of diamagnetic Zn(II) (purple form) were also studied by the ESR method (Zn^{2+} cation: [Ar] $3d^{10}$) [5]. Main difference of ESR spectra of Zn(II) 1,10-phenanthrocyanines in solid glassy state from ESR spectra of Pt(II) 1,10-phenanthrocyanines is that the first is missing thin structure. In present work were investigated ESR spectra of Cd(II) 1,10-phenanthrocyanine $[(OAc^{-})_2Cd^{2+}(\mu\text{-phencya-nine'})Cd^{2+}(OAc^{-})_2]$ (yellow form) of (Cd^{2+} cation: [Kr] $4d^{10}$) – electron analog of Zn(II) and biology active cation, in solid state.

Synthesis of electron-rich Cd(II) 1,10-phenanthrocyanine

Electron-rich Cd(II) 1,10-phenanthrocyanine $[(OAc^{-})_2Cd^{2+}(\mu\text{-phencyanine'})Cd^{2}(OAc^{-})_2]$, yellow form, was synthesized in the two stages. Initially based on the $C(sp^2)H$ coupling methodolo-gy of coordinated 1,10-phenanthrolines [1] in melt was synthesized $[(OAc^{-})_2Cd^{2+}(\mu\text{-phencyanine})\ Cd^{2+}(OAc^{-})_2]$, glassy purple form. Thereafter purple form $[(OAc^{-})_2Cd^{2+}(\mu\text{-phencyanine})Cd^{2+}(OAc^{-})_2]$ was transferred into yellow form $[(OAc^{-})_2Cd^{2}(\mu\text{-phencyanine'})Cd^{2+}(OAc^{-})_2]$ [2]. This substance is poorly soluble in water, dissolves well in a mixture of DMSO – water (1:1).

Results and Discussion

The electron-rich 1,10-phenanthrocyanine complex of Cd(II) $[(OAc^{-})_2Cd^{2+}(\mu\text{-phencyani-ne'})Cd^{2+}(OAc^{-})_2]$ (yellow form) has been investigated by the ESR spectroscopy in solid glassy state in the temperature range of 112,6 – 300,0 K. The ESR spectrum of $[(OAc^{-})_2Cd^{2+}$ (μ-phencyanine') $Cd^{2+}(OAc^{-})_2]$ (yellow form) at a temperature 300 K is represented on Fig. 1.

The spectrum has the one signal. There is a single anisotropic band with value ΔB_p 8,43 Gs with intensity and g-factor value: I 16,4 rel. un. and g_{eff} 2,0043 on the spectrum. 300 K (ano-ther series of measurements): unbalanced signal, anisotropy, g_{eff} 2,0043, ΔB_p 7,43 Gs, a_{asim} 1,58, I 26,6 rel. un. The temperature was lowered to 112.6 K, then slowly raised. 112,6 K: g_{eff} 2,0036, ΔB_p 8,70 Gs, a_{asim} 1,40, I 13,8 rel. un. – drop in asymmetry, significant drop in signal intensity, band broadening. 156,0 K: g_{eff} 2,00375, ΔB_p 8,30 Gs, a_{asim} 1,40, I 17,2 rel. un. – increase in signal intensi-ty. 198,0 K: g_{eff} 2,0038, ΔB_p 8,00 Gs, a_{asim} 1,40, I 20,8 rel. un. 232,0 K: g_{eff} 2,0038, ΔB_p 7,80 Gs, a_{asim} 1,45, I 23,9 rel. un. We have found the similar narrow bands with $\Delta B_p \sim 5–7$ Gs for the electron-rich Zn(II) 1,10-phenanthrocyanines as well [5]. According to their genesis they have been assig-ned to the electron-rich bridge 1,10-phenanthrocyanine ligand in the coordination structure of Zn^{2+} (μ-phencyanine)Zn^{2+}.

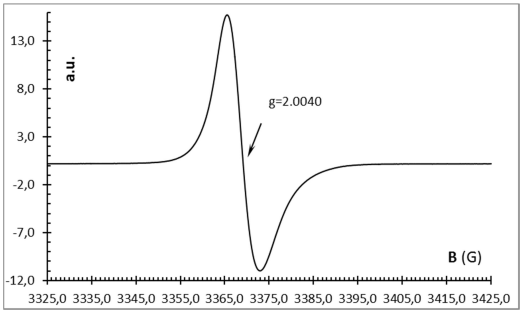

Figure 1. ESR spectrum of complex [$(OAc^{-})_2Cd^{2+}$(μ-phencyanine')$Cd^{2+}(OAc^{-})_2$] in the solid state

Conclusions

According to chemical genesis of fragment μ-phencyanine signals in ESR spectra of [$(OAc^{-})_2Cd^{2+}$(μ-phencyanine')$Cd^{2+}(OAc^{-})_2$] have been assigned to the electron-rich bridge 1,10-phenanthrocyanine ligand in the coordination structure of Cd^{2+}(μ-phencyanine')Cd^{2+}.

ESR Measurements

The ESR investigation of 1,10-phenanthrocyanine complex of Cd(II) in the solid state (in the temperature range of 112,6 – 300,0 K) has been carried out in the Resource Centre "Magneto-reso-nance methods of investigation" of the Scientific Park of St. Petersburg State University on the spectrometer ELEXSYS E580 (X-BAND).

References

1. V.N. Demidov, S.A. Simanova, A.I. Savinova, et al. *Ross. Khim. Zhurn.* (*Zhurn. Ross. Khim. Ob. D.I. Mendeleev*) (in Russ.), 53, No. 1, 128-134 (2009); Russ. *J. Gen. Chem.*, 79, No. 12, 2807-2814 (2009).
2. V.N. Demidov. – Diss. D. Chem. Sci. (in Russ.), St. Petersburg State Technol. Inst. (Techn. Univ.), 2010.
3. S.V. Paston, V.M. Bakulev, V.N. Demidov, et al. *News St. Petersburg State Univ.* (in Russ.), Ser. 4, Phys., Chem., 2 (60), No. 3, 299-304 (2015).
4. J.K. Barton, J.J. Dannenberg, A.L. Raphael. *J. Amer. Chem. Soc.*, 104, 4967-4969 (1982).
5. V.N. Demidov, S.M. Sukharzhevsky, S.V. Paston, et al. *News St. Petersburg State Univ.* (in Russ.), Ser.4, Phys., Chem., 4 (62), No. 2, 138-145 (2017).
6. K.K. Kalninsh, E.F. Panarin. Excited States in Chemistry of Polymers (in Russ.). – IPC St. Petersburg State UTD, 2007.
7. V.N. Demidov, S.M. Sukharzhevsky, L.N. Vedeneeva, A.V. Zinchenko, T.B. Pakhomova. 15th International School-Conference MAGNETIC RESONANCE AND ITS APPLICATI- ONS (SPINUS-2018). April 1-6, 2018, St. Petersburg, Russia, Abstr., p. 160-162.

The COSY spectrum in the sugar unit of a tetrapyrrole

Nina Djapic

[1]*University of Novi Sad, Technical Faculty "Mihajlo Pupin", Zrenjanin, Serbia*
E-mail: nidjapic@gmail.com

Introduction

The 2D ^{1}H-^{1}H COrrelation SpectroscopY (COSY) is a technique used to assign the different proton signals based on the couplings through bonds (*J*-coupling). The COSY spectrum shows distinct spots on a diagonal, extending from the upper right corner of the spectrum down to the lower left corner. The diagonal peaks represent the actual proton spectrum and the cross diagonal peaks show which protons are *J*-coupled to each other. The cross peaks have different values for each frequency coordinate and appear off the diagonal. Each coupling gives two symmetrical cross peaks above and below the diagonal. It can be determined which atoms are connected to one another, by looking for cross-peaks between various signals, by extending vertical and horizontal lines from each spot on the diagonal. An easy visual way to determine which couplings have a cross peak is to find the diagonal peak which is directly above or below the cross peak, and the other diagonal peak which is directly to the left or right of the cross peak. In the off diagonal response, only signals on one part of the diagonal can be used. The atoms represented by those two diagonal peaks are coupled.

The Sugar Unit of a Tetrapyrrole

In tetrapyrroles with one sugar unit, the sugar protons are positioned within the short ppm range. In the COSY spectrum, the sequential "walk" through sugar unit allows assignment of all sugar proton signals (Fig. 1). Starting from the anomeric proton, through the cross-peaks in the COSY spectrum followed is the sequence of coupled protons in the sugar ring by a sequential "walk".

The sequential "walk", in the sugar region of the glycosylated tetrapyrrole, in the COSY spectrum can be, to a certain extent, compared to a dot to dot puzzle. In the puzzle dots should be connected by the numbers and the solved puzzle gives the object. In the dot to dot puzzle every dot can be used only once. When the dot is used twice, the players can blame their pencil. The Theseus' paradox does not play an important role, the sugar unit with the replacement of its components remains the same sugar unit.

Kat' exochen, nothing new.

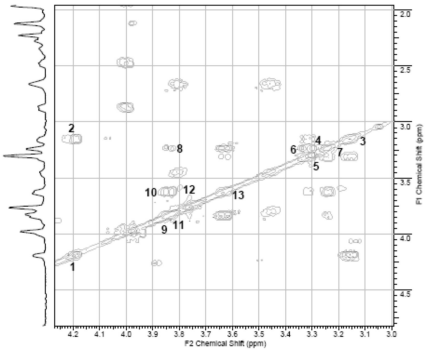

Figure 1. COSY spectrum of the sugar unit in a glycosylated tetrapyrrole, a dot to dot puzzle

Development and study of polyacrylonitrile membranes modified with titanium dioxide for enhanced pervaporation dehydration

Mariia Dmitrenko[1,2], Anna Kuzminova[1,2], Andrey Zolotarev[1,2], Aleksandra Korniak[1], Anton Mazur[1], Anastasia Penkova[1,2]

[1]St. Petersburg State University, 7/9 Universitetskaya nab., St. Petersburg 199034, Russia
[2]Sirius University of Science and Technology, 1 Olympic Ave, 354340, Sochi, Russia
E-mail: m.dmitrienko@spbu.ru

Introduction

One of the promising sustainable membrane methods for separation of liquid mixtures of low molecular weight substances is pervaporation, which is actively used for the separation of azeotropic and isomer mixtures, mixtures of close-boiling and thermally unstable substances and an alternative to traditional separation methods. The rapid development of this technology and active its implementation in various industries (chemical, petrochemical, water treatment, etc.) require the creation of novel materials and membranes based on them with tailored characteristics. In this work the most commonly used polymer - polyacrylonitrile (PAN) was used as membrane matrix for pervaporation dehydration due to its advantages as a stability in organic solvents, relatively high chemical and thermal stability, low cost, and high hydrophilicity. To achieve improved characteristics of PAN membranes, titanium dioxide (TiO_2) nanoparticles were used as a modifier.

Membrane investigation

The effect of various TiO_2 concentration introduction into PAN matrix on structural, physicochemical and transport properties was studied. The structural changes of developed composites and membranes based on them was investigated by spectroscopic (FTIR and NMR) and microscopic (SEM and AFM) methods. The physicochemical characteristics of the obtained PAN-based membranes were explored by swelling experiments, thermogravimetric analysis, and contact angle measurements. The PAN-based membranes were evaluated in pervaporation dehydration of isopropanol.

Results

It was demonstrated that the introduction of TiO_2 into the PAN membrane led to an increase in the productivity in pervaporation dehydration of isopropanol, which was especially important for the application in post-purification of water streams from organic substances.

Acknowledgements

This work is supported by RFBR, Sirius University of Science and Technology, JSC Russian Railways and Educational Fund "Talent and success", project number 20-38-51022. The experimental work of this study was facilitated by the equipment from the Resource Centre of Geomodel, Chemical Analysis and Materials Research Centre, Centre for X-ray Diffraction Methods, Magnetic Resonance Research Centre, Centre for Innovative Technologies of Composite Nanomaterials, Nanophotonics Centre, Cryogenic department, Thermogravimetric and Calorimetric Research Centre and the Interdisciplinary Resource Centre for Nanotechnology at the St. Petersburg State University.

Determination of differences in the chemical structure of softwood dioxane lignin using chemometric analysis of two-dimensional HSQC spectra

Anna V. Faleva, Dmitry S. Kosyakov

Laboratory of Natural Compounds Chemistry and Bioanalytics, Core Facility Center "Arktika", M.V. Lomonosov Northern (Arctic) Federal University, Northern Dvina Emb. 17, 163002 Arkhangelsk, Russia
E-mail: a.bezumova@narfu.ru

Introduction

Lignin is one of the most abundant biopolymers in the plant world, which, due to its unique chemical structure, has become a popular object of research. In this regard, there is a large number of publications in the literature devoted to the study of the structure of lignins [1], but many aspects still remain unclear.

Two-dimensional nuclear magnetic resonance (2D NMR) spectroscopy is considered the most promising technique for studying the structure of lignin. The advantages of this method in comparison with optical spectroscopy and 1D NMR involve, first of all, higher resolution allowing for obtainment a larger amount of information and determination of lignin chemical structure [1]. However, the methodology for studying the structure of lignin by 2D NMR spectroscopy has not been sufficiently developed. In this regard, the improvement of existing approaches for the accurate and efficient determination of the chemical composition and structure of lignin according to 2D NMR is an urgent task. One of the most promising approaches to revealing the minor features of lignin structure is multivariate data analysis, which alleviates the problems associated with cross-peaks overlapping and allows analyzing a large volume of spectral data [2, 3]. In particular, the authors of work [3] demonstrated that chemometric approaches applied to 2D NMR spectra can reveal subtle differences between samples that are not obvious when simply viewing the spectra.

Therefore, purpose of this work is to determine the features of the chemical structure of lignins using principal component analysis (PCA) of 2D NMR spectra on the example of softwood dioxane lignin.

Experiment and Samples

As real samples, dioxane lignins isolated from larch, cedar pine, spruce and juniper wood using the Pepper method [4] were used.

Registration and preliminary qualitative analysis of the NMR spectra of the studied coniferous lignins was performed as described earlier [5].

For multivariate analysis, preprocessing of all 2D ^{1}H-^{13}C HSQC spectra was performed in MATLAB (Mathworks Inc.) as described in [2]. PCA analysis was performed by MarkerView Software (ABSciex, Canada), using Pareto scaling.

Results and discussion

Differences in the composition and structure of softwood dioxane lignins were visualized using multidimensional analysis in the form of high-resolution 2D NMR load spectra. The obtained results of PCA analysis demonstrate that 99.8% of the variations in the data are explained by five principal components, among which 37.8% and 29.7% are explained by the first (PC1) and second (PC2) principal components, respectively. The clear separation between the samples observed in PC1-PC2 coordinates indicates a significant difference in the structure of the studied lignins (Fig. 1a).

The load vectors, containing spectral information strongly correlating with the main differences, were converted back into a 2D NMR load spectrum (Fig. 1b). In this spectrum,

the value of each variable (spectral data point) corresponds to its correlation with PC1. Thus, the positive cross-peaks (yellow) correlate with samples with positive values along PC1 in Fig. 1a, namely with dioxane lignin samples of Cedar Pine (1 and 2), Juniper (1 and 2), as well as Larch (2) and Spruce.

Comparison with previously performed assignments [5] confirmed that the most intense of them resonate mainly from fragments of methyl substituted phenylcoumarone and other degradation products (vanillin, vanillic acid, acetovanillone, etc.), which indicates their higher content in the composition of spruce dioxane lignin.

The Larch (1) lignin preparation, both along PC1 and PC2, is located separately from all samples, which is explained by the presence in its composition of an increased content of sugars and taxifolin, as well as fragments of β-aryl ether and phenylcoumaran, the blue cross-peaks of which are clearly observed on the NMR spectra of PC1 and PC2 loads.

A clear distinguishing feature of the dioxane lignins grouped in the right part of the PC2 score is the presence of *p*-hydroxyphenylpropane units in their structure.

Interestingly, in some cases, the differences between individual dioxane lignins within a single wood species turn out to be greater than the differences between wood species. This suggests a predominant contribution of random impurities to PC1-PC2, which may be the result of a phasing error of some cross peaks, for example, associated with residual solvents.

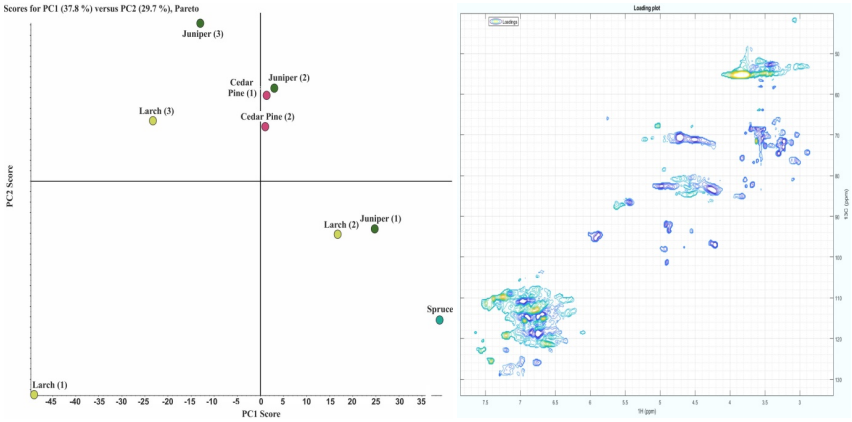

a *b*

Figure 1. Visualization of 2D HSQC data of dioxane lignin by the principal component analysis: a) a score plot; b) a part of PC1 load plot in the form of a 2D NMR spectrum

Conclusions

The application of a multivariate PCA analysis to 2D HSQC spectra of lignins made it possible to analyze more deeply the differences in their chemical structure and establish some patterns. In the future, this approach will be applied to the analysis of a wider range of lignins, including more complex lignins of hardwood and grass, characterized by significant variability of structural fragments.

Acknowledgements

This study was performed using an instrumentation of the Core Facility Center "Arktika" of the Lomonosov Northern (Arctic) Federal University. Russian Science Foundation, grant number 21-73-20275, funded this research. The authors thank M. Hedenström for providing the MATLAB script.

References

1. J. Ralph, L.L. Landucci. NMR of Lignins. In Lignin and Lignans: Advances in Chemistry, 2nd ed.; Heitner, C., Dimmel, D.R., Schmidt, J.A., Eds.; CRC Press (Taylor & Francis Group): Boca Raton, FL, USA, 137-234 (2010).
2. M. Hedenström, S. Wiklund, B. Sundberg, U. Edlund. – *Chemom. Intell. Lab. Syst.,* 92 (2), 110-117 (2008).
3. M. Hedenström, S. Wiklund-Lindström, T. Öman, F. Lu, L. Gerber, P. Schatz, B. Sundberg, J. Ralph. – *Mol Plant*, 2 (5), 933-942 (2009).
4. J.M. Pepper, P.E.T. Baylis, E. Adler. – *Can. J. Chem.*, 37, 1241–1248 (1959).
5. A.V. Faleva, A.Y. Kozhevnikov, S.A. Pokryshkin, D.I. Falev, S.L. Shestakov, J.A. Popova. – *J. Wood Chem. Technol.,* 40, 178-189 (2020).

Multifrequency EPR Study and DFT-Assisted Identification of Radicals in γ-Irradiated Sodium Gluconate

Gafarova A.R., Gumarov G.G., Zaripov R.B., Bakirov M.M.

Zavoisky Physical-Technical Institute, Kazan, Russian Federation
E-mail: albina-gafarova@mail.ru

Sodium gluconate, like other salts of gluconic acid, is widely used in various industries. In this regard, there is interest in studying the structure of these substances. Previously, we have shown the possibility of determining the conformational structure of other salts of gluconic acid - salts of calcium gluconate, using the DFT method [1]. Since the initial salts of gluconic acid do not have an EPR signal, artificial defects can be introduced into it to obtain information about the system; For this, we used ionizing radiation in our work by creating paramagnetic centers in them when irradiated with gamma rays. In this paper, we consider the application of the EPR method at different frequencies and the quantum chemical calculation of the EPR spectrum parameters based on the density functional theory (DFT) for the identification of radicals created by irradiation in sodium gluconate.

The starting material was a sodium gluconate powder manufactured by Sigma Aldrich. The samples were preliminarily irradiated with photons on a Rokus gamma-therapeutic apparatus with a Co^{60} source with an average energy of 1.25 MeV. The resulting radiation doses were 400, 600, 800 and 1000 Gy. EPR spectra were obtained at room temperature on an an Elexsys E680 spectrometer in the Q-band and on in the W-band at various powers.

The following sequence of actions was used to decompose the experimental EPR spectra. Using X-ray diffraction data, a model of the sodium gluconate molecule was built using a specially adapted version of the Avogadro software. Further, with the help of quantum-chemical calculations, we obtained the HFI parameters and the g-factor. Quantum chemistry calculations were performed using the ORCA software package [2, 3]. In this work, we used the density functional theory (DFT) calculation method, namely the unrestricted Kohn-Sham method. The meta-GGA functional (TPSS) [4] and the cc-pVDZ basis [5] were used. When calculating the HFI parameter, the isotropic and anisotropic contributions of all protons were taken into account. The HFI and g factor parameters obtained as a result of quantum chemical calculations were used to decompose the experimental EPR spectra using the Pepper function of the EasySpin program [6]. The simulation was carried out simultaneously for the Q and W– bands with one set of g factors and hyperfine interaction parameters.

The result of the decomposition of the EPR spectrum of the Q- and W-bands of a sample of sodium gluconate irradiated with a dose of 1000 Gy is shown in Fig. 1.

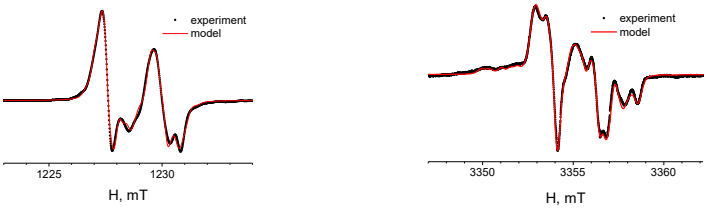

a) Q-band b) W-band

Fig1. Spectrum of calcium gluconate irradiated with a dose of 1000 Gy (experiment) and the result of a quantum-chemical calculation on ORCA with fit in EasySpin (model).

The spectra of radicals located on the C2, C3, C4, and C5 atoms of sodium gluconate were used as components of the full EPR spectrum (Fig 2).

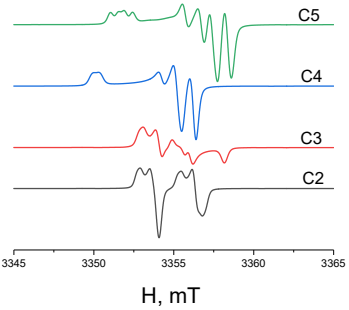

Fig 2. EPR spectra of radicals in sodium gluconate corresponding to the parameters calculated using the ORCA package and fitted to experimental spectra using the EasySpin software.

It should be noted that when fitting the results of quantum-chemical calculations to the experimental spectra, the parameters of the spectrum (HFI and g-factor) changed insignificantly (Fig 3). It can be seen that the calculation for the radical on the C2 carbon atom located closer to the sodium atom turned out to be the most accurate. Small deviations of the calculated values from the values fitted to the experimental ones indicate the correctness and accuracy of the calculation.

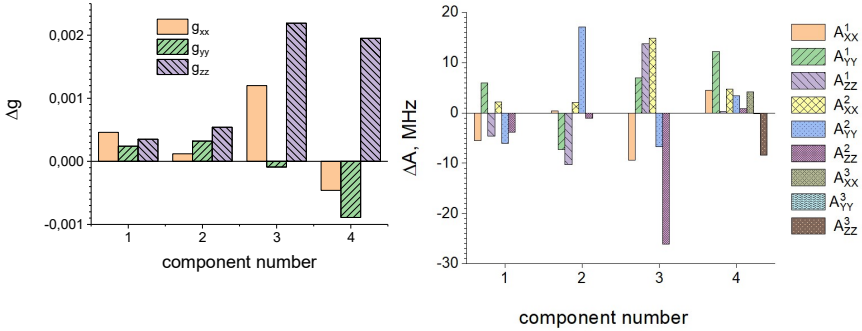

a) g-factor difference (Δ g) b) HFI difference (Δ A)

Fig 3. The difference between the spectrum parameters obtained by quantum-chemical calculations and the spectrum parameters obtained by fitting the results of quantum-chemical calculations to experimental spectra

Also, for all radicals, the distribution of spin density with the same surface isoline was constructed (Fig 4). Based on these figures, it can be seen that the spin density of radicals on C2, C3 atoms is more extensively distributed over the molecule. It can be assumed that such an effect arises due to the “pulling” of a part of the spin density by the sodium atom.

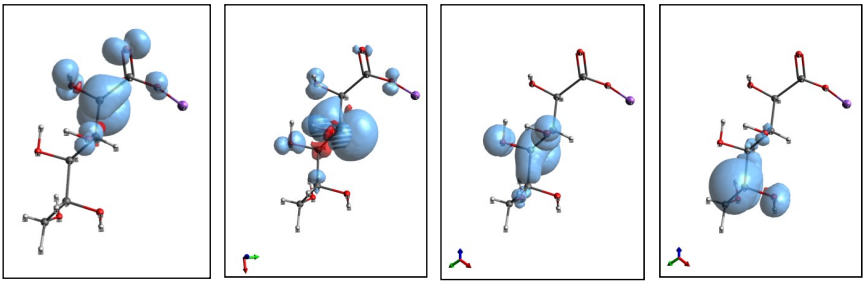

a) radical on C2 carbon atom | b) radical on C3 carbon atom | c) radical on C4 carbon atom | d) radical on C5 carbon atom

Fig 4. Spin density distribution for radicals on different carbon atoms in sodium gluconate

Thus, gamma rays with an energy of 1.25 MeV can be used to create artificial defects in gluconic acid salts. The radicals obtained in this way can be identified using the DFT method and the multifrequency EPR study. This indicates the possibility of using this method for the conformational analysis of the studied compounds.

Acknowledgments

G.A.R. thank RFBR (Project Nr. 20-33-90201) for supporting of this research activity. G.G.G., B.M.M. and Z.R.B are thankful to the Government assignment for FRC Kazan Scientific Center of RAS (Reg. Nr. AAAA-A18-118030690040-8) for supporting EPR study.

References

1. 1. A. R. Gafarova, G. G. Gumarov, M. M. Bakirov, M. Yu. Volkov, R. B. Zaripov, V. Yu. Petukhov, Applied Magnetic Resonance (2021) https://doi.org/10.1007/s00723-021-01431-1
2. 2. F. Neese, The ORCA program system, WIREs Comput. Mol. Sci. 2 (2012) 73–78. https://doi.org/10.1002/wcms.81
3. 3. F. Neese, Software update: the ORCA program system, version 4.0, Wiley Interdiscip. Rev.: Comput. Mol. Sci., 8 (2017), e1327. https://doi.org/10.1002/wcms.1327
4. 4. J. Tao, J. P. Perdew, V. N. Staroverov, and G. E. Scuseria, Phys. Rev. Lett. https://doi.org/10.1103/PhysRevLett.91.146401 91, 146401 (2003)
5. 5. Dunning, Thom H. Gaussian basis sets for use in correlated molecular calculations. I. The atoms boron through neon and hydrogen J. Chem. Phys., 90, 1007-1023 (1989) 10.1063 / 1.456153.
6. 6. S. Stoll, A. Schweiger, J. Magn. Reson. 178 (1), 42 (2006)

Anomalous magnetic properties of micro- and nanoscale DyF_3 powders

A. M. Garaeva[a], E. M. Alakshin[a, b], E. I. Kondratyeva[a, b], I. V. Romanova[a], A. S. Sakhatskii[c], M.S. Tagirov[a, b]

[a] *Kazan Federal University, Institute of Physics, Kazan, Russia*
[b] *Tatarstan Academy of Sciences, Kazan, Russia*
[c] *Saint Petersburg State University, Saint Petersburg, Russia*
E-mail: adeliagaraeva84@gmail.com

The DyF3 compound has unique properties, which makes it possible to use it as an MRI contrast agent [1] and electrocatalyst [2]. Dysprosium fluoride is a ferromagnet with an easy magnetization axis along the [010] axis of the crystal lattice; space symmetry group Pnma (orthorhombic); the Curie temperature is 2.55 K along the [010] axis for the single crystal [3].

DyF3 powders with character sizes of 30 nm x 16 nm, 50 nm x 30 nm, 70 nm x 40 nm, 220 nm x 150 nm were obtained by hydrothermal synthesis through the chloride reaction [4], powder up to 45 μm in size – by crushing a single crystal. The control of the chemical composition and confirmation of crystallinity were carried out using X-ray diffraction analysis on a Bruker D8 Advance Cu Kα, λ=1.5418 Å. The shape and characteristic size of the particles in the powders were determined from photographs obtained using transmission electron microscopy on a HitachiHT Exalens microscope.

In this work, the temperature (1.8 – 300 K) and field (0 – 7 T) dependences of the magnetization of the samples were measured using Magnetic Properties Measurement System (Quantum Design), SPbU. The simulation of the energy spectrum and magnetization in the model of exchange charges in the full basis of the electronic configuration Dy^{3+} $4f^9$ in DyF_3 was carried out. From the temperature dependences of the magnetization the temperature of the phase transition to the ferromagnetic state was determined for all samples. A decrease in the Curie temperature with a decrease in the particle size in the powder is observed. Magnetic hysteresis loops with a reversal of the magnetization curve in the ferro- and paramagnetic phases were found. The dependence of the saturation of the magnetic moment in the strong magnetic fields on the particle size in the samples is considered.

The work was carried out at the expense of funds, subsidies, allocated to the Kazan Federal University for the implementation of the state task in the field of scientific activity (project number 0671-2020-0051).

References

1. González-Mancebo D. et al. *Particle & Particle Systems Characterization*, 2017, 34, 10, 1700116.
2. Li Y. et al. *Chemistry–An Asian Journal*, 2020, 15, 4, 487-489.
3. Savinkov A. V. et al. *Journal of Physics: Condensed Matter*, 2008, 20, 48, 485220.
4. Yi G. S., Chow G. M. *Journal of Materials Chemistry*, 2005, 15, 41, 4460-4464.

NMR assignments of the Ribosome maturation factor P of *Staphylococcus aureus* (*Sa*RimP)

Natalia S. Garaeva[1,2], Aydar G. Bikmullin [1], Evelina A. Klochkova [1], Shamil Z. Validov [1], Vladimir V. Klochkov [1], Albert V. Aganov [1], Marat M. Yusupov [1,3] and Konstantin S. Usachev[1,2]

1 Kazan Federal University, 18 Kremlevskaya, Kazan 420008, Russian Federation
2Federal Research Center «Kazan Scientific Center of Russian Academy of Sciences» Russia, 420008 Kazan, Lobachevskogo, 2/31, Russian Federation
3 Institut de Génétique et de Biologie Moléculaire et Cellulaire, CNRS UMR7104, INSERM U964, Université de Strasbourg, 1 rue Laurent Fries, F-67400 Illkirch, France
E-mail: k.usachev@kpfu.ru

Introduction

Staphylococcus aureus (*S. aureus*) is one of the major human pathogens causing numerous nosocomial soft tissue infections and among the best-known causes of bacterial infections. The bacterial 70S ribosome consists of two subunits, designated the 30S (small) and 50S (large) subunits. The small subunit (30S) consists of 16S ribosomal RNA (rRNA), from which the assembly of 30S begins, and 21 ribosomal proteins (r-proteins). The ribosome maturation factor P (RimP) is a 17.7 kDa protein and is the assembly factor of the 30S subunit. RimP is essential for efficient processing of 16S rRNA and maturation (assembly) of the 30S ribosome, avoiding the kinetic trap. Strains lacking RimP accumulate immature 16S rRNA, and fewer polysomes and an increased amount of unassociated 30S and 50S subunits compared to wild-type strains are observed in the ribosomal profile[1]. Structural studies of the ribosome maturation factor RimP will make it possible in the future to develop an antibiotic that slows down or completely stops the translation of *Staphylococcus aureus*, which will complicate the synthesis and isolation of its pathogenic factors. Here we present the 13C/15N NMR assignments of the RimP

Methods

Recombinant RimP protein from *S. aureus* was expressed in *E. coli* strain BL21star(DE3) and purified by Ni-NTA chromatography and size exclusion chromatography. The NMR investigation was done using 0.7 mM sample of ^{13}C, ^{15}N-labeled RimP in NMR buffer (90%H_2O+10%D_2O) at pH 7.4 with 250 mM NaCl and 10 mM Tris-HCl concentration. NMR spectra were acquired at 25 °C on a Bruker Avance III HD 700 MHz spectrometer equipped with a quadruple resonance (^1H, ^{13}C, ^{15}N, ^{31}P) CryoProbe. Sequential assignments for the backbone were obtained using the following 3D spectra: HNCO, HNCA, HN(CA)CO, HNCACB, CBCA(CO)NH, CC(CO)NH and HCC(CO)NH. Spectra were processed by TOPSPIN 3.1 (Bruker), and analyzed with Collaborative Computing Project for NMR (CCPN)[2].

Results

Chemical shift assignments were made for resonances from 132 of 154 residues (84.6 %) of the RimP protein. Unassigned residues were clustered in the unstructured loops between RimP beta-sheet β1 and beta-sheet β2 (Gly33-Phe 37) and alpha-helices α2 and beta-sheet β (Asp 68- Val 78).

Analysis of the backbone chemical shifts by TALOS+ [3] suggests that RimP contains four α-helices and nine β-strands (α1-β1-β2-α2- β3-β4-α3-β5- β6- β7-β8-α4-β9 topology). We observed variable signal intensities in the spectra, which mean that we have flexible parts in the RimP protein. Signals with increased line broadening correspond to regions of the

secondary structure in the main part of the RimP (α1-β1-β2-α2- β3-β4-α3-β5- β6- β7-β8-α4-β9), while signals of high intensity correspond to flexible disordered parts of the protein.

Detailed analysis of protein structure, dynamic properties and protein-ribosome interactions is a subject of ongoing studies.

Acknowledgements

The work is supported by the Russian Foundation for Basic Research (RFBR): grant 20-34-70021.

References

1. Dipali G Sashital, Candacia A Greeman, Dmitry Lyumkis, Clinton S Potter, Bridget Carragher, James R Williamson. – *Biochemistry*., 3, 1-26 (2014)
2. Vranken WF et al. – *Proteins.*, 59, 687-696 (2005)
3. Shen Y, Delaglio F, Cornilescu G, Bax A. – *J Biomol NMR.*, 44, 213-223 (2009)

Magnetic fields in natural semiconductor minerals from NMR data

Stanislav O. Garkavyi, Ecaterina V. Schmidt, Vadim L. Matukhin.

Kazan State Power Engineering University, Kazan, 420066, Russia
E-mail: ololoiev77@mail.ru

Introduction

In recent years, magnetic semiconductors have been used as new promising materials for efficient thermoelectric energy conversion. The classical antiferromagnetic semiconductor - chalcopyrite was chosen as an example due to the influence of spin effects on its thermoelectric properties. This work is devoted to the study of internal magnetic fields in natural hydrothermal samples of the semiconductor mineral chalcopyrite $Cu_{1+x}Fe_{1-x}S_2$ by pulsed $^{63,65}Cu$ NMR in a local field.

Methods

For measurements, four natural samples of chalcopyrite were taken from deep-sea hydrothermal vents and on land. The samples were polycrystalline powders with grain sizes ranging from 0.1 to 1 mm. The first and second samples were obtained from the deep ocean fields of the Mid-Atlantic Ridge, Pobeda and Semenov-2, respectively. Continental samples were obtained from the ores of the Talnakh deposit (the third sample, Norilsk) and from ores mined in the vicinity of the city of Sibay (fourth sample, the Republic of Bashkortostan). The measurements were carried out on a Tecmag-Redstone multipulse NQR/NMR spectrometer.

Results

In the spectrum of each of the samples, six resonance lines were found, the parameters of which are in good agreement with the lines of previously known samples of chalcopyrite [1]. Each copper isotope corresponds to three spectrum lines, consisting of a line from the central transition and two quadrupole satellites. For the samples, the values of internal magnetic fields, presented in the table, were obtained.

Table 1. Values of internal magnetic fields on ^{63}Cu nuclei in hydrothermal and continental samples of chalcopyrite.

Sample	Pobeda	Semenov-2	Talnakh	Sibay
B_{int}, T	1,63	1,64	1,64	1,63

Increasing the figure of merit (ZT) of thermoelectric materials is one of the most important problems solved for several decades. However, traditional approaches to improve the efficiency of thermoelectric energy conversion, based on the modification of the electronic and phonon transport properties of materials, have practically reached the limit of their technical capabilities by now. For this reason, a new approach has been proposed involving the use of magnetic semiconductor compounds [2, 3]. Due to the appearance of a connection between magnetic moments and charge carriers in $Cu_{1+x}Fe_{1-x}S_2$, at a temperature of 400 K, a thermoelectric power factor $PF=10\cdot10^{-6}$ $WK^{-2}cm^{-1}$ was obtained. The obtained value of the quality factor ZT turned out to be less than 0.1, which meant that the optimization of the general thermoelectric characteristics was not implemented. However, the fact that the $CuFeS_2$ mineral still retains a large thermo-EMF coefficient at a relatively high concentration of charge carriers indicates that the thermoelectric properties can be improved by changing the magnetism of the material by doping. In order to find out what role magnetism plays in $CuFeS_2$, the thermoelectric properties of natural samples of hydrothermal origin were previously studied in detail [3]. To explain the results obtained, a theoretical model of magnon drag was proposed. The experimental data on the temperature dependence of the thermo-EMF

coefficient agreed relatively well with the theoretical description. This result showed that the thermo-EMF coefficient in the semiconductor mineral $Cu_{1+x}Fe_{1-x}S_2$ is determined by the mechanism of electron-magnon scattering, which is caused by the interaction between antiferromagnetic magnons and charge carriers. In the presence of a temperature gradient, in addition to the flow of charge carriers in the magnetic material, there is a flow of magnons. Due to the interaction with the carriers, the magnons transfer a part of their momentum to them, "dragging" the carriers in the direction of the flow. For this reason, the thermo-EMF coefficient can be markedly increased. Within the framework of the hydrodynamic theory, the thermo-EMF coefficient in the effect of electron dragging by magnons can be represented as follows [4, 5]:

$$S = (2/3)(C_m/n_e e)\, 1/(1 + \tau_{em}/\tau_m)$$

where C_m is the specific heat capacity of magnons, τ_m and τ_{em} are the average times for electron-electron and magnon-electron collisions, e is the charge of carriers, and n_e is the concentration of carriers.

Conclusions

The experimental data obtained for several $Cu_{1+x}Fe_{1-x}S_2$ samples are well explained within the framework of the proposed theory. Based on the results obtained, a conclusion was made about the dominant contribution of electron-magnon scattering to the formation of features in chalcopyrite in the temperature dependence of thermo-EMF. It should be noted that the magnon drag effect can be used to improve the thermoelectric efficiency by appropriate doping of thermoelectric semiconductor materials.

References

1. Garkavyi S., Matukhin V., Schmidt E. (2022) New Materials for Thermoelectricity Based on Natural Minerals. In: Vankov Y. (eds) Proceedings of ICEPP 2021. ICEPP 2021. Lecture Notes in Civil Engineering, vol 190. Springer, Cham.
2. Tsujii N., Mori T. High Thermoelectric Power Factor in Carrier-Doped Magnetic Semiconductor $CuFeS_2$. Appl. Phys. Express, 2013, 6, 043001.
3. Ang R., Khan A.U., Tsijii N., Takai K., Nakamura R., Mori T. Thermoelectricity Generation and Electron-Magnon Scattering in a Natural Chalcopyrite Mineral from a Deep-Sea Hydrothermal Vent. Angew. Chem., Int. Ed. 2015, 54, 12909.
4. Watzman S.J., Duine R.A., Tserkovnyak Y., Boona S.R., Jin H., Prakash A., Zheng Y., Heremans J. Magnon-drag thermopower and Nernst coefficient in Fe, Co, and Ni. Phys. Rev. B, 94,144407, 2016.
5. Zhao C.C., Xiao C. When thermoelectric materials come across with magnetism. Rare Met. 2021 40(4), 752.

Development and investigation of ultrafiltration polyacrylonitrile membranes modified with titanium dioxide

Aleksandra Korniak[1], Evgeniia Loginova[1], Mariia Dmitrenko[1,2], Anna Kuzminova[1,2], Andrey Zolotarev[1,2], Anton Mazur[1], Anastasia Penkova[1,2]

[1]St. Petersburg State University, 7/9 Universitetskaya nab., St. Petersburg 199034, Russia
[2]Sirius University of Science and Technology, 1 Olympic Ave, 354340, Sochi, Russia
E-mail: kornyaksandra@gmail.com

Introduction

Ultrafiltration is related to sustainable processes and the most actively applied membrane method in various industrial fields (food, chemical, microbiological, water treatment, and etc.). The creation of novel ultrafiltration membranes with improved transport and antifouling properties is required due to its active using. Polyacrylonitrile (PAN) as a polymer often used in the manufacture of ultrafiltration membranes was used as membrane matrix. But PAN membranes have the main disadvantage: the decreased filtration productivity due to significant membrane fouling. To solve this problem, various modification strategies with a photocatalyst titanium oxide (TiO_2) was applied to the PAN membrane.

Membrane investigation

In this work, ultrafiltration membranes based on PAN modified with titanium oxide by various approaches (ex situ and in situ methods, surface modification) were developed. The PAN-based membranes were investigated by NMR spectroscopy, scanning electron and atomic force microscopies, swelling experiments, and contact angle measurements. The membrane performance and antifouling stability under UV irradiation were tested in ultrafiltration of industrially important feeds (bovine serum albumin solution (BSA) and coolant lubricant emulsion).

Results

It was found that modification with titanium dioxide significantly improved the transport and antifouling properties of PAN-based membranes.

Acknowledgements

This work is supported by RFBR, Sirius University of Science and Technology, JSC Russian Railways and Educational Fund "Talent and success", project number 20-38-51022. The experimental work of this study was facilitated by the equipment from the Resource Centre of Geomodel, Chemical Analysis and Materials Research Centre, Centre for X-ray Diffraction Methods, Magnetic Resonance Research Centre, Centre for Innovative Technologies of Composite Nanomaterials, Nanophotonics Centre, Cryogenic department, Thermogravimetric and Calorimetric Research Centre and the Interdisciplinary Resource Centre for Nanotechnology at the St. Petersburg State University.

Study of TiO_2@SiO_2 composite nanoparticles by solid state NMR ^{29}Si

Anastasiya S. Kovalenko[1], Anton M. Nikolaev[1], Olqa A. Shilova[1], Alexandr A. Sinelnikov[2], Anatolij V. Dobrodumov[3], Stanislav I. Selivanov [1,4], Alexandra G. Ivanova[1]

[1]Institute of Silicate Chemistry of the Russian Academy of Sciences, Saint-Petersburg, Russia
[2]Voronezh State University, Voronezh, Russia
[3]Institute of High Molecular Compounds of the Russian Academy of Sciences, Saint-Petersburg, Russia
[4] St. Petersburg State University, Saint-Petersburg, Russia
E-mail: anastasiya.bychk@mail.ru

Introduction

Nanocomposite materials based on TiO_2@SiO_2 have been of great interest to scientists in recent years due to their specific properties, such as increased photocatalytic activity and high adsorption capacity, which allow them to be used in many areas [1-4].

Earlier, we synthesized and studied the composite TiO_2@SiO_2-syn (syn – means that composite were synthesized by us) и composite TiO_2@SiO_2-com (com – means that we have synthesized a silica-containing shell on commercial TiO_2) with the core-shell structure, which occurred to have increased photocatalytic activity and high specific surface area (152 and 102 m^2/g, respectively) in comparison to TiO_2 nanopowder. The TEM image of the obtained TiO_2@SiO_2-sin nanopowder is shown in Fig.1. The research methods used by us earlier, such as XRD, IR, TEM, SAXS and low-temperature nitrogen adsorption do not provide exhaustive information about the composition and structure of the silica-containing shell, its formation features on the surface of the core of TiO_2 nanoparticles.

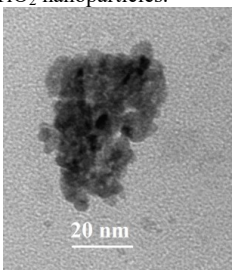

Figure 1. TEM image of the synthesized composite nanopowder TiO_2@SiO_2-syn. (The darker inclusions are TiO_2 nanoparticles)

One of the most effective methods for establishing structural units containing silicon atoms in solid oxide is magic angle spinning (MAS) solid state (SS) NMR spectroscopy on ^{29}Si nuclei [5-7].

In this regard, the purpose of this work was to study the composition and structure of the silica-containing shells of two types of nanocomposite powders TiO_2@SiO_2-syn and TiO_2@SiO_2-com by ^{29}Si MAS NMR spectroscopy

Experiments and results

The “core-shell” composite TiO_2@SiO_2 nanopowders were prepared via sol-gel procedure. TiO_2 nanopowder synthesized by precipitation from acidic solutions of $TiCl_4$ was used as the core of the TiO_2@SiO_2-syn composite nanopowder, and TiO_2 commercial nanopowder from Plasmoterm was used for the TiO_2@SiO_2-com composite nanopowder. To carry out the sol-gel synthesis, 6 g of the initial TiO_2 powder was ground in a mortar, followed

by the addition of 60 mL of distilled water. Then the resulting suspension was subjected to ultrasonic treatment using an ultrasonic disperser (22 kHz) for 30 seconds. Subsequently, 150 ml of silica sol (previously prepared by acid hydrolysis of TEOS in a water-alcohol medium with a lack of water) was added. The resulting solution was stirred on a magnetic stirrer for 3.5 hours. Then the resulting mixture was separated by centrifugation and the supernatant was decanted. The remaining precipitate was dried in an oven at 100°C.

Solid-state ^{29}Si MAS NMR and ^{29}Si CP MAS NMR spectroscopy (CP MAS - cross-polarization ^{1}H-^{29}Si transfer experiment under MAS condition) were performed on a Bruker Avance II 500WB spectrometer at room temperature and the rate of MAS was equal to 8 kHz.

Figure 2 shows MAS NMR ^{29}Si spectra (a) and CP MAS NMR ^{29}Si spectra (b) approximated by Gaussian functions for the "core-shell" composite TiO_2@SiO_2 nanopowders.

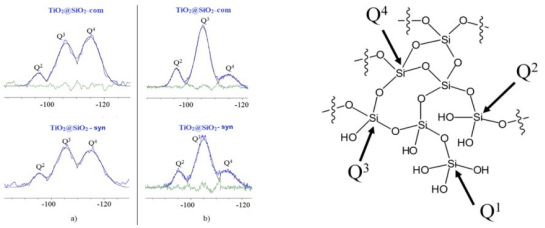

Figure 2. Solid-state NMR ^{29}Si spectra of TiO_2@SiO_2-com and TiO_2@SiO_2-syn, approximated by Gaussian functions, where a – MAS NMR ^{29}Si spectrum and b – CP MAS NMR ^{29}Si spectrum. The right insert shows the designations corresponding to the Q-nomenclature [7]

The values of the chemical shifts of the ^{29}Si NMR signals allow to strictly determining the degree of condensation (degree of crosslinking) of silicon tetrahedra in silica. These tetrahedra, in accordance with the accepted nomenclature, are designated Q^1, Q^2, Q^3 and Q^4, depending on the number of silicon atoms bonded through an oxygen atom to the SiO_4 tetrahedron in question (see Fig.2, insert) [7].

As it can be seen from ^{29}Si MAS NMR (Fig.2 (a)) and ^{29}Si CP MAS NMR (Fig.2 (b)) spectra of two TiO_2@SiO_2-com and TiO_2@SiO_2-sin composites are an overlay of three broad peaks at -115.2, -105.8 and -95.2 ppm, which correspond to such structural units as Q^4 – $[Si(SiO)_4]$, Q^3 – $[Si(SiO)_3(OH)]$, and Q^2 – $[Si(SiO)_2(OH)_2]$, respectively [9]. Structural units Q^1 – $[Si(SiO)_1(OH)_3]$ at about -85 ppm were not detected. These three overcrowded signals of Q^2, Q^3 and Q^4 were separated with the help of deconvolution procedure by using Gaussian line shape approximation and relative contents of fragments Q^2, Q^3 and Q^4 of two studied TiO_2@SiO_2 composites are given in Table 1.

Table 1. Relative content of fragments Q^4, Q^3 and Q^2, calculated from approximated peak areas in ^{29}Si MAS NMR and ^{29}Si CP MAS NMR of two TiO_2@SiO_2 composites

Sample	Relative content $Q^2/Q^3/Q^4$ from ^{29}Si MAS NMR spectrum	Relative content $Q^2/Q^3/Q^4$ from ^{29}Si CP MAS NMR spectrum
TiO_2@SiO_2-com	1/5,62/6,89	1/4,81/1,13
TiO_2@SiO_2-syn	1/4,03/4,49	1/4,22/1,77

It can be seen from Figure 2(a) and Table 1 that Q^4 fragments dominate in the spectra of both composites, indicating that the TiO_2@SiO_2-syn and TiO_2@SiO_2-com composites have a sufficiently voluminous silica-containing shell. At the same time, the TiO_2@SiO_2-syn nanocomposite contains fewer Q^4 fragments than the TiO_2@SiO_2-com composite, which

indicates that TiO_2@SiO_2-com has a more developed polymer structure of the silica shell than TiO_2@SiO_2-syn. An increase in the Q^3/Q^4 ratio for the TiO_2@SiO_2-syn composite compared to the TiO_2@SiO_2 composite may also indicate the formation of a larger number of Si–O–Ti bonds between the shell and the core of the composite TiO_2@SiO_2-syn [8].

The incorporation of Ti atoms into the SiO_4 tetrahedron structure can be studied using CP ^{29}Si MAS NMR spectroscopy It is known [8] that in composites obtained by the sol-gel method TiO_2@SiO_2 at a ratio of Ti/Si 1:8 observed an increase in the Q^4 peak in ^{29}Si CP MAS NMR, which may be evidence of the formation of Si–O–Ti heteroconnections. With a further increase in the TiO_2 content, a decrease in the Q^4 peak was observed with the simultaneous appearance of the Q^1 peak, which indirectly indicates that Ti atoms displace Si atoms from various structural fragments with the formation of silicic acid - structural fragments $[Si(SiO)_1(OH)_3]$.

In our case (Figure 2b), there is a strong decrease in the intensity of the Q^4 peak in the CP ^{29}Si MAS NMR spectra of two composites, while the Q^1 peak is not formed, and Q^3 increases greatly, which indicates that most of the silicon dioxide particles are directly related to hydroxyl groups, and Si–O–Ti bonds are present in insignificant amount. It is possible to notice a decrease in the ratio $(Q^2+Q^3)/Q^4$ due to an increase in the intensity Q^4 (Table1) for the composite TiO_2@SiO_2-syn – 2.95 compared to the composite TiO_2@SiO_2-com – 5.14. This probably indicates the presence of more Si–O–Ti bonds between the SiO_2 shell and the TiO_2 core of the TiO_2@SiO_2-syn composite. Especially since, the TiO_2 synthesized by us has a more developed specific surface area (~70 m^2/g) than commercial TiO_2 (~13 m^2/g) [9].

Conclusion

Thus, use of the solid state NMR ^{29}Si allowed confirming that TiO_2@SiO_2-com and TiO_2@SiO_2-syn composite particles with the core-shell structure consist of the sufficiently voluminous silica-containing shell with a significant number of OH groups and the core of TiO_2. Analysis of CP MAS NMR ^{29}Si spectra showed insignificant formation of Si-O-Ti bonds between the shell and the core of composites. It is possible that Ti-O-Si bonds are poorly determined due to the very insignificant content of titanium dioxide in composites. Further studies using solid state NMR of composites with different TiO_2/SiO_2 ratios will make it possible to determine their structure.

Acknowledgements

The work was carried out within the framework of the State Assignments for the Institute of Silicate Chemistry of the Russian Academy of Sciences (0081-2022-0006).

References

1. M. A. M. L. Jesus, A. M. Ferreira, L. F. S. Lima, et. al. – *Ceramics International*, 7, 23844-23850 (2021).
2. K. Pham, S. Pelisset, N. Kinnunen, et. al. – *Materials Chemistry and Physics*, https://doi.org/10.1016/j.matchemphys.2021.125533. (2022).
3. S. Angela, V. B. Lunardi, K. Kusuma, et. al. – *Monitoring & Management*, https://doi.org/10.1016/j.enmm.2021.100598. (2021).
4. K. Musaev, D. Mirkhamitova, A. Yarbekov, et. al. *SN Applied Sciences*, https://doi.org/10.1007/s42452-019-1192-y (2019).
5. T. Gutmann et al. *Annual Reports on NMR spectroscopy*, 97(1), 1-82 (2019)
6. G. De Paëpe. *Annu. Rev. Phys. Chem.*, 63, 661-684 (2012).
7. G. Engelhardt, D. Michel. High resolution solid-state NMR of silicates and zeolites. Chichester: John Wiley & Sons, Australia, Limited, 1987.
8. Z. Liu, G. M. Crumbaugh, R. J. Davis. – *Journal of Catalysis*, 159, 3-89 (1996).
9. T. V. Khamova, G. P. Kopitsa, A. M. Nikolaev, et al. – *Biointerface Research in Applied Chemistry*, 11(4), 12285-12300 (2021).

Comparison of calculated and experimental data of ^{1}H and ^{13}C-NMR spectra of 4´,4´´-di-(1-methyl-1-hydroxyethynyl)-dibenzo-18-crown-6

Lyubov K. Kozinskaya, Dilorom H. Mirkhamitova

Faculty of Chemistry, National University of Uzbekistan, Uzbekistan
E-mail: lubasha_1985@mail.ru

Introduction

The spectra of large molecules with little difference in substituent position or length often have many similar signals.

In the issue of identifying the structure of a new substance or a number of new compounds, the generation of spectra in computer programs is often used, as well as the method of comparing the generated and experimental spectra [1].

Dibenzo-18-crown-6 tertiary acetylenic alcohol was obtained by the Favorsky method in the interaction of 4′,4′′-diacetyldibenzo-18-crown-6 with acetylene in the presence of alkali.

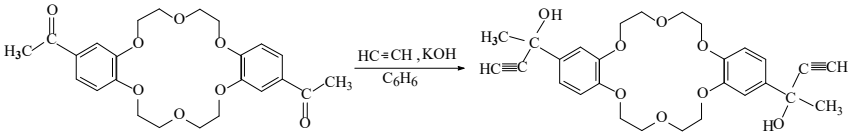

Figure 1. Scheme for the synthesis of 4′,4′′-di-(1-methyl-1-hydroxyethynyl)-dibenzo-18-crown-6

Comparison method

To identify the structure of 4′,4′′-di-(1-methyl-1-hydroxyethynyl)-dibenzo-18-crown-6, a comparison of ^{1}H- and ^{13}C-NMR spectra was used.

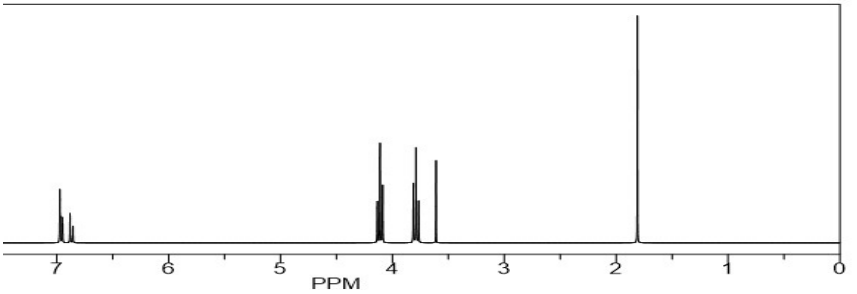

Figure 2. Calculation of ^{1}H-NMR spectrum of 4′,4′′-di-(1-methyl-1-hydroxyethynyl)-dibenzo-18-crown-6

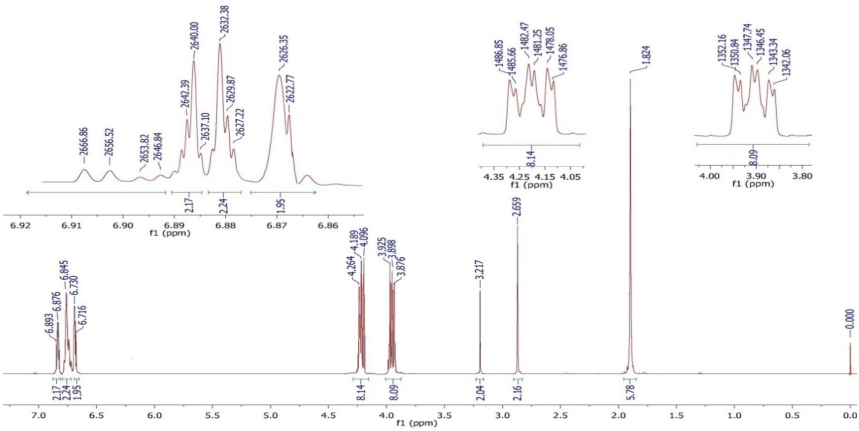

Figure 3. [1]H-NMR spectrum of 4′,4′′-di-(1-methyl-1-hydroxyethynyl)-dibenzo-18-crown-6

Table 1. Comparison of experimental and calculated data of [1]H-NMR spectra 4',4''-di-(1-methyl-1-hydroxyethynyl)-dibenzo-18-crown-6

	α-CH_3	-OH	≡CH	β-O-CH_2	α-O-CH_2	Ar-C**H** 6′,6′′	Ar-C**H** 3′,3′′	Ar-C**H** 5′,5′′
Experiment	1.82	2.65	3.21	3.87-3.92	4.09-4.26	6.71-6.73	6.84	6.87-6.89
Calculation	1.81	8.19	3.61	3.79	4.11	6.87	6.97	6.96

The signals of the protons of the hydroxyl group under the influence of the substituent appear at 2.65 ppm, the signals of the protons of the benzene rings are shifted to the strong region, and the signals of the macrocyclic fragment (O-C**H**$_2$) are shifted to the weak region. But in general, the calculated and recorded NMR spectra have an identical construction. It can be concluded that all functional groups are present and the structure is identified.

Also, to confirm the proposed structure, the ^{13}C-NMR spectrum of 4′,4′′-di-(1-methyl-1-hydroxyethynyl)-dibenzo-18-crown-6:

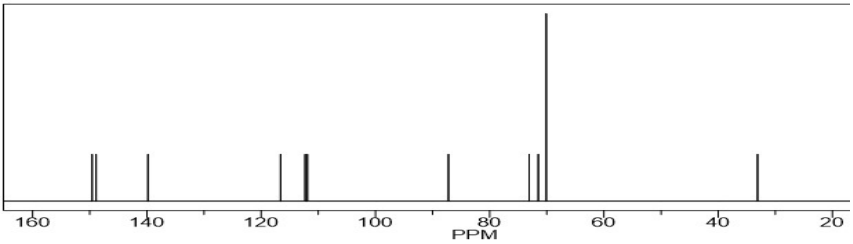

Figure 4. Calculation of [13]C-NMR spectrum of 4′,4′′-di-(1-methyl-1-hydroxyethynyl)-dibenzo-18-crown-6

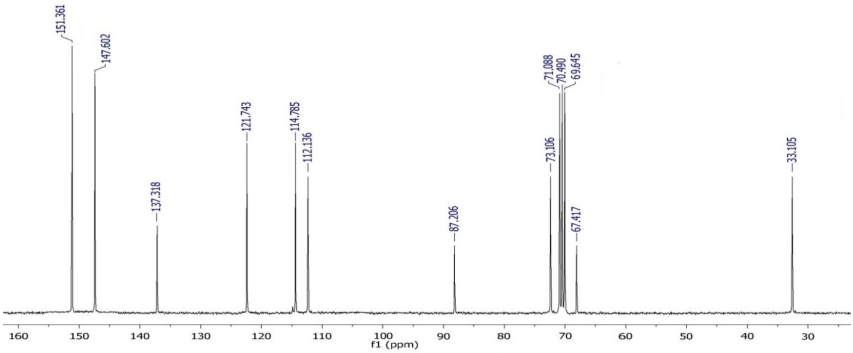

Figure 5. ^{13}C-NMR spectrum of 4′,4′′-di-(1-methyl-1-hydroxyethynyl)-dibenzo-18-crown-6

Table 2. Comparison of experimental and calculated data of ^{13}C-NMR spectra 4',4''-di-(1-methyl-1-hydroxyethynyl)-dibenzo-18-crown-6

	-**C**H$_3$	—**C**—	β-O-**C**H$_2$ α-O-**C**H$_2$	-**C**≡C	-C≡**C**	Ar-**C**H 3′,3′′ 6′,6′′	Ar-**C**H 5′,5′′ 4′,4′′	Ar-**C**H 1′,1′′ 2′,2′′
Experiment	33.10	67.41	69.64 70.49-71.08	73.10	87.20	112.13 114.78	121.74 137.31	147.60- 151.36
Calculation	33.1	71.5	70.1	73.1	87.2	111.9 112.3	116.6 139.8	148.9 149.6

Analysis of the generated and experimentally obtained ^{13}C-NMR spectra of 4′,4′′-di-(1-methyl-1-hydroxyethynyl)-dibenzo-18-crown-6 suggests that the calculation is compatible with the experimental data.

Small deviations in the signals of protons in ^{1}H-NMR, as well as quaternary hydrocarbons and aromatic ring ^{13}C-NMR spectra can be explained by the spatial arrangement of the molecule, interaction with the solvent, or the mutual influence of groups of atoms.

References

1. K.S. Usachev, S.V. Efimov, A.R. Yulmetov, A.V. Filippov, O.N. Antzutkin. – *Magnetic Resonance in Chemistry.,* **50,** 784-792 (2012).

Fibrinogen translational diffusion and intermolecular interactions depending on electrolyte solution

Aleksandra Kusova, Aleksandr Sitnitsky, Yuriy Zuev

Kazan Institute of Biochemistry and Biophysics, Russian Academy of Sciences, Lobachevsky Str., 2/31 Kazan, Russian Federation.
e-mail: alexakusova@mail.ru

Introduction

Fibrinogen (Fg) is the one of the most abundant blood plasma proteins, playing a fundamental role in the processes of clotting, thrombocytosis and wound healing. The Fg intermolecular interactions prelude to protofibril formation due to high natural concentration of Fg in plasma. In vitro, fibrin self-assembly is sensitive to physicochemical conditions like the solution pH and ionic strength, which tune the strength of the non-covalent driving forces. Despite pH and ionic strength are strictly determined for biological systems, the study of Fg intermolecular interactions in the distinct electrolyte environment can clarify various steps of Fg functioning. The ionic strength of a protein solution leads to the thickness of the electric double layer around charged protein molecules. Electrostatic repulsion actually emanates from entropy decrease when the double layers of two approaching surfaces overlap and specific ion influence results in screening of electrostatic repulsion. The pH affects protein interactions in a direct way by adjusting protein charge and altering its conformation. Near the isoelectric point (IEP) the proteins have small net charge and therefore the lateral electrostatic interactions between molecules are minimized while the hydrogen bonding and van der Waals forces become substantial. The minimization of intermolecular repulsions of Fg contributes in the fibril formation at physiological conditions. In this work we determined the self-diffusion coefficients, which characterize conformations and protein-protein interactions of Fg depending on external conditions.

Experimental

The Fg powder (Sigma Aldrich) was dissolved in appropriate (NaCl, phosphate buffer, acetate, carbonate buffer) solutions for fixed pH values equal to 3.5, 7.4, and 9.5 respectively and the ionic strength equals 0.1 M, 0.5 M, 1.0 M. ^{1}H NMR experiments were carried out on a Bruker AVANCE III NMR spectrometer operating at 600.13 MHz equipped with a standard z-gradient inverse probe head (TXI, 5 mm tube) capable of producing gradients with a maximum strength of 55.7 G*cm-1. The amplitude of field gradient was varied from 2% to 95% of its maximum value over 16-32 increments under constant diffusion time (Δ=50 ms) and gradient pulse duration (δ=8-16 ms).

Results and discussion

Fg conformation and functional activity depend on the ionic strength and pH of solution, which play an essential role in the hydrodynamic behavior of the molecule. One of the most important parameter characterizing the dynamics of the protein molecules in solution is the translational diffusion coefficient. We conducted the PFG NMR experiments for Fg solutions with various pH and ionic strength values to check possible protein oligomirization in different ionic environment. Fig. 1 shows the diffusion decays for Fg solutions (A. 10-12 mg/ml; B 30-40 mg/ml). One can see that for all protein solutions the diffusive decays have the mono-exponential shape. There is no noticeable distribution in the size of the Fg diffusing spices irrespectively of protein structural state either it is molecular or supramolecular one.

For the first step, the hydrodynamic radius R_h in dilute solutions at various conditions was determined with the Stokes-Einstein equation $D_0=kT/6\pi\eta R_h$. The advantage of using PFG NMR for interpreting the R_h is avveraged self-diffusion coefficient D_s. As can be deduced

from the results shown in Fig. 2A, the trend of the hydrodynamic radius decreases with increasing pH. The most expanded conformation is observed for pH =3.5. Low pH characterized by the large angle between the Aα chains and the body of the molecule equal to 115°, and the high net positive charge (+26e). Also the R_h tends to rise with increasing ionic strength of solution. With ionic strength increasing, a more expanded protein conformation is observed.

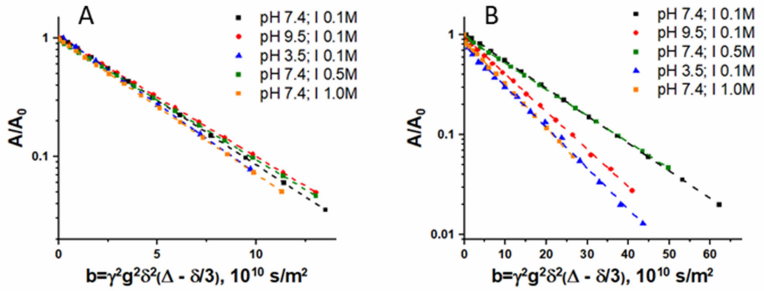

Fig. 1 Diffusion decays of signal intensity in Fg solutions A) 10-12 mg/ml B) 30-40mg/ml

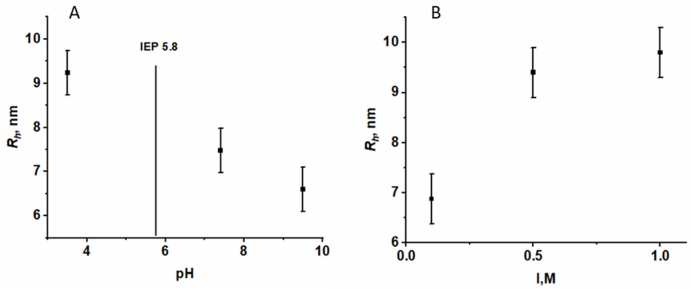

Fig. 2. The dependence of the hydrodynamic radius R_h of the Fg molecule on the pH (A), ionic strength (B)

The concentration dependences of the self-diffusion coefficient $D_s(\varphi)$ of Fg was obtained at pH 3.5, 7.4, 9.5. The data are presented in Fig. 3A. The shape of the curve $D_s(\varphi)$ at pH 7.4 is close to ones at 9.5. A slight shift of D_s values at $\varphi \to 0$ was considered in terms of R_h. Fig. 3B shows $D_s(\varphi)$ of Fg as a function of protein volume fraction at different ionic strength values I. At high ionic strength the curvature of $D_s(\varphi)$ is smoothed expanding the dilute solutions range. In an acidified medium the similar behavior is observed.

As in our previous papers [1] for a theoretical description of concentration dependence of protein self-diffusion coefficient we used the phenomenological approach based on the frictional formalism of non-equilibrium thermodynamics (Vink approach) [2], which allows to analyze the solvent–solute and solute–solute friction in solution.

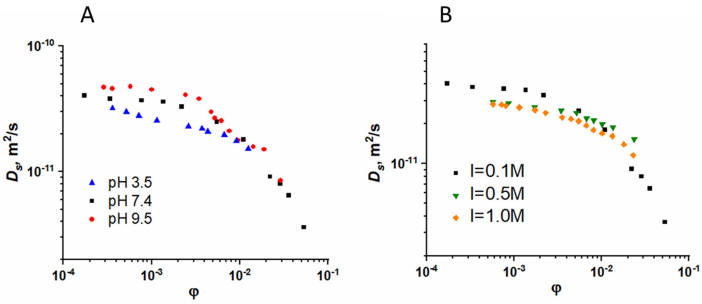

Fig. 3 Concentration dependences of the protein self-diffusion coefficient (D_s) as a function of protein volume fraction at different: A) pH, B) ionic strength values.

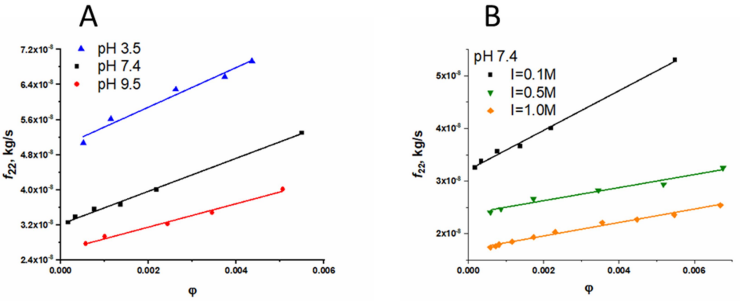

Fig. 4 Concentration dependences of the protein-protein friction coefficients derived from the analysis of self-diffusion coefficients

The curves of the Fg friction coefficients at pH 3.5 are placed higher and have a strong slope (Fig. 4). This is explained by the more expanded structure and low mobility of Fg at low pH. When Aα domains become mobile, they are able to interact with other molecules side domains by a mechanical friction reflected in the protein-protein friction coefficients. Intermediate values of mobility and friction coefficients are observed at pH 7.4. Following pH grow leads to decreasing friction coefficients because of change in the conformation of Fg depending on the position of Aα domains. Protein-protein friction coefficient decreases due to the weak intermolecular interaction ability of highly screened protein molecules.

Acknowledgements

This work was partly supported by the government assignment for Federal Research Center Kazan Scientific Center of Russian Academy of Sciences and the Russian Foundation for Basic Research [Grant N 20-04-00157].

References

1. A.M. Kusova, A.E. Sitnitsky, D.A. Faizullin, Yu.F. Zuev, Protein translational diffusion and intermolecular interactions of globular and intrinsically unstructured proteins. J. Phys. Chem. A 123 (2019) 10190–10196.
2. H. Vink, Mutual diffusion and self-diffusion in the frictional formalism of non-equilibrium thermodynamics, J. Chem. Soc. Faraday Trans. 1 81 (1985) 1725–730.

Development and characterization of novel pervaporation and ultrafiltration membranes based on polyphenylenesulphone

Anna I. Kuzminova[1,2], Maria E. Dmitrenko[1,2], Andrey A. Zolotarev[1,2], Aleksandra S. Korniak[1], Danila D. Myznikov[1], Anton S. Mazur[1], Anastasia V. Penkova[1,2]

[1]Saint Petersburg State University, Saint-Petersburg, Russia
[2]Sirius University of Science and Technology, 1 Olympic Ave, 354340, Sochi, Russia
E-mail: a.kuzminova@spbu.ru
https://go.spbu.ru/rgpenkova

Introduction

Membrane methods are promising methods for both separating mixtures of low molecular weight components (pervaporation) and removing high molecular weight components from low molecular weight components (ultrafiltration). Membrane methods allow the separation and concentration of components using low power consumption and compact equipment, and without the use of additional components. For the implementation of membrane methods, a properly selected membrane material is required. In recent years, mixed matrix membranes (MMMs) have become especially popular among membranes, in which an inorganic and/or organic modifier is introduced into the polymer matrix to obtain tailoring properties.

In the present work two types of membranes were developed for ultrafiltration (porous membrane) and for pervaporation (nonporous, dense membrane). Polyphenylenesulphone (PPSU) was chosen as the polymer material due to its physiochemical properties, thermal and chemical resistance and high tensile strength. Titanium dioxide (TiO_2) was chosen as a modifier due to its low cost, high reusability and chemical stability. Physical and chemical properties of ultrafiltration and pervaporation PPSU/TiO_2 membranes were studied by atomic force microscopy (AFM), scanning electron microscopy (SEM), Fourier-transform infrared spectroscopy (FTIR), nuclear magnetic resonance (NMR), X-ray diffraction analysis, swelling experiments, thermogravimetric analysis and contact angle measurement. The transport properties of UF membranes were investigated in separation of the bovine serum albumin (BSA) and cutting fluid solutions in water. Transport properties of PV membranes were investigated by separation of isopropanol/water and ethyl acetate/water mixtures. It was found that introduction of TiO_2 modifier leads to significant improvements of physiochemical and transport properties of pervaporation and nanofiltration membranes based on PPSU.

Acknowledgements

The reported study was funded by RFBR, Sirius University of Science and Technology, JSC Russian Railways and Educational Fund "Talent and suc-cess", project number 20-38-51022. The experimental work of this study was facilitated by the equipment from the Resource Centre of Geomodel, Chemical Analysis and Materials Research Centre, Centre for X-ray Diffraction Methods, Magnetic Resonance Research Centre, Centre for Innovative Technologies of Composite Nanomaterials, Nanophotonics Centre, Cryogenic department, Thermogravimetric and Calorimetric Research Centre and the Interdisciplinary Resource Centre for Nanotechnology at the St. Petersburg State University.

Development and characterization of novel Zr-MOFs-modified membranes based on polyvinyl alcohol

Anna I. Kuzminova[1], Maria E. Dmitrenko[1], Andrey A. Zolotarev[1], Aleksandra S. Korniak[1], Anton S. Mazur[1], Anastasia V. Penkova[1]

[1]*Saint Petersburg State University, Saint-Petersburg, Russia*
E-mail: a.kuzminova@spbu.ru
https://go.spbu.ru/rgpenkova

Introduction

Pervaporation is one of the most popular membrane processes for the separation of low molecular weight components, including mixtures of isomers, azeotropic mixtures, and thermally unstable mixtures. The separation of such mixtures of low molecular weight components by traditional methods is difficult. Currently, the improvement of the transport properties of polymeric pervaporation membranes occurs due to the creation of mixed matrix membranes (MMMs), by modifying the polymer matrix with an inorganic and/or organic modifier to obtain tailoring properties.

In the present work the novel green membranes based on polyvinyl alcohol (PVA) were prepared by introducing the three metal-organic frameworks (Zr-MOFs): MIL-140A, MIL-140A-AcOH-EDTA and MIL-140A-AcOH into the PVA matrix. The improvement of the transport properties of the membranes based on PVA modified by Zr-MOFs was expected due to the porous structure, hydrophilic/hydrophobic properties, excellent chemical and thermal stability of the Zr-MOFs. The most important investigation of Zr-MOFs inclusion in PVA matrix is analysis of membranes by spectroscopic methods. Among these methods, nuclear magnetic resonance (NMR) is the best tool for the investigation of polymer nanocomposite materials. NMR allowed to study the interaction between Zr-MOFs and polymer PVA matrix and to confirm the complex structure of MMMs in the present work. The additional characterizations of the polymer samples were studied by Fourier-transform infrared spectroscopy, scanning electron microscopy, atomic force microscopy, thermogravimetric analysis, and swelling experiments. Transport properties of the developed membranes were investigated by pervaporation during separation of water-isopropanol mixtures at 22 °C.

Acknowledgements

This work is supported by Scholarship of the President of the Russian Federation СП-2506.2022.1. The experimental work of this study was facilitated by the equipment from the Resource Centre of Geomodel, Chemical Analysis and Materials Research Centre, Centre for X-ray Diffraction Methods, Magnetic Resonance Research Centre, Centre for Innovative Technologies of Composite Nanomaterials, Nanophotonics Centre, Cryogenic department, Thermogravimetric and Calorimetric Research Centre and the Interdisciplinary Resource Centre for Nanotechnology at the St. Petersburg State University.

Ionic liquid in the process of extraction cleaning of various fractions of Azerbaijani oil

Kenan Mammadhasanov[1*], Sabina A. Seidova[2**], Minaver D. Ibragimova[2], Andrei V. Komolkin[1]

[1]Faculty of Physics, Saint Petersburg State University, Saint Petersburg, 199034, Russia
[2]Y. H. Mammadaliyev Institute of Petrochemical Processes of Azerbaijan National Academy of Sciences, AZ 1025, Baku, 30 Khojaly ave., Azerbaijan
*E-mail: mammadhasanov@yandex.ru
**E-mail: sabina.seidova.ai@mail.ru

Introduction

The existing environmental problem entails the imposition of more stringent quality requirements for various petroleum products. Despite the fact that traditional hydrogenation purification methods are used in industry to obtain high-quality petroleum products, extraction is considered as an alternative to these methods.

Currently, among the selective solvents used in the process of extraction purification of various oil fractions, environmentally acceptable extractants – ionic liquids – are attracting the active attention of researchers. Due to the unique properties and versatility of the fields of application of ionic liquids, interest in them is constantly growing.

Experimental investigations

For several decades, the Institute of Petrochemical Processes of the National Academy of Sciences of Azerbaijan has been conducting research in the field of synthesis and application of ionic liquids that differ in cation-anion combination in the extraction purification of various petroleum fractions – oil distillates of various viscosities, transformer oil, hydraulic fluid distillate, catalytic cracking gasoline, gasoline reformer, diesel distillate, etc. The studies carried out in this direction show that for each fractional composition it is necessary to select an ionic liquid with a suitable cationic-anionic component, which, under the optimal conditions found for a given extraction system, has the highest selectivity.

Computer simulation methods

For a more detailed study of extraction systems, the use of computer simulation is important. In view of this, successful research is being carried out with St. Petersburg State University in the field of determining the microstructure and dynamics of ionic liquids in the process of selective purification of petroleum fractions based on the molecular dynamics method. Modeling of an extraction system consisting of a model fuel and extractants of various compositions using the AKMD-14 molecular dynamics program. The calculations were performed using the OPLS-AA atom-atom interaction potentials.

Molecules of furfural, N-methyl-2-pyrrolidone, and ionic liquids were chosen as extractants in the simulation. Oil fractions were represented by mixtures of metaxylene (representative of the aromatic components of oil), thiophene (sulfur compounds), and hexane (aliphatic component). In modeling, special attention is paid to identifying specific interactions of ionic liquids with aromatic and sulfurous components of oil for the purpose of their selective extraction. The simulation was carried out at room temperature and at normal atmospheric pressure, the composition of mixtures of ionic liquids was varied. Modeling showed the promise of using ion-liquid extractants in the process of extraction purification.

Acknowledgements

Computer simulations were carried out at Computer Center of SPbU.

Composite pulses with discrete phase modulation, optimized using genetic algorithm

Ivan Mershiev, Galina S. Kupriyanova

Immanuel Kant Baltic Federal University, Kaliningrad, Russian Federation
E-mail: IMershiev@kantiana.ru

In NMR spectroscopy, a composite pulse in general case is a series of radiofrequency pulses with phase modulation, tuned for compensation of instrumental imperfections. Since their introduction over the forty years ago [1], composite pulses remain in high demand in various NMR applications. With the progress in NMR, composite pulses found their use in NMR not only as a tool for compensation of RF and B_0 field inhomogeneity, but also for precise spin manipulation in complex experiments, such as polarization transfer, construction of quantum logical gates, and for efficient broadband decoupling. In recent years, a lot of advanced composite pulses were proposed: broadband universal rotation [2], triple-compensated [3], antisymmetric dual-compensated with zero phase distortion [4], and much more.

It could be seen that early composite pulses were strictly limited by the capabilities of NMR equipment of that time, using 2- or 4-step phase modulation [5,6], and, rarely, modulation of individual pulse length [7]. With further developments in composite pulses theory and progress in NMR spectrometers hardware, accuracy of phase modulation for most newly designed composite pulses increased up to 0.1°, which obviously made it incompatible with legacy equipment. In this paper, we present dual-compensated composite pulses with 5-bit (32-step) phase modulation, matching the phase modulation capabilities of Tecmag Inc. Apollo and LapNMR spectrometers, that are still widely in use.

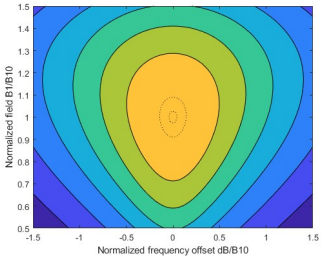

Figure 1. Fidelity profile of a single 180 pulse. 0.999 and 0.99 fidelity areas are shown with dashed lines.

There is no unified theory of composite pulses. Their design evolved from empirical methods to use of numerical optimization or optimal control theory, usually for minimization of Hamiltonian error terms. Other approach is to use fidelity function as an optimization target [8–10], e.g. an extent of similarity of action of the composite pulse with a perfect 90 or 180 pulse at the presence of magnetic field inhomogeneity and frequency offset.

One of the most convenient ways of describing composite rotations is using quaternions [11].

For a perfect on-resonance pulse,

$$q_{\theta,\varphi} = \{s, v\} = \left\{\cos\left(\frac{\theta}{2}\right), \sin\left(\frac{\theta}{2}\right)(\cos(\varphi), \sin(\varphi), 0)\right\}.$$

In the presence of simultaneous magnetic field inhomogeneity and frequency offset,

$$q_{\theta,\varphi} = \left\{ \cos\left(\frac{\theta'}{2}\right), \frac{\sin\left(\frac{\theta'}{2}\right)}{\sqrt{1+\left(\frac{\Delta\omega}{\omega_1}\right)}} \left(\cos(\varphi), \sin(\varphi), \frac{\Delta\omega}{\omega_1}\right) \right\}$$

Where

$$\theta' = \sqrt{(\gamma B_1 \left(\frac{\Delta B_0}{B_1^0}\right))^2 + \left(\frac{\Delta\omega}{\Delta B_0}\right)^2}\, t$$

Composite pulse can be compared with a perfect 900 or 1800 pulse using quaternion fidelity operator:

$$\lambda = |\boldsymbol{q} \cdot \boldsymbol{q}_0|$$

For 90° pulse,

$$q_{90°,0°} = \left\{ \sin\left(\frac{\pi}{4}\right), cos\left(\frac{\pi}{4}\right), 0, 0 \right\}$$

Fidelity function λ should be equal to unity for the perfect rotation.

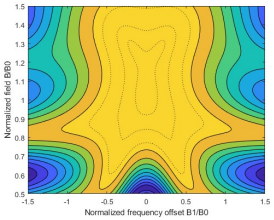

Figure 2. Fidelity as a function of pulse length error and frequency offset for a 90° composite pulse 11,25°[26 22 1 30 20 28 23 23 22 0 0 22 23 23 28 20 30 1 22 26], total length 10π. 0.999, 0.99 and 0.95 fidelity areas are shown with dashed lines.*

Genetic algorithm, being a heuristic method, has a good chance of finding a global minima solution in a complex space. Another useful property of genetic algorithm is ability to handle mixed-integer optimization procedures. We used GA implementation from MATLAB Optimization toolbox. Following the guidelines for the mixed integer optimization, maximum elite count was increased from 0.05 to 0.25, and number of generations was set to the value far exceeding the number of variables (from 100 to 1000-2000).

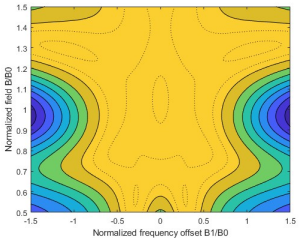

Figure 3. Fidelity as a function of pulse length error and frequency offset for a 180° composite pulse 11.25° [23 22 20 25 23 12 14 27 25 31 31 25 27 14 12 23 25 20 22 23], total length 10π. 0.999, 0.99 and 0.95 fidelity areas are shown with dashed lines.*

Composite pulses can be described with quaternion algebra by consequently multiplying quaternions for each individual pulse according to quaternion multiplication rule:

$$q_1 * q_2 = \{s_1 \cdot s_2 - v_1 \cdot v_2, s_1 v_2 + s_2 v_1 + v_1 * v_2\}$$

For the whole pulse train consisting of N pulses,

$$q_{CP} = \prod_{N} q_{\theta_n \varphi_n}$$

The composite pulses designed by following procedure will belong, according to M. Levitt classification [9], to class A composite pulses, or universal rotors. Such kind of composite pulses can perform a fully compensated rotation, similar to the action of perfect 90 or 180 pulse, with respect of an initial phase of the pulse.

Finding a global minimum in a complex solution space is a demanding task. Genetic algorithm, being a heuristic optimization method, performs well in tasks with a lot of local minima. There are few implementations of genetic algorithm in design of composite pulses [3,8,12].

Another property of genetic algorithm is possibility to perform optimization on functions with integer and mixed-integer variables [link to Matlab website]. In our case, it allows to optimize the fidelity function using discrete phase modulation values for a composite pulse. Mixed-integer optimization, in turn, allows to include length or magnitude modulation of individual pulses of the train, thus greatly increasing the potential solution space and utilizing the amplitude modulation capabilities of the spectrometer.

Optimization of the fidelity function was performed using MATLAB Optimization toolbox genetic algorithm implementation. Optimization parameters were chosen according to recommendations for mixed integer variables: generation count was increased to 5000 to reduce the risk of being trapped in local minima, and elite count was increased to 0.25. Function was optimized by the integral value of fidelity function. Total pulse length was set to 10π. To enforce compliance with ordinary pulses and to achieve maximum pulse fidelity on resonance, an additional nonlinear constraint was enforced to keep the fidelity function maximal at zero error condition.

Acknowledgements

This work is supported by the Ministry of Science and Higher Education (grant #05-04-03) and DAAD foundation.

References

1. M. H. Levitt and R. Freeman, J. Magn. Reson. 33, 473 (1979).
2. K. Kobzar, S. Ehni, T. E. Skinner, S. J. Glaser, and B. Luy, J. Magn. Reson. 225, 142 (2012).
3. V. S. Manu and G. Veglia, J. Magn. Reson. 260, 136 (2015).
4. S. Odedra, M. J. Thrippleton, and S. Wimperis, J. Magn. Reson. 225, 81 (2012).
5. A. . Shaka and R. Freeman, J. Magn. Reson. 55, 487 (1983).
6. M. H. Levitt, J. Magn. Reson. 48, 234 (1982).
7. A. J. Shaka, Chem. Phys. Lett. 120, 201 (1985).
8. V. S. Manu and G. Veglia, J. Magn. Reson. 273, 40 (2016).
9. M. H. Levitt, Prog. Nucl. Magn. Reson. Spectrosc. 18, 61 (1986).
10. H. K. Cummins, G. Llewellyn, and J. A. Jones, Phys. Rev. A - At. Mol. Opt. Phys. 67, 7 (2003).
11. B. Blümich and H. W. Spiess, J. Magn. Reson. 61, 356 (1985).
12. Y. Xia, P. Rossi, M. V. Subrahmanian, C. Huang, T. Saleh, C. Olivieri, C. G. Kalodimos, and G. Veglia, J. Biomol. NMR 69, 237 (2017).
13. M. Sass and D. Ziessow, J. Magn. Reson. 25, 263 (1977).
14. K. Van Putts, J. Magn. Reson. 2, 174 (1970).
15. A. Kumar and C. S. Johnson, J. Magn. Reson. 7, 55 (1972).
16. S. Fisher, B. I. Yachtman. – Vacuum State Comm., 7, 1234-1237 (2003).

Novel pervaporation membranes based on hydroxyethyl cellulose/sodium alginate for separation of isopropanol/water mixture

Danila D. Myznikov[1], Anna I. Kuzminova[1], Maria E. Dmitrenko[1], Andrey A. Zolotarev[1], Aleksandra S. Korniak[1], Anastasia V. Penkova[1]

[1]St. Petersburg State University, 7/9 Universitetskaya nab., St. Petersburg 199034, Russia; tel. +7812 3636000 additional code 3367
E-mail: dan.myznikov@gmail.com
https://go.spbu.ru/rgpenkova

Introduction

Recently, membrane processes are quickly growing up. At the same time, industry requires effective membrane materials based on biopolymers for separation of mixtures used in many areas. In addition, the issue of environmental safety is on the agenda, the impact of industrial development on it becomes more and more controlled. Therefore, the industry is improving its production methods by using novel technologies to improve productivity and efficiency of processes, and make them environmentally friendly and economically beneficial. Pervaporation is one of the most advanced and rapidly developing membrane processes applied for separation of mixtures with low molecular weight components, azeotropic mixtures, isomer mixtures and other due to its characteristics: environmental friendless, low energy consumption and compact modular equipment.

In this work biopolymers sodium alginate (SA) and hydroxyethyl cellulose (HEC) were selected for the development of novel dense and supported blend HEC/SA membranes for separation of water/isopropanol mixture using bulk and surface modification. Water-soluble fullerenol ($C_{60}(OH)_{22–24}$) was used as modifier. Citric acid, phosphoric acid and calcium chloride were used as cross-linking agents for polymers. Poly(sodium 4-styrenesulfonate) (PSS) was used as polyanion, while poly(allylamine hydrochloride) (PAH) and SA were used as polycations for the surface modification by layer-by-layer (Lbl) assembly. It was shown that the HEC/SA (30/70) membrane had the optimal transport properties with dehydration of isopropanol (12 wt.% water). The modification of HEC/SA with fullerenol led to the increase in permeation flux by 17%, maintaining high selectivity to water (99.99 wt.% in the permeate), in pervaporation dehydration of isopropanol (12 wt.% water). The dense membrane based on HEC/SA/fullerenol (5%) composite cross-linked with $CaCl_2$ (HEC/SA-5^{CaCl2}) demonstrated the highest permeation flux and constant 99.99 wt.% water content in the permeate in dehydration of isopropanol in wide concentration range (12–100 wt.% water). Also, the supported membrane consisting of thin selective layer deposited on the PAN substrate was developed (HEC/SA-5/PAN^{CaCl2}). It allowed increasing the permeation flux ~2 times compared to the cross-linked modified dense membrane, but with the decrease of selectivity. Thus, two alternative solutions may be offered for industrial dehydration, depending on the separation task: either the HEC/SA-5/PAN^{CaCl2}—Lbl^{PSS,PAH} membrane with the highest permeation flux or the most selective HEC/SA-5/PAN^{CaCl2} membrane. It was demonstrated that the use of the surface or/and bulk modifications led to notable improvement of the membrane transport properties due to significant changes in membrane inner and surface structure.

Structure and physicochemical properties of the developed membranes were investigated by Fourier-transform infrared spectroscopy, scanning electron microscopy, atomic force spectroscopy, thermogravimetric analysis, swelling degree, contact angle and nuclear magnetic resonance (NMR). NMR spectroscopy is important method that shows what effect the introduction of modifier and cross-linking agents has on the bold length and

structure of membrane, also it allows to confirm the embedding of the modifier in the polymer structure. All that is important data that explains the changes of selectivity, permeation flux and other parameters of the membrane.

Acknowledgements

This research was funded by the Russian Science Foundation, grant number 20-79-10064. The experimental work of this study was facilitated by the equipment from the Resource Centre of Geomodel, Chemical Analysis and Materials Research Centre, Centre for X-ray Diffraction Methods, Magnetic Resonance Research Centre, Centre for Innova-tive Technologies of Composite Nanomaterials, Nanophotonics Centre, Cryo-genic department, Thermogravimetric and Calorimetric Research Centre and the Interdisciplinary Resource Centre for Nanotechnology at the St. Petersburg State University.

MRI methods in the diagnosis of accumulation of iron complexes in the brain

Nikitina A.V., Bogachev Yu.V.

Department of Physics, Saint-Petersburg Electrotechnical University "LETI", 5, prof. Popov st., Saint-Petersburg, 197376, Russia,
E-mail: nastya_nikitina1996@mail.ru

Introduction

Recently, there has been considerable interest in the accumulation of iron complexes in the brain, their metabolism and role in the functioning of the brain, the connection with various diseases. It is well known that iron accumulates in the brain with age in people with Huntington's, Parkinson's, Alzheimer's, multiple sclerosis, other neurodegenerative diseases, as well as in chronic hemorrhages, cerebral infarction, anemia, thalassemia, hemochromatosis and some other diseases [1], [2]. Since the brain contains various forms of iron, their separation and quantification of each type can contribute to the early diagnosis of a number of diseases, lead not only to a better understanding of the causes and course of these diseases, but also to identify ways of treatment. Magnetic resonance imaging (MRI) is the most informative method for visualizing the accumulation and quantification of iron complexes in the brain. The report discusses various MRI methods used for both qualitative and quantitative assessment of iron content in brain tissues.

T_2, T_2* and T_2' NMR relaxometry

T_2 NMR relaxometry allows one to directly calculate T_2 or R_2 ($1/T_2$) maps with a slight influence of inhomogeneities of the external magnetic field. On the other hand, the relaxation time T_2* and, consequently, its inverse parameter R_2* refer to the attenuation of transverse magnetization caused by a combination of spin-spin relaxation and local inhomogeneity of the magnetic field. Inhomogeneities of the main magnetic field have less effect on R_2* when the voxel size is smaller; therefore, it is desirable to reduce the thickness of the slice.

The relaxation rate R_2', defined as the difference between R_2* and R_2, is directly related to the local inhomogeneity of the magnetic field caused by the presence of iron, as well as other sources. Although the parameter R_2' is theoretically more sensitive to the iron content compared to R_2, however, in reality R_2' has limited sensitivity due to its small value.

A more efficient way to measure R_2* and R_2' is to receive multiple echoes during a single reception. These multi-sectional measurements during a single reception can be performed using gradient echo sampling of free induction decay and echo signal (GESFIDE) [2]. Multiecho sequences are able to provide data sufficient to construct multi-sectional maps of R_2*, R_2' and R_2 in one step.

In general, T_2- or T_2*-weighted images are often considered more sensitive to the disease (fewer false negative results), while relaxation maps can be considered more specific (fewer false positive results). That is, if the goal is to detect a disease, for example, associated with increased local iron deposition, searching for a local decrease signal in T_2*-weighted images can be especially useful. However, many artifacts may also appear as iron deposits, which leads to an overestimation of the extent of the disease. With the help of the T_2* value map, it is possible to more accurately determine those regions that contain higher concentrations of iron, and even estimate the local concentration of iron.

Susceptibility weighted imaging (SWI)

This method, like T_2* MRI, is based on spin dephasing caused by local field inhomogeneities, but in addition to amplitude information, it also uses phase information.

Local changes in the frequency of precessing protons, that is, the phase of the T_2*w gradient echo signal, bring additional, independent information concerning tissue contrast. As a rule, SWI uses a fully flow-compensated three-dimensional fast gradient echo sequence with shooting at small angles [2]. SWI involves combining amplitude and filtered phase data for further post-processing when constructing projection images with minimal intensity to display smaller hemorrhages that are not visible when T_2* imaging.

Phase images display field changes regardless of the amplitude response and, thus, are a reliable means of measuring local changes in susceptibility. In SWI, the phase image is used as a mask to enhance the contrast of the amplitude image [2]. Paramagnetic substances, such as ferritin or hemosiderin, enhance the magnetic field, and their presence leads to a positive phase shift relative to the surrounding parenchyma. Diamagnetic substances, such as calcium or myelin, cause a negative phase shift. The limitation of this method with respect to the measurement of iron is that the phase values are affected not only by the iron content, but also by the difference in the magnetic susceptibility of the surrounding tissue. Low-frequency background field effects from the air/tissue and tissue/bone interfaces lead to unwanted phase information and must be removed by a high-frequency phase filter.

It is assumed that most of the phase-dependent tissue contrast in the basal ganglia is due to the concentration of ferritin. However, the phase value of SWI in some areas of the brain does not always correlate well with iron content [2]. Especially in the globus pallidus (GP), the iron content estimated from the phase image was significantly lower compared to the R2* relaxation or the reference chemical measurement. Presumably, GP is rich not only in iron, but also in calcium, which can shift the phase in the opposite direction, interfering with the quantitative determination of iron. Due to the diamagnetic properties of myelin, which, by analogy with calcium, cancel the effect of iron, phase images cannot be used to measure iron in white matter if the contribution of myelin is not corrected. Susceptibility to deoxygenated hemoglobin is another potential factor interfering with the quantification of iron in tissues. Especially in hypoxemic conditions, hemoglobin contributes to the contrast between gray and white matter in phase images due to differences in the local volume of brain blood and, thus, can obscure estimates of the concentration of non-heme iron.

The SWI method has been tested under conditions of various magnetic fields, including 1.5, 3 and 7 T [3]. Higher magnetic fields enhance the effects of magnetic susceptibility and, consequently, create SW images with a higher signal-to-noise ratio, which allows better visualization of small brain structures, tumors, as well as deep and smaller vessels. However, ultrahigh magnetic field (> 7 T) in SWI can distort the size of brain structures in areas characterized by high concentrations of iron. However, phase images can be used to distinguish between diamagnetic (for example, calcium) and paramagnetic (deoxyhemoglobin, hemosiderin and ferritin) substances.

Thus, the SWI method is a highly sensitive imaging method capable of displaying magnetic substances and making it possible to study neurological diseases, tumors and predict their development. The SWI method can be used to demonstrate the response to treatment in neuro-oncology, monitoring recovery after stroke in vascular neurosurgery and predicting results in neurotraumatology, as well as for better anatomical localization in functional neurosurgery and radiosurgery using a gamma knife. SW images can be combined to plan the trajectory of the operation, which gives more information about the venous vascular network, offering more information for stereotactic biopsy and planning surgical approaches [3].

Quantitative Susceptibility Mapping (QSM)

Quantitative susceptibility mapping (QSM) is a method that, like SWI, uses the phase information of a three-dimensional gradient echo sequence to obtain maps of the magnetic properties of tissues [2]. Using advanced postprocessing, QSM solves the inverse problem of

the magnetic field to the source of susceptibility and generates images where the voxel intensity is linearly proportional to the apparent magnetic susceptibility of the underlying tissue. Although preference is given to double echo sequences, susceptibility maps can be retrospectively calculated based on single echo GRE measurements typically obtained during SWI. Compared to SWI, QSM provides quantitative and spatially specific image contrast, which is differentially sensitive to the content of myelin and iron. QSM provides maps of relative susceptibility differences, not absolute values, and all points on the map should be associated with a reference area, usually cerebrospinal fluid or occipital white matter.

The quantitative sensitivity mapping (QSM) technique also uses normalized regularized QSM algorithms to assess the susceptibility of tissues to magnetic fields based on changes in the phase of the MRI signal [3,4]. The regularized QSM methodology includes a preprocessing step that removes unwanted background phase effects caused by volumetric susceptibility fluctuations between air and tissues, and requires data collection at only one value of the field strength. Regularized algorithms help to estimate the local iron concentration by studying the phase changes of the gradient echo image. Since the background phase makes up most of the observed phase, high-frequency filtering is used to obtain an estimate of the phase from the accumulated tissue iron, while eliminating slowly changing background effects.

Performing QSM and R_2* images simultaneously can theoretically distinguish the contribution of iron and myelin through their differential effect on these contrasts. An increase in the concentration of both iron and myelin causes an additive increase in R_2*, while the paramagnetic properties of the former increase, and the diamagnetic properties of the latter decrease the magnetic susceptibility [5]. Similarly, the combination of T_2*w imaging and QSM will help overcome the contradictory results caused by the diamagnetic effects of calcium.

Conclusion

The use of T_2, T_2* and T_2' NMR relaxometry, SWI and QSM methods have shown a good correlation with the measurement of iron in various tissues in vitro and in some in vivo studies. All these methods have their inherent advantages and disadvantages for various research purposes, but so far none of them is preferable over the others. However, limited understanding of the behavior of iron substances in a magnetic field, insufficient knowledge of the exact proportions of various forms of iron in tissues and sensitivity to other concomitant factors still prevent the use of these methods in routine clinical practice.

References

1. Haacke E.M., Cheng N.Y.C., Hause M.J., et al. Imaging iron stores in the brain using magnetic resonance imaging // Magnetic Resonance Imaging. 2005. Vol. 23. P. 1–25.
2. Dusek P., Dezortova M., Wuerfel J. Imaging of Iron // International Review of Neurobiology. 2013. Vol. 110. P. 195–239.
3. Di Ieva A., Lam T., Alcaide-Leon P., Bharatha A., Montanera W., Cusimano M.D. et al. Magnetic resonance susceptibility weighted imaging in neurosurgery: current applications and future perspectives // J. Neurosurg. 2015. Vol. 123. P. 1463–1475.
4. Acosta-Cabronero J., Betts M.J., Cardenas-Blanco A., Shan Yang, Nestor P.J. *In Vivo* MRI Mapping of Brain Iron Deposition across the Adult Lifespan // J. Neurosci. 2016. Vol. 36(2). P.364 –374.
5. Deistung A., Schafer A., Schweser F., Biedermann U., Turner R., Reichenbach J. R. Toward in vivo histology: A comparison of quantitative susceptibility mapping (QSM) with magnitude-, phase-, and R2*-imaging at ultra-high magnetic field strength // NeuroImage. 2013. Vol.65. P. 299–314.

NMR studies of two polymorphic $MoTe_2$ modifications at room temperature

Vladislav Panov, Anastasiia Antonenko

Faculty of Physics of Saint Petersburg State University, St. Petersburg. Russia.
E-mail: st069302@student.spbu.ru.

Introduction

Layered transition-metal dichalcogenides, which include the $MoTe_2$ compound, have been actively studied for a long time due to their excellent electronic properties. $MoTe_2$ occurs in several polymorphic modifications, namely in $\alpha\,(2H)$ and $\beta\,(1T')$ phases. The phases have different types of crystal symmetry [1-3]. The difference in the crystal structure of the two phases is reflected in the physical properties of the studied systems. The $2H$-phase is a semiconducting phase, and the $1T'$-phase corresponds to Weyl semimetal [4], a recently discovered class of materials with unique properties.

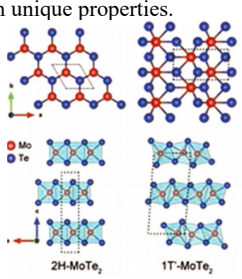

Figure 1. Crystal structures of $MoTe_2$ in $2H$ and $1T'$ phases [5]. The dotted line indicates a unit cell.

Method

NMR studies of molybdenum ditelluride $MoTe_2$ at room temperature are carried out using pulse NMR spectrometer Bruker Avance 400. The ^{125}Te NMR spectra are obtained for $1T' -$ and for $2H - MoTe_2$ powders. The ^{125}Te NMR spectra for both $2H - MoTe_2$ and $1T' - MoTe_2$ are very broad. To detect NMR signals, the Hahn spin echo [6] method with pulse sequence $\frac{\pi}{2} - \tau - \pi$ was used, with different frequency offsets [7] (the difference between the frequency at which the spin echo was measured and ^{125}Te resonant frequency), set by the parameter o1p (in ppm). Two types of spectra were obtained: the total spectrum and the envelope. For each frequency offset, the intensity of the spin echo signal was measured and the integral intensity with a constant integration interval was found. The normalized "envelope" spectrum is constructed using these values. The "total" spectrum can be obtained by overlapping echo signals at all measured frequencies, and it is also normalized for subsequent analysis.

To measure the nuclear spin-lattice relaxation time T_1 the "inversion recovery" method [7] with the addition of a spin echo was used.

Experiment

The collected spectra at room temperature for different phases of molybdenum ditelluride differ significantly (Fig. 2). The one for $1T'$-phase is considered to be a superposition of 4 resonant lines from four crystallographically nonequivalent tellurium positions, while for $2H$-phase the spectrum consists of one line as all positions of tellurium atoms are crystallographically equivalent.

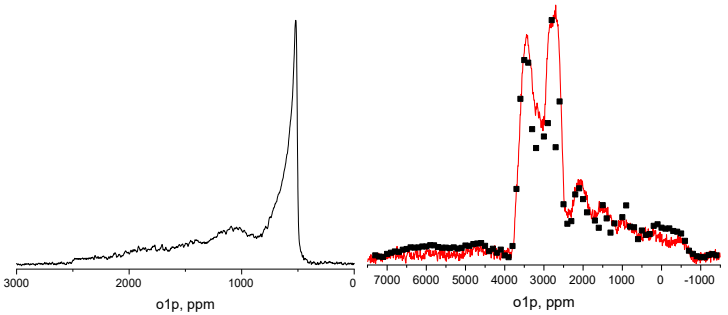

Figure 2. Total ^{125}Te NMR spectrum for $2H - MoTe_2$ (left). Overlay of integral intensities with different frequency offsets (dots) on the ^{125}Te envelope spectrum (line) for $1T' - MoTe_2$ powder (right).

For the $2H - MoTe_2$ powder spectrum the total isotropic shift $\delta_{iso} = 1169\ ppm$, the anisotropy factor $\delta = 1313\ ppm$, and the asymmetry η are determined using the Bruker TopSpin 3.2 software package under the assumption of $\eta \approx 0$.
The nuclear spin-lattice relaxation times for both phases at room temperature are measured. Relaxation curves are given in fig. 3.

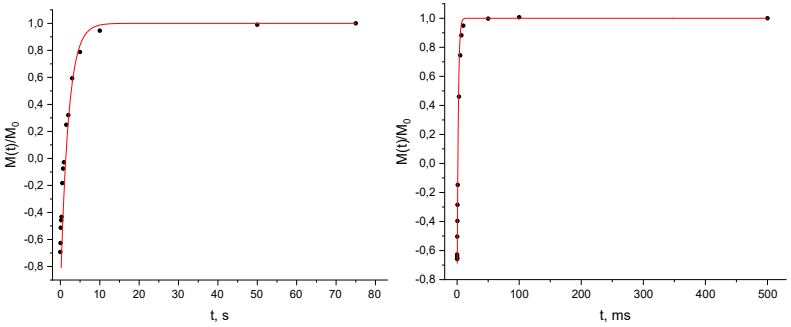

Figure 3. Magnetization recovery curve for $2H$ −phase (left) and for $1T'$-phase (right).

In the case of $1T' - MoTe_2$, $T_1 = 2{,}77 \pm 0{,}08\ ms$. In the case of $2H - \mathrm{MoTe_2}$, relaxation was drastically slower, $T_1 = 1{,}991 \pm 0{,}005\ s$.

References

1. D. Puoyine, R. E. Newnha. The crystal structure of $MoTe_2$. Acta Cryst. 14, 691, 1961
2. H. P. Hughes, R. H. Friend. Solid State Phys. J. Phys. C: 11 L103, 1978
3. B. E. Brown. The crystal structures of WTe2 and high-temperature MoTe2. Acta Crystallographica, 20 268-74, 1966
4. X.-J. Yan. Investigation on the phase-transition-induced hysteresis in the thermal transport along the c-axis of MoTe2. npj Quantum Materials 2, 31, 2017
5. X. Wan. Topological semi-metal and Fermi-arc surface states in the electronic structure of pyrochlore iridates. Phys. Rev. B 83, 205101, 2011
6. E. L. Hahn. Spin echoes. Phys Rev 80, 1950
7. A. O. Antonenko. Nuclear magnetic resonance in topological insulators Bi_2Te_3 and Bi_2Se_3. 2018

Homo- and heteronuclear experiments of NMR spectroscopy in the structural study of polysubstituted furans

Pelipko V. V., Gomonov K. A., Baichurin R. I., Makarenko S. V.

Herzen State Pedagogical University of Russia, Department of Organic Chemistry, Center of collective use at the Faculty of Chemistry "Instrumental methods for the study of nitro compounds, coordination, biologically active substances and nanostructured substances"
48 Moyka River Embankment, Saint Petersburg 191186, Russia
E-mail: kohrgpu@yandex.ru
http://kohrgpu.ru, http://ckpo.herzen.spb.ru/?page=organic-chemistry

Previously, it was shown that the reactions of alkyl 3-bromo-3-nitroacrylates with representatives of cyclic CH-acids lead to the synthesis of benzofurancarboxylates [1]. As a result of studying the interaction of alkyl 3-bromo-3-nitroacrylates with acyclic CH-acids (pentane-2,4-dione, methyl- and ethyl 3-oxobutanoates), we obtained polysubstituted furans **1-6**.

The aim of this work was to study the structure of such furans **1-6** by ^{1}H, ^{13}C NMR spectroscopy, including homo- (^{1}H–^{1}H COSY) and heterocorrelation (^{1}H–^{13}C HMQC, HMBC) experiments.

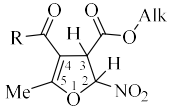

Alk = Me (**1-3**), Et (**4-6**);
R = Me (**1**, **4**), OMe (**2**, **5**), OEt (**3**, **6**).

A structural feature of the substances **1-6** is the presence in their molecule of vicinal protons $C^{2}H$, $C^{3}H$, which form an *AMX*-type spin system with the protons of the methyl group at C^{5} in the ^{1}H NMR spectra.

Thus, in the ^{1}H NMR spectrum of compound **4**, the $C^{2}H$ proton resonated as a doublet at 6.12 ppm (^{3}J 2.0 Hz), the $C^{3}H$ proton resonated as a multiplet at 4.36-4.39 ppm, and the protons of the methyl group at C^{5} formed a doublet at 2.41 ppm (^{5}J 1.4 Гц) (Fig. 1).

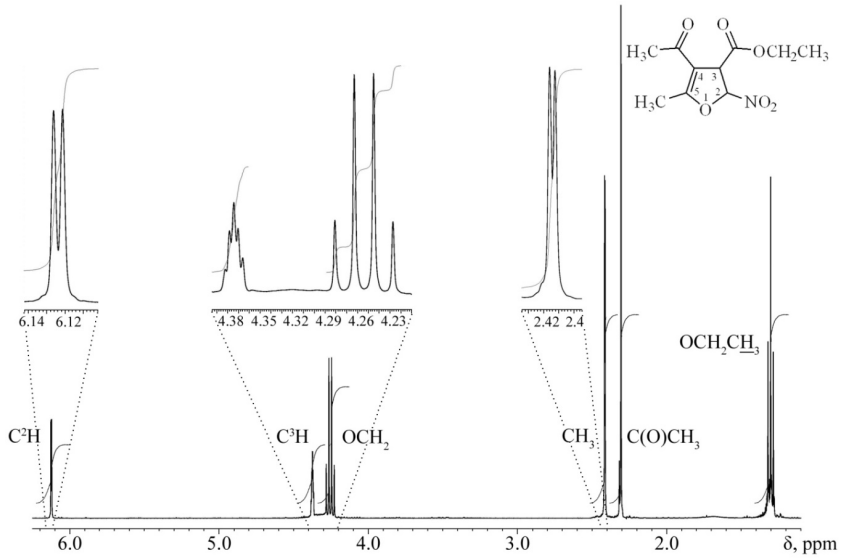

*Figure 1. ^{1}H NMR spectrum of compound **4** ($CDCl_3$)*

The assignment of signals is confirmed by the results of ^{1}H-^{1}H dqf-COSY experiments obtained for compound **4** (Fig. 2).

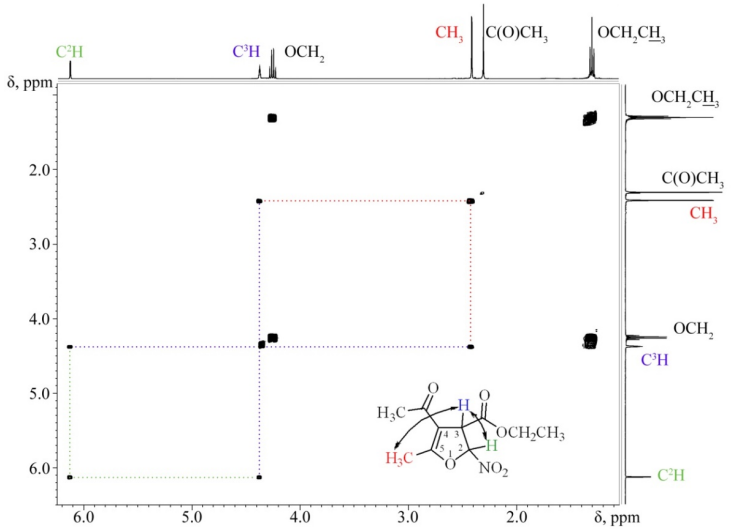

*Figure 2. ^{1}H–^{1}H dqf-COSY spectrum of compound **4** ($CDCl_3$)*

^{13}C-{^{1}H} NMR spectra of furans **1-6** contain signals of all structural fragments. At the same time, the structural feature of the synthesized molecules is the presence of four quaternary carbon atoms (Fig. 3).

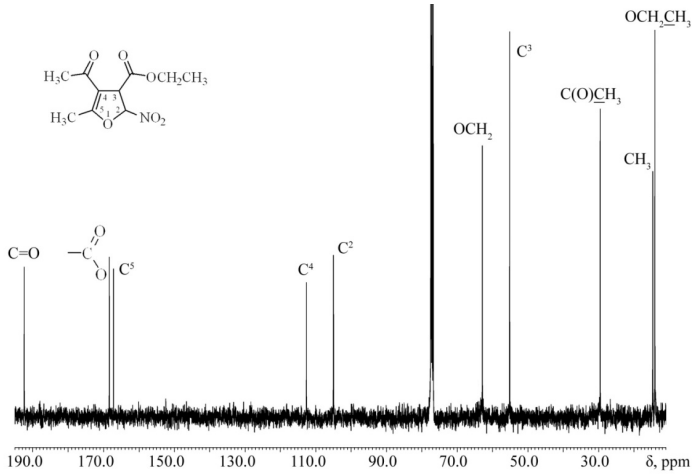

*Figure 3. ^{13}C NMR spectrum of compound **4** ($CDCl_3$)*

The assignment of signals in the ^{13}C-{^{1}H} NMR spectra was based on the results of the ^{1}H-^{13}C HMQC and ^{1}H-^{13}C HMBC experiments.

Thus, in the ^{1}H-^{13}C HMQC spectrum of compound **4**, the signal of $C^{2}H$ proton (δ_H 6.12 ppm) forms a cross-peak with the carbon atom at δ_C 105.00 ppm, $C^{3}H$ proton (δ_H 4.36-4.39 ppm) and carbon at δ_C 55.18 ppm, methyl group protons at C^{5} (δ_H 2.41 ppm) and carbon at δ_C 14.69 ppm. The proton signals of the CH_3CH_2O ester fragment (δ_H 1.30, 4.25 ppm) form cross peaks with carbon atoms at δ_C 14.10 ppm and δ_C 62.89 ppm, respectively. The signal of the methyl protons of the acetyl fragment (δ_H 2.31 ppm) forms a cross peak with the signal of the carbon atom at δ_C 29.55 ppm (Fig. 4).

The assignment of the signals of quaternary carbon atoms was based on the results of the ^{1}H-^{13}C HMBC experiment. The spectrum of compound **4** (Fig. 5) shows cross peaks of the signal of the methylene protons CH_2O (δ_H 4.25 ppm) and the carbon atom at δ_C 168.35 ppm (O–C=O), methyl protons of the acetyl fragment (δ_H 2.31 ppm), and carbon atoms at δ_C 112.60 ppm (C^{4}) and δ_C 192.41 ppm (C=O), as well as cross peaks of protons of the methyl group at C^{5} (δ_H 2.41 ppm)/C^{5} (δ_C 167.18 ppm).

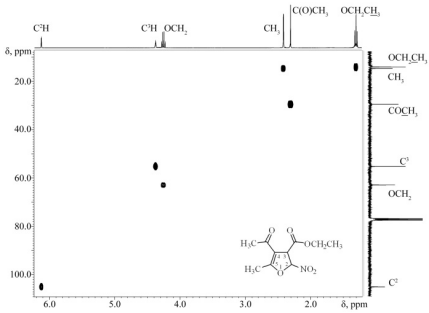

*Figure 4. ^{1}H–^{13}C HMQC spectrum of compound **4** ($CDCl_3$)*

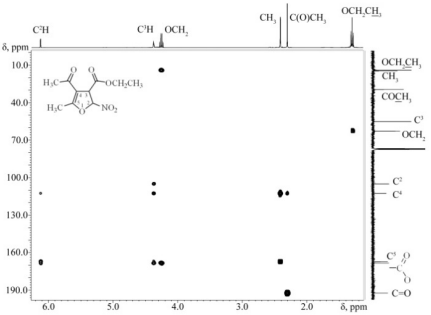

*Figure 5. ^{1}H–^{13}C HMBC spectrum of compound **4** ($CDCl_3$)*

Thus, the study of polysubstituted furans using a complex of homo- and heterocorrelation experiments of NMR spectroscopy makes it possible to completely describe their structure and to assign the signals of 1H, 13C atoms of all fragments of the molecule.

The studies were carried out in the center of collective use at the Faculty of Chemistry of the Herzen State Pedagogical University of Russia on the Jeol ECX-400A spectrometer at 399.78 (1H) and 100.53 (13C) MHz with standard experimental settings. The residual signals of a non-deuterated solvent (for 1H nuclei) or the signals of a deuterated solvent (for 13C nuclei) were used as a standard.

This work was carried out within the framework of a state assignment with financial support from the Ministry of Education of Russia (project No. FSZN-2020-0026).

References

1. Pelipko, V. V., Baichurin, R. I., Kondrashov, E. V., Makarenko, S. V. Russ. J. Gen. Chem. 2021, 91, 167.

Identification of diastereomeric forms of vicinal bisphosphonates and bisphosphine oxides using NMR spectroscopy

Alexey V. Salin

A.M. Butlerov Institute of Chemistry, Kazan Federal University, Kremlevskaya 18, Kazan, 420008, Russian Federation
E-mail: salin555@mail.ru

Introduction

Bisphosphonates and bisphosphine oxides attract considerable interest due to their use in medicine for treatment and diagnostics of various bone and calcium-metabolism diseases and in industry – as extractants for transuranic elements, corrosion inhibitors, and flame-retardant agents [1,2]. Knowledge of stereochemistry of these compounds is crucial for their practical application.

Results and Discussion

Recently, we developed a novel method for preparation of vicinal bisphosphonates and bisphosphine oxides through phosphine-catalyzed tandem α-umpolung/β-Michael addition of P(O)–H bonds to β-substituted alkynoates (Fig. 1) [3]. The products were obtained as a mixture of *anti*- and *syn*-diastereomers.

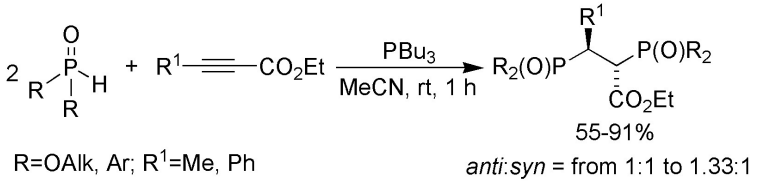

Figure 1. Synthesis of vicinal bisphosphonates and bisphosphine oxides

The structures were deduced from ^{1}H, $^{13}C\{^{1}H\}$, ^{31}P NMR, IR and high resolution mass spectrometry. These bis-adducts are easily recognizable in $^{31}P\{^{1}H\}$ NMR spectra by diagnostic pair of doublets for each diastereomer resulted from vicinal phosphorus-phosphorus spin coupling ($^{3}J_{PP}$). We found that NMR spectroscopy serves as a useful tool for the identification of *anti*- and *syn*-diastereomeric forms.

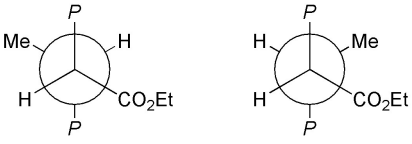

	anti-diastereomer	*syn*-diastereomer
	$^{3}J_{HH}$ 11 Hz	$^{3}J_{HH}$ 1-2 Hz
Bisphosphonates:	$^{3}J_{PP}$ 75 Hz	$^{3}J_{PP}$ 80 Hz
Bisphosphine oxides:	$^{3}J_{PP}$ 41 Hz	$^{3}J_{PP}$ 47 Hz

P=P(O)R$_2$

Figure 2. Newman projections of vicinal bisphosphonates and bisphosphine oxides and typical values of spin coupling constants

The Karplus relationship based on $^3J_{HH}$ and $^3J_{PP}$ coupling constants predicts that both diastereomers mainly exist in antiperiplanar conformation in solution [4-6], with dihedral angle P–C–C–P between +150° to –150° (on average, 180°) (Fig. 2). The coupling constants $^3J_{HH}$ are significantly different for *anti*- (ca. 11 Hz) and *syn*- (ca. 1-2 Hz) diastereomers; whereas constants $^3J_{PP}$ are close enough and have rather high values (75-80 Hz for bisphosphonates and 41-47 Hz for bisphosphine oxides).

Based on the characteristic spin coupling constants, the *anti*- and *syn*-diastereomers may be easily distinguished, when the X-ray diffraction data are unavailable.

References

1. E. Chmielewska, P. Kafarski. – Molecules, 21, 1474 (2016).
2. M. Gnant, P. Clézardin. – Cancer Treat. Rev., 38, 407-415 (2012).
3. A. V. Salin, A. V. Il'in, R. I. Faskhutdinov, R. R. Fayzullin. – Tetrahedron, 75, 2676-2686 (2019).
4. S. V. Kruglov, V. M. Ignat'ev, B. I. Ionin, A. A. Petrov. – Zh. Obshch. Khim., 43, 1470-1478 (1973).
5. G. Grossmann, R. Lang, G. Ohms, D. Scheller. – Magn. Res. Chem. 28, 500-504 (1990).
6. G. Hägele, J. Dettmann, K. Huben, S. Jankowski, E. Bálint, G. Keglevich. – Phosphorus, Sulfur, Silicon Relat. Elem. 189, 1315-1327 (2014).

Transport properties of Ionic Liquid [Bmim][SCN] obtained by Molecular Dynamic Method

Selivanov A.A., Komolkin A.V., Ievlev A.V.

Department of Nuclear Physics Research Methods, Saint Petersburg State University, 199034, 7/9 Universitetskaya nab., Saint Petersburg, Russia
E-mail: st068986@student.spbu.ru

Introduction

Recently, ionic liquids (IL) have been increasingly used as components of polymer electrolytes for new current sources. They have several advantages, such as low flammability, low vapor pressure, wide space of thermal, chemical and electrochemical stability, which make it possible to produce more environmentally friendly current sources on the basis of IL. IL [Bmim][SCN] was selected, because an experimental work was provided to study its physico-chemical properties [1]. Also, work was carried out to optimize the system under study [2] and the system was simulated at different temperatures in the NVT ensemble [3]. The purpose of this work is to study IL with the Molecular Dynamic Modeling and analyze the data obtained [4], [5].

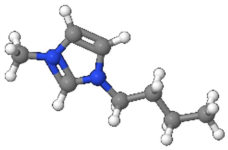

Figure 1. Cation $[Bmim]^+$

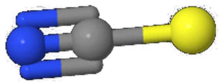

Figure 2. Anion $[SCN]^-$

Experimental section

The main problem that we tried to solve was obtaining diffusion coefficients that would be consistent with the real experiment. To do this, we simulated systems in 2 ensembles - NpT and NVT - at different temperatures in the range from 300 to 460 K. Then, using the Einstein's equality, $SD = lim_{t\to\infty}\langle\|\boldsymbol{r}_i(t) - \boldsymbol{r}_i(0)\|^2\rangle = 6D_i t$, we have obtained diffusion coefficients for $Bmim^+$ cation and SCN^- anion as in [6].

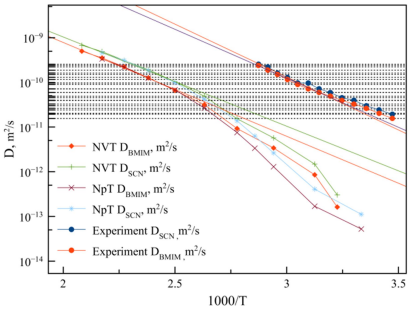

Figure 3. Temperature dependence of the diffusion coefficient

As we see in Figure 3 the diffusion coefficients for our models are the same in any ensemble at high temperatures. Also, we can notice that they coincide numerically with the real diffusion coefficients, but at different temperatures. Due to the simplifications used in the simulation, we can observe the temperature dependences shift. For example, water begins to boil at temperatures well above 100 °C. At low temperatures, a chaotic spread of the coefficients is observed, which is a consequence of the high viscosity of the computer ionic liquid.

Also, we are interested in the density of the systems. Using the internal commands of the Gromacs software, we obtained the following temperature dependence in figure 4. The red dot shows the real value, which, according to [7], is 1069.7 $\frac{kg}{m^3}$ under normal conditions. Figure 4 also shows the formula by which we approximated the dependence of density on temperature. Approximation parameters: $A = 1125 \pm 2\frac{kg}{m^3}, Q = 7{,}41 \pm 0.04\ kJ$. As we can see, the value of the density of a real liquid fits the experimental curve quite well. This suggests that the potential used is capable of describing the chosen ionic liquid.

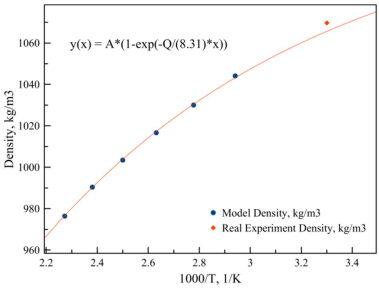

Figure 4. Temperature dependence of the density

Another interesting object is the radial distribution function, which can show the distribution of [SCN] molecules relative to the imidazole ring in the [Bmim] cation.

As we know, the main charge carrier in the anion is the nitrogen atom N, so the former RDF peak belongs to it. The next peak belongs to the carbon atom C and the latter one, respectively, to the sulfur atom S.

To study the mobility of the molecule as a whole, as well as its individual parts, we found autocorrelation functions for the following vectors: 1) between nitrogen atoms, 2) between carbon atoms in the imidazole ring, 3) perpendicular to the plane of the imidazole ring, 4) perpendicular to the plane of the methyl group , 5) perpendicular to the plane of the methyl group in the butyl tail.

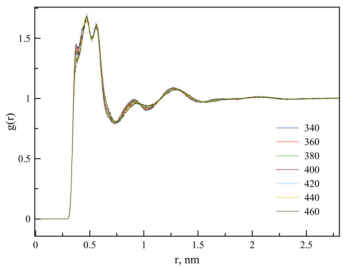

Figure 5. Radial Distribution Function of the anion SCN relative to Bmim cation

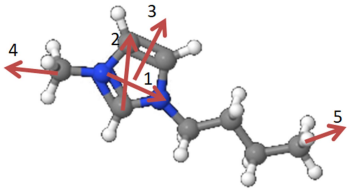

Figure 6. Cation [Bmim]$^+$

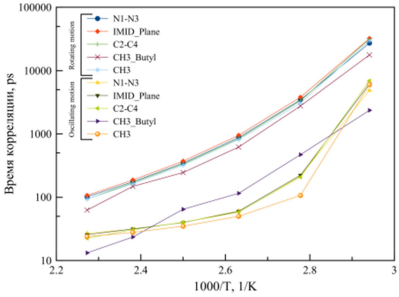

Figure 7. Temperature dependence of correlation times

In the obtained autocorrelation functions, we could observe two exponentials with two characteristic correlation times. Based on the fact that one of the correlation times for each group is the same, we can draw the following conclusion: the motion of the cation [Bmim] can be divided into isotropic rotational motion and oscillatory motion. Moreover, for each

group there will be different correlation times of the oscillatory motion. The entire dependence of the correlation times on temperature can be seen in figure 7.

The most telling way to represent the motion of molecules is to construct a three-dimensional distribution function of the motion of each atom in the molecule. Let us consider this using the example of the [BMIM] cation at a temperature of 400K. In figure 8 you can see the section in plane of the imidazole ring of the distribution.

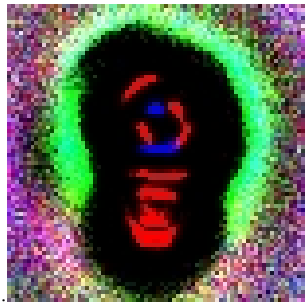

Figure 8. Section in the plane of the imidazole ring of the three-dimensional distribution of atoms in the [Bmim] cation

In this figure, the distribution of carbon atoms C is shown in red, the nitrogen atom N is shown in blue, and the [SCN] anion is shown in green. As we can see, the anion is more attracted to the cation ring, which confirms our idea that the entire charge of the cation is concentrated in the imidazole ring.

Acknowledgment

Scientific research, were performed at the «Computing Centre» of Research park of St.Petersburg State University.

References

1. Cabeza O. et al. Strange behaviour of transport properties in novel metal thiocyanate based ionic liquids // J. Mol. Liq. The Author(s), 2021. Vol. 340. P. 117164.
2. Selivanov A.A., Ievlev A. V., Komolkin Andrey V. Diffusion Coefficients of Ionic Liquid [BMIM][SCN] Calculated by Molecular Dynamic Method. 2021.
3. Selivanov A.A., Ievlev A.V., Komolkin A.V. Optimization of parameters for molecular dynamics modeling of ionic liquid [BMIM][SCN] // Magnetic Resonance and Its Applications. Saint-Petersburg, 2021. 253–256 p.
4. Неелов И.М. Введение В Молекулярное Моделирование Биополимеров. 2014. P. 101.
5. Lindahl E. et al. GROMACS 2019.4 Manual // GROMACS Doc. 2019.
6. Khusnutdinova N.R., Markelov D.A. Modeling the system of the carbosilane dendrimer of various generations // MAGNETIC RESONANCE AND ITS APPLICATIONS Proceedings 17th International School-Conference. 2020. 2020. 93–95 p.
7. Domańska U., Królikowska M. Density and viscosity of binary mixtures of thiocyanate ionic liquids +water as a function of temperature // J. Solution Chem. 2012. Vol. 41, № 8. P. 1422–1445.

Interaction of surfactant with albumin protein according to NMR data

L.V. Sharipova[1,2], B.I. Khayrutdinov[1,2], Yu.F. Zuev[1]

[1]Kazan Institute of Biochemistry and Biophysics, FRC Kazan Scientific Center of RAS, Kazan 420008, Russian Federation
[2]Institute of Physics, Kazan Federal University, Kazan 420008, Russian Federation
E-mail: lv.sharipova@yandex.ru

Introduction

Complexes of surfactants with globular proteins are widely used in many branches of medicine. However, the mechanism of surfactants interaction with macromolecules has not been sufficiently studied and requires new investigations to establish patterns and factors that control the efficiency of complexation in such systems. The use of surfactants is based on the uniqueness of their properties associated with the organization of targeted delivery of drugs to a specific place in the body with their controlled release

Results

The surfactant tetradecylmethylmorpholinium bromide with bovine serum albumin (BSA), was chosen as the object of study. Methods of nuclear magnetic resonance studied the mechanism of interaction of a surfactant with a protein. The NMR method with a pulsed magnetic field gradient was used to obtain the concentration dependences of the self-diffusion coefficients of surfactants in the presence and absence of BSA. It makes possible to describe the translational mobility of the system. Changes of chemical shifts and linewidths of peaks in ^{1}H NMR spectra of surfactants in presence of BSA were observed. On the basis of the experimental data, the formation of the complex in an aqueous solution was proved.

Acknowledgements

The authors gratefully acknowledge the Assigned Spectral-Analytical Center of FRC Kazan Scientific Center of RAS for possibility to fulfill the NMR experiments.

Internal mobility of hydroquinone pillar[5]arene fragment in a inclusion complex according to NMR spectroscopy data

L.V. Sharipova[1,2], *B.I. Khayrutdinov*[1,2], *D.N. Shurpik*[3], *I.I. Stoikov*[3], *Yu.F. Zuev*[1]

[1]*Kazan Institute of Biochemistry and Biophysics, FRC Kazan Scientific Center of RAS, Kazan 420008, Russian Federation*
[2]*Institute of Physics, Kazan Federal University, Kazan 420008, Russian Federation*
[3]*Institute of Chemistry, Kazan Federal University, Kazan 420008, Russian Federation*
E-mail: lv.sharipova@yandex.ru

Introduction

Nowadays one of the actual problems of supramolecular chemistry is the development of principles for constructing new receptors capable of recognizing biologically important substrates. Pillar[n]arenes are a class of novel macrocyclic compounds which are capable of forming host-guest complexes. The unique properties of the pillar[n]arene are: planar chirality, step-by-step functionalization, a tubular spatial structure that forms an electron-donor cavity, and the ability to encapsulate small molecules in it.

Results

In this work, the intramolecular mobility of the pillarar[5]arene complex with thioctic acid, which is a biologically active substance, was studied by high-resolution nuclear magnetic resonance methods. The formation of the complex was confirmed by ^{1}H-^{1}H NOESY spectra. Based on experimental NMR data, a three-dimensional structure of the complex was constructed using the molecular modeling method. To characterize the proton mobility of the hydroquinone fragment of pillar[5]arene in a complex with thioctic acid, a pulsed sequential CPMG (Carr-Purcell-Meiboom-Gill) was used. From the analysis of the CPMG spectra, the rate constants of the chemical exchange of the dynamic process were obtained. The thermodynamic parameters of the proton mobility of the hydroquinone fragment of pillar[5]arene were obtained from the temperature dependences of the chemical exchange rate constant.

Acknowledgements

The authors gratefully acknowledge the Assigned Spectral-Analytical Center of FRC Kazan Scientific Center of RAS for possibility to fulfill the NMR experiments.

1. S. Fisher, B. I. Yachtman. – *Vacuum State Comm.*, **7**, 1234-1237 (2003).

Study of the influence of mechanical stress on the splitting of spin sublevels in hexagonal SiC

A.M. Skomorokhov[1,2,*], I.D. Breev[1,2], A.N. Anisimov[1,2], P.G. Baranov[1]

[1]Ioffe Physical-Technical Institute, [2]Northern (Arctic) Federal University
[*]e-mail: artomskom@gmail.com

Recently, spin sublevels in silicon carbide have received a lot of attention, all because of the possibility of creating various quantum devices. For example, they can be used for quantum sensing and information processing, as well as for elements of nanophotonics. Centers based on silicon vacancies with spin 3/2 have a unique property of optical alignment at room temperatures. Therefore, the quantum state of the center can be read using optical magnetic resonance detection (ODMR).

In this work we investigated AlN/SiC heterostructures for two silicon carbide polytypes - 4 and 6H. Using Raman spectroscopy as well as optical magnetic resonance detection on a confocal optical circuit, the shifts of the 4H/6H-SiC Raman phonon modes and splitting of spin sublevels were simultaneously determined. The formation of mechanical stresses at the heterostructure interface was elucidated by analyzing the shifts of the Raman peaks. For the AlN/4H-SiC heterostructure, the maximum values of the strein tensor components $\sigma_\perp = -0.19$ GPa and $\sigma_\parallel = -0.87$ GPa are observed at the heterointerface. And for the AlN/6H-SiC heterostructure the maximum values of the tensor components are $\sigma_\perp = -0.64$ GPa and $\sigma_\parallel = -0.15$ GPa, they also lie on the heterointaerface [1].

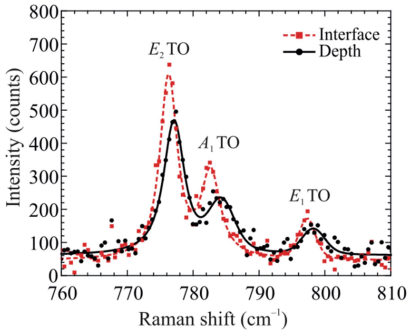

It was found that the ODMR resonance of V2 center for AlN/4H-SiC heterostructure is shifted to higher frequencies in comparison with ODMR resonance at free surface of 4H-SiC by 0.35 GHz [2]. And the shift of ODMR resonance line in AlN/6H-SiC heterostructure is 0.75 GHz for V1/V3 centers and 0.5 GHz for V2 centers [3].

Acknowledgements

This paper was partly supported by the Russian Science Foundation (Project No. 20-12-00216). The research was partly supported by the state task of the Russian Federation No. FSRU-2021-0008.

References

1. Breev, I. D., et al. "Stress distribution at the AlN/SiC heterointerface probed by Raman spectroscopy." *Journal of Applied Physics* 129.5 (2021): 055304;
2. Бреев И.Д. и др., Письма в ЖЭТФ 114, вып. 5, 323-327, 2021;
3. Breev, I. D., et al. "Stress-controlled zero-field spin splitting in silicon carbide." *Applied Physics Letters* 118.8 (2021): 084003.

Structure and membranotropic properties of peptides and synthetic macrocycles

P. Skvortsova[1], D. Shurpik[2], I. Stoikov[2], B. Khairutdinov[1,2], Y. Zuev[1], E. Ermakova[1]

[1]Kazan Institute of Biochemistry and Biophysics, FRC Kazan Scientific Center of RAS, Kazan, Russian Federation
[2]Kazan Federal University, Kazan, Russian Federation
E-mail: skvpolina@gmail.com

Introduction

The rapid increase in the number of infections resistant to modern drugs poses a serious challenge to antimicrobial therapy. The emergence of antibiotic-resistant microorganisms causes an urgent need for the development of other drugs. One of the directions in the development of antimicrobial drugs is the development of drugs based on antimicrobial peptides (AMPs). The development of new AMPs as therapeutic agents requires an understanding of their structure and mechanisms of action [1].

The activity of AMPs is often associated with their membranotropic properties [2]. Membranotropic molecules can modify the structure and properties of membranes, primarily transport characteristics. Changing the membrane permeability for different reagents can lead to various effects, including its destruction. However, membranotropic molecules can not only cause cell death, but also promote membrane transport of biologically active compounds and act as transport molecules.

Megin-1 secondary structure

Here we investigated the structure of a new antimicrobic peptide named megin-1 extracted from skin venoms of spadefoot toad *Megophrys minor.* Megin-1 consists of 18 amino acid residues (FLKG**C**WTKWYSLKPK**C**PF) with two cysteine residues and can exist in an oxidized form with a disulfide bond (M1) or in a reduced form with a broken disulfide bond (M1R).

The content of secondary structures were determined by circular dichroism (CD) spectroscopy (Figure 1).

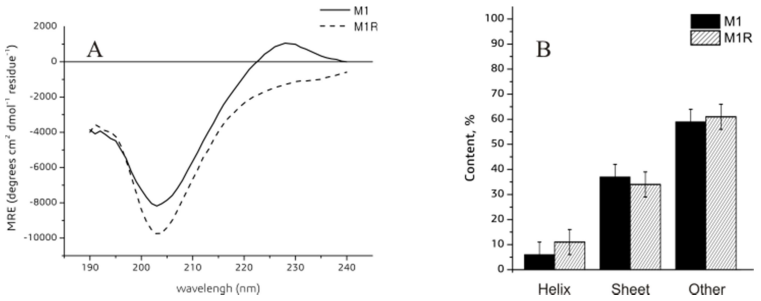

Figure 1. A – CD spectra of M1 and M1R at 25 ºC. B – Secondary structure content obtained from CD

In both M1 and M1R alpha structures are practically absent, some beta structures are present, and larger half of the peptides are disordered. A positive band at ~ 228 nm is relatively weak and is observed for megin-1 with intact disulfide bonds and disappears in

reducing conditions and characterizes the subtle conformational changes of peptide upon disulfide cleavage [3].

The three-dimensional structure of the two megin-1 forms was determined by solution NMR spectroscopy. The ^{1}H NMR spectra were assigned via the standard methods using the sequential assignment procedure, which involved the combined use of homo- and heteronuclear correlation experiments [4] such as ^{1}H–^{1}H-COSY, ^{1}H–^{1}H-TOCSY, ^{1}H–^{1}H-NOESY, ^{1}H–^{13}C-HSQC, ^{1}H–^{13}C-HMBC. Based on the chemical shifts of protons and carbons of the main chain, dihedral angle constrains were obtained by Talos+ [5]. Using the predicted dihedral angle constraints and distance constraint from NOE spectroscopy data, the peptide M1 and M1r structures (Figure 2) were calculated by Cyana 2.1 [6].

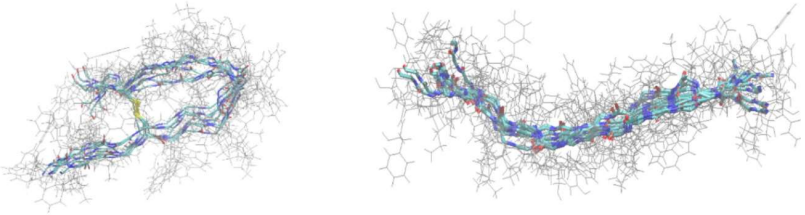

Figure 2. Three-dimensional NMR structure of megin-1 (left – M1, right – M1R). Superposition of six lowest-energy structures. The backbone is shown in color, whereas side chains are shown in gray lines. Cysteine residues are shown as yellow bonds

M1R takes an elongated shape in solution, which is probably stabilized by four positively charged lysine residues. M1 assumes a loop-like shape by forming a disulfide bond between 5 and 16 cysteine residues.

Interaction with membrane mimetic

The interaction of antimicrobial peptides with a membrane, followed by a change in its transport properties, is an important aspect of studying antimicrobial activity. The interaction with the membrane is also important for molecules that can be used as delivery system.

Here we studied the interaction with the membrane of the AMP M1 and 4,8,14,18,23,26,28,31,32,35-deca - [(N- (2 ', 2', 2'-triethylaminoethyl) -carbamoylmethoxy] pillar[5]arene, which is able to bind to DNA and increase the efficiency of bacterial transformation [7] (Figure 3).

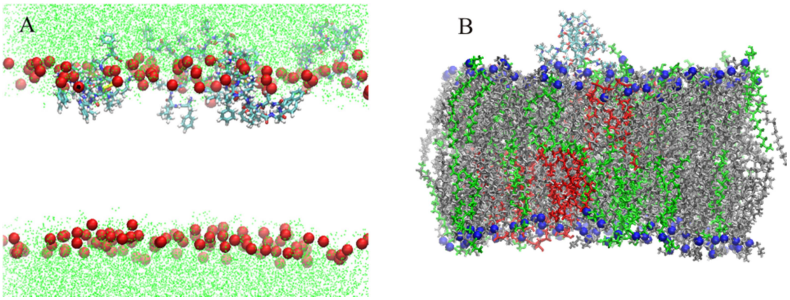

Figure 3. Snapshot of the MD trajectory. (A – M1, B – pillar[5]arene)

Molecular dynamics experiments have shown that the peptide M1 and pillar[5]arene both interact with the membrane surface model. In addition, M1 increases the permeability of the membrane for water molecules [8].

The effect of membranotropic molecules on the membrane permeability can correlate with the effect on the electrical conductivity of water/AOT/decane microemulsions (reverse micelles with a water core).

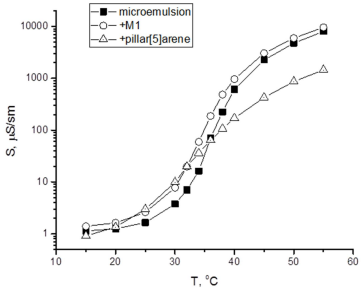

Figure 4. Temperature dependence of the electrical conductivity of the microemulsion

As can be seen from the figure 4, the M1 and pillar[5]arene both affect the electrical conductivity of the microemulsion. The electrical conductivity of a microemulsion with M1 or pillar[5]arene is higher than in the absence of a membranotropic additive at room temperature.

Thus, we can conclude that megin-1 and pillar[5]ararene both interact with the membrane, change its transport properties and act differently on bacterial cells.

Acknowledgements

This work was partially supported by the Russian Foundation for Basic Research and the Government of Tatarstan Republic (№ 18-44-160013)

This work was performed by the financial support from the government assignment for Federal Research Center (FRC) Kazan Scientific Center of Russian Academy of Sciences (RAS)

The authors gratefully acknowledge the Assigned Spectral-Analytical Center of FRC Kazan Scientific Center of RAS for possibility to fulfill the NMR experiments.

References

1. Ali Adem Bahar, Dacheng Ren. – Pharmaceuticals., 6(12), 1543-1575 (2013).
2. K. He, S.J. Ludtke, D.L. Worcester, H.W. Huang. Biophys. J., 70, 2659–2666 (1996).
3. A. Ravi, P. Balaram. Biochim. Biophys. Acta, 745, 301-309 (1983).
4. J. Cavanagh, W.J. Fairbrother, A.G. Palmer, N.J. Skelton, M. Rance. Protein NMR Spectroscopy. Academic Press, San Diego, 1996.
5. Y. Shen, F. Delaglio, G. Cornilescu. J. Biomol. NMR, 4, 213-223 (2009).
6. P. Güntert, C. Mumenthaler, K. Wüthrich. J. Mol. Biol., 273, 283-298 (1997).
7. P.V. Skvortsova, D.A. Faizullin, E.A. Ermakova, D.N. Shurpik, N.E. Gogoleva, Yu.V. Gogolev, S.A. Ziganshina, I.I. Stoikov, Yu.F. Zuev, B.I. Khairutdinov J. Mol. Liq. 319, 114178 (2020).
8. P. Skvortsova, Y. Valiullina, N. Baranova, D. Faizullin, Y. Zuev, E. Ermakova. Spectrochim. Acta A Mol. Biomol. Spectrosc., 264, 120273 (2022).

Ionic properties of pentafluoridozirconic acid hydrates according to NMR spectroscopy

Slobodyuk A.B., Didenko N.A.

Institute of chemistry, FEB RAS, 159, Pr. Stoletiya Vladivostoka, 159, Vladivostok, Russia
E-mail: ampy@ich.dvo.ru

Most of the zirconium(IV) fluorides or its mixed-ligand compounds can be synthesized from the solution of penta- or hexafluoridozirconium acids with liquid-phase methods [1]. Fluoridozirconates crystallizing under certain conditions can be considered as derivatives of $HZrF_5$ and H_2ZrF_6 existing only in hydrated forms. The presence of acidic protons H^+ in hydration network of acids and the formation of specific proton structures $H(H_2O)_n^+$ determines significant differences between these networks and those of salts. The structure of network depends on the degree of hydration (n) and external H-bonds with the anion determining the protonic mobility and conductivity of these compounds.

The ^1H NMR spectrum of the $HZrF_5 \cdot 3H_2O$ at temperature 150 K and below is presented by a pair of Pake doublets. The shoulders of doublets are resolved in the strong field and overlap in the weak field side of the spectrum, which leads to spectrum asymmetry (Fig. 1, a). The absence of a central signal in the spectra recorded at the indicated temperatures suggests that H_3O^+ or $H_5O_2^+$ groups are absent in the structure of the compound. At 170 K, the spectrum is completely transformed - a central component emerges, and individual components of the doublets are no longer observed. At higher temperatures the transformation of both components and redistribution of their intensity takes place. At temperature as low as 270 K, the half-width of the spectrum decreases to 1.8 kHz. The observed transformation of the ^1H NMR spectra suggests that the compound undergoes a superionic phase transition in the temperature range 150-170 K. The low-temperature phase $HZrF_5 \cdot 3H_2O$ contains protons bound to F^- ions into HF molecules according to the reaction: $F^- + H_3O^+ \leftrightarrow HF + H_2O$, which corresponds to the decomposition of the $H(H_2O)_3ZrF_5 \leftrightarrow ZrF_4 + HF + 3H_2O$.

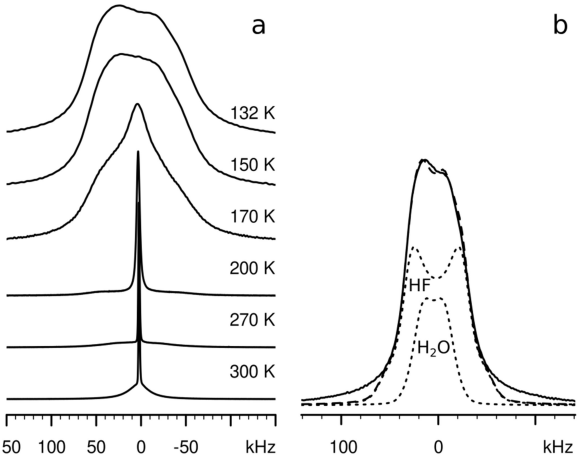

Figure 1. ^1H NMR spectra of $HZrF_5 \cdot 3H_2O$ at various temperatures (a), and its deconvolution of the 150 K spectrum (b, solid line) into components (dotted lines). The sum of components is plotted with a dashed line.

The splitting of the doublet (Fig. 1 b) corresponding to HF molecules (51.6 kHz) is in good agreement with the literature data. Thus, the internuclear distance in the HF molecule in the solid state according to ^{19}F NMR data was 1.01 Å, which corresponds to the 51.6 kHz splitting of the ^{1}H NMR spectrum [2]. Close values of the splitting in the ^{1}H NMR spectra were obtained for the crystal solvates $K_2SnF_6 \cdot HF$ and $K_2SnF_6 \cdot 4HF$ (α = 49.2 and 46.6 kHz, respectively) [3]. The splitting of the narrower doublet from the molecules of crystallization water (25.9 kHz) corresponds to the interproton distance of 1.52 Å, which is also typical of crystal hydrates [3].

Above the temperature of the assumed phase transition (≈160 K), a central component appears in the spectrum, indicating the formation of groups of an odd number of interacting spins (H_3O^+). The high-temperature modification is characterized by the presence of proton diffusion, as evidenced by a decrease in the width of the central component and a change in the shape of the entire spectrum with increasing temperature.

The retention of the wide component in the spectrum indicates the presence of immobile proton-containing groups in the $H(H_2O)_3ZrF_5$ acid composition and can be explained by its incomplete ionization. The presence of a certain amount of $ZrF_4 \cdot HF \cdot 3H_2O$ associate in the mixture can explain the signal with the CS of -127 ppm in the ^{19}F NMR spectrum of the compound. This value corresponds to a significant increase in the Zr-F distance, which can be due to the replacement of fluoride ligands with HF molecules in both modifications of the compound. It should be noted that this component becomes apparent as a result of the motion of the HF group. The activation energy of the motion can be estimated from the Waugh-Fedin relation and constitutes 0.27 eV.

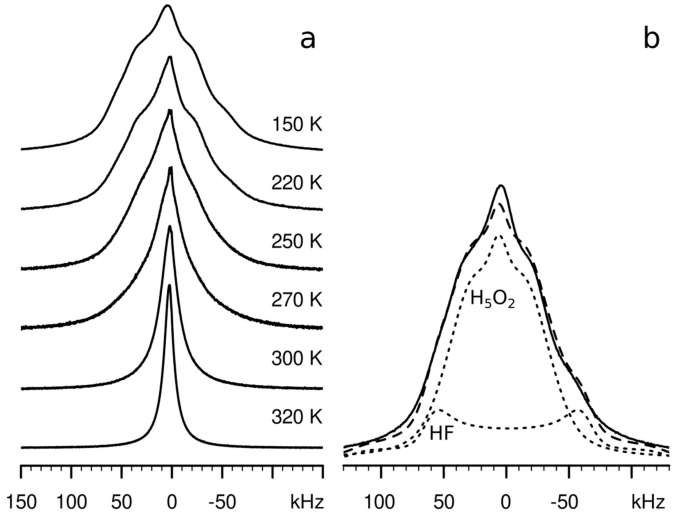

Figure 2. ^{1}H NMR spectra of $HZrF_5 \cdot 2H_2O$ at various temperatures (a), and its deconvolution of the 150 K spectrum (b, solid line) into components (dotted lines). The sum of components is plotted with a dashed line.

The ionized form of the high-temperature modification $HZrF_5 \cdot 3H_2O$ is characterized by the presence of proton diffusion, as evidenced by a decrease in the width of the central component and a change in the overall shape of the ^{1}H NMR spectrum with increasing temperature. In the case of translational diffusion of a proton, the latter will be coordinated in

turn by all oxygen ions of the cationic chain. However, the presence of the non-ionized acid "molecules" excludes the participation of some protons in the diffusion process.

The presence of the central component in the ^{1}H NMR spectrum of $HZrF_5 \cdot 2H_2O$ (Fig. 2, a) at 150 K indicates that a dipole-dipole interaction of an odd number of particles takes place. Such a spectrum can either be represented by the sum of signals from non-interacting H_2O molecules and H_3O^+ ions, or correspond only to $H_5O_2^+$ ions. The calculation of the spectrum under the last of the assumptions makes it possible to obtain the better fit to the experimental spectrum. For the calculation, we used a configuration of five protons located at the vertices and at the intersection of the diagonals of a rectangle with sides of 1.5 and 3.7 Å; the chemical shielding was assumed to be isotropic. The feature at -50 kHz cannot be simulated by varying the geometry of the $H_5O_2^+$ ion and shielding parameters; therefore, the only possible explanation is the existence under these conditions a certain amount of the non-ionized form of acid, which is also noted for $HZrF_5 \cdot 3H_2O$.

The broad component in the ^{1}H spectrum (Fig. 2 b) is explained by the presence of HF molecules in the structure of compound (the non-ionized acid form). The area of the Pake component corresponding to HF in the ^{1}H NMR spectrum constitutes 18%. The splitting of the component (58.3 kHz) is slightly higher compared to the values available in the literature. At 200–220 K, the onset of the spectrum transformation is observed (Fig. 2, a). The onset is associated with the emergence of motions in the proton subsystem of the compound. The transformation consists in the gradual smoothing of the features of the triplet and the transition of the spectrum at 320 K to the Lorentzian form with a half-width of 11.9 kHz. This value suggests that the motions consist in the exchange of protons within the $H_5O_2^+$ group, as a result of which the protons become dynamically equivalent, the intramolecular contribution to the shape of the spectrum disappears, and the width of the latter is determined mainly by the dipole-dipole interactions of protons with the nuclei of fluorine atoms.

Acknowledgements

This work was supported by the RFBR fund; project no 20-03-00279.

References

1. Davidovich R.L., Marinin D. V., Stavila V., Whitmire K.H. Stereochemistry of fluoride and mixed-ligand fluoride complexes of zirconium and hafnium, Coord. Chem. Rev. 257 (21-22) (2013) 3074–3088. doi:10.1016/j.ccr.2013.06.016.
2. Gabuda S.P., Gagarinskiy Yu.V. Doklady Akademii Nauk SSSR **1972**, 2 (5), 1065–1067.
3. Gabuda S.P., Gagarinskiy Yu.V., Polishchuk S.A., NMR in the Inorganic Fluorides, Atomizdat, Moscow, Russia, **1978**. 260 p. (In Russian)

^{1}H High-resolution NMR relaxometry for olive oil research

Mark Smirnov, Ivan Mershiev, Galina Kupriyanova

Institute of Physics, Mathematics and Information Technology, *Immanuel Kant Baltic Federal University, 236041, Kaliningrad, Russia*
E-mail: smirnov.mark2015@yandex.ru
http://kantiana.ru

Introduction

The regular addition of extra virgin olive oil to diet has a positive effect on human health, because the high content of mono-unsaturated acids (primarily oleic acid) in olive oil helps maintain normal blood cholesterol level. At the same time, polyphenols contained in extra virgin olive oil contribute to the protection of blood lipids from the oxidative process [1]. Also, olive oil may also be considered as functional food, because it helps to reduce blood pressure, destroys cancer cells, and also helps to reduce hardening of arteries [2].

Many of these health benefits are unique to extra virgin olive oil. Extra virgin olive oil is obtained exclusively by mechanical methods, such as pressure or centrifugation without any chemical treatment. This results in relatively limited production and high price, which in turn makes extra virgin olive oil susceptible to counterfeiting, in which olive oil is adulterated with cheaper oil, most commonly rapeseed or soybean.

Thus, the authentication and quality control of extra virgin olive oil is a complex and crucial task for the olive oil industry, but traditional methods are often laborious, complicated and require sample preparation.

Nuclear magnetic resonance spectroscopy has been successfully used for researching the quality of food products, including vegetable oils. In the article [3], it was found out the possibility of using the method of high-resolution ^{1}H NMR spectroscopy to detect the adulteration of extra virgin olive oil with cheaper soybean oil. It was possible to establish that high-resolution NMR is able to detect up to 4.5% adulterant of soybean oil in olive oil.

The aim of this work was to determine the content of main fatty acids in four different samples of olive oil produced in Spain and Turkey using high-resolution ^{1}H NMR spectra, and also to find out the possibility of using NMR relaxometry to identify olive oil samples.

Experiment

High-resolution NMR spectra of olive oil were obtained on a Varian 400 MHz NMR spectrometer with a constant magnetic field B = 9 T with the following parameters: spectral width was 16 ppm, relaxation delay was 1 second, and the number of scans was 16. A small amount of TMS was added to one of the samples to determine chemical shifts.

Spin-lattice relaxation times of protons T_1 were measured using the inversion-recovery pulse sequence, and spin-spin relaxation times T_2 were measured using the Carr-Purcell-Meiboom-Gill (CPMG) pulse sequence. Relaxation measurements were carried out at the temperature t = 26°C. T_1 relaxation times were obtained with following parameters: scans – 4, relaxation delay – 20 s, total time of the experiment - 20 min., while the parameters for measuring T_2 relaxation times was: scans – 4, relaxation delay – 10 s and total experiment time – 8 min and 48 s.

Results and discussion

High-resolution ^{1}H NMR spectra of four olive oil samples were obtained (Fig. 1). The integral intensity of the main signals in the ^{1}H NMR high-resolution spectrum was calculated using the MagicPlot program. To calculate the percentage of basic acids in the olive oil, the method proposed in the article [4] was used. The percentage of linolenic, linoleic acids, as well as mono-unsaturated and saturated fatty acids was established. The results are shown in

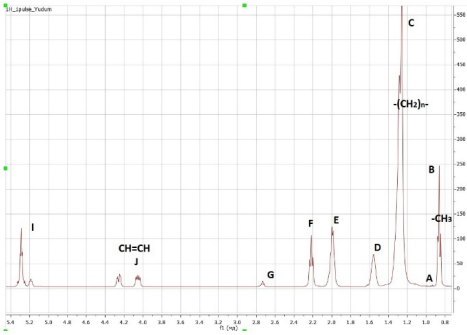

Figure 1. High-resolution 1H NMR spectra of the Yudum brand olive oil.

Table 1, where one sample of soybean oil was also added for comparison, the composition of which was obtained in the article [5].

The advantage of using high-resolution NMR to measure relaxation times is that in one experiment it is possible to determine the relaxation times of all nonequivalent protons and compare them with their chemical shifts. The results of determining the longitudinal T_1 and transverse T_2 relaxation times for olive and soybean oils are shown in Fig.2.

Figure 2 (a) shows T1 relaxation profiles of four olive oil samples and one soybean oil sample (from [5]), which clearly demonstrate differences in the nature of the longitudinal relaxation of CH_3, CH_2 and CH=CH protons, as well as changes in time longitudinal relaxation, different varieties of olive oils.

Table 1. Percentage of main fatty acids in olive oil.

Samples	Linolenic, %	Linoleic, %	Mono-unsat.FA, %	Saturated FA, %
Yudum	2,37	14,2	65	18,43
ITLV	2,07	16,1	57,63	24,2
Kamili	2,12	17,5	54,4	25,7
Borges 2021	2,49	13,1	59	25,5
Soybean oil	14	37	28	21

A number of characteristic regions of the relaxation profile depending on the sample can be distinguished:

1. The proton signals of the CH_3 groups (line B) are characterized by the longest T_1 relaxation times. For olive oils, they lie in the range of 0.9 to 1.03 s, while for soybean oils, an increase to a range of 1.08 - 1.5 s is observed. The relaxation time of signal A, which is responsible for the relaxation of protons of the CH_3 group of linolenic acid, in soybean oils ranges from 1.08 to 2.23 s, while in olive oils the relaxation time is shorter and ranges from 0.84 to 1.89 s.

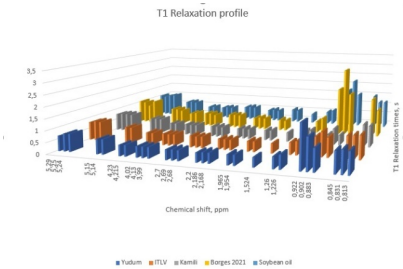

Figure.2 (a). T1 relaxation profile of four olive and one soybean oils.

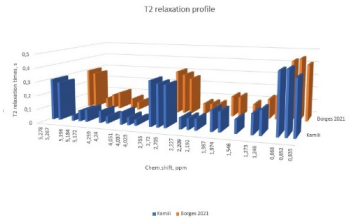

Figure.2 (b). T2 relaxation profile of two olive oil samples – Kamuli and Borges 2021.

2. The relaxation times of CH=CH protons (line J) of unsaturated acids in olive oil samples vary slightly in the range from 0.47 to 0.61 s.

3. The relaxation times of protons of CH_2 groups (lines D, E, F) for each type of oils have very close values. For olive oils, T_1 ranges from 0.41 to 0.56 s.

Figure 2(b) shows the T_2 relaxation profiles of two olive oil samples. The analysis showed that four characteristic regions of transverse relaxation times can be distinguished for olive oils:

1. Relaxation times of CH_3 group protons (B line) are in the range from 0.4 s to 0.46 s and are also the longest.
2. Relaxation times of CH group protons (line J) are in the range from 0.04 s to 0.09 s.
3. The relaxation times of the protons of the all CH_2 groups (D, E, F lines) with the exception of glyceride CH_2 group protons are in the range from 0.08 s - 0.15 s.
4. The relaxation times of the protons of the glyceride CH_2 groups are shortest and have the value in the range from 0.04 - 0.09 s.

The high-resolution NMR method makes it possible not only to analyze the distribution of relaxation times for nonequivalent protons, but also to estimate the fraction of protons with relaxation times related to each of the selected time ranges. Figure 3 shows the distribution of longitudinal relaxation times for olive oil samples as the dependence of proton relaxation times on the total integral of spectral lines, which is proportional to the fraction of protons with a certain relaxation time.

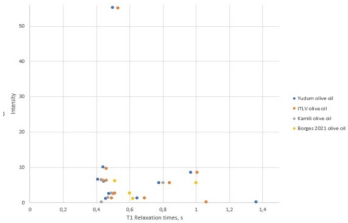

Figure.3. Distribution of time Tl relaxation of four samples of olive oils depending on the integral intensity of the

Conclusion

The percentage of essential fatty acids in olive oil samples was determined.

Characteristic areas of the T_1 and T_2 relaxation profile of oils can be used to distinguish between samples, as well as markers to automate the process of searching for counterfeit products.

References

1. Are health claims a useful tool to segment the category of extra-virgin olive oil? Threats and opportunities for the Italian olive oil supply chain / Luigi Roselli, Maria Lisa Clodoveo, Filomena Corbo, Bernardo De Gennaro. // Trends in Food Science & Technology. – 2017. – № 68. – C.176–181.
2. Maninder Meenu. A critical review on analytical techniques to detect adulteration of extra virgin olive oil / Maninder Meenu, Qianxi Cai, Baojun Xu // Trends in Food Science & Technology. – 2019. – № 91. – C.391–408.
3. Comparison of 19F and 1 H NMR spectroscopy with conventional methods for the detection of extra virgin olive oil adulteration / X.Y. Jiang, C. Li, Q.Q. Chen, X.C. Weng // Grasas y Aceites. – 2018. – № 69 (2). – https://doi.org/10.3989/gya.1221172
4. Nicoleta-Aurelia Chira, Maria-Cristina Todasca, Alina Nicolescu, Aurelia Rosu, Mihaela Nicolae, Sorin-Ioan Rosca. Evaluation of the Computational Methods for Determining Vegetable Oils Composition using ^{1}H NMR Spectroscopy. REVISTA DE CHIMIE, 2011, 62, https://www.researchgate.net/publication/267802323
5. Mark Smirnov, Ivan Mershiev, Galina Kupriyanova. 1H high-resolution NMR spectrometry and relaxometry for soybean oil research. Magnetic Resonance and its Applications. Spinus-2021. Proceedings. Saint Petersburg State University, 2021. 282 pp. ISSN 2542–2049

Mapping of experimental vs quantum-calculated 15N-C spin interactions sharply increases the reliability of elucidating the structure of nitrogen-containing compounds

Vladislav V. Stanishevskiy[1], *Alla K. Schestakova*[2], *Vyacheslav A. Chertkov*[1]

[1] *Department of Chemistry, Moscow State University, Moscow, 119991 Russia*
[2] *State Scientific Research Institute of Chemistry and Technology of Organoelement Compounds, Moscow, 105118 Russia*
E-mail: Stvladislav@yandex.ru

Introduction

Experimental NMR spectroscopy, combined with modern quantum mechanical calculations, has now become an indispensable tool for studying the structure of organic compounds. In particular for nitrogen containing compounds, ^{15}N chemical shifts and indirect spin-spin coupling constants ^{15}N-^{13}C are very promissing to determine the alkylation position in purines and to study tautomeric, acidic, complexing equilibria and intermolecular interactions.

^{15}N NMR spectroscopy has proven particularly useful for studying these phenomena because nitrogen atoms are directly involved in many of these processes. It has long been known that indirect spin-spin coupling constants are invaluable parameters for determining protonation sites and studying tautomeric equilibria in solution.

Comparison of the experimental and calculated values of the spin-spin interaction constants makes it possible to judge the accuracy of the quantum mechanical method. Such comparisons make it possible to predict with a high degree of accuracy the values of the direct and long-range spin-spin interaction constants between the nitrogen and carbon nuclei.

Methods

Quantum chemical calculations.

All quantum chemical calculations were performed using the GAUSSIAN 09 W software package.

The structures of the studied objects were optimized in the vacuum approximation by the density functional method (DFT) with the hybrid density functional (B3LYP) and basis functions 6-311++G(2d,p). We have chosen the DFT method, as it is more satisfactory according to required calculation time and convergence of self-consistency procedure (SCF). The nuclear spin-spin couplings ^{13}C-^{15}N were calculated by the FPT-DFT method in the B3LYP approximation with the 6-311++G(2df,2p) basis. All four component terms: Fermi-contact, spin-dipole, orbital-paramagnetic, and orbital-diamagnetic were calculated to obtain the SCF.

The calculations were performed in the "mixed" mode, which allows us to significantly reduce the level of computational costs during the calculation. A characteristic feature of this mode is the subdivision of the calculation into two stages. At the first stage, the Fermi-contact term is calculated using a basis set containing somewhat larger number of polarization components. At the second stage, the remaining three terms with somewhat simpler basis functions are calculated, which allows to optimize the calculation time by a factor of two or three without appreciable loss of accuracy. The nuclear spin-spin couplings were calculated for the previously optimized conformation of the molecule.

In this work, we used experimental data on one-bond and long-range spin-spin coupling constants of ^{15}N-^{13}C from [1-3].

Results

Comparison of the experimental and calculated values reveals a good correlation for the entire set of spin-spin interaction constants through one, two, three, and four bonds, see Fig. 1.

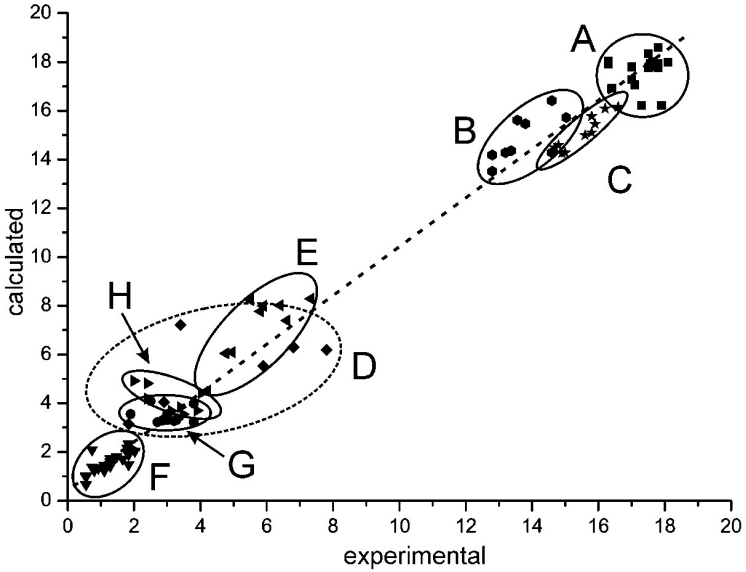

Figure 1. Comparison of experimental and calculated nuclear spin-spin couplings $^{n}J_{CN}$, where n = 1-4 in the series of compounds studied. A(■ - $^{1}J_{CN}$ in nitriles), B(⬢ - $^{1}J_{CN}$ of indole nitrogen atom), C(★ - $^{1}J_{CN}$ in aromatic nitro compounds), D(♦ - $^{1}J_{CN}$ of sp^2-hybridized nitrogen atom), E(◄ - $^{2}J_{CN}$ in aromatic compounds), F(▼ - $^{n}J_{CN}$, n≥3), G(● - $^{2}J_{CN}$ in nitriles), H(► - $^{3}J_{CN}$ of the quaternized nitrogen atom).

Area A corresponds to the spin-spin interaction constant $^{1}J_{CN}$ in substituted benzonitriles and aliphatic compounds containing the nitrile group. Both, calculated and experimental values of these constants are in a narrow range. The introduction of substituents into the benzene ring of benzonitriles as well as changes in the structure of aliphatic nitriles weakly affect the values of $^{1}J_{CN}$ constants, which allows this type of spin coupling to be reliably recognized.

Area B corresponds to the spin-spin coupling constants of the indole nitrogen atom with the carbon atom through one bond. The indole nitrogen atom is found in many of organic compounds and their natural derivatives. The values of these couplings are characterized also by a narrow range of values, both for the unsubstituted nitrogens and for the N-substituted analogues.

The $^{1}J_{CN}$ couplings in aromatic nitro compounds are characterized also by a narrow range of values and are represented in Fig. 1 by area C. As in the case of the nitriles, the direct spin-spin interaction constant weakly depends on the nature of other substituents in the benzene ring and provides a reliable indication of the presence of the nitro group in the aromatic ring studied.

The D region corresponds to a wide range of values of the $^{1}J_{CN}$ couplings for the sp^2-hybridized nitrogen atom. This type of nitrogen atom is widely represented in organic compounds. The variety of values of the $^{1}J_{CN}$ couplings in these systems emphasizes the significant influence of electronic and structural factors on the value of the couplings.

In contrast, the presented in the E region germinal spin-spin coupling of carbon with nitrogen in aromatic compounds has scattered range of values. In the aromatic ring the nitrogen atom can have either pyrrolic-N or pyridinic-N type, which significantly affects the value of corresponding coupling. These couplings also depend on the spin-spin coupling pathway and therefore varies over a wide range of values.

The F region again corresponds to a narrow range of values of the long-range couplings of the nitrogen atom and carbon in various objects. The study of long-range spin-spin couplings can allow detailed characterization of the molecular structure and electronic properties of atoms, but special high resolution NMR techniques are needed for accurate experimental observation of so small couplings. The high degree of correlation between experimental and theoretical values allows the NMR experiment to be planned in advance for reliable observation of some specific long-range couplings between nitrogen and carbon atoms.

The $^{2}J_{CN}$ couplings also appears for compounds containing a nitrile group. Comparison of experimental and calculated values (region G) indicates a narrow range of values of this type of couplings. Like $^{1}J_{CN}$, the couplings across two bonds are weakly dependent on the structure of the organic substance.

The H region corresponds to the $^{3}J_{CN}$ couplings with the quaternized nitrogen atoms. The narrow range of values overlaps with many other couplings, however, allows us to reliably predict value of the specific couplings, which in turn can serve as important argument in study of acid-base interactions in nitrogen containing systems.

Statistical treatment of all data used in current study (102 spin-spin couplings) was performed in terms of the one-parameter linear regression model:

$$\mathbf{J^{exptl} = \alpha J^{calcd} + \beta.} \qquad \mathbf{(1)}$$

For equation **1**, the correlation coefficient is 0.99 with the value of the slope coefficient, insignificantly different from unity ($\boldsymbol{\alpha} = 0.97 \pm 0.01$) and the free term ($\boldsymbol{\beta} = 0.70 \pm 0.14$). The root-mean-square deviation of the experimental and calculated nuclear spin-spin couplings is 0.90 Hz, which is comparable with the accuracy of our experimental measurements and the entire set of quantum-mechanical calculations.

Conclusions

In our opinion, the form of representation of theoretical and experimental data used in this work as a two-dimensional cross-correlation mapping can give a clear and reliable idea of the structure of a nitrogen-containing compound according to nuclear magnetic resonance data.

References

1. R. Marek. NMR Applications, ^{15}N. *Encyclopedia of Spectroscopy and Spectrometry*, 110–116 (2017).
2. R. Marek, A. Křístková, K. Maliňáková, J. Toušek, J. Marek, M. Hocek, V.G. Malkin. *The Journal of Physical Chemistry A*, **114(24),** 6689–6700 (2010).
3. V.V. Stanishevskiy and cow., 2022, to be published.

Orientational and translational mobility in ionic liquid propylammonium nitrate

Milosh Ubovich, Vladimir V. Matveev, Vladimir. I. Chizhik

Faculty of Physics, Saint-Petersburg State University, Russia
E-mail: ubovich.milosh@yandex.ru

Introduction

Nowadays alkylammonium nitrate protic ionic liquids (AN PILs) are being investigated intensively. Ionic liquids (ILs) are compounds that are composed entirely of ions. Unlike "classical" salts, they are in a liquid state at the room temperature or close to it [1]. It is known that due to their remarkable properties ILs are prospect substances in enormous number of different practical applications (such as lubricants, lithium ion batteries, fuel cells, etc.) [2-7]. ILs have high thermal stability and ionic conductivity, negligible vapor pressure, wide electrochemical window, etc. It is also worth noting that AN PILs have a relatively low cost and low toxicity. In the present investigation the propylammonium nitrate (PAN) was explored by NMR. PAN consists of the propylammonium cation (Fig. 1) and the nitrate-anion.

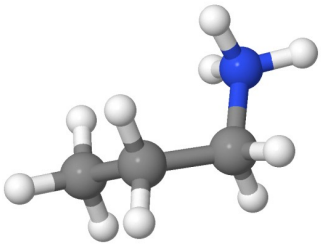

Figure 1. The schematic representation of cation propylammonium nitrate (hydrogen – white, nitrogen – blue, carbon – grey)

Results and discussion

Initially, the ^{1}H NMR spectrum of the investigated sample was registered. It was found that the sample of PAN contains a certain amount of water. The sample was dried using the device consisting of a heater and fore-vacuum pump with a nitrogen trap. Dependences of spin-lattice relaxation times (T_1) and diffusion coefficients on the temperature were measured for the dried PAN sample using spectrometer Bruker Avance III 500 MHz.

The measurements of ^{1}H relaxation times were made in the temperature range from 5 to 100 ^{o}C in increments of 5 K, the measurements of ^{13}C relaxation times were made in the temperature range from 25 to 100 ^{o}C in increments of 5 K. The dependence of the ^{1}H diffusion coefficients on the temperature was also measured in the range from 25 to 100 ^{o}C and the dependence of the ^{13}C diffusion coefficients on the temperature was measured in the range from 25 to 70 ^{o}C. The examples of results are presented in Fig. 2 and 3.

Temperature dependences of the spin-lattice relaxation rates and diffusion coefficients were investigated in order to analyze the molecular mobility of the PAN. Regretfully, the explored temperature range was not enough to reach a maximum in relaxation rates, and measurements are required at higher magnetic field. However, the correlation times were roughly estimated using the initial part of the dependences and SBPP equation [8]:

$$\frac{1}{T_{1\mathrm{H}}} = s_{\mathrm{H}}^2 A_{0\mathrm{H}} \left(\frac{\tau_c}{1+(\omega_{\mathrm{H}}\tau_c)^2} + 4\frac{\tau_c}{1+(2\omega_{\mathrm{H}}\tau_c)^2} \right) ,$$

where τ_c is the correlation time; ω_H is the cyclic resonant frequency ($2\pi\upsilon_0$) for ^{1}H; $s_H^2(\leq 1)$ is the order parameter; A_{0H} is the constant which does not depend on temperature and frequency.

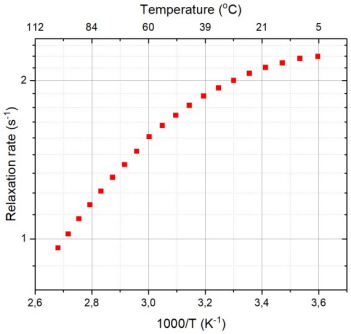

Figure 2. The dependence of the ^{1}H spin-lattice relaxation rates on the temperature (for NH_3 line)

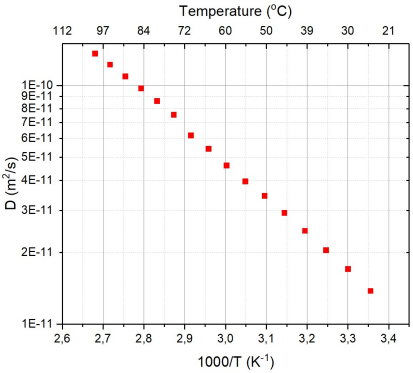

Figure 3. The dependence of the ^{1}H diffusion coefficients on the temperature (for NH_3 line)

Acknowledgments

The NMR measurements have been carried out in the Center for Magnetic Resonance of Research Park of Saint Petersburg State University.

References

1. Hayes R., Warr G. G., Atkin R. – Chem. Rev. 2015. V. 115. P. 6357.
2. Ghandi K. A. – Green Sustainable Chem. 2014. V. 4. No. 1. P. 44.
3. Lu X., Burrell G., Separovic F., et al. – J. Phys. Chem. B. 2012. V. 116. No. 30. P. 9160.
4. Fedorov M. V., Kornyshev A. A. – Chem. Rev. 2014. V. 114. No. 5. P. 2978.
5. Menne S., Pires J., Anouti M., et al – Electrochem. Commun. 2013. V. 31. P. 39.
6. Timperman L., Béguin F., Frackowiak E., et al. – J. Electrochem. Soc. 2014. V. 161. No. 3. P. A228.
7. M. Salanne – Top. Curr. Chem. 2017. V. 375. No. 3. P. 63.
8. Solomon I. – Phys. Rev. 1955. V. 99. No. 2. P. 559.

Hole burning in ODMR spectra in isotope-modified SiC

Veyshtort I.P.[1,2], Breev I.D.[1], Baranov P.G.[1], Anisimov A.N.[1]

[1]Ioffe Institute
[2]ETU «LETI»
E-mail: igorveyshtort@gmail.com

Introduction

Optically addressable, controlled by microwaves, and retaining quantum coherence even at room temperature, the electronic spin of the V-center in SiC can be used as a magnetic sensor. An increase in sensitivity is possible when using hole burning (HB) optically detectable magnetic resonance (ODMR) methods and choosing the optimal silicon carbide material with a reduced concentration of paramagnetic defects and a modified content of ^{29}Si and ^{13}C isotopes with nuclear magnetic moments

Samples

Samples of silicon carbide 6H-SiC crystals with different isotope concentrations were studied (fig.1). Sample 1 had a natural concentration. Sample 2 had decreased Si isotope concentration, and increased C. The third sample was enriched with isotope 13C. These concentrations are summarized in table 1.

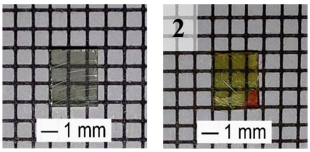

Figure 2. 6H-SiC samples

Table 1. Isotope concentrations of samples

№	^{28}Si, %	^{29}Si, %	^{30}Si, %	^{12}C, %	^{13}C, %
1	92.23	4.67	3.10	98.93	1.07
2	99.92	0.076	0.006	95.28	4.72
3	92.23	4.67	3.10	84.77	15.23

Structure of V-centers

The object of the study is negatively charged silicon vacancy centers in SiC. Fig. 2 shows energy diagram and crystalline structure of these centers.

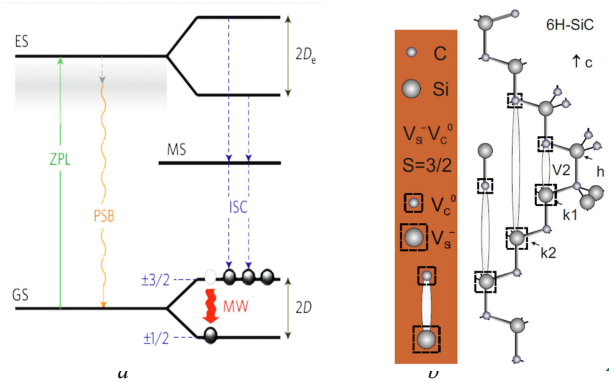

a *b*

Figure 3. Structure of V-centers: a) energy configuration, b) crystalline

Scheme of the experiment

Fig. 3 shows optical-electrical scheme of experimental stand. The arrows indicate the wired connections of the devices. The red lines represent the course of the laser beam and the collected luminescence. Focusing on the sample is done with a confocal microscope. Registration is carried out in an asynchronous mode.

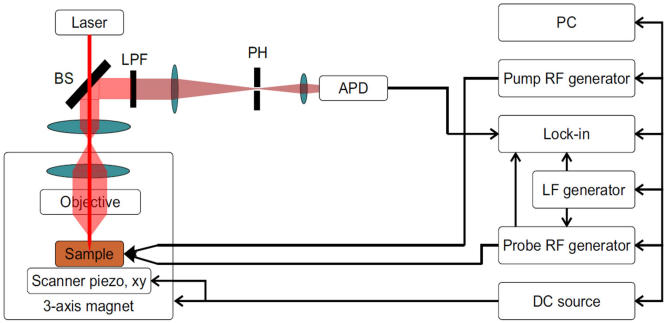

Figure 4. Experimental setup

Experimental data

ODMR spectrum of the V3-center for the three studied samples is shown in fig. 4. The broadening is due to ^{13}C isotopes. The shift is due to a change in the crystal structure, due to a higher concentration of doping impurities.

The result of hole burning of the gap in sample 2 presented on fig. 5a. We assume that the effect we observe is related to the polarization of the spins of the 13C nuclei, through a superfine interaction. At 15/30 MHz pumping, a dip in the 30/15 MHz region is observed. At the same time, the phase of the dip at 30 MHz is reversed, which may indicate effective polarization of ^{13}C nuclei. This effect is not observed on sample 1.

Fig. 5b shows, that in both samples, the appearance of a maximum at 3 MHz associated with the ν_5 transition is observed when the gap is burned out directly on the 27 MHz line.

Results

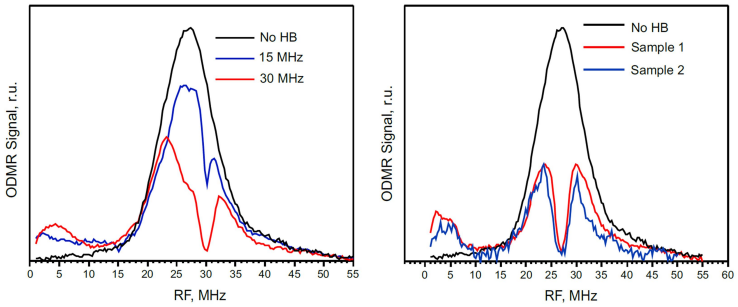

a *b*

Figure 5. Spectra with HB for samples 1 and 2

The effect of the concentration of ^{29}Si and ^{13}C native isotopes on the spin properties of the V-center ensemble in 6H-SiC was investigated. Increasing the concentration of ^{13}C leads to a frequency shift and spectral broadening of the center line (see table 2).

Table 2. Resonant line maximum position

Sample 1	Sample 2	Sample 3
5.47 MHz	7.21 MHz	7.54 MHz

The sample with a reduced concentration of 29Si and 30Si isotopes shows spin packets associated with superfine interactions with 13C isotopes.

Hole burning in the vicinity of the 27 MHz line, regardless of the isotopic concentration of the sample, leads to an intensification of the transition, to which the maximum at MHz corresponds. Probably, the observed phenomena are related to the polarization of nuclear spins through electronic states.

Acknowledgements

The study was carried out with a grant from the Russian Science Foundation (project № 20-12-00216)

References

1. "Scanning optical quantum magnetometer based on the phenomenon of hole burning" A.N. Anisimov, R.A. Babunts, I.D. Breev, A.P. Bundakova, I.V. Ilyin, M.V. Muzafarova, P.G. Baranov Letters to JETP 45, no. 10, 22-26 (2019).
2. Experimental characterization of spin-3/2 silicon vacancy centers in 6H-SiC H. Singh, A.N. Anisimov, S.S. Nagalyuk, E.N. Mokhov, P.G. Baranov, D. Suter Phys. Rev. B 101, iss. 13, #134110 (2020).

Molecular Dynamics simulation of Zinc(II) and Copper(II) binding to amyloid-β(1–16) peptide in aqueous solution, saline solution and double saline solution with Na^+ ion

Irina Yefimova[1*], *Andrei V. Komolkin*[1]

Faculty of Physics, Saint Petersburg State University, St. Petersburg, 199034, Russia
**E-mail: yefir2000@gmail.com*

Introduction

The amyloid-β peptide is observed to aggregate into fibrils in diseased brains, that's why the trigger for aggregation is one focus of research into Alzheimer's disease onset. One hypothesis on disease onset involves the role of transition metals, like copper, zinc or iron. All three ions are known to bind to amyloid-ß through the residues 1-16 and affect the structure and dynamics of the peptide, which may in turn affect aggregation properties [1].

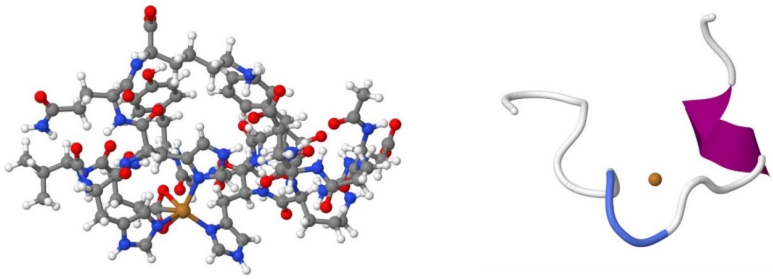

Figure 1. Copper(II) binding to amyloid-β(1–16) peptide (two forms of representation)

Computational methods

Used Software

All simulations were performed within the AKMD package with the use of OPLS-AA forcefield. Tests of forcefield and solvent model were carried out using the NMR study of Zn(II) bound to the 16 nitrogen-terminal residues of amyloid-ß (1ZE9.pdb) [2]. Then Zn(II) ion was replaces by Cu(II) ion.

Research objects

To obtain information about the behavior of Zinc(II) and Cu(II) ions with amyloid-β will be calculated the number of Hydration Bonds. It demonstrates how well has been maintained the structure of the α-helix. Also the radial distribution functions of water oxygens from Zn^{2+} and Cu^{2+} ions, the diffusion coefficients of Zinc(II) and Cu(II) ions bound to amyloid-β in solutions will be calculated.

References

1. N. Al-Shammari, L. Savva, O. Kennedy-Britten, J. A. Platts. Forcefield evaluation and accelerated molecular dynamics simulation of Zn (II) binding to N-terminus of amyloid-β. Computational Biology and Chemistry 93. 2021.
2. S. Zirah, S. A. Kozin, A. K. Mazur, A. Blond, M. Cheminant, I. Ségalas-Milazzo, P. Debey, S. Rebuffat. Structural Changes of Region 1-16 of the Alzheimer Disease Amyloid beta-Peptide upon Zinc Binding and in Vitro Aging. Journal of Biological Chemistry 281(4):2151-61. 2006.

Evaluation of zeolites acidity by ^{31}P MAS NMR spectroscopy of adsorbed phosphine oxides

Dmitry S. Zasukhin, Ivan A. Kasyanov, Yury G. Kolyagin

[1]Faculty of Chemistry, Lomonosov Moscow State University, Leninskiye Gory 1, bld. 3, 119991 Moscow, Russia
E-mail: zasuhinds@gmail.com

Introduction

^{31}P MAS NMR spectroscopy of adsorbed alkyl-substituted phosphine oxides has witnessed tremendous progress during the last years and has become one of the most informative and sensitive methods of heterogeneous catalyst acidity investigation. However, quantitative evaluation of the number of sites is still a challenge. This study clarifies the main origin of errors occurring during NMR experiments, introduces the appropriate standards (both internal and external), determines the relaxation parameters and the conditions for spectra acquisition and integration. As a result, the methodology for quantitative measurement of the acid sites' content and the amount of internal and external silanol groups is established. The application of probe molecules different in size (namely, trimethylphosphine (TMPO), tri-n-butylphosphine (TBPO) and tri-n-octylphosphine (TOPO) oxides) is shown to be a good tool for distinguishing between the active sites inside the zeolite pores, mesopores and on the outer crystal surface [1-3]. The methodology proposed is verified on BEA zeolites different in composition, texture and morphology.

The statistical analysis of the data (Table 1) shows significant deviations from the average values. The relative error for different probe molecules is within 26-33%, which is rather high for quantitative assessment of acidity. The average acidity measured by TMPO and TBPO is similar and close to the theoretical amount of Al in the sample but does not correspond to the total acidity measured by FTIR of adsorbed Py. The acidity measured by TOPO is much lower than the values obtained with other probe molecules, pointing that only part of acid sites is accessible for TOPO.

Table 1. Preliminary assessment of the acidity of AlBEA-25 zeolite

Probe molecules	Total acidity, μmol/g	Relative error, %	Total acidity by IRS of adsorbed Py, μmol/g	Theoretical amount of Al in zeolite, μmol/g
TMPO	620 ± 160	26	425	600
TBPO	600 ±170	28		
TOPO	240 ± 80	33		

The analysis of the reasons for high errors observed during NMR data quantification led us to the conclusion that there are three main sources of errors: i) the loss of probe molecules during preparation procedure; ii) incomplete relaxation of ^{31}P nuclei; iii) incorrect integration of NMR spectra.

Technique development

1) To ensure quantitative results, different external and internal standards for ^{31}P MAS NMR measurements were examined, the relaxation parameters and the conditions for spectra acquisition were determined and the procedure for quantitative integration of ^{31}P MAS NMR spectra was developed. Among the different external and internal standards investigated, $(NH_4)_2HPO_4$, GaP and $AlPO_4$-tridymite are proposed as external standards, whereas $AlPO_4$-tridymite is selected as the internal standard for NMR spectroscopic measurements. Although the use of an external standard is found to be simpler, the application of an internal standard is concluded to be more reliable.

2) The accurate measurement of spin-lattice relaxation times for all individual and adsorbed TMPO, TBPO and TOPO probe molecules, as well as for the reference compounds, suggests that for quantitative measurements of adsorbed TMPO and TBPO relatively short RDTs (40 s) are required, but to obtain quantitative data for TOPO probe molecules and $AlPO_4$-tridymite internal standard long RDT of 150 and 3600 s is needed.

3) Another important source of errors mentioned earlier is the baseline distortions observed in single-pulse experiments, which makes it difficult to integrate spinning sidebands (SSB) correctly. To solve this problem, we recorded the spectra with a Hahn-echo (HE) pulse sequence. Due to the peculiarities of such spectra, no baseline distortion is observed in them. Although these spectra are not quantitative, the ratio of intensities of the central line and SSB is the same as in single-pulse experiments (assigned further as k_{CSA}). Multiplying the intensity of the central line signal from the single-pulse experiment by this constant allows us to take into account the intensity of SSB. This approach was used for quantitative spectra integration.

Taking that, the overall formula for the calculation of the content of *i*-th sites (C_i, μmol/g) was as follows:

$$C_i = \frac{n_i}{m_{zeol}} = \frac{I_i^{cl} * k_i^{CSA}/NS}{I_{std}^{cl} * k_{std}^{CSA}/NS_{std}} * \frac{n_{std}}{m_{zeol}}$$

where n_i - the amount of probe molecules adsorbed on *i*-th sites (μmol); m_{zeol} – mass of zeolite in MAS rotor (g); I^{cl}_i – integral intensity of the central line in *i*-th region of the spectrum under study; I^{cl}_{std} – integral intensity of the central line in the spectrum of standard material; k_{CSA} – correction factors associated with the intensity of SSB signals; *NS* – the number of scans in the sample spectrum; NS_{std} – the number of scans in the spectrum of standard material; n_{std} – amount of ^{31}P nuclei in the reference sample (μmol).

Applying this methodology, we repeated the experiments on the adsorption of various probe molecules over AlBEA-25 using $AlPO_4$-tridymite as an internal standard and Hahn-echo pulse sequence to take into account the contribution of SSB. The ^{31}P MAS NMR spectrum of adsorbed TBPO on AlBEA-25 surface is given in Figure 1; the assignment of signals and regions has been performed according to literature data. The results of quantitative assessment are presented in Table 2.

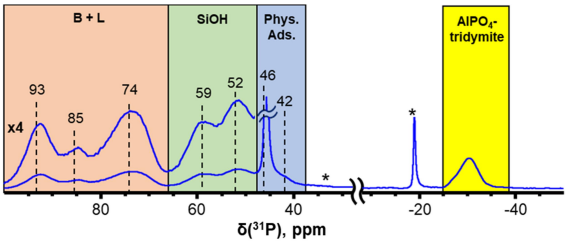

Figure 1. ^{31}P MAS NMR spectra of TBPO adsorbed on AlBEA-25 materials with $AlPO_4$-tridymite as internal standard (NS = 512; RDT = 40 s). Asterisks denote spinning sidebands. The amount of adsorbed TBPO was 2000 μmol/g. B + L – the region with overlapping Brønsted and Lewis acid sites, SiOH – the region with interaction of TBPO with silanol groups, "Phys. Ads." – physically adsorbed TBPO.

The data analysis shows that the relative error decreased to 4 – 6%, and the main errors are associated with baseline and phase correction procedures. The data obtained became more reasonable as compared to FTIR Py and the content of Al in the zeolite:

- TMPO probe molecule has the smallest size (~ 0.55 nm mean diameter). It can easily enter the pores of BEA zeolite and can interact with all its acidic sites. The number of sites

measured by TMPO corresponds to the content of Al in the sample. But overdose of probe molecules in the sample can lead to overlapping of signals in ^{31}P MAS NMR spectra, resulting in incorrect determination of acid sites content and preventing distinguishing of the peaks corresponding to silanol groups. Therefore, the amount of TMPO adsorbed should be close to the amount of acid sites in the studied sample.

- The number of sites measured by TBPO coincides with the data obtained by FTIR Py. Most probably, TBPO can enter the pores of zeolite BEA, but it cannot measure all the sites owing to sterical hindrances. In particular, it cannot measure the sites located close to each other.

- TOPO molecule has the biggest size and, most probably, cannot enter the pores of zeolite BEA. It measures the sites at the outer surface of the crystals and in the pore mouths. The results show that almost half of the zeolite acid sites are located close to the external surface of the crystal.

Table 2. Quantitative assessment of the acidity of zeolite AlBEA-25

Probe molecules	Total acidity, μmol/g	Relative error, %	Total acidity by IRS of adsorbed Py, μmol/g	Theoretical amount of Al in zeolite, μmol/g
TMPO	550 ± 20	4	425	600
TBPO	405 ± 15	4		
TOPO	160 ± 10	6		

Conclusions

Considering different sources of errors, the methodology for quantitative measurement of the content of acid sites by ^{31}P MAS NMR of adsorbed probe molecules is established. The use of internal or external standard is necessary for correct estimation of sites.

It has been suggested that for quantitative measurements of adsorbed probe molecules relatively short RDTs (40 s) are required, but to obtain quantitative data, for example, for $AlPO_4$-tridymite internal standard long RDT of 3600 s is needed.

It is proposed that the problems with baseline distortion observed in single-pulse experiments and leading to incorrect integration of SSB, can be solved by recording the spectra with a Hahn-echo pulse sequence and the determination of correction factor, which takes into account the intensity contribution of SSB.

The proposed methodology is verified on BEA zeolites with different composition, texture and morphology. The application of probe molecules different in size (namely, TMPO, TBPO and TOPO) is shown to be a good tool for distinguishing between the active sites inside the zeolite pores, mesopores and on the outer crystal surface.

Acknowledgements

The authors gratefully acknowledge Russian Science Foundation (project № 19-73-10160) for the financial support.

References

1. Zheng, A.; Huang, S.J.; Chen, W.H.; Wu, P.H.; Zhang, H.; Lee, H.K.; De Menorval, L.C.; Deng, F.; Liu, S.B. ^{31}P Chemical shift of adsorbed trialkylphosphine oxides for acidity characterization of solid acids catalysts. *J. Phys. Chem. A* **2008**, *112*, 7349–7356.
2. 2. Zhao, Q.; Chen, W.H.; Huang, S.J.; Wu, Y.C.; Lee, H.K.; Liu, S.B. Discernment and quantification of internal and external acid sites on zeolites. *J. Phys. Chem. B* **2002**, *106*, 4462–4469.
3. Freitas, C.; Barrow, N.; Zholobenko, V. Accessibility and Location of Acid Sites in Zeolites as Probed by Fourier Transform Infrared Spectroscopy and Magic Angle Spinning Nuclear Magnetic Resonance. *Johnson Matthey Technol. Rev.* **2018**, *62*, 279–290.

Poems about School

* * *

Чижик-Spinus, где ты был?
– «Я сигнал за хвост ловил!
Сделал я ему “Фурье” –
Закружилось в голове!»

Цели «Spinus»’а просты:
Дать научные мосты!
Пусть у вас здесь будет шанс
Пообщаться «в резонанс»!

В Школе здесь научат всех
Сочетать с наукой смех,
Дискотеки с Э-Пе-эР,
Я-Ка-эР и Я-эМ-эР!

В Школе много новых лиц,
Будем превращать их в птиц:
Вдруг хотя б одной из ста
Дастся «Нобель-высота»!

2010

* * *

Spinus, Spinus, where you were?
Did you dive in the Resonance world?
– “Yes! I dived with my great joy –
Resonance is a pleasant toy!”

“Spinus” school invited you
To look for a knowledge clue.
We will show the signal birth
In the field of our Earth!

If you wish to have success,
At the School achieve progress!
We will teach you all to fly
In the scientific sky!

We desire you to get
Many victories-побед!
It will be a good surprise
If you catch the Nobel prize!

2010

Author Index

Magnetic Resonance and its Applications

Proceedings

Saint Petersburg State University
March 28 — April 1, 2022

Подписано в печать 25.03.2022. Формат 60 × 84 1/16.
Бумага офсетная. Гарнитура Times. Печать цифровая.
Усл. печ. л. 15,75. Тираж 150 экз. Заказ № 1695.

Отпечатано в Издательстве ВВМ.
198095, Санкт-Петербург, ул. Швецова, 41.

Schedule of Spinus-2022 (Moscow time!)

	28.03.22 Monday	29.03.22 Tuesday	30.03.22 Wednesday	31.03.22 Thursday
Chairman	Prof. Markelov	Dr. Komolkin	Prof. Bunkov	Prof. Tolstoy
10:00 – 11:50	**Opening 20** Chizhik 50 Shushakov 20 Salikhov 35	Tupikina 40 Shavykin 15 Chakalov 15 Antonova 15 Titova 15 Nikiforova 15	Pestryaev 40 Gorbunova 20 Ivanova 15 Bogaychuk 15 Kosogornova 15	Matveev 40 Dvinskikh 20 Ubovich 15 Pronina 15 Khudozhitkov 15
11:50 – 12:10	**COFFEE BREAK**			
Chairman	Prof. Charnaya	Prof. Pirogov	Prof. Tagirov	Prof. Skrynnikov
12:10 – 14:50	Shelyapina 40 Sevastyanov 20 Gervits 20 Cherepanova 15 Pichugina I Chepeleva 15 Liamin 15 Karpov 15	Eichhof 50 Koloskov 15 Puchnin 15 Kalugina 15 Nasonov 15 Pavlova 15 Marcolan 15 Cabal Mirabal 25	Bunkov 40 Soltamov 20 Makarchenko 15 Vasilev A. 15 Yakovlev 15 Kan 15 Semakin 15 Andreev 15 Musabirova 15	Vasil'ev S. 20 Pokhvishcheva 15 Shpotya 15 Slesarenko 15 Kaplanskiy 15 Sheludiakov 15 Lezova 15 Korostelev 15 Gavrilova 20
14:50 – 15:50	**LUNCH**			**MEETING OF AWARDING COMMISSION**
Chairman	Prof. Shelyapina	Dr. Egorov	A. Ievlev	
15:50 – 17:40	Gavrilenko 20 Anisimov A. 20 Slobodyuk 20 Pichugina II 15 Zasukhin 15 García Naranjo 15	Pirogov 40 Anisimov N. 20 Solcia 15 Reyes-Molina 15 Viña-González 15	**POSTER SESSION** Oral blitz reports of young scientists (5min x 15) **15:50 – 18:40**	**Awarding (16:00)** **Closing**